Evaluating the suitability of Li_8PbO_6 as a tritium breeding material using first-principles simulations

Andrew William Davies,

Department of Engineering

Lancaster University

A thesis submitted for the degree of

Doctor of Philosophy

March, 2024

Evaluating the suitability of Li_8PbO_6 as a tritium breeding material using first-principles simulations

Andrew William Davies.

Department of Engineering, Lancaster University

A thesis submitted for the degree of *Doctor of Philosophy.* March, 2024.

Abstract

A desire to move away from ceramic breeder materials that display a dependence on the use of a beryllium multiplier, has seen octalithium compounds and particularly, Li_8PbO_6, being considered for application in a future fusion reactor. Although, there is little understanding of many of the basic properties of the material, importantly how it might behave as a tritium breeding material.

By virtue of proximity to the fusion plasma, the extreme operating environment the breeding material will be subject to inherently gives rise to a significant population of defects throughout the operational lifetime. This has implications for the not only the macroscopic physical properties of the material, but also the mechanisms for tritium accommodation and release.

Modern first-principles simulations such as Density Functional Theory are widely used to study the fundamental properties of crystalline materials, including the behaviour of both intrinsic and extrinsic point defects. In this thesis, DFT is used to assess the feasibility of Li_8PbO_6 as a breeder material and aims to provide a comprehensive understanding of the underlying defect chemistry and the mechanisms for tritium release. But also, when combined with simple thermodynamics, how the defect population controls the underlying stoichiometry, and how ultimately, the burn-up of lithium may result in the stability of octalithium phase being lost.

It is shown that the defect chemistry, given the intrinsically high concentration of lithium in Li_8PbO_6, is largely dominated by lithium vacancy defects (namely V_{Li}^{-1}),

regardless of the operating conditions considered.

It is expected Li_8PbO_6 when accounting for point defect populations will only be stable under Li-rich stoichiometries and may begin to undergo a phase transformation into Li_4PbO_4 as lithium is depleted throughout the operational lifetime.

Migration barriers for tritium diffusion as an interstitial and bound to a lithium vacancy were found to be comparatively low compared to other lithium ceramics. The low migration barriers for the defect complex in particular suggest the lithium vacancy performs a collaborative role in assisting tritium escape from the bulk crystal, which suggests aging of the blanket will be of low significance in comparison with other leading candidate ceramics.

The works presented in this thesis provide a baseline theoretical understanding of the potential performance of Li_8PbO_6 to operate as a breeding material. It is hoped the works presented can be experimentally validated, and more importantly to serve as encouragement for others to explore the viability of other, previously dismissed materials.

Acknowledgements

I would like to begin by first thanking my supervisor Dr Samuel Murphy for not only providing me the opportunity to work as part of the Murphy Materials Modelling Group, but also for his excellent supervision throughout the duration of my PhD. I would also like to express my gratitude towards everybody in the Murphy Materials Modelling Group, namely Dr Becky Gray, Dr William Neilson and Dr Jade Li for helping me in my first few months of the PhD, if it weren't for which I don't think I would have made it to the finish line! I would also like to thank Robert Woodman for his investment into the research project, and for Mike Pacey for his technical support concerning the High End Computing facility at Lancaster University.

There were many points throughout this PhD I seriously considered quitting, but thanks to the unwavering support of my family and friends, who stood by my side every step of the way, I was able to refrain from doing so. For the countless hours of moaning about writing and simulations misbehaving that they sadly had to endure, I will be forever grateful to them.

Declaration

I declare that the work presented in this thesis is, to the best of my knowledge and belief, original and my own work. The material has not been submitted, either in whole or in part, for a degree at this, or any other university. This thesis does not exceed the maximum permitted word length of 80,000 words including appendices and footnotes, but excluding the bibliography.

Andrew William Davies

Contents

List of Tables

List of Figures

Chapter 1

Introduction

Beginning in the industrial revolution, the past 300 years have seen the widespread adoption of hydrocarbon fuels as an energy source. The rapid increase in global population, due to improved living conditions throughout the period, continues with current estimates projecting a peak between 8.84 - 10.9 billion people by 2064 [1]. In conjunction with projected population increases, the collective energy use of individuals is also rising. This is particularly evident in many developing countries, which are experiencing major upward shifts in socioeconomic status towards the middle class [2].

In recent decades, it has become clear that the burning of hydrocarbons is having a significant impact on the Earth's climate [3]. The emission of greenhouse gases, primarily carbon dioxide and carbon monoxide (which eventually decomposes into carbon dioxide) due to the widespread burning of hydrocarbon fuels such as coal, oil and natural gas have already had a dramatic effect on the atmosphere, with the 10 warmest years on record occurring since 2010, and an average global temperature increase in 2023 of 1.36 °C since the 1850-1900 pre-industrial average [4, 5]. By 2100, the Earth is projected in the 2023 IPCC report to have an average global temperature rise of 3.2 °C, with a medium confidence range between 2.1 and 3.4 °C [6].

Aside from reducing energy consumption, the burning of hydrocarbon fuels for energy has numerous alternatives, which can be broken down into 2 main categories: renewable and nuclear energy. The reliability of renewable energy sources such as solar, hydro and wind is routinely criticised due to concerns surrounding inconsistent and unpredictable input into the energy grid, and thus must be sustained with some form of base load in the form of either nuclear fission plants or vastly expanding our energy storage capabilities. Fission reactors are also notoriously expensive and take a significant time to construct due to the understandably extensive regulatory environment. The construction of the Hinkley Point C site in the UK provides an excellent demonstration of this, which began construction in 2017 and, at present, is projected to take a minimum of 10 years to construct. The total cost of construction for the Hinkley Point C site is also projected to increase to up to £46 billion (accounting for inflation) [7]. Widespread fear of nuclear energy has propagated over recent decades due to a combination of the publicity of a small number of prominent accidents (i.e. Chernobyl, Fukushima Daiichi, Three Mile Island and Windscale) [8].

Nuclear fusion offers a favourable alternative to traditional fission reactors from a safety perspective as utilising a nuclear fusion reaction design completely eliminates the risk of a catastrophic failure on the scale of the most prominent nuclear accidents seen in the late 20th and early 21st centuries. Fusion reactions are not self-sustaining, as is seen in fission. Due to the delicate conditions required to facilitate a fusion reaction, total failure of a single component will quickly extinguish the reaction [9]. Not only do fusion reactor designs offer a safer alternative for nuclear energy production, but also offers the opportunity to utilise an effectively renewable source of fuel should the challenges of demonstrating a sustainable reaction be achieved.

Unfortunately, the technological challenges presented in producing a sustainable fusion reaction with a high enough energy yield to be used as an energy source have proven to be far more formidable than for fission, primarily in areas of reaction confinement, energy efficiency and the procurement of fuel despite significant research effort.

The most suitable reaction for the nuclear fusion process is the D-T reaction, which utilises a 1:1 mixture of the hydrogen isotopes, deuterium and tritium. Although deuterium exists naturally in abundance in seawater [10], tritium is only produced naturally at a rate of 0.4 kg per year by cosmic rays striking nitrogen molecules in the atmosphere [11]. At present, the proposed method for tritium procurement to sustain a fusion reactor is to exploit the highly energetic neutrons produced by the D-T fusion reaction itself to fission lithium into tritium, and will be done by surrounding the plasma with a lithium-rich material with the breeding capability to sustain the reaction.

There are numerous options for breeding blanket concepts, which are broadly categorised into ceramic and liquid blanket designs, with each offering various benefits and shortcomings. Liquid blanket designs utilise either a liquid metal or molten salt, which offer high thermal conductivities in comparison with ceramic designs, making them effective heat exchangers. They also offer superior tritium breeding rates, although, liquid lithium concepts are also highly reactive and pose a significant safety concern. Despite the lower tritium breeding rates offered by ceramics, ceramic concepts are chemically relatively unreactive, and thus are significantly safer than the liquid designs.

The most viable method for the short-term is to utilise a ceramic material due to their chemical inactivity compared with alternatives (typically liquid metal or molten salt), their high operational temperatures and reasonable thermal conductivities which allow them to doubly operate as heat exchangers.

The two largest projects attempting to demonstrate a fully functional fusion reactor are the ITER (formally the International Thermonuclear Experimental Reactor) and the DEMOnstration power plant DEMO. The extensive timeline for the realisation of such large projects means these projects have seen many advancements in nuclear fusion research that will not be tested or implemented in their final construction. This has left a vacuum in the sector for the development of smaller, cheaper reactors that are much quicker to produce, and most importantly allow for much more rapid experimentation of potential components in a real reactor setting. Numerous smaller scale private enterprises have appeared in recent years, each aiming to demonstrate a fully operational fusion reactor design. An example of just one contender in the sector is Tokamak Energy, who aim to demonstrate a fully realised reactor by the 2030s [12].

Many of the blanket concepts to be trialled on both ITER and DEMO projects will be lithium ceramics, namely materials such as Li_2TiO_3 [13] and Li_4SiO_4 [14], which despite being (at present) the most suitable candidate ceramics, they are only theoretically barely capable of producing tritium at a sufficient rate to sustain a reactor, and are highly dependent on beryllium to act as a neutron multiplier. Beryllium poses a serious problem for fusion reactor design as not only is beryllium intrinsically toxic (the most toxic non-radioactive element) [15], it is also a scarce resource and contains trace quantities of uranium [16] which will result in the accumulation of numerous fission waste products during operation [17].

Due to the drawbacks of the current leading candidate ceramics, there has been a shift in focus in recent years to return to exploring alternative candidates. Major contenders for research are the octalithium ceramics, which offer the highest theoretical tritium breeding capabilities compared with other ceramics [18], and allow for a reduction in the amount of beryllium required to ensure the fuel cycle is sustainable. Of the lithium ceramics, octalithium plumbate (Li_8PbO_6) offers the highest theoretical tritium breeding, although unfortunately very little is known about this material.

1.1 Thesis Outline

The overall aim of this thesis is to evaluate the suitability of Li_8PbO_6 as a tritium breeding material for future fusion reactors. To achieve this, the overall aim is broken down into several objectives. Firstly, by establishing an understanding of the fundamental properties, such as the electronic, basic thermodynamic and mechanical properties to establish a baseline understanding of the inert behaviour of the material, and to draw inferences as to how these qualities might translate to operational settings (e.g. heat capacity). Next, the phase stability of the material under predicted reactor operational temperatures is explored, and compared to a range of other potential octalithium compounds. Then the intrinsic defect chemistry and its evolution during operation is examined, particularly when accounting for the phase stability of the material. Finally the behaviour of tritium in the ceramic is explored, in particular, how it is accommodated at point defects and how these can facilitate the release process. Importantly we also look to predict how these will change during operation.

The works of this thesis demonstrate a complete description of the tritium solubility and release characteristics for Li_8PbO_6. A modified point defect model is used to describe the tritium solubility under different environmental conditions. The modified point defect model presented incorporates temperature-dependent Gibbs free energies into the description of the constituent chemical potentials as a computationally inexpensive way of including thermal effects into point defect descriptions of solids. The optimal migration pathways for tritium in bulk Li_8PbO_6 are characterised. For total escape from the bulk crystal, activation energy barriers for escape were found to be very low (< 0.91 eV), supporting previous evidence provided by Hayashi [19] and [20] that Li_8PbO_6 has excellent tritium release characteristics. It is hoped the defect chemistry and mechanisms for tritium migration in this thesis will be experimentally validated, and encourage the exploration of the feasibility of other previously discarded ceramics for use as tritium breeding materials. An in-depth discussion of the concluding remarks and direction for future works is included in chapter 8.

Chapter 2

Literature review

2.1 Nuclear Fusion

The process which powers all stars, including our very own Sun, is thermonuclear fusion. In the fusion process, two lighter nuclei are fused together to form a heavier product. If the product is lighter than the sum of the reactants, the mass loss is released as the 'binding energy' according to Einstein's energy-mass relationship:

$$\Delta E = \Delta m c^2 \tag{2.1}$$

where, ΔE is the binding energy, m is the atomic mass, and c is the speed of light. If the binding energy per nucleon for the resulting product is higher, the reaction is exothermic and thus will release energy. As a general rule, the lighter the reactants and products in a fusion reaction, the higher the energy released. Figure 2.1 shows an illustration of the binding energy per nucleon as a function of the number of nucleons in a nucleus.

As can be seen in Figure 2.1, the peak binding energy as it relates to stars is found at iron, and is known as the 'iron peak'. Although, this is slightly misleading as the iron peak is only a local maximum, the true peak binding energy occurs at ^{62}Ni. Fusion reactions occurring past the iron peak return a net energy loss, as the reaction is no longer exothermic. In stellar bodies, once a star begins to produce

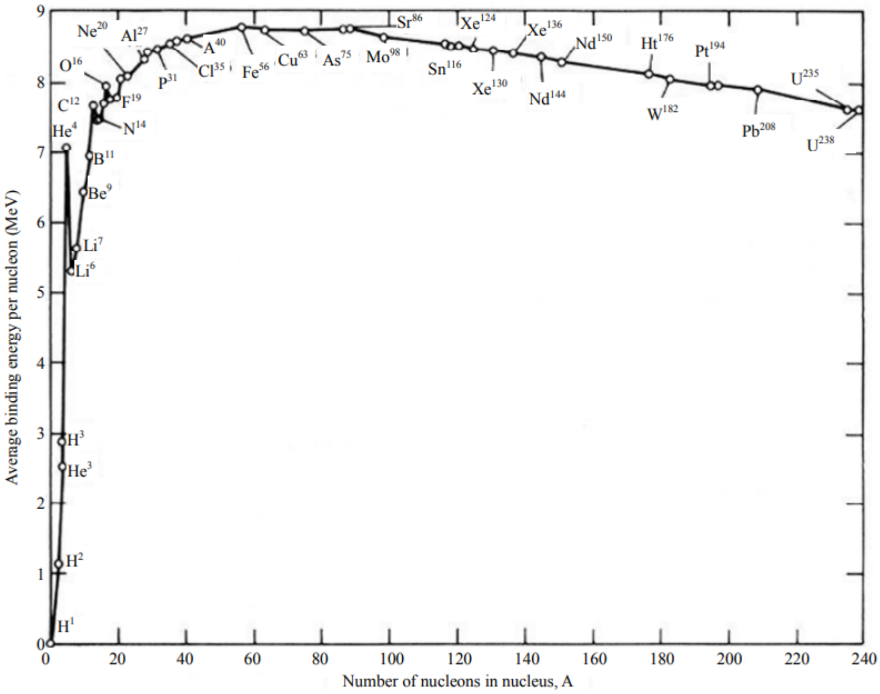

Figure 2.1: Binding energy per nucleon for a selection of typical atomic nuclei [21].

iron from the fusion process, it is doomed to die, as the star no longer has the means of producing energy from the fusion process. Another major criteria for a successful fusion reaction to occur is for the reactants to overcome the electrostatic repulsion between them. As the electrostatic repulsion experienced by the reactants is proportional to the number of protons in each of their nuclei, the electrostatic repulsion is minimised by choosing nuclei with a low number of protons. Regardless, overcoming the electrostatic repulsion requires the reactants to have extremely high kinetic energies. For artificial fusion reactions which occur at significantly lower densities than within a stellar core, significantly higher temperatures are required.

To demonstrate the extreme kinetic temperatures required to overcome electrostatic repulsion, the interaction between two deuterons is considered. Coulomb's law of electrostatic repulsion between two like nuclei can be expressed in terms of the proton number Z, and is given by equation 2.2.

$$V_c = \frac{2Ze^2}{4\pi\epsilon_0 \times 2R} \tag{2.2}$$

where, R is the radius of deuteron, (roughly 2 fm) V_c is the Coulomb barrier, e is the elementary charge, and ϵ_0 is the permittivity of free space. As deuteron has 1 proton, V_c can be roughly approximated to 720 keV. Assuming a single degree of freedom, the kinetic energy is given by the expression in equation 2.3.

$$KE = \frac{1}{2} k_B T \tag{2.3}$$

where, KE is the kinetic energy, k_B is the Boltzmann constant, and T is the kinetic temperature. Equating V_c and KE results in a kinetic temperature of 1.6×10^{10} K. Thankfully, temperatures of this magnitude do not need to be achieved to overcome the repulsive force, as at sufficiently high energies quantum tunnelling through the Coulomb barrier becomes increasingly more likely.

The likelihood of three-body (or greater) reactions occurring outside of stellar densities is exceptionally low, and for terrestrial fusion is generally ignored, and only two-body reactions (of which only those which have suitably high cross-sections) are considered. Figure 2.2 illustrates the likelihood of fusion for some of the most typically considered two-body fusion reactions.

The deuterium-tritium (i.e. D-T) reaction (shown in equation 2.4) is considered the most energetic artificial fusion reaction, due to its extremely high energy output of 17.6 MeV. It also possesses the highest cross-section, particularly for lower kinetic energies.

$${}^2_1\mathrm{D} +^3_1 \mathrm{T} \rightarrow^4_2 \mathrm{He} +^1_0 n \tag{2.4}$$

The majority of the energy output from the D-T reaction is in the form of kinetic energy possessed by the neutron (14.1 MeV). Due to the high energy possessed by the neutron, the materials required for operating a fusion reactor will be subjected to extremely high heat loads and radiation damage, and must be able to continue to function in such an environment.

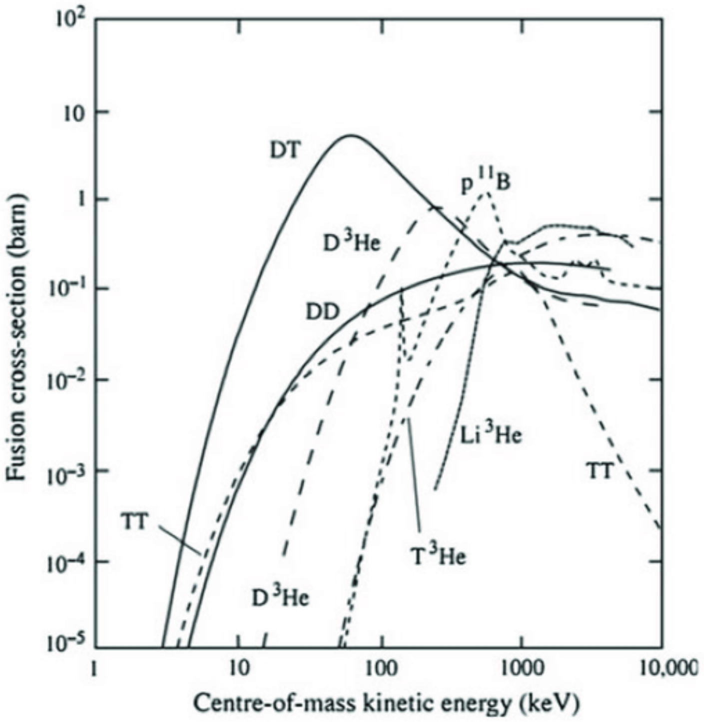

Figure 2.2: Cross-sections of two-body fusion reactions as a function of the incident particle energy [22].

An integral concept to describe the necessary parameterisation to achieve successful fusion is the Lawson parameter [23], which provides a lower boundary condition for the product of ion density n and mean residence time τ_E (rate of energy loss to the environment) of energetic ions in a plasma that leads to a net energy output. The Lawson criterion is given in equation 2.5:

$$n\tau_E \geq \frac{12T}{E_{ch}\langle\sigma v\rangle} \tag{2.5}$$

where E_{ch} is the energy of the charged fusion products, and $\langle\sigma v\rangle$ is the averaged fusion cross-section in the Maxwell-Boltzmann distribution. More conventionally, the 'triple product' (also referred to as the 'Lawson criterion') of T, n and τ_E is used as a figure of merit, shown in equation 2.6:

$$nT\tau_E \geq \frac{12T^2}{E_{ch}\langle\sigma v\rangle} \tag{2.6}$$

The Lawson criterion serves as the primary motivating factor for pursuing the

D-T fusion reaction, as D-T yields the lowest fusion triple product relative to other reactions, and is best illustrated in Figure 2.3, which shows a comparison of the triple product with other commonly proposed fusion reactions:

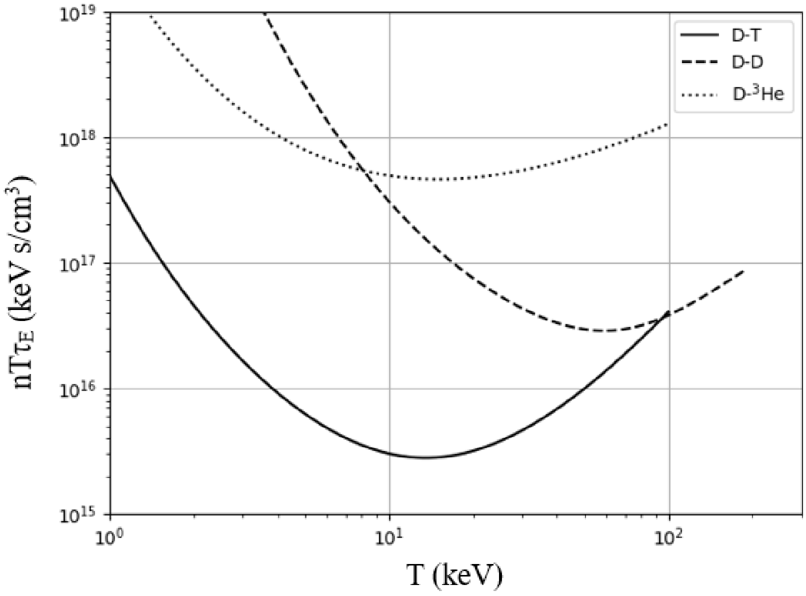

Figure 2.3: Lawson criterion of commonly proposed fusion reactions. Data taken from Bosch and Hale [24].

As is evident from Figure 2.3, D-T requires a significantly lower triple product compared to other types of reaction at significantly lower temperatures. As it is comparatively easier to reach the minimum conditions required for self-sustaining fusion using D-T, it is the reaction of choice for modern fusion reactor design.

At present, a controlled and sustained fusion reaction satisfying the Lawson criterion has yet to be demonstrated, due to the extreme environments required to perform the reaction. Although, observing experimental fusion reactor designs over time (illustrated by Figure 2.4), it is likely the threshold for self-sustained fusion will soon be achieved. Currently, the approaches towards reactor design for sustaining a controlled fusion reaction can be broadly divided into two categories, the first of which is Magnetic Confinement Fusion (MCF), in which a plasma containing a mixture of reactants (generally deuterium and tritium) is suspended

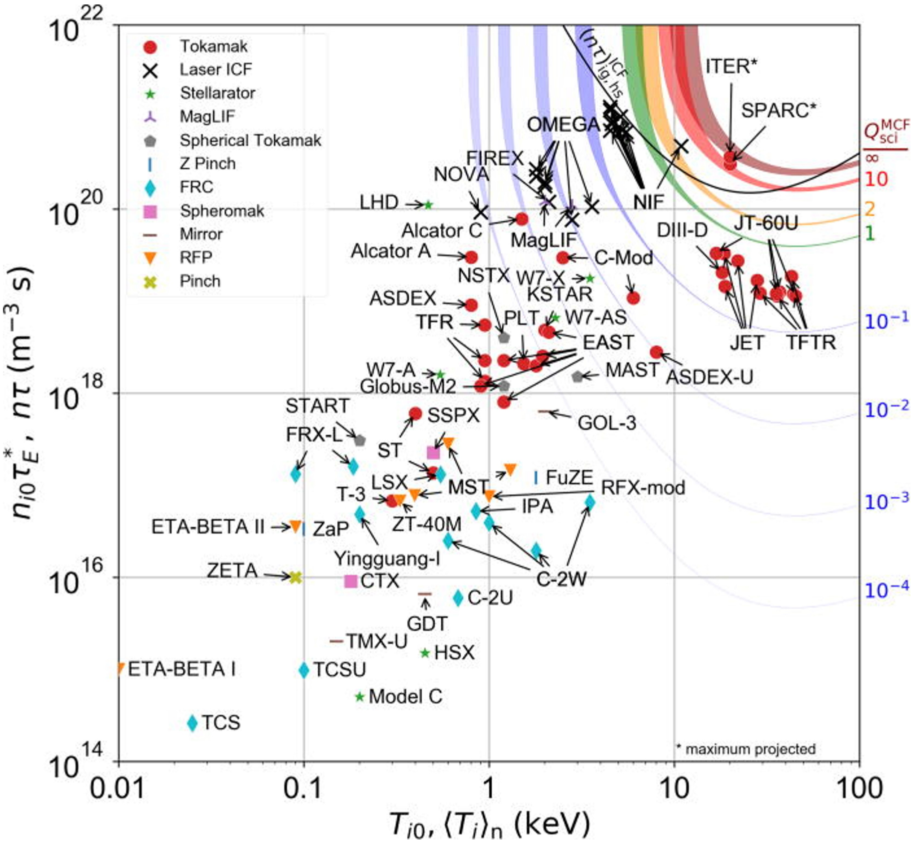

Figure 2.4: Lawson criterion met by numerous reactor concepts [25].

in a magnetic field using either a tokamak or a stellarator. The second category is Inertial Confinement Fusion (ICF) in which the reactants are compressed using a shock-wave such that the density and temperature are high enough for the fusion process to occur.

2.2 Magnetic Confinement

One of the earliest advancements in MCF design was the Soviet T-1 tokamak (Figure 2.5), credited to the works of Natan Yavlinsky and developed at the Kurchatov Institute in Moscow in 1958, which successfully demonstrated the need for magnetic field lines to coil around a torus-shaped reactor vessel for a stable plasma equilibrium to be achieved [26], which previous iterations of fusion reactor design such as the

Z-pinch were unable to accomplish. The success of the T-1 tokamak design built on the initial conceptualisations of Soviet physicists Igor Tamm and Andrei Sakharov by Yavlinsky would lay the groundwork for MCF reactor design in the proceeding decades as the tokamak reactor concept.

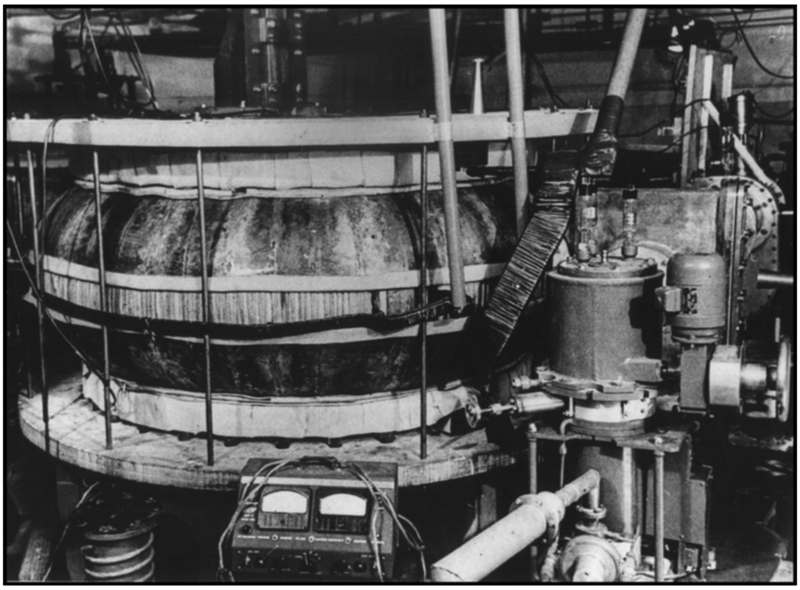

Figure 2.5: Photograph of the Russian T-1 tokamak reactor taken at the Kurchatov Institute in Moscow. (Wikicommons)

The core of the MCF concept is to confine the fusion plasma using a magnetic trap arranged in such a manner as to prevent interaction with the reactor vessel surface, and consequentially damage to the first wall. The toroidal shape of the reactor vessel allows for a circular flow of the plasma within the vessel, and contact with the surface can be prevented by confining the charged particles within the plasma using an external magnetic field. The arrangement of the magnets used is broken down into 3 classifications: the toroidal field coils; the poloidal field coils; and finally the central solenoid. A diagram illustrating the arrangement of magnets is given in Figure 2.6.

A major flaw with the toroidal configuration of the tokamak reactor design is the spacing of the toroidal field coils which wrap vertically around the reactor vessel are more closely spaced towards the centre of the reactor, and this difference in spacing

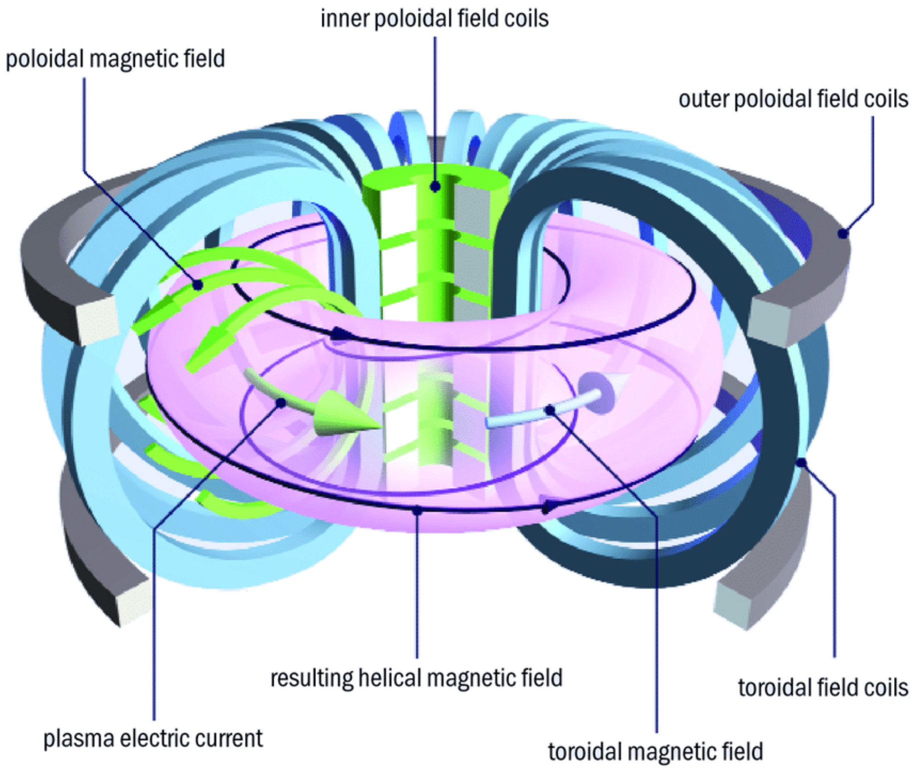

Figure 2.6: Illustration of the arrangement of magnets used in modern tokamak reactor designs, taken from EUROfusion [27].

Enrico Fermi proposed would separate the electrons from the nuclei in the plasma, causing the volume of the plasma to expand throughout operation until contact with the reactor vessel itself is made [28].

One solution to the problem of plasma volume expansion is to induce an electric current inside the fusion plasma itself to generate a magnetic field perpendicular to the current, which allows the particles inside the plasma to move helically, yet remain within the torus of the tokamak reactor vessel.

An alternative solution is to modify the geometry of the torus-shaped pathway of the plasma so the magnetic field lines turn in on themselves such that the charged particles in the plasma are allowed to circulate indefinitely, preventing the charged particles from interacting with the surface of the vessel. Such a design is called a stellarator, and an example illustration of the complex geometry of the plasma chamber and the field coils used by the Wendelstein 7-X (W7-X) experimental stellarator [29] constructed in 2015 by the Max Planck Institute for Plasma Physics (IPP) is given in Figure 2.7.

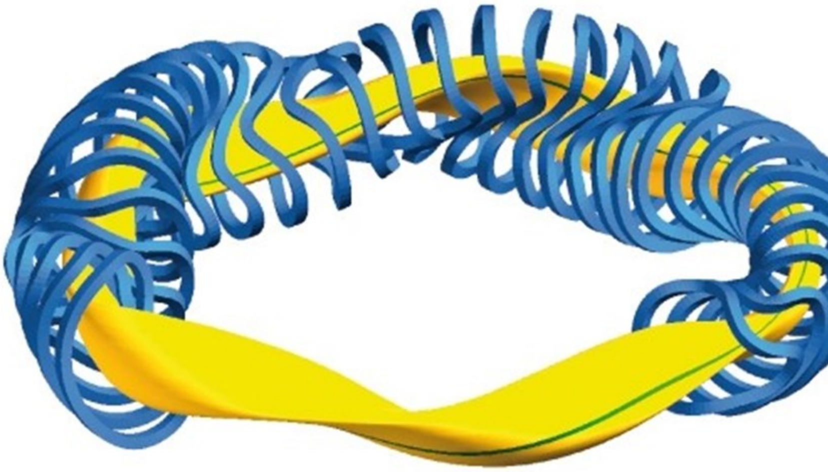

Figure 2.7: Illustration of the complex geometry of the magnetic field coils (blue) and reactor chamber (yellow) for the W7-X experimental stellarator (taken from the IPP website) [30].

Owing to the complex geometry, the stellarator concept was largely dismissed until sufficient computational design tools to design such complicated magnets could be developed, and thus in recent years with such tools now available, the stellarator concept has seen a reemergence of interest. Although, the complex geometry still remains one of the primary disadvantages of the stellarator approach, as it restricts the use of superconducting magnets. Once constructed, the safety factor (the ratio the magnetic field line traverses the minor vs major radius) is limited, and would require the construction of an entirely new reactor to change.

Until recently, most MCF reactor designs such as the Joint European Torus (JET), or in the private sector Tokamak Energy's ST-40 (shown in Figure 2.8) have employed the use of copper magnets, whereas ITER will utilise low-temperature superconducting (LTS) materials Nb_3Sn and NbTi [31], possessing critical temperatures of 18 K and 9.3 K, and critical fields up to 30 T and 11.5 T respectively [32, 33].

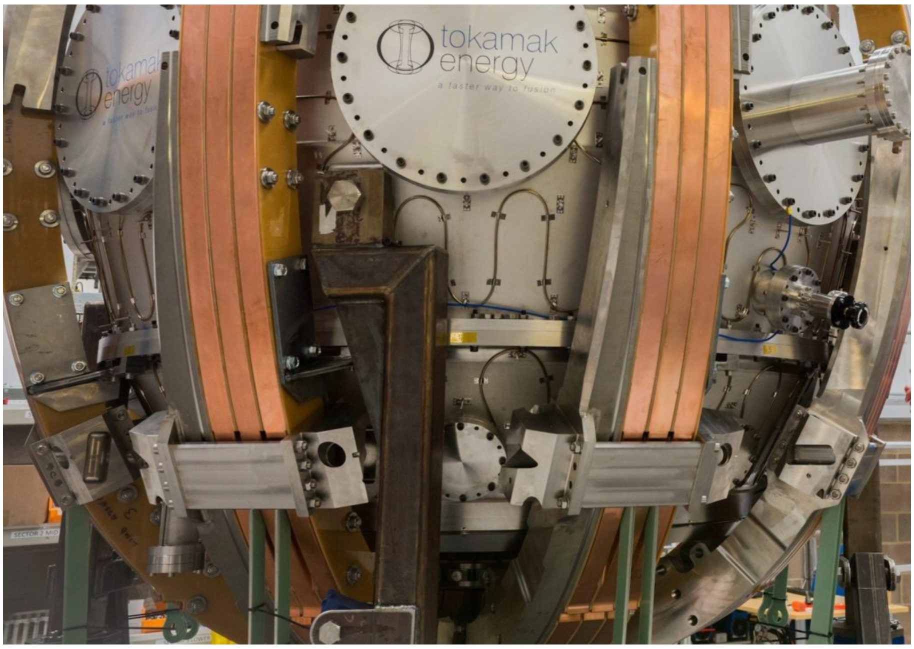

Figure 2.8: Photograph of the ST-40 spherical tokamak reactor (taken from the Tokamak Energy website) [34].

Based on the critical fields offered by LTS magnets, it was previously expected that LTS magnets would require very large plasma volumes to be used for the reaction to be self-sustaining, and results in a major radius of 6.2 m and a plasma volume of 837 m^3 [35] for ITER, relative to the much smaller JET experimental reactor which offers a major radius of merely 2.96 m and a volume of 91 m^3 [36].

The works of Bednorz and Müller in 1986 demonstrated a critical temperature for the superconducting ceramic lanthanum barium copper oxide ($LaBa_2Cu_3O_7$) of T_c = 35 K [37], much higher than LTS magnets. This discovery gave rise to the family of high-temperature superconducting (HTS) rare earth barium cuprates (REBCO), demonstrating critical temperatures exceeding 90 K [38]. The advent of HTS magnets, with their favourable critical fields offered the possibility to construct reactors with a much smaller major radius, and are thus smaller and cheaper to produce, and are known as compact spherical tokamaks.

2.3 Tritium Breeding

As a consequence of the short half-life of 12.32 years of tritium [39], our current global inventory of tritium is insufficient to supply and sustain a single fusion reactor, let alone an entire fleet. The annual tritium consumption of a fusion power plant operating at 1 GW fusion power is expected to be 55.6 kg per full power year (FPY) or roughly 152g per full power day (FPD) [40].

There are a few possible sources for acquiring and building a sufficient supply of tritium. Naturally, tritium is produced as a byproduct of cosmic rays which fission nitrogen in the atmosphere and are deposited into seawater to form HTO [41], although tritiated water in oceans has a concentration of the order of 10^{-18} parts tritium to hydrogen [42], which completely rules out acquisition by extraction unlike deuterium which occurs at a rate of approximately 1 part for every 6420 hydrogen atoms [10]. There is also the option of finding a source of $^3_2$He to convert into tritium via the ^{3}He(n,p)T reaction. The only viable method for obtaining a natural source at present is to extract it from lunar regolith where it exists in great quantities due to solar bombardment, although this pathway presents a number of challenges and does not present a suitable near-term solution to procuring more tritium.

Currently tritium is primarily requisitioned as a byproduct of CANDU fission reactors at a rate of approximately 130 grams per CANDU reactor per year [43], although the total yield is insufficient. Pressurised and Boiling Water Reactors (PWRs and BWRs respectively) are capable of producing tritium with the introduction of TPBARs (Tritium Producing Burnable Absorber rods), although are limited to a maximum production of 1.2 grams of tritium across the 600 day lifetime of the rod [44]. The only remaining option is to procure tritium from the transmutation of lithium.

The consensus for the manufacture of tritium is to extract it as a fission byproduct of the Li(n,α)T reaction using a high energy neutron:

$$ {}^{6}_{3}\mathrm{Li} +^{1}_{0} n \rightarrow^{3}_{1} \mathrm{T} +^{4}_{2} \mathrm{He} \tag{2.7}$$

and depending on the isotope of lithium used (^{6}Li/^{7}Li), a neutron may also be produced:

$$ {}^{7}_{3}\mathrm{Li} +^{1}_{0} n \rightarrow^{3}_{1} \mathrm{T} +^{4}_{2} \mathrm{He} +^{1}_{0} n \tag{2.8}$$

Conveniently, the D-T fusion reaction itself produces high energy neutrons which are intended to be used as a heating agent to extract power from the reactor. Although, only one neutron is generated for every D-T reaction which occurs in the plasma, and as it is unreasonable to expect 100% of all neutrons to react with the lithium, it is necessary to introduce a neutron multiplier such as beryllium or lead (shown in equations 2.9 and 2.10 respectively) to increase the number of neutrons available for tritium breeding. This will help to ensure the tritium breeding ratio (TBR), defined as TBR = Number of tritium atoms generated/Number of tritium atoms consumed in the plasma remains above 1, to make the whole process sustainable.

$$ {}^{9}_{4}\mathrm{Be} +^{1}_{0} n \rightarrow 2^{4}_{2}\mathrm{He} + 2^{1}_{0}n \tag{2.9}$$

$$ {}^{82}_{207}\mathrm{Pb} +^{1}_{0} n \rightarrow^{82}_{206} \mathrm{Pb} + 2^{1}_{0}n \tag{2.10}$$

The combination of a lithium-rich material with some form of neutron multiplier is known as a 'tritium breeding blanket'. This breeding blanket will line the reactor vessel behind the first wall of the reactor as part of the 'tritium breeding module' (TBM). The first wall acts as a thermodynamic and radiation shield for the other components of the reactor, and is generally comprised of tungsten tiles [45] as they offer significantly reduced pollution of the plasma chamber compared to the previously proposed graphite walls [46].

In addition to breeding tritium, the blanket region is where the neutron energy is converted into heat for electricity generation while simultaneously providing shielding for the magnets and other ancillary systems. Given the multiple roles for the blanket region, it is perhaps unsurprising, that the choice of breeder material is complicated and inevitably impacts other choices in the construction of a future reactor. There are an array of different breeder blanket concepts that are due to be tested on ITER [13]. In general, these employ either a lithium ceramic or liquid lithium lead eutectic as breeder material.

2.3.1 Tritium Breeding Module Concepts

The following subsection highlights the various TBM concepts proposed for use in a MCF tokamak reactor.

2.3.1.1 Liquid Blanket Concepts

In most instances, the preferred choice of liquid is the Pb-15.8Li (atomic fraction) eutectic alloy [47], although alternatives to Pb-15.8Li have been proposed. The first of which is to use pure lithium which offers superior tritium breeding capability in comparison with other liquid breeder materials, and also possesses a high tritium solubility which minimises permeation of tritium to the coolant [48]. Unfortunately, lithium is highly reactive in both air and water, which in the event of blanket leakage, could result in a dangerous hydrogen explosion [49]. In fact, liquid lithium is so reactive it is capable of dissolving numerous structural materials, such as SiC/SiC [50]. On top of the severity of an accident due to blanket leakage, the high tritium solubility presents an issue for extraction of the tritium itself in comparison with the Pb-15.8Li eutectic [51]. Another alternative is the FLiBe molten salt (Li_2BeF_4), which offers a much higher tritium solubility in comparison to pure lithium, reducing the complexity of tritium recovery from the blanket [52]. FLiBe is much more chemically stable and can operate up to temperatures in excess of 650 °C [53], although the tritium breeding capability is the lowest of the three liquids, and use of FliBe may result in the production of tritiated hydrofluoric acid [54].

- **HCLL** - Helium Cooled Lithium Lead (HCLL) TBM concept [55] proposed for testing in the ITER and DEMO projects uses the Pb-15.8Li eutectic alloy as both the tritium breeder and the neutron multiplier material, and uses helium gas as coolant [56]. The lithium is enriched to 90% ^{6}Li [57]. Connected to the rear of the breeding units are the horizontal cooling plates, where high pressure helium gas of 8 MPa is allowed to flow to extract heat for power generation, with inlet/outlet temperatures of 300/500 °C respectively [57]. The eutectic is circulated at low velocity to allow for the extraction of tritium.

- **DCLL** - Similar to the HCLL concept, the Dual Coolant Lithium Lead (DCLL) concept also employs the use of the Pb-15.8Li eutectic to act as both the tritium breeder and the neutron multiplier. Although in the DCLL case, the eutectic also acts as a secondary coolant where it is circulated at higher velocity compared to HCLL into large coolant channels composed of Eurofer steel [56] to remove heat from the breeding zone. The helium in this instance is used as the primary coolant for the first wall, and allows for higher operational temperatures of the blanket. Much like the HCLL concept, the lithium is enriched to 90% ^{6}Li, with a helium pressure of 8 MPa and inlet/outlet temperatures of 300/500 °C respectively [58].

- **WCLL** - The Water Cooled Lithium Lead (WCLL) concept due to be tested in the TBM test modules of DEMO, and similarly to the HCLL and DCLL utilises the Pb-15.8Li eutectic [59]. Although, the coolant is replaced with pressurised water, which flows in small pipes which pass through the eutectic pool, similar to that of a fission Pressurised Water Reactor (PWR).

2.3.1.2 Ceramic Blanket Concepts

Ceramic TBM concepts are advantageous due to the high lithium densities and low chemical reactivity of the ceramics [60]. This ensures a degree of safety even in the event of a loss of coolant accident. However, ceramic materials have relatively low thermal conductivities of 2.5 W/mK [61] versus 10 W/mK for liquid metal concepts

[62], which will impact the thermal efficiency of the reactor [62]. By contrast the liquid lithium lead concepts offer a higher thermal efficiency, however, the reactivity of the liquid metal poses a safety issue, particularly if water is used as a coolant [63]. The liquid breeder concepts also offer an easier refuelling route that may reduce reactor downtime, thereby increasing availability. Ceramic breeder materials currently offer a more near-term solution for effective tritium breeding due to the lack of technological innovation required in comparison with liquid breeder concepts [64].

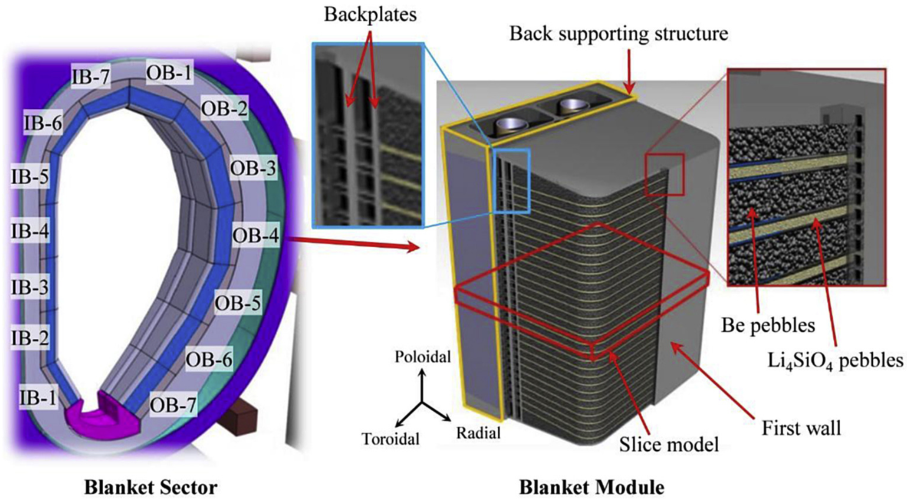

Figure 2.9: Example design of the HCPB blanket module, taken from Zhou *et al.* [65].

- **HCPB** - The Helium Cooled Pebble Bed (HCPB) concept will use either Li_4SiO_4 or Li_2TiO_3 pebble beds for tritium breeding, and neutron multiplication supplied by pellets of beryllium [13]. The HCPB utilises Eurofer steel as the structural material. For the DEMO project, the lithium in both Li_4SiO_4 and Li_2TiO_3 is enriched to 60% ^6Li [66]. Similar to the cooling system of the HCLL liquid blanket, the HCPB is cooled by helium gas with a pressure of 8 MPa and inlet/outlet temperatures of 300/500 °C respectively [67, 20]. The tritium is purged from the blanket using a low-pressure helium stream called the 'purge gas', where the tritium on the pebble surface undergoes isotope exchange with hydrogen in the helium gas in order to be extracted. The purge gas flows initially through the beryllium pebble beds before reaching the ceramic pebbles. The maximum operational temperature for the ceramic pebbles are 920 °C, 650 °C for the beryllium pebbles and 550 °C for the Eurofer steel [20]. An example of the HCPB design is shown in Figure 2.9.

- **WCCB** - The Water Cooled Ceramic Breeder (WCCB) [68] uses a Li_2TiO_3 pebble bed as the tritium breeding substance, utilises a beryllium pebble bed for neutron multiplication, and uses a lithium enrichment of ^{6}Li of 30% for DEMO [56]. Unlike the HCPB, the WCCB utilises F82H steel as the structural material, and uses pressurised water as the primary coolant. The ceramic and beryllium pebble beds are divided by cooling panels, consisting of a series of F82H steel tubes. Maximum operational temperatures for each component is similar to that of the HCPB, with maximum temperatures of 900/600/550 °C for the ceramic, beryllium and F82H steel respectively [13].

- **HCCB** - The Helium Cooled Ceramic Breeder (HCCB) similar to the WCCB and the HCPB uses a combination of ceramic and beryllium pebbles for the tritium breeding and neutron multiplication respectively, except the HCCB utilises Li_4SiO_4 as the ceramic material, with a ^{6}Li enrichment of 80% [13], compared to the 60% used by the HCPB TBM concept. Much like the HCPB, helium is used as both a coolant and the purge gas to extract the tritium from the breeding zone. The breeding zone is comprised of a sequence of rows of circular coolant channels.

- **LLCB** - The Lithium Lead Ceramic Breeder (LLCB) is a unique combination of both the solid ceramic breeder and the liquid breeder concepts [69, 70]. The design uses a Li_2TiO_3 pebble bed in combination with a Pb–16Li eutectic alloy for tritium breeding. The Pb-16Li also acts dually as a neutron multiplier, eliminating the need for solid beryllium pellets. The Pb-16Li eutectic alloy also serves as the primary coolant for the ceramic pebbles which flows around the pebble bed compartments to extract heat from both the ceramic pebbles and the eutectic itself, with inlet/outlet temperatures of 300/480 °C respectively [13]. A secondary coolant of pressurised helium (8 MPa) is used for the first wall and the structural materials, with inlet/outlet temperatures of 300/360 °C respectively [71]. Similarly to the HCPB, the tritium is extracted from the ceramic via the use of a low-pressure helium purge gas, although tritium produced in the eutectic must be extracted separately using an external detritiation system.

2.4 Ceramic Blanket Materials

The choice of ceramic breeder material is constrained by the desire to use readily available low activation materials to reduce the amount of radioactive waste byproduct. The ideal material must possess a high lithium density such that sufficient tritium fuel can be bred to sustain the reactor, it must be tolerant to thermal stresses in order to avoid excessive fragmentation during operation, it must have sufficient heat transfer properties as well as being able to resist and tolerate excessively high neutron fluxes, resulting in potential radiation damage of the order of >150 dpa [67], whilst also having sufficient tritium release characteristics such that the tritium produced within the ceramic can be requisitioned [72]. Because of these limitations, a wide range of potential materials have been considered, including Li_2O [73], Li_2TiO_3 [13], Li_2ZrO_3 [74], Li_4SiO_4 [14], γ-$LiAlO_2$ [75], to name a few.

In recent years, the primary ceramic breeder materials selected for application in the test blanket modules for ITER are lithium metatitanite (Li_2TiO_3) and lithium orthosilicate (Li_4SiO_4) [13]. While Li_4SiO_4 offers a higher lithium density (and consequentially, a higher potential for tritium breeding) and better tritium release characteristics at lower temperatures in comparison with Li_2TiO_3, Li_2TiO_3 offers a more favourable thermomechanical stability [76] and is much more insensitive to moisture [77]. Li_2TiO_3 and Li_4SiO_4 both adopt complex crystal structures, with

Li_2TiO_3 adopting a monoclinic unitcell in the $C2/c$ space group [78], whereas Li_4SiO_4 adopts the low-symmetry $p21/m$ space group [79]. Li_2TiO_3 compared to Li_4SiO_4 is much more flexible towards deviations in stoichiometry. The Li_2O-TiO_2 phase diagram shows Li_2TiO_3 is able to accommodate stoichiometries ranging between 47 - 51.5 mol % TiO_2 [80], allowing for fabrication with an excess in lithium content and increasing the tritium breeding potential, and is able to accommodate the loss of lithium due to transmutation [81] in comparison with Li_4SiO_4, which cannot accommodate such non-stoichiometry as it is a line compound [82] and accommodates excess lithium in the Li_2SiO_3 secondary phase.

Fabrication and characterisation of ceramic breeder pebbles has been studied extensively, and a brief summary of the approaches used by various entities is presented in Table 2.1.

Table 2.1: Fabrication processes of solid breeder blankets Li_2TiO_3 and Li_4SiO_4 adopted from Knitter *et al.* [83]

Entity	Compound	Fabrication method	Pebble diameter (mm)	Density (%)	Open/closed porosity	Pebble bed density (%)	Reference
China	Li_4SiO_4	Melt-spraying	0.9-1.0	94	<4/<1.5	60.5	[83, 84]
	Li_2TiO_3	Extrusion-spheronization	0.8-1.2	85	<11/<3	53	[83, 85]
EU	Li_4SiO_4	Melt-spraying	95	0.25-0.63	<1/<5	61	[86]
	Li_2TiO_3	Extrusion-spheronization	0.8-1.2	90	5 / 5	55	[85]
India	Li_2TiO_3	Solution combustion/ solid state	1.0-1.25	90	6-9/2-5	60	[87]
Japan	Li_2TiO_3	Sol-gel	1.18	89	N.A.	64	[88]
Korea	Li_4SiO_4	Slurry dropping	0.9-1.1	77	11/12	48	[83]
	Li_2TiO_3	Sol-gel	0.9-1.1	91	5/4	56	[83]

The neutrons ejected by the fusion plasma are able to penetrate deep into the pebbles such that the tritium ions generated as the product of the Li(n,α)T reaction form within the ceramic matrix. From the ceramic matrix, the tritium must then diffuse to the pebble surface, where it can be extracted via isotope exchange reactions with hydrogen in the helium purge gas. There are a number of competing processes for diffusion of tritium through the bulk, which include inter/intra-granular diffusion as well as trapping and de-trapping of defects. An illustration of the process of tritium escape from from the ceramic matrix to the purge gas is shown in Figure 2.10.

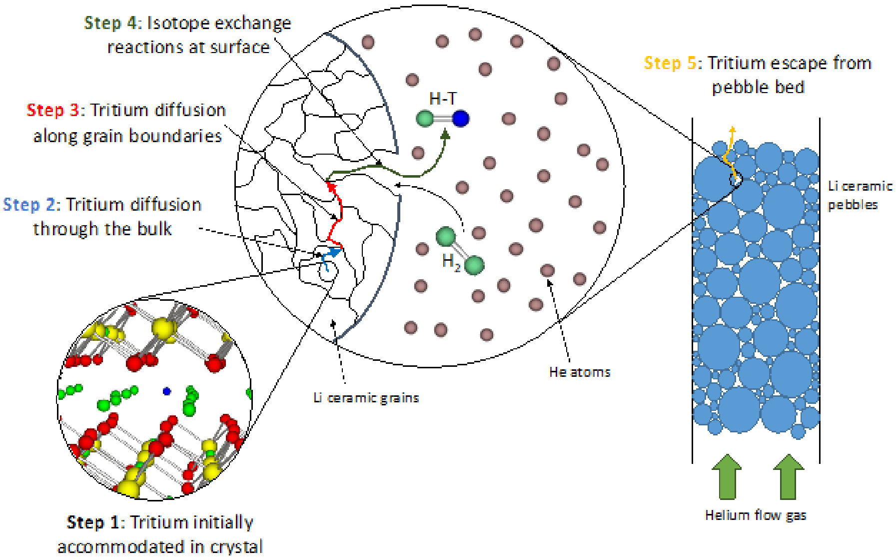

Figure 2.10: Illustration of the diffusion process of tritium from the pebble ceramic matrix to the He purge gas. Taken from Goswami and Murphy [89].

The rate limiting step for tritium recovery is the migration of the tritium through the bulk until reaching a grain boundary. In neutron-irradiated lithium ceramics, multiple peaks in the thermal desorption spectra are found, suggesting that there are multiple distinct mechanisms in the tritium release process [90, 91, 92]. An example of the multiple peaks seen in the thermal desorption spectra for Li_4SiO_4 is shown in Figure 2.11.

Experimental activation energies for tritium diffusion for Li_2TiO_3 and Li_4SiO_4 vary between 0.63 - 1.5 eV [93, 94] and 0.4 - 0.88 eV [95, 96, 97] respectively. The broad variation in activation energies measured is likely due to different experimental

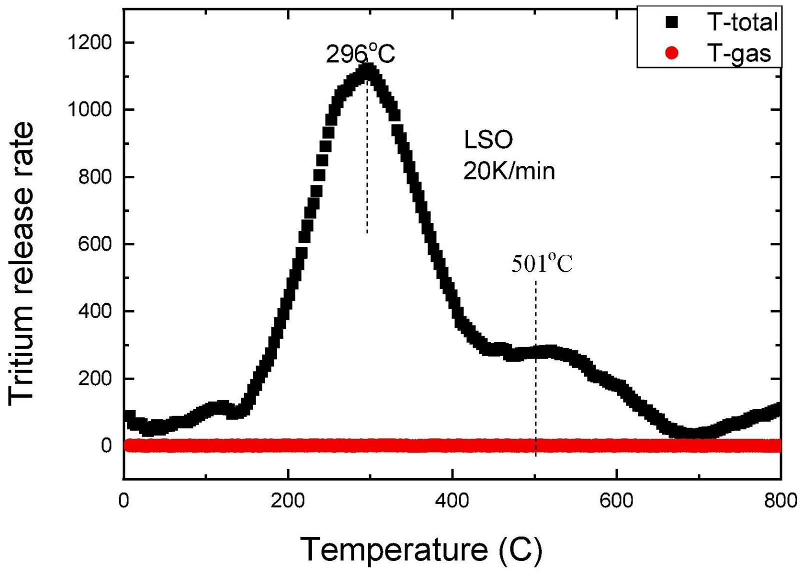

Figure 2.11: Thermal desorption spectra of tritium release for Li_4SiO_4, taken from Qi *et al.* [92]. Tritium release rate is measured in Bq/g.

conditions, but nonetheless demonstrates the complexity of the diffusion process. Tritium diffusion has also been studied computationally via the use of atomistic simulation techniques such as Density Functional Theory (DFT) [98, 99]. The activation energy barrier for tritium diffusion as an interstitial defect in Li_2TiO_3 was predicted to be 0.33 eV [100], although the introduction of lithium vacancy defects into the crystal can act as trapping sites for the tritium, as the tritium interstitial becomes bound to the lithium vacancy. Introducing lithium vacancies leads to an increase in the activation energy for tritium migration to as high as 1 eV when tritium is bound to the lithium vacancy defect [89]. The presence of defects in the ceramic matrix arising throughout the lifetime of the blanket from either lithium burn-up as lithium is transmuted into tritium, or from radiation damage, are expected to prohibit tritium mobility, as decreasing rates of hydrogen release have been observed due to irradiation by energetic particles [101] and γ-rays [102]. Regardless of the origin of defects, the production of defects in the ceramic pebbles may significantly hinder the rate and quantity of tritium recovered from the ceramic pebbles.

The ceramic pebbles also need to meet numerous secondary criteria. These include: possession of a high lithium density; a high thermo-mechanical stability; a high crush load to deal with high thermo-mechanical loads; small grain size to facilitate tritium recovery; be chemically compatible with beryllium; and depending on coolant used, be unreactive to water/air to mitigate an accident scenario [103, 104]. Although, none of the current candidate materials satisfy all of these criteria. For example as discussed previously, although Li_4SiO_4 has excellent low-temperature tritium release properties compared to Li_2TiO_3, Li_2TiO_3 offers more favourable thermo-mechanical stability and is insensitive to moisture. In recent years, there has been an effort to examine the use of multiple phases in the ceramic pebbles to combine the advantages of each phase and overcome the limitations presented by using single-phase pebbles. To improve lithium density and radiation resistance, $Li_{2+x}TiO_3$ [105] and Li_4SiO_4-Pb [106] pebbles have been fabricated respectively, whereas Li_4SiO_4-SiO_2 [107] pebbles have been fabricated in an effort to increase the mechanical strength of Li_4SiO_4. Knitter *et al.* introduced a small amount of titania into Li_4SiO_4 pebbles to improve the mechanical properties of Li_4SiO_4 instead, creating secondary Li_2TiO_3 phases [76]. Xiang *et al.*, developing on the biphasic Li_2TiO_3-Li_4SiO_4 system studied by Knitter *et al.* fabricated 50% Li_2TiO_3-50% Li_4SiO_4 core-shell pebbles, which exhibited significantly higher crush strengths [108]. The use of core-shell pebbles has enabled reconsideration of previously discarded candidate ceramics, such as Li_4TiO_4, which was discarded as a candidate due to air sensitivity, by coating a Li_4TiO_4 core with a protective Li_2TiO_3 shell [109]. Similar thinking has lead to a number of previously discarded candidate materials now being investigated in hybrid materials.

Regardless, the current candidate materials alone may not be sufficient for use as a ceramic breeding material for tokamak reactors. Outside of the thermo-mechanical drawbacks of the leading candidate materials, the TBRs of Li_2TiO_3 and Li_4SiO_4 depend significantly on the heavy use of beryllium as a neutron multiplier to increase their TBRs to the required level. The use of beryllium also poses additional concerns due to not only the scarcity of beryllium as a resource, but also in that beryllium naturally contains trace impurities of uranium. Uranium impurities in beryllium generally don't pose any significant concerns in environments where there is a low fluence of neutrons. However, due to the proximity of the beryllium to the fusion plasma, the presence of trace impurities of uranium pose a serious concern for the production of radioactive waste. The uranium content in the beryllium for ITER have a maximum requirement of 30 weighted parts per million (wppm) [110], although even with such content, the total quantity of $Be_{12}Ti$ to be supplied to DEMO as a neutron multiplier is estimated to be 700 tons [111], or 490 tons of beryllium [112] every 4 years, and results in a total uranium content of 14.7 kg.

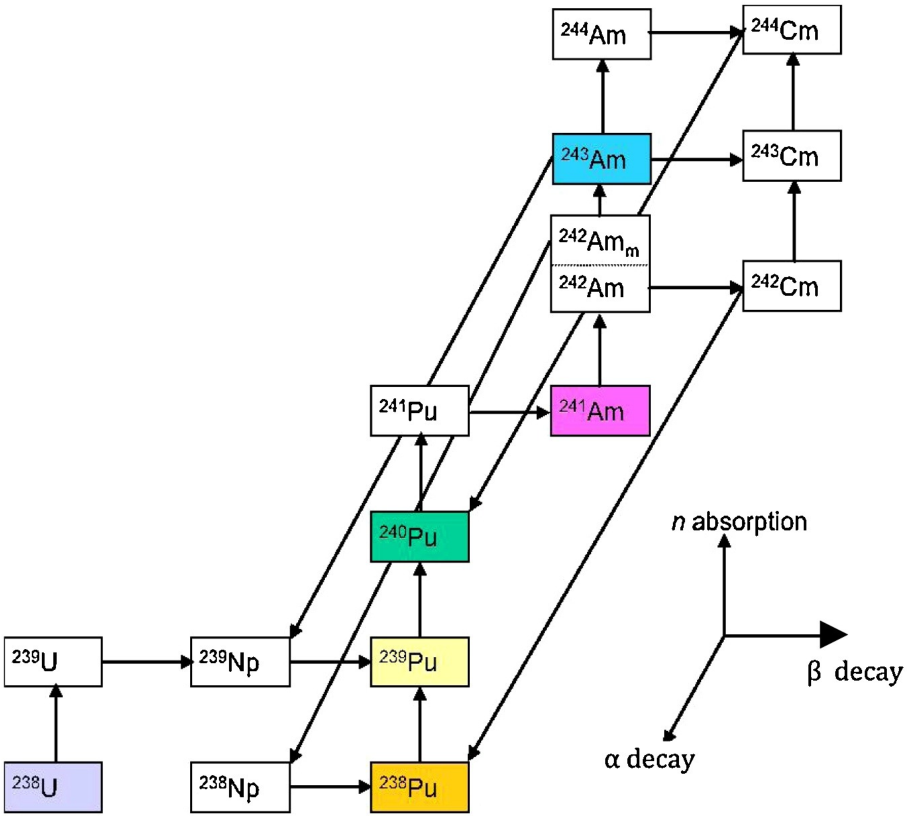

Figure 2.12: Activation processes of U trace impurities in Be. Taken from Kolbasov *et al.* [16].

As seen from the activation processes of uranium shown in Figure 2.12, the high neutron fluxes generated by the D-T fusion reactions activates the uranium and facilitates the production of a number of fissile isotopes, in particular ^{239}Pu within the neutron multiplier. As well as the generation of fissile isotopes, the decay products of these radioactive nuclides also pose a concern. Thus, there is a drive to reduce the amount of beryllium used and is a major motivating factor for exploring alternative ceramic breeding materials with higher TBRs to compensate for the reduction of beryllium, on top of the thermo-mechanical issues with current leading candidates.

2.5 Octalithium Plumbate

A review article examining the current landscape of candidate breeding blanket materials was published recently by Hernández and Pereslavtsev [18]. In this article, they performed a neutronics analysis to show that the octalithium ceramics offer highly favourable tritium release rates in comparison with other candidate materials, most importantly Li_2TiO_3 and Li_4SiO_4, with predicted TBRs in the range of 1.17 - 1.21, owing to their high lithium densities and in some cases, the intrinsic neutron multipliers within their crystal structures. Of particular note from this neutronics analysis is the material octalithium plumbate (Li_8PbO_6), which offered the highest TBR of all the ceramics analysed with a TBR of 1.21 (using a simplified DEMO configuration of ^{6}Li enrichment of 60%), due to the intrinsic neutron multiplication offered by lead and the impressive lithium density the octalithium ceramic affords. This can be compared to breeding ratios of 1.15 and 1.12 for the Li_4SiO_4 and Li_2TiO_3 respectively under the same conditions. A comparison of the lithium densities of the octalithium ceramics with Li_2TiO_3 and Li_4SiO_4 taken from Hernández and Pereslavtsev is presented in Table 2.2.

Li_8PbO_6 was previously dismissed as a potential candidate for use as a breeding blanket due to concerns surrounding the thermal stability of octalithium ceramics at high temperatures and the potential appearance of secondary phases such as Li_4PbO_4 during fabrication. Due to the early dismissal of Li_8PbO_6 and other

Table 2.2: Comparison of atomic density of lithium between the octalithium ceramics and the leading candidate ceramic materials Li_2TiO_3 and Li_4SiO_4. Taken from Hernández and Pereslavtsev [18]. (RT = Room temperature)

Compound	Atomic density (a/$Å^3$)	Li atomic density (a/$Å^3$)	% Li	Density at RT (kg/cm^3)	Ref.
Li_8PbO_6	0.1077	0.0575	53.4	4.28	[19]
Li_8GeO_6	0.1062	0.0567	53.4	2.64	[113]
Li_8CeO_6	0.1006	0.0537	53.3	3.25	[114]
Li_8ZrO_6	0.1109	0.0591	53.3	2.98	[115]
Li_8SnO_6	0.1140	0.0608	53.3	3.41	[116]
Li_8CoO_6	0.1060	0.0565	53.3	2.47	[117]
Li_2TiO_3	0.1129	0.0376	33.3	3.43	[118]
Li_4SiO_4	0.1085	0.0482	44.4	2.40	[119]

octalithium ceramics, many of the fundamental properties of Li_8PbO_6 are largely unknown. Li_8PbO_6 has successfully been produced by Konishi *et al.* using solid-state synthesis, by sintering a 4:1 mixture of Li_2O:PbO_2 at 873 K under a dry oxygen atmosphere for several hours [120]:

$$4Li_2O_{(s)} + PbO_{2(s)} \rightarrow Li_8PbO_{6(s)} \tag{2.11}$$

In the same work they studied the lithium diffusivity using NMR, and concluded that Li_8PbO_6 is stable under dry oxygen atmospheres at 973 K. The sintering process demonstrated by Konishi *et al.* for Li_8PbO_6 was successfully reproduced by Colominas *et al.* under different temperature conditions [121], and they observed that a secondary phase of Li_4PbO_4 tends to form as a trace impurity. The production of the Li_4PbO_4 secondary phase can be reduced by using high temperatures (1273 K) and reducing the sintering time. At temperatures below 873 K, trace impurities of Li_2O and PbO_2 are measured, indicating insufficient temperatures for the reaction to reach completion. Furthermore, recent experiments by Pedr Charlesworth of Oxford University have suggested that high quality Li_8PbO_6 samples can be fabricated and are stable up to 1004 °C, before melting (personal communication, 2023).

An initial assessment by Hayashi *et al.* [19] analysing the tritium diffusivity in a range of lithium oxide ceramics previously indicated that octalithium plumbate offers the highest tritium diffusivity of all the lithium ceramics they tested with an activation energy of 0.78 eV, compared to 0.4 - 0.88 eV [95, 96, 97] for Li_2TiO_3 and 0.63 - 1.5 eV for Li_4SiO_4 [93, 94]. A comparison of the tritium diffusivity is taken from Hayashi *et al.* and presented in Figure 2.13. Although they were able to demonstrate that tritium primarily takes the form of T^{1+}, they did not establish an understanding of the mechanisms for tritium migration.

Understanding the mechanisms for tritium migration through the bulk crystal of ceramic breeding materials allows for the characterisation of the tritium release properties throughout the entire lifetime of the material as lithium is exhausted through burn-up. As mentioned previously, there has been significant growth in recent years in the use of atomistic simulation to characterise the solubility of tritium and the mechanisms for tritium migration through ceramic materials, in particular Li_2TiO_3 which has been extensively studied using DFT [89, 100, 122, 123]. The works of this thesis aim to provide a complete description of the tritium solubility and release mechanisms for Li_8PbO_6 using atomistic simulation.

2.5.1 Crystallography

As illustrated in Figure 2.14, Li_8PbO_6 crystallises into the $R\bar{3}H$ [148] space group and forms a complex layered structure, alternating between a mixed lithium-lead and pure lithium layers in the sequence $PbLi_2$-O_3-Li_3-Li_3. There are two symmetrically distinct lithium sites, a tetrahedrally-coordinated site existing exclusively in the pure lithium layer (18f Wyckoff site) and an octahedrally-coordinated site in the mixed lithium-lead layer (6c). Lead ions are octahedrally coordinated in the +4 charge state, surrounded by 6 oxygen ions. The oxygen and lead ions occupy the

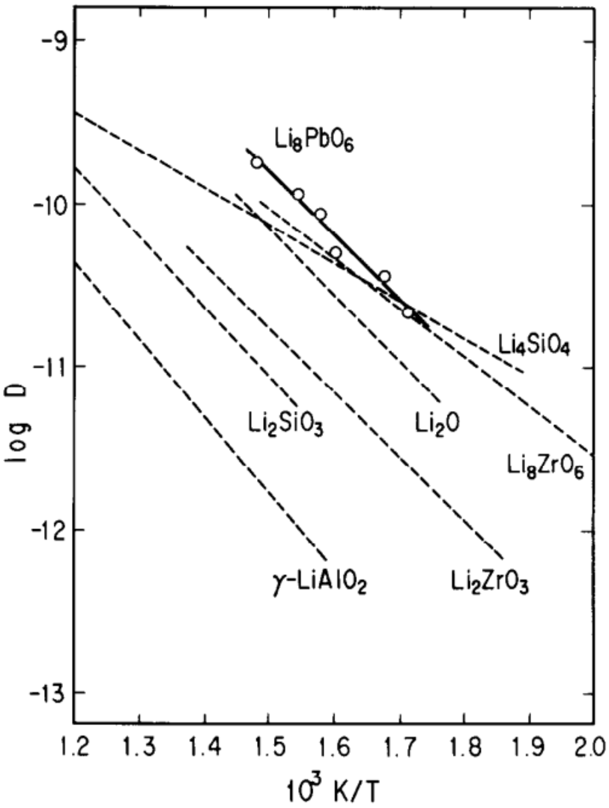

Figure 2.13: Arrhenius plots of diffusion coefficients for tritium in Li_8PbO_6, crystals (open circles, solid line), comparing with those of the other lithium-based oxide ceramics (dotted lines). Taken from Hayashi *et al.* [19].

18f and 3a sites respectively.

The lattice parameters of Li_8PbO_6 have been measured experimentally, by Brazel and Hoppe [125], with lattice parameters of a (=b) = 5.55 Å and c = 15.64 Å, in agreement with Trömel *et al.*, whom initially measured the lattice parameters to be a = 5.54 Å and c = 15.63 Å [126], In both instances, α (= β) = 90°, γ = 120°.

As the works of this thesis aim to provide a complete description of the tritium solubility and mechanisms for tritium migration in Li_8PbO_6, it is therefore important to consider the role of defects in ceramics. In particular, how the presence of defects in the crystal structure can influence the macroscopic properties of the material, such as the tritium solubility. Section 2.6 provides an overview of how solid structures can

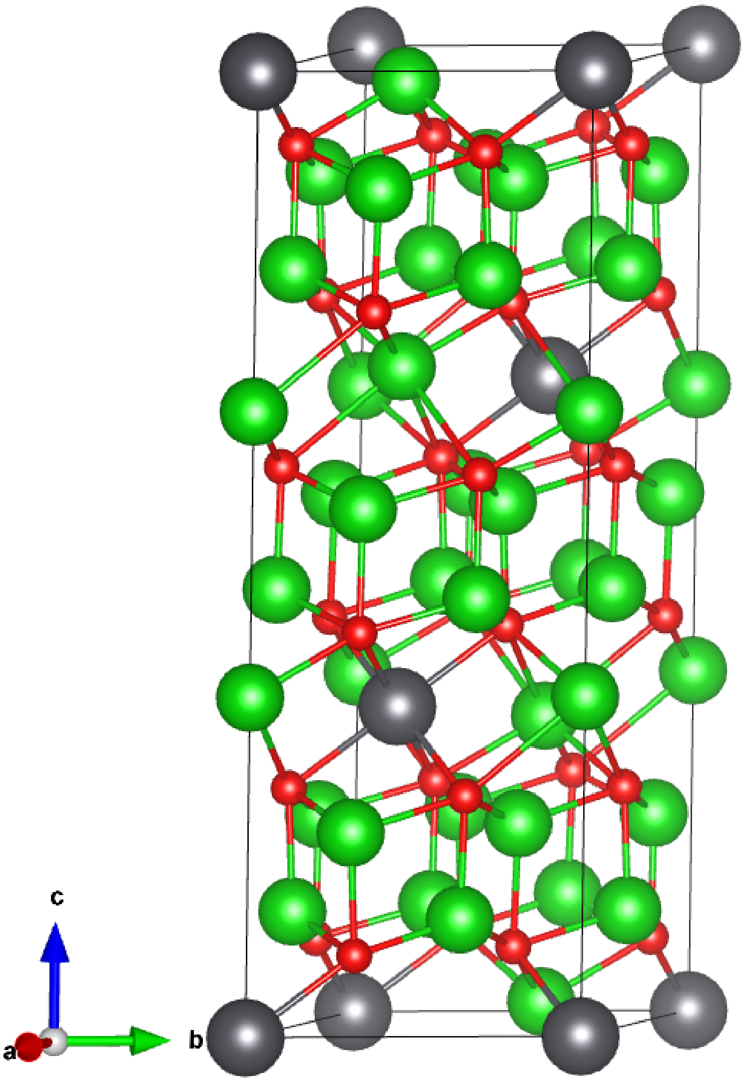

Figure 2.14: 45-atom unitcell of Li_8PbO_6. Grey ions indicate lead, red ions indicate oxygen and green ions indicate lithium. Visualisation of all crystal structures shown throughout this thesis is done so using the Vesta 3D visualisation software [124].

be conveniently described using a simple crystallographic description, followed by a description of the appearance and behaviour of point defects in crystalline solids.

2.6 Crystalline Point Defects

Broadly speaking, the structure of solids can be broken down into two categories depending on the ionic ordering. If the structure is disordered, it is considered amorphous, conversely if the structure is ordered it is crystalline. The law of rational intercepts [127] states that the form of crystal structures can be described by reference to their crystal axes, their relative lengths and angles of inclination. In crystalline structures, the symmetry allows the structure to be described by a single unit cell, which when periodically expanded describes the lattice points of the entire crystal structure. An illustration of the periodicity of a unit cell for a generic crystal structure is shown in Figure 2.15.

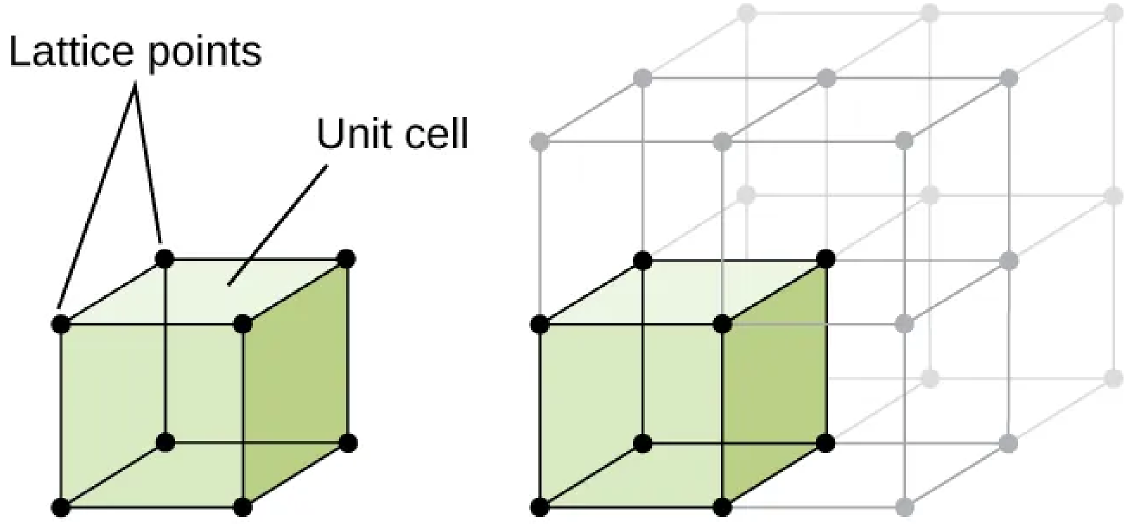

Figure 2.15: A unit cell shows the locations of lattice points repeating in all directions. Illustration taken from the Chemistry 2e (2014) textbook [128].

In total, the unique systems of crystal symmetry which represent the simplest shapes which can be periodically repeated are: cubic, hexagonal, tetragonal, orthorhombic, rhombohedral, monoclinic and triclinic. Within these systems, Bravais determined there are 14 unique ways of arranging the lattice points [129].

In reality, crystal structures contain slight imperfections, or defects. Defects described by the disordering of either a single, or a few localised atomic sites are considered 'point defects', and those which extend over many atomic sites are described as extended defects. If the defect does not contain the presence of any foreign atoms, the defect is intrinsic to the crystal and is suitably labelled an intrinsic defect, conversely if the defect does contain atoms foreign to the crystal, the defect is an extrinsic defect. The presence of point defects in a material can have a significant impact on the macroscopic behaviour of a material, such as the stoichiometry, or semiconductors which use defects to modify the local electronic properties of the material, and consequentially the band gap. Or, in the case of ceramic breeding materials, the solubility and diffusivity of tritium through the ceramic.

2.6.1 Intrinsic Point Defects

Point defects can arise in a crystalline material from a number of different mechanisms. This includes during crystal growth, thermal dissociation, or in the context of ceramic breeding materials from radiation damage as a consequence of the neutrons ejected from the fusion plasma. The simplest defect is the vacancy defect, wherein an ion in the crystal is missing from its respective lattice point. An example illustrating a lithium vacancy defect in Li_2O is shown in Figure 2.16.

The removal of an ion from the lattice site causes deformation of the crystal in the surrounding environment due to the disruption of bonding with neighbouring ions, and such deformation is known as the strain field of the defect. At sufficient temperatures, the vacancy defect may migrate to a neighbouring lattice site, as a neighbouring ion (in the example given in Figure 2.16, a lithium ion) moves to occupy the vacant space. If the vacancy is formed via the displacement of an ion, the ion may reside somewhere within the lattice as an interstitial, and this dissociation of an ion from its lattice site is known as a Frenkel pair:

$$\mathrm{O_O} \rightarrow \mathrm{O}_i + \mathrm{V_O} \tag{2.12}$$

where $\mathrm{O_O}$ represents an oxygen occupying an oxygen site, O_i represents an oxygen interstitial, and $\mathrm{V_O}$ represents an oxygen vacancy defect. This representation is

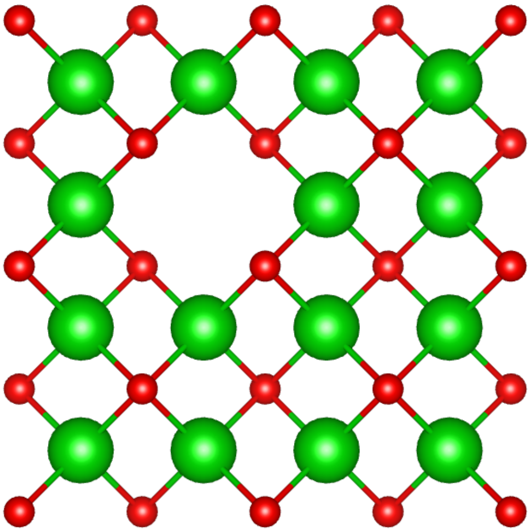

Figure 2.16: Example of a lithium vacancy defect in Li_2O, which is used as generic example for easier comprehension of the defect compared to Li_8PbO_6. Green ions represent lithium, and red ions represent oxygen.

known as Kröger-Vink notation [130].

Kröger-Vink notation is typically used to describe the occupation and charge states of defects in crystalline solids, and takes the format $\boldsymbol{X_Y^Z}$:

- $\boldsymbol{X}$ - Represents the species occupying the defect site.

- $\boldsymbol{Y}$ - The defect site. If the defect exists on a lattice point in the perfect crystal, $\boldsymbol{Y}$ is represented as the species of that site. Otherwise, if the defect exists as an interstitial, i is used.

- $\boldsymbol{Z}$ - Represents the relative charge to the normal charge on site $\boldsymbol{Y}$. Typically a dot is used to represent positive relative charges, primes for negative charges and an x for net-zero relative charge. For this thesis, the relative charge is represented numerically, however, in the initial formulation positive charges were represented with a $\cdot$ and negative charges by $'$.

When a stoichiometric amount of anions and cations are displaced from their lattice positions, this is known as a Schottky defect. For example, in Lead(II) oxide:

$$\mathrm{Pb_{Pb}} + \mathrm{O_O} \rightarrow \mathrm{V_{Pb}} + \mathrm{V_O} + \mathrm{Pb}_i + \mathrm{O}_i \tag{2.13}$$

An interstitial defect does not necessarily have to be intrinsic, and may be an extrinsic defect also, for example in the case of tritium which is extrinsic to the crystal structure of ceramics. An example of an interstitial defect is shown in Figure 2.17.

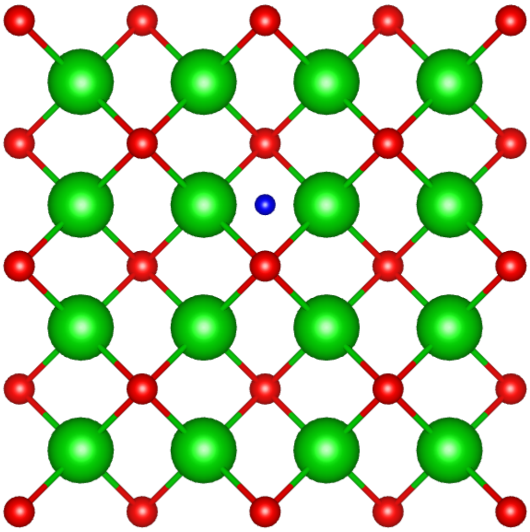

Figure 2.17: Example of an interstitial defect in Li_2O. Green ions represent lithium, and red ions represent oxygen. The blue ion represents an interstitial defect of any species.

A lattice site in the crystal may also in some cases be occupied by a different species. This species can be intrinsic (known as an antisite), or extrinsic to the crystal. In the case of ceramic breeding materials, tritium may occupy a lattice site in the crystal, either by transmutation of lithium in the crystal or through occupation of a vacancy defect. An example of a substitutional defect is given in Figure 2.18.

In ceramic breeding materials, the tritium substitutional on the lithium vacancy defect is displaced, and forms a hydroxyl bond with a neighbouring oxygen ion, as

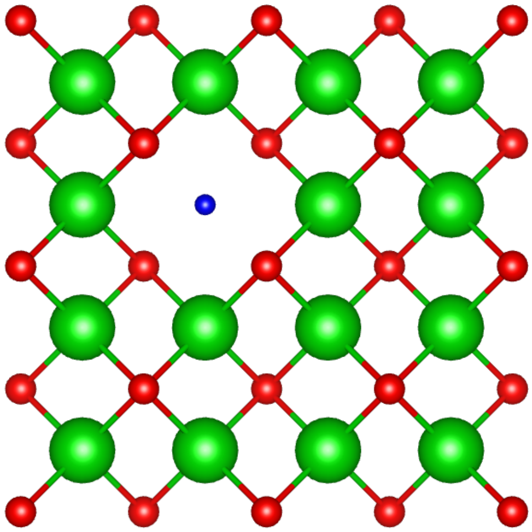

Figure 2.18: Example of an substitutional defect in Li_2O. Green ions represent lithium, and red ions represent oxygen. The blue ion represents a substitutional defect of any species (excluding lithium).

is seen in Li_2TiO_3 [131]. An example is shown in Figure 2.19 of the substitution of tritium on the lithium vacancy site in Li_2TiO_3, taken from Murphy [122].

2.6.2 Point Defect Concentrations

The total number of defects in a crystalline system is a direct function of temperature. Introducing point defects into a system will invariably increase the internal energy and the disordering (i.e. entropy) of the system, and in turn, the free energy. Consider first the free energy of a thermodynamically isolated system. The change in Gibbs free energy is given as:

$$\Delta G = \Delta H - T \Delta S_{conf} \tag{2.14}$$

where, ΔH is the internal energy change in the crystal (ΔU is used if the pressure in the system is not constant), and ΔS_{conf} is the change in configurational entropy. Considering the case of a simple vacancy defect in a crystal, the change in energy by introducing a vacancy is the formation energy of the defect, or if multiple vacancies

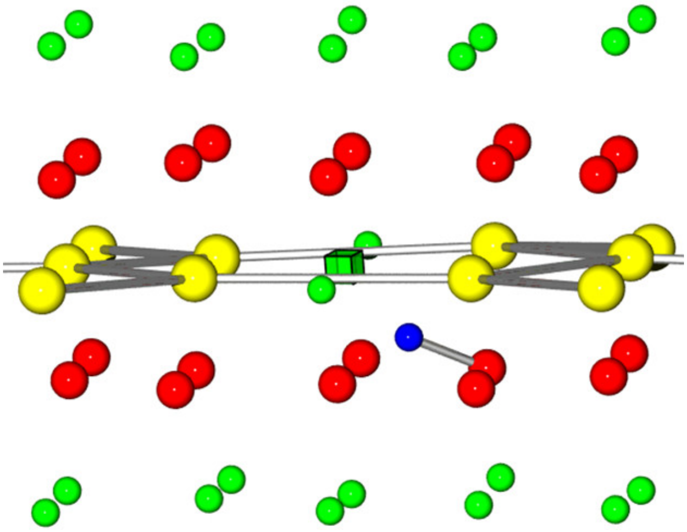

Figure 2.19: Example of a tritium ion bound to a lithium vacancy defect in Li_2TiO_3. The green, yellow, red, and blue spheres represent the lithium, titanium, oxygen, and tritium, respectively. The tritium ion has moved off the substitutional site in the mixed cation layer leaving a negatively charged lithium vacancy (transparent green cube) and bonded with a neighbouring oxygen ion to form a hydroxide species. This figure was taken from the works of Murphy [122].

of the same type are introduced, the change in energy is equivalent to:

$$\Delta H = n_v E_f \tag{2.15}$$

where, n_v is the number of vacancy defects, and E_f is the defect formation energy. Using Boltzmann statistics, it is possible to derive the concentration of defects of a species in a system. The configurational entropy increase from introducing the defects can be found using the Boltzmann relation [132]:

$$\Delta S_{conf} = k_B \ln(W) \tag{2.16}$$

where, k_B is the Boltzmann constant, and W is the total number of ways to arrange n_v vacancies onto N lattice sites within the system:

$$W = \frac{N!}{(N - n_v)!n_v!} \tag{2.17}$$

Taking the natural logarithm of W results in the new expression:

$$\ln(W) = \ln(N!) – \ln[(N - n_v)!] – \ln[(n_v)!] \tag{2.18}$$

The natural logarithm of $N!$ can be simplified using the Sterling approximation $\ln(N!) \simeq N\ln(N) - N$. Applying this approximation to $\ln(W)$ results in the equation:

$$\ln(W) = N\ln\left(\frac{N}{N - n_v}\right) + n_v\ln\left(\frac{N - n_v}{n_v}\right) \tag{2.19}$$

Combining equations 2.19 and 2.16 into equation 2.14 and taking the differential $\frac{d}{dn_v}$ of the resulting expression gives the equation:

$$\frac{dG}{dn_v} = E_f - k_B T\ln\left(\frac{N - n_v}{n_v}\right) (= 0) \tag{2.20}$$

where, the derivative $\frac{d\ln(W)}{dn_v}$ is $\ln(\frac{N-n_v}{n_v})$, and as the system is considered to be in thermodynamic equilibrium, the free energy is at a minimum, therefore $\frac{dG}{dn_v} = 0$. For large N, $N - n_v \simeq N$. Rearranging equation 2.20 for the defect concentration n_v/N results in the final expression for the concentration of vacancy defects in a system as a function of temperature and formation energy:

$$\frac{n_v}{N} = \exp\left(-\frac{E_f}{k_B T}\right) \tag{2.21}$$

Derivation of expressions for the interstitial and substitutional defects follows a similar process, and the concentrations of all three defects can be expressed much the same way.

2.7 Point Defect Diffusion

2.7.1 Fick's Laws of Diffusion

Diffusion in solid state materials can be summarised as a chemical process describing the mixing of dissimilar materials. The primary driving force for diffusion is the presence of a chemical or concentration gradient between materials. Solid state materials, as previously discussed, possess an intrinsic population of defects which allow for the exchange of atoms. The concentration gradient establishes a migratory pathway for a collective of atoms within a system to move from a region of high concentration to low concentration.

Alfred Fick, inspired by the experimental works of chemist Thomas Graham on the diffusion of gases [133], posited two laws mathematically formalising the diffusion process [134]. It should be noted that due to the widespread assumption during the period of Fick that diffusion in solids is not possible, his work considered diffusion in liquids. Regardless, Fick's laws apply to the case of solid state diffusion. Fick's first law is given by the differential equation:

$$\mathbf{J} = -D\nabla C \tag{2.22}$$

which, relates the diffusion flux, $\mathbf{J}$, to the concentration gradient ∇C, whereby C represents the concentration of a substance and D represents the diffusion coefficient, or the diffusivity.

As the concentration gradient encourages homogeneity between materials, the concentration is a time dependent process, i.e., it is typically a non-steady-state process for solid materials. Fick's second law introduces time dependence in the form of a partial differential equation:

$$\frac{\delta C}{\delta t} = D\Delta C \tag{2.23}$$

2.7.2 Diffusion Mechanisms

Solid state diffusion is described largely by the occurrence of random migratory "hops" of atoms in the crystal lattice. Each type of defect constitutes their own unique mechanism for migration through the host structure. For simple, isolated point defects these mechanisms are relatively simple, but in environments where the population of defects is high, these simple point defects can combine to form much more complicated diffusion mechanisms.

For temperatures above 0 K, there will be an intrinsic population of vacancy defects for any crystalline structure. Thus, due to their commonality, provide abundant pathways for diffusion. Isolated vacancy point defects will generally migrate using the vacancy mechanism, wherein the atom from a neighbouring atomic site randomly migrates to occupy the vacancy, leaving a new vacancy at the previously occupied site. An illustrative example of the vacancy mechanism is given in Figure 2.20.

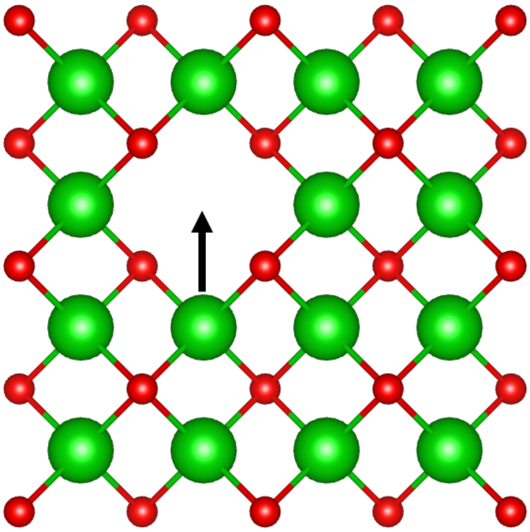

Figure 2.20: Example of the vacancy mechanism for the migration of a lithium vacancy defect in Li_2O. Green ions represent lithium, and red ions represent oxygen.

Migration of an interstitial defect to a neighbouring interstitial site is known as the interstitial mechanism, and is illustrated in Figure 2.21. Interstitial migration becomes especially important when considering interstitial atoms which are much smaller than the atoms in the host lattice. Due to their relatively low interaction with atoms in the host compared with other much larger atoms (or even intrinsic species), smaller atoms generally do not significantly displace atoms in the host lattice.

A slightly more complicated mechanism compared to the previous examples is the interstitialcy mechanism. In this case, the interstitial does not move directly from

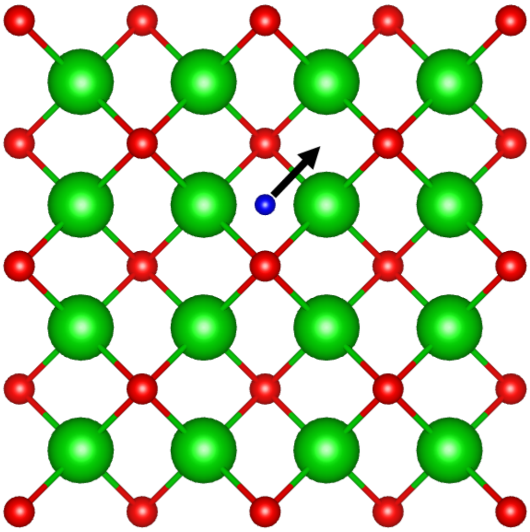

Figure 2.21: Example of an oxygen interstitial defect migrating via the interstial mechanism. Green ions represent lithium, and red ions represent oxygen, and the blue ion represents any generic species.

one interstitial site to the next, but rather it will displace an atom already situated within the host lattice, replacing and pushing it into an interstitial configuration. An illustration of the interstitialcy mechanism is given in Figure 2.22.

2.7.3 Diffusivity

As mentioned in the discussion on Fick's laws, diffusivity is a proportionality factor which relates the flow of a substance through a unit area to the concentration gradient. More simply, diffusivity describes the flow rate of a substance.

As diffusion is inherently kinetic, it is a thermally-activated process, thus diffusivity is dependent on temperature. The Arrhenius equation provides a useful empirical relationship between the reaction rate of a chemical process and temperature [135], and is generally found to be highly predictive for the diffusion rate in solids. The Arrhenius relationship as it relates to diffusivity is

$$D = D_0 exp(-E_\alpha/k_B T) \tag{2.24}$$

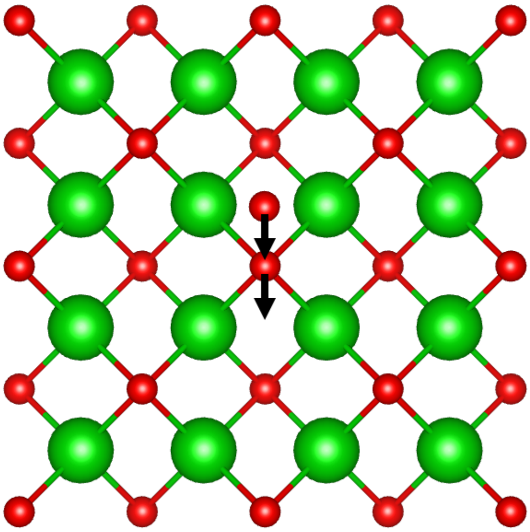

Figure 2.22: Example of an oxygen ion migrating via the interstitialcy mechanism. Green ions represent lithium, and red ions represent oxygen.

where, D_0 is the maximal diffusivity (at infinite temperature), and E_α is the activation energy for diffusion, i.e., the energy threshold for a reaction to occur.

A major shortcoming of the Arrhenius relationship is that it provides no precise definition of what the activation energy E_α represents. A more rigorous approach to understanding reaction rates is to use Transition State Theory (TST) [136], although in this instance, only the basic ideas behind TST are required to understand the activation energy.

The potential energy surface is a topographical function which describes the relationship between the molecular geometry and energy of a system. Atoms in their ground states within a system are confined to minima on the energy surface, and are able to escape by climbing the potential energy surface, provided there is sufficient thermal activation. In general, the thermal energy atoms possess under finite temperatures is low enough that atoms are unlikely to escape their respective minima. Although, should an atom acquire sufficient thermal activation, it may reach a 'transition state' (at, or close to a saddle point in proximity to the energy minimum) and successfully escape. The activation energy is defined as the energy required for an atom to reach the transition state. An example of the activation energy barrier along a generic reaction pathway is given by Figure 2.23.

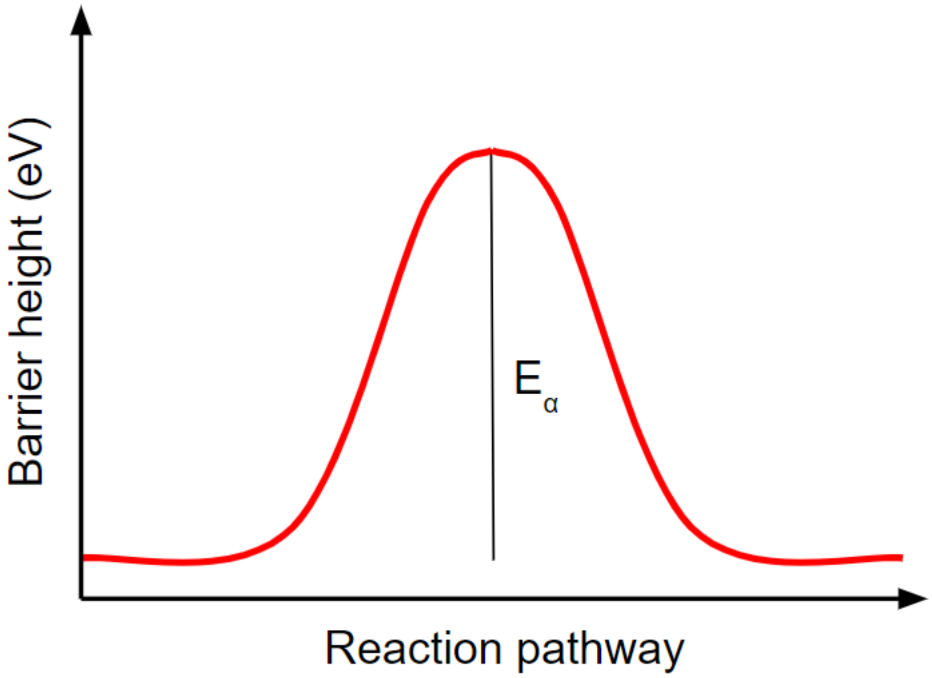

Figure 2.23: Illustrative example of a potential energy surface in a single dimension. In this example, the transition state is located at the peak of the potential energy surface.

Chapter 3

Methodology

This chapter provides an overview of the fundamental theories underlying the atomistic simulation techniques covered throughout this thesis. In Section 3.2, the underlying principles of quantum mechanics are covered before introducing Hartree-Fock theory, and subsequently, the development of Density Functional Theory. Section 3.3 continues with a brief discussion exploring thermodynamics in DFT, namely the quasi-harmonic approximation within the finite displacement method. Section 3.4 provides a detailed formalism for the defect chemistry of a system using a point defect model. Finally, in Section 3.5 the nudged elastic band method for optimising reaction pathways is described.

3.1 Atomistic simulation

Atomistic simulations can be broken down broadly into two main branches: quantum mechanical simulations (i.e. *ab initio*) which aim to solve to the many-body Schrödinger equation, and classical simulations, which are based on using empirically derived parameters to model interactions between atoms and molecules.

Classical simulations are generally significantly cheaper to run computationally in comparison with quantum mechanical simulations due to their reliance on simple inter-atomic potentials to model ionic interactions. Due to this, they are often the method of choice due to their ability to reveal the underlying mechanisms of quite complex phenomena, particularly in the field of nuclear engineering they are often the go-to tools to use for problems such as ionic mobility [137], radiation damage [138] and bubble formation in nuclear fuels [139]. Although, a core limitation of the classical approach is that they provide no details on the electronic structure.

Quantum mechanical methods, unlike classical methods such as molecular dynamics, rely on solving the many-body Schrödinger equation. The quantum mechanical method allows for analysis of the electronic structure of a system, and in cases of simple systems can generally be considered formally exact. Although, this comes at the cost of significantly higher computational demand in comparison with classical methods, and for larger and more complex simulations, it may be necessary to introduce corrections to reduce computational load.

In this thesis, the majority of the works conducted utilise the quantum mechanical modelling method Density Functional Theory, as no set of inter-atomic potentials for octalithium plumbate currently exists.

3.2 Quantum Mechanics

As discussed, fundamental to the works presented in this thesis is Density Functional Theory, a quantum mechanical modelling tool developed by Kohn and Hohenberg for modelling molecular and crystalline systems [99], which uses the electron density as an allegory for the ground-state energy derived from Schrödinger's equation. In this section, the core principles behind Density Functional Theory are outlined, beginning with discussion of the many-body Schrödinger equation, which is central to understanding the fundamentals of all quantum mechanical modelling methods.

3.2.1 The Many-Body Schrödinger Equation

Prior to discussing Density Functional Theory itself, it's important first to cover the core principles surrounding the many-body Schrödinger equation:

$$\hat{\mathrm{H}}\Psi(\mathbf{R}_I, \mathbf{r}_i) = \mathrm{E}\Psi(\mathbf{R}_I, \mathbf{r}_i) \tag{3.1}$$

where $\Psi(\mathbf{R}_I, \mathbf{r}_i)$ is the many-body wave function and E is the total energy of the system. $\hat{\mathrm{H}}$ is the Hamiltonian, which contains all of the operators for the ionic-ionic, electronic-electronic and ionic-electronic interactions, and is given by:

$$\hat{\mathrm{H}} = -\sum_i \frac{\bar{h}^2}{2m_e}\nabla^2_{\mathbf{r}_i} + V_{ext}(\mathbf{R}_I) + V_{e-e}(\mathbf{r}_i) \tag{3.2}$$

where $\bar{h}$ is the reduced Plank's constant, m_e is the electron mass, V_{ext} is the external potential imposed by the ionic configuration $\{\mathbf{R}_I\}$, and V_{e-e} is the electronic interaction potential, given by the Hartree term:

$$V_{e-e} = \sum_{i<j} \frac{e^2}{|\mathbf{r}_i - \mathbf{r}_j|} \tag{3.3}$$

where e is the constant for elementary charge. The ionic and electronic degrees of freedom have been separated according to the Born-Oppenheimer approximation [140], as due to the huge discrepancy in mass between the electrons and the ionic nuclei and the comparable forces both experience, the electrons will respond to any small perturbation of the nuclei much more quickly compared to the reverse.

The Born-Oppenheimer approximation ignoring any ion-ion interaction, allows for exclusive treatment in the wave function of the electron position alone, resulting in the new Hamiltonian:

$$\hat{\mathrm{H}} = -\sum_i \frac{\bar{h}^2}{2m_e}\nabla^2_{\mathbf{r}_i} - \sum_{I,i} \frac{Z_I e^2}{|\mathbf{R}_I - \mathbf{r}_i|} + \sum_{i<j} \frac{e^2}{|\mathbf{r}_i - \mathbf{r}_j|} \tag{3.4}$$

where $-\sum_{I,i} \frac{Z_I e^2}{|\mathbf{R}_I - \mathbf{r}_i|}$ is the attractive potential interaction between the nuclei and the electrons in the system, which are assumed to respond instantaneously, and the eigenvalue E resulting from the modified Hamiltonian operator gives the electronic potential energy.

3.2.2 Hartree-Fock Theory

Thanks to the Born-Oppenheimer approximation, only the wave functions of the electrons in the system need to be considered. The most straightforward way of constructing the wave function of the system is to treat the electrons within the system as a series of non-interacting particles, i.e.:

$$\Psi_{HP}(r_1, r_2, \ldots, r_N) = \prod_{i=1}^{N} \psi_i(r_i) \tag{3.5}$$

where $\psi_i(r_i)$ represents the normalised wave function for the ith electron in a system of N electrons. Treating the electrons as independent of one another is a bold assumption, but nonetheless, it is a good starting point, and this approximation is known as the Hartree product Ψ_{HP}. Although the Hartree product is a reasonable initial approximation to begin with, it fails to satisfy the Pauli exclusion principle [141] as it does not recognise the electrons are fermions and have an intrinsic spin component, i.e. that the wave function of the electrons should be treated as anti-symmetric with respect to any interchange in electron coordinates:

$$\chi(\mathbf{x}_1)\chi(\mathbf{x}_2) = -\chi(\mathbf{x}_2)\chi(\mathbf{x}_1) \tag{3.6}$$

where $\chi(\mathbf{x}_i)$ represents the spin orbital of an electron at the spacial coordinate $\phi(\mathbf{r}_i)$, and includes the spin component ω_i.

In the simple case of two electrons, we can express a wave function which satisfies the anti-symmetry requirement using the following normalised wave function:

$$\Psi(\mathbf{x}_1, \mathbf{x}_2) = \frac{1}{\sqrt{2}} |\chi(\mathbf{x}_1)\chi(\mathbf{x}_2) - \chi(\mathbf{x}_2)\chi(\mathbf{x}_1)| \tag{3.7}$$

or, in determinant form:

$$\Psi(\mathbf{x}_1, \mathbf{x}_2) = \frac{1}{\sqrt{2}} \begin{vmatrix} \chi(\mathbf{x}_1) & \chi(\mathbf{x}_2) \\ \chi(\mathbf{x}_1) & \chi(\mathbf{x}_2) \end{vmatrix} \tag{3.8}$$

Extrapolating the simple case to a system of N orbitals, we arrive at the Slater determinant [142]:

$$\Psi = \frac{1}{\sqrt{N!}} \begin{vmatrix} \chi_1(\mathbf{x}_1) & \chi_2(\mathbf{x}_1) & \dots & \chi_N(\mathbf{x}_1) \\ \chi_1(\mathbf{x}_2) & \chi_2(\mathbf{x}_2) & \dots & \chi_N(\mathbf{x}_2) \\ \vdots & \vdots & \ddots & \vdots \\ \chi_1(\mathbf{x}_N) & \chi_2(\mathbf{x}_N) & \dots & \chi_N(\mathbf{x}_N) \end{vmatrix} \tag{3.9}$$

With the Slater determinant, we now have a description of each electron within a system, and each electron is now associated with every orbital. A consequence of using the Slater determinant is that each electron is described as moving independently of one another, aside from the Coulomb repulsion force arising from the *average* positions of the other electrons in the system, i.e. it is an independent particle or *mean field* theory, and known as Hartree-Fock theory [143].

Using Dirac notation, the total energy of a system can now be described as:

$$E = \langle \Psi | \hat{H} | \Psi \rangle \tag{3.10}$$

where Ψ is the normalised wave function in Slater determinant form.

3.2.3 Density Functional Theory

Attempting to solve the many-body wave-function for more complex systems such as molecules or crystals is no small feat, so instead through a series of works published by Hohenberg, Kohn and Sham [99, 98] the problem was reformulated to instead rely on the electron density $n(r)$ (equation 3.11) rather than the wave-function itself, and resulted in the development of Density Functional Theory (DFT).

The electron density $n(r)$ is defined in terms of single-particle wave-functions in the following equation:

$$n(r) = \sum_i |\psi_i(\boldsymbol{r})|^2 \tag{3.11}$$

The basis of DFT is that the single-electron density can be treated as a fundamental variable, which is a consequence of the Hohenberg-Kohn theorem [99] that states the ground-state density $n_0(r)$ minimises the energy functional:

$$E[n(\boldsymbol{r})] = F[n(\boldsymbol{r})] + \int n(\boldsymbol{r})V_{ext}(\boldsymbol{r})d^3\boldsymbol{r} \tag{3.12}$$

where V_{ext} is the external potential, and $F[n(\mathbf{r})]$ is a universal functional which describes the electron-electron interaction and the kinetic energy, and the lowest value of E is the ground-state electron energy E_0. As this result is exact, it is possible in theory to describe both the electron density and ground-state energy using a variational minimisation over $n(\mathbf{r})$.

The universal functional which encapsulates the electron-electron interaction and the kinetic energy of a system is defined as the following:

$$F[n(\mathbf{r})] = \langle\Psi|(\hat{T} + \hat{U})|\Psi\rangle \tag{3.13}$$

where $\hat{T}$ and $\hat{U}$ represent operators for the kinetic energy and the electron-interaction respectively. If $F[n(\boldsymbol{r})]$ were a known and relatively simple functional, determining the ground-state would be relatively straightforward since it would be a simple case of minimising the functional relative to the electron density function. Although, currently no universal functional for $F[n(\boldsymbol{r})]$ has been found.

For the sake of convenience, the Hartree electron-electron interaction can be removed from the $F[n(\boldsymbol{r})]$ functional:

$$E[n(\boldsymbol{r})] = \int n(\boldsymbol{r})V_{ext}(\mathbf{r})d^3\mathbf{r} + \frac{e^2}{2}\iint \frac{n(\boldsymbol{r})n(\boldsymbol{r}')}{|\boldsymbol{r} - \boldsymbol{r}'|}d\boldsymbol{r}d\boldsymbol{r}' + G[n(\boldsymbol{r})] \tag{3.14}$$

where $G[n(\boldsymbol{r})]$ is a new universal function.

Using the one-particle density matrix $n_1(\boldsymbol{r}, \boldsymbol{r}')$ and the two-particle correlation function $C_2(\boldsymbol{r}, \boldsymbol{r}')$, an expression for $G[n(\boldsymbol{r})]$ can be obtained:

$$G[n(\boldsymbol{r})] = -\frac{\hbar^2}{2m_e}\int \nabla^2_{\boldsymbol{r}} n_1(\boldsymbol{r}, \boldsymbol{r}')|_{\boldsymbol{r}=\boldsymbol{r}'}d\boldsymbol{r} + \iint \frac{C_2(\boldsymbol{r}, \boldsymbol{r}')}{|\boldsymbol{r} - \boldsymbol{r}'|}d\boldsymbol{r}d\boldsymbol{r}' \tag{3.15}$$

where the first term is the kinetic energy contribution, the one-particle density matrix is equivalent to the charge density $n_1(\boldsymbol{r}, \boldsymbol{r}') \equiv n(\boldsymbol{r})$ and the two-particle correlation function is defined as:

$$C_2(\boldsymbol{r},\boldsymbol{r}') = n_2(\boldsymbol{r},\boldsymbol{r}';\boldsymbol{r},\boldsymbol{r}') - n_1(\boldsymbol{r},\boldsymbol{r})n_1(\boldsymbol{r}',\boldsymbol{r}') \tag{3.16}$$

The expression for $E[n(\boldsymbol{r})]$ can now be reduced to a set of single-particle equations:

$$\left[-\frac{\hbar^2}{2m_e}\nabla_{\boldsymbol{r}}^2 + V_{eff}(\boldsymbol{r}, n(\boldsymbol{r}))\right]\psi = \epsilon_i\psi(\boldsymbol{r}) \tag{3.17}$$

where V_{eff} contains the external potential, the electron-electron interaction and the exchange-correlation interactions:

$$V_{eff}(\boldsymbol{r}, n(\boldsymbol{r})) = V_{ext}(\boldsymbol{r}) + e^2\int \frac{n(\boldsymbol{r})}{|\boldsymbol{r}-\boldsymbol{r}'|}d\boldsymbol{r} + \frac{\delta E_{XC}[n(\boldsymbol{r})]}{\delta n(\boldsymbol{r})} \tag{3.18}$$

The exchange-correlation functional $E_{XC}[n(\boldsymbol{r})]$ encapsulates the effects of self-interaction. Currently, an exact form for $E_{XC}[n(\boldsymbol{r})]$ has not yet been found. Up until now, the Kohn-Sham approach can be considered formally exact. As the $E_{XC}[n(\boldsymbol{r})]$ functional is defined in the Kohn-Sham approach as the difference between the 'true' universal functional $F[n(\boldsymbol{r})]$ and the known terms, an approximation must be used.

Many approximations to the exchange-correlation functional have been proposed. The simplest is the Local Density Approximation (LDA) [144] in which the exchange-correlation energy is treated as a uniform electron gas for every infinitesimal point of density:

$$E_{XC}[n(\boldsymbol{r})] = \int \epsilon_{XC}(n(\boldsymbol{r}))n(\boldsymbol{r})d\boldsymbol{r} \tag{3.19}$$

where $\epsilon_{XC}(n(\boldsymbol{r}))$ is the exchange-correlation energy per unit volume of electron gas with density $n(\boldsymbol{r})$, and has previously been calculated using Quantum Monte Carlo methods by Ceperley and Alder [145].

As the electron density is evidently non-uniform, the LDA approximation is generally appropriate for systems where the electron density is somewhat uniform. Building on the LDA method by accounting for the non-uniformity of the electron density, we arrive at the Generalised Gradient Approximation (GGA) [146], which includes a dependence on the gradient of the electron density into the exchange-correlation energy:

$$E_{XC}[n(\boldsymbol{r})] = \int \epsilon_{XC}(\nabla n(\boldsymbol{r}), n(\boldsymbol{r}))n(\boldsymbol{r})d\boldsymbol{r} \tag{3.20}$$

There are many options for the choice of GGA functional. Generally, LDA tends to overbind atoms, resulting in smaller bond lengths in comparison with GGA which is generally more physically consistent, although sometimes GGA may overcorrect and result in slightly larger bond lengths. Both approximations remain highly effective for calculating differences in energy which generally aren't significantly impacted by such overestimation.

Another option is to use the Hartree-Fock method [143] as a hybrid functional. The hybrid functional is able to negate the effects of the self-interaction energy by cancelling out the contributions to the energy in the Hartree-Fock method:

$$E_{XC}[n(\boldsymbol{r})] = E_{XC}^{GGA} + \alpha(E_{XC}^{HF} - E_{EX}^{GGA}) \tag{3.21}$$

where E_{XC}^{GGA} and E_{XC}^{HF} are the GGA and Hartree-Fock exchange energies, and α is a mixing parameter.

For the majority of the works presented in this thesis, the GGA functional of Perdew, Burke and Ernzerhof (PBE) [146] has been used. In instances where the self-interaction is expected to have a significant contribution (i.e. in predicting the electronic density of states), a hybrid functional as defined in equation 3.21 is used instead.

3.2.4 Plane-Wave DFT

The Kohn-Sham wave-functions can easily be represented by a complete basis set. Typically in DFT, the plane-wave basis set is used for periodic crystal structures due to its efficiency in calculating ionic forces, the lack of any inherent superposition error and that the plane-wave basis set makes no assumptions about the general form of the final solution.

Introducing a periodic boundary condition onto the plane-wave basis set allows for much more efficient calculation, as there is no requirement for a continuous basis set. This is done via the use of Bloch's Theorem [147], where the solutions to Schrödinger's equation can be represented by a periodic basis set.

Representing the wave-function as a Bloch state:

$$\psi_{\boldsymbol{k}}(\boldsymbol{r}) = u_{\boldsymbol{k}}(\boldsymbol{r})e^{i(\boldsymbol{k}\cdot\boldsymbol{r})} \tag{3.22}$$

where $\boldsymbol{r}$ and $\boldsymbol{k}$ represent the real vector and reciprocal wave vector for the electron associated by the wave-function $\psi_{\boldsymbol{k}}(\boldsymbol{r})$, and $u_{\boldsymbol{k}}(\boldsymbol{r})$ is a periodic function with the same periodicity as the crystal, a generalised description for the wave-function is obtained.

As the wave-function is expressed in terms of the wave vector $\boldsymbol{k}$, the wave-function can also be expressed in terms of $\boldsymbol{k}+\boldsymbol{G}$, where $\boldsymbol{G}$ is any generic reciprocal lattice vector. i.e. wave vectors that differ by a reciprocal lattice vector are equivalent, and $\boldsymbol{k}$ can be treated as a symmetry label. The Brillouin zone is an area containing a restricted set of non-equivalent values of $\boldsymbol{k}$, with every value of $\boldsymbol{k}$ being equivalent to a $\boldsymbol{k}$ in the first Brillouin zone, i.e. only the k-points within the first Brillouin zone are necessary.

Expressing the periodic function $u_{\boldsymbol{k}}(\boldsymbol{r})$ as a Fourier series:

$$u_{\boldsymbol{k}}(\boldsymbol{r}) = \sum_{\boldsymbol{G}} c_{\boldsymbol{G}} e^{i(\boldsymbol{G}\cdot\boldsymbol{r})} \tag{3.23}$$

where $c_{\boldsymbol{G}}$ are plane expansion coefficients, and combining this with equation 3.22 we arrive at the full periodic description of the wave-function in terms of real and reciprocal lattice vectors:

$$\psi_{i,\boldsymbol{k}}(\boldsymbol{r}) = \sum_{\boldsymbol{G}} c_{i,\boldsymbol{G}+\boldsymbol{k}} e^{i(\boldsymbol{G}+\boldsymbol{k})\cdot\boldsymbol{r}} \tag{3.24}$$

Equation 3.24 implies there is an infinite amount of $\boldsymbol{G}$ vectors allowed, although in practice the set of plane waves is restricted to a sphere in reciprocal space according to a pre-defined energy cut-off E_{cut}:

$$\frac{\hbar^2|\boldsymbol{G}+\boldsymbol{k}|^2}{2m_e} \leq E_{cut} \tag{3.25}$$

As seen by equation 3.25, the convergence of the simulation is highly dependent on not only the choice of basis set, but also on the number of k-points chosen, so it is essential to ensure the k-point density and E_{cut} are high enough such that the energy of the system is sufficiently converged.

The electron density and the total energy for the system can be found by averaging all values over $\boldsymbol{k}$ found within the first Brillouin zone:

$$n(\boldsymbol{r}) = \frac{1}{V_{1BZ}} \int_{1BZ} n_{\boldsymbol{k}}(\boldsymbol{r}) d^3\boldsymbol{k} \tag{3.26}$$

and

$$E = \frac{1}{V_{1BZ}} \int_{1BZ} E(\boldsymbol{k}) d^3\boldsymbol{k} \tag{3.27}$$

where V_{1BZ} is the volume of the first Brillouin zone.

The primary disadvantage with using a plane-wave basis set is that a very large amount of plane-waves is generally required for an adequate Fourier expansion. This can be mitigated by instead using pseudo-potentials, which are discussed briefly in the following subsection.

3.2.5 Pseudo-potentials

Due to the strong potential in the region close to atomic nuclei and the rapid oscillations in such regions, a very large number of k-points is typically required to describe regions close to the atomic core. Fortunately, the core electrons of atoms rarely show any significance to the local environment surrounding the atom and thus it is appropriate to incorporate the core electrons into the nucleus and consider only the impact the valence electrons have on the local environment, in the form of a pseudo-potential [148]. The pseudo-potential is designed such that the rapid oscillations within the core region are smoothed, greatly reducing both the number of plane-waves and the energy cut-off E_{cut} required. An example schematic taken from Payne *et al.* [149] is shown in Figure 3.1.

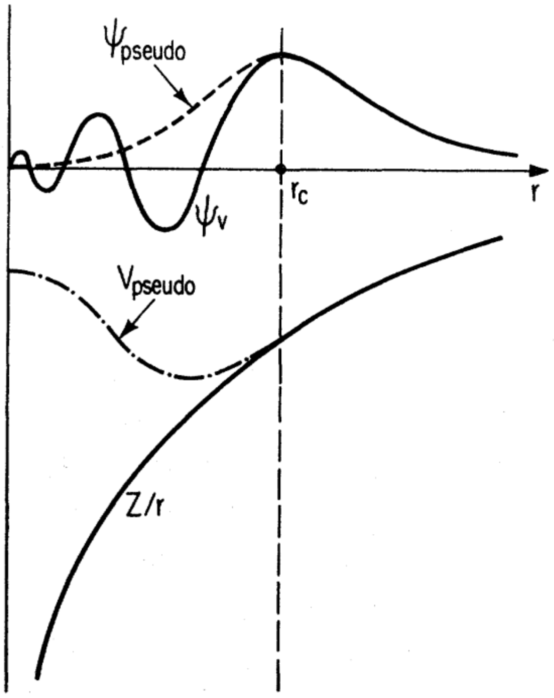

Figure 3.1: Illustrative example of the all-electron (ψ_V, Z/r) and pseudo-electron (ψ_{pseudo}, V_{pseudo}) potentials (bold and dotted lines respectively). r_c represents the cut-off radius under which both schemes match, and for $r > r_c$, both schemes are identical. This schematic is taken from Payne *et al.* [149].

Outside the cut-off radius r_c, the pseudo-potential is designed in such a way to match the true potential, as well as the charge-density outside the core region, i.e. the integral of the squared amplitudes over both the real and pseudo-potentials must be the same, and is known as norm-conservation [150].

Broadly speaking the choice of pseudo-potentials can be broken down into two main categories, which are 'soft' and 'hard' pseudopotentials. Soft (or even ultra-soft) pseudo-potentials require fewer plane-waves (and thus a lower E_{cut}) compared to hard pseudo-potentials, i.e. the degree of hardness of a pseudopotential describes the number of plane-waves required to perform a sufficient calculation. Ultra-soft pseudopotentials are an extreme case of the soft potential, and relax the norm-conserving requirement to reduce the amount of plane-waves necessary to perform an accurate calculation [151]. The most commonly used pseudopotentials are the soft/norm-conserving pseudopotentials.

The works presented throughout this thesis utilise projector augmented wave (PAW) pseudopotentials [152], which are a development of the ultra-soft pseudopotential, and utilise a localised basis set close to the the atomic cores.

3.3 Thermodynamics in DFT

Many of the physical properties of a material can't be investigated using energy minimisation alone. This is because it does not account for time dependence making it difficult to examine properties that are dependent on the presence of perturbations in the crystal structure. Methods such as Density Functional Perturbation Theory (DFPT) [153] or the finite displacement method [154] allow for this by introducing small perturbations onto atoms in the crystal to obtain the phonon density of states. Using the phonon density of states, many of the thermodynamic properties of a material can be measured. For this work, the finite differences method in the Phonopy post-processing package [155] is used to extract temperature-dependent properties such as the specific heat capacity.

3.3.1 Harmonic Approximation

The Helmholtz free energy is taken to be the sum of the electronic and phonon contributions $F = U + F_{phonon}$ where U is the internal energy of the unit cell obtained directly from DFT. The phonon contribution to the Helmholtz free energy F_{phonon} is given by the equation:

$$\begin{aligned} F_{phonon} = {} & \frac{1}{2}\sum_{\bar{q},v} \hbar\omega_{\bar{q},v} \\ & + k_B T \sum_{\bar{q},v} ln\left(1 - e^{-\hbar\omega_{\bar{q},v}/k_B T}\right) \end{aligned} \tag{3.28}$$

where $\bar{q}$ is the wave vector, v is the band index, $\omega_{\bar{q},v}$ is the phonon frequency [156], T is the temperature, and k_B is the Boltzmann constant.

The specific heat capacity for constant volume can be calculated using:

$$\begin{aligned} C_V &= \left(\frac{\delta F}{\delta T}\right)_V \\ &= \sum_{\bar{q},v} k_B \left(\frac{\hbar\omega_{\bar{q},v}}{k_B T}\right) \frac{e^{-\hbar\omega_{\bar{q},v}/k_B T}}{\left(e^{-\hbar\omega_{\bar{q},v}/k_B T} - 1\right)^2} \end{aligned} \tag{3.29}$$

and for a fixed volume V, the vibrational entropy can be given by the the following equation:

$$\begin{aligned} S = &- k_B \sum_{\bar{q},v} ln\left(1 - e^{-\hbar\omega_{\bar{q},v}/k_B T}\right) \\ &- \frac{1}{T} \sum_{\bar{q},v} \frac{\hbar\omega_{\bar{q},v}}{e^{-\hbar\omega_{\bar{q},v}/k_B T} - 1} \end{aligned} \tag{3.30}$$

3.3.2 Quasi-Harmonic Approximation

In order to fully understand the thermodynamic properties of a material at high temperature it is important to consider the thermal expansion. The volume dependence must, therefore, be introduced into the calculation to account for volume expansion and relaxation. To do this, the quasi-harmonic approximation (QHA) [156] is implemented in Phonopy [155]. The volume-dependent thermodynamic properties can be predicted by trialling a series of different unit cell volumes and using the pressure-dependent internal energies and respective phonon frequencies of each chosen volume to estimate the minimum Gibbs free energy of the system regardless of volume, effectively replacing pressure for volume dependence. For all materials, 11 different volumes were chosen in equal steps of 3% within a range of ±15% of the relaxed unit cell volume.

The pressure-dependent Gibbs free energy can be found by measuring the lowest internal energy and respective phonon contribution for the volume range trialled:

$$G(T, p) = \left(U(V) + F_{phonon}(T; V) + pV\right)_{min} \tag{3.31}$$

The specific heat capacity for constant pressure can be derived either directly from the Gibbs free energy $G(T,p)$ obtained from equation 3.31, or from the specific heat for constant volume C_V and the entropy $S(T;V)$:

$$C_p = -T\frac{\delta^2 G(T,p)}{\delta T^2} = T\frac{\delta V}{\delta T}\frac{\delta S(T;V)}{\delta V} + C_V(T,V) \tag{3.32}$$

where $V = V(T,p)$ represents the volume for the minimum Gibbs energy state at T and p given by equation 3.31 and $S(T;V)$ is given by equation 3.29. As entropy increases with increasing temperature, C_p must always be greater than C_V.

3.4 Defect Chemistry

Central to the works of this thesis is the characterisation and evolution of point defects in different environments. In this subsection, the process for analysing the defect chemistry of Li_8PbO_6 using a point defect model is outlined.

3.4.1 Point defect concentrations

The charge neutrality condition requires an overall balance between the ionic and electronic defects in the system, i.e.:

$$\sum_i q_i c_i - c_e + c_h = 0 \tag{3.33}$$

where, c_i is the concentration of any point defect, i, with a charge q_i and c_e and c_h are the concentrations of electrons in the conduction band and holes in the valence band respectively.

The concentration of any point defect in a material is related to the Gibbs formation energy according to:

$$c_i \propto m_i exp\left(\frac{-\Delta G_f^i}{k_B T}\right) \tag{3.34}$$

where, m_i is the multiplicity of the defect, k_B is the Boltzmann constant and T is the temperature.

It is typically assumed that the vibrational contributions to the free energy of a defect are negligible and so the Gibbs formation energy can be approximated to be the change in internal energy associated with formation of the defect i, using:

$$\Delta E_f^i = E_{\text{defect}} - E_{\text{perfect}} + \sum_{\alpha} n_\alpha \mu_\alpha + q_i(E_{\text{VBM}} + \varepsilon_f) + E_{corr} \tag{3.35}$$

where, E_{defect} and E_{perfect} are the DFT total energies of the supercell with and without the presence of the point defect, respectively, n_α is the number of atoms, of species α, added/removed from the supercell to construct the defect, μ_α is the chemical potential of the species α, q_i is the charge of the defect i, E_{VBM} is the valence band maximum (VBM) of the defect-free system, ε_f is the Fermi energy relative to the VBM and E_{corr} is a charge correction term used to mitigate for finite-size effects (discussed in Section 6.3.1.1).

3.4.2 Constituent chemical potential contribution

To calculate the chemical potentials of the constituents of $\mathrm{Li_8PbO_6}$, we first assume $\mathrm{Li_8PbO_6}$ can be formed from the two binary oxides $\mathrm{Li_2O}$ and $\mathrm{PbO_2}$ (as is done by Colominas *et al.* [121]) via the reaction:

$$4\mathrm{Li_2O_{(s)}} + \mathrm{PbO_{2(s)}} \rightarrow \mathrm{Li_8PbO_{6(s)}} \tag{3.36}$$

For any condition, the sum of the chemical potentials of the constituents must equal the chemical potential of $\mathrm{Li_8PbO_6}$:

$$4\mu_{\mathrm{Li_2O}}(p_{O_2}, T) + \mu_{\mathrm{PbO_2}}(p_{O_2}, T) = \mu_{\mathrm{Li_8PbO_{6(s)}}}(T) \tag{3.37}$$

where, $\mu_{\mathrm{Li_2O}}(p_{O_2}, T)$ and $\mu_{\mathrm{PbO_2}}(p_{O_2}, T)$ are the chemical potentials of $\mathrm{Li_2O}$ and $\mathrm{PbO_2}$ as a function of oxygen partial pressure and temperature respectively, and $\mu_{\mathrm{Li_8PbO_{6(s)}}}(T)$ is the chemical potential of solid $\mathrm{Li_8PbO_6}$.

At low temperatures, vibrational contributions to the constituent chemical potentials can be safely assumed to be negligible, and so $\mu(p^\circ_{O_2}, T^\circ) \approx \mu(0, 0)$. However, for breeder blankets that typically operate at high temperatures, vibrational and entropic factors may contribute strongly to the formation energy of a defect. Therefore, the works of this thesis introduce a novel method for incorporating temperature effects into defect formation energies.

The chemical potentials of the solid oxide reference states are traditionally bound to their respective DFT lattice energy. Although, it is possible to introduce temperature dependence into the chemical potentials by substituting the DFT lattice energies for their respective Gibbs free energies. If the chemical potential exceeds this upper bound, it becomes thermodynamically favourable for a precipitate to form. At the $\mathrm{Li_2O}$ saturation limit, or $\mathrm{Li_2O}$-rich conditions, the chemical potential of the binary oxide can be determined using DFT as:

$$\mu_{\mathrm{Li_2O}}^{\mathrm{Li_2O-rich}}(T) = \mu_{\mathrm{Li_2O_{(s)}}}(T) \tag{3.38}$$

To calculate the lower bound for the chemical potential of each binary compound, we assume the other component must be at their upper bound:

$$\mu_{\mathrm{Li_2O}}^{\mathrm{Li_2O-poor}}(T) = \frac{\mu_{\mathrm{Li_8PbO_{6(s)}}}(T) - \mu_{\mathrm{PbO_{2(s)}}}(T)}{4} \tag{3.39}$$

The values for the chemical potentials can fall anywhere in this rich/poor range, therefore we define a fraction, f, for each oxide which controls where in this range the chemical potential falls:

$$\mu_{\mathrm{Li_2O}}^{f} = f\mu_{\mathrm{Li_2O}}^{\mathrm{Li_2O-rich}}(T) + (1-f)\mu_{\mathrm{Li_2O}}^{\mathrm{Li_2O-poor}}(T) \tag{3.40}$$

The fraction, f, assigned to each oxide is constrained by the following equation:

$$\sum f^{\mathrm{Li_2O}}(T) + f^{\mathrm{PbO_2}}(T) = 1 \tag{3.41}$$

The two constituent oxides can also be decomposed to their sub-components to determine the chemical potentials of the elements Li, Pb, and O. Using $\mathrm{Li_2O}$ once again as an example:

$$\mu_{\mathrm{Li_2O_{(s)}}}(p_{O_2}, T) = 2\mu_{\mathrm{Li}}(p_{O_2}, T) + \mu_O(p_{O_2}, T) \tag{3.42}$$

where, $\mu_{\mathrm{Li}}(p_{O_2}, T)$ and $\mu_O(p_{O_2}, T)$ are the chemical potentials of Li and O in $\mathrm{Li_2O}$. Rather than determining the chemical potential of oxygen from the $\mathrm{O_2}$ molecule directly from DFT, which is problematic due to self-interaction, the method of Finnis *et al.* [157] is adopted, and the experimental formation energy of the oxide compound is used:

$$\Delta G_f^{\mathrm{Li_2O}}(p^{\circ}_{O_2}, T^{\circ}) = \mu_{\mathrm{Li_2O_{(s)}}} - 2\mu_{\mathrm{Li_{(s)}}} - \mu_O(p^{\circ}_{O_2}, T^{\circ}) \tag{3.43}$$

where, $\Delta G_f^{\mathrm{Li_2O}}(p^{\circ}_{O_2}, T^{\circ})$ is the known experimental formation energy for $\mathrm{Li_2O}$, taken as -6.205 eV, and -2.845 eV for $\mathrm{PbO_2}$ according to Chase [158]. $\mu_{\mathrm{Li_{(s)}}}$ is the chemical potential of Li metal, obtained with DFT. This method results in $\mu_O(p^{\circ}_{O_2}, T^{\circ})$ being calculated twice, once for each oxide. A final value of $\mu_O(p^{\circ}_{O_2}, T^{\circ})$ is calculated as a weighted average of the contributions by the fractions of oxides present:

$$\mu_{\mathrm{O}}(p^{\circ}_{\mathrm{O_2}}, T^{\circ}) = \sum_j f^j \mu^j_{\mathrm{O}}(p^{\circ}_{\mathrm{O_2}}, T^{\circ}) \tag{3.44}$$

The temperature and pressure dependence of the oxygen chemical potential cannot be neglected, and is extrapolated from $\mu_O(p^{\circ}_{\mathrm{O_2}}, T^{\circ})$ using the relationship:

$$\begin{aligned}\mu_O(p_{O_2}, T) = \mu_O(p^{\circ}_{O_2}, T^{\circ}) + G(p^{\circ}_{O_2}, T) \\ - G(p^{\circ}_{O_2}, T^{\circ}) + k_B T ln\left(\frac{p_{O_2}}{p^{\circ}_{O_2}}\right)\end{aligned} \tag{3.45}$$

where, $G(p^{\circ}_{O_2}, T)$ is determined from the description of the real heat capacities for the $\mathrm{O_2}$ molecule using the Shomate equations:

$$G(p^{\circ}_{\mathrm{O_2}}, T^{\circ}) = H(p^{\circ}_{\mathrm{O_2}}, T^{\circ}) - TS(p^{\circ}_{\mathrm{O_2}}, T^{\circ}) \tag{3.46}$$

$$H(p^{\circ}_{\mathrm{O_2}}, T^{\circ}) = 1000(\mathrm{A}t + \mathrm{B}\frac{t^2}{2} + \mathrm{C}\frac{t^3}{3} + \mathrm{D}\frac{t^4}{4} - \frac{\mathrm{E}}{t} + \mathrm{F} - \mathrm{H}) \tag{3.47}$$

$$S(p^{\circ}_{\mathrm{O_2}}, T^{\circ}) = \mathrm{A}ln(t) + \mathrm{B}t + \mathrm{C}\frac{t^2}{2} + \mathrm{D}\frac{t^3}{3} - \frac{\mathrm{E}}{2t^2} + \mathrm{G} \tag{3.48}$$

where, t = T/1000 K. Coefficients for the Shomate equations used for the $\mathrm{O_2}$ molecule are taken from the NIST Chemistry WebBook [159], and are given in Table 3.1.

Table 3.1: Shomate equation coefficients for gaseous O_2 [159].

Temperature (K)	100-700	700 - 2000	2000 - 6000
A ($\times 10^3$)	0.324659	0.311288	0.215745
B ($\times 10^3$)	-0.209741	9.09326×10^{-2}	0.111121
C ($\times 10^3$)	0.559979	-4.13373×10^{-2}	-2.09426×10^{-2}
D ($\times 10^3$)	-0.37839	8.17093×10^{-3}	1.51796×10^{-3}
E ($\times 10^3$)	-7.64321×10^{-5}	-7.68674×10^{-3}	9.58327×10^{-2}
F ($\times 10^3$)	-9.22852×10^{-2}	-0.117381	5.53252×10^{-2}
G ($\times 10^3$)	2.558046	2.447884	2.462936
H	0	0	0

3.4.3 Electronic defects

The concentrations of electronic defects in the system can be determined from Fermi-Dirac statistics according to:

$$c_e = \int_{E_{CBM}}^{\infty} \frac{g_c(E)}{1 + exp\left(\frac{E-\varepsilon_f}{k_B T}\right)} dE \tag{3.49}$$

and

$$c_h = \int_{-\infty}^{E_{VBM}} \frac{g_v(E)}{1 + exp\left(\frac{\varepsilon_f - E}{k_B T}\right)} dE \tag{3.50}$$

where, $g_{\mathrm{c}}(E)$ and $g_{\mathrm{v}}(E)$, are calculated from the electronic density of states for Li_8PbO_6 found using the hybrid functional of Heyd, Scuseria and Ernzerhof (HSE06) [160], and E_{VBM} and E_{CBM} are the energies of the valence band maximum and the conduction band minimum respectively.

3.4.4 Finite size effects

The Coulombic interaction between a defect and its periodic images in neighbouring unit cells results in an artificial inflation to the calculated total energy of the cell.

This is in part reduced by the interaction with the charge-neutralising background. As these interactions are slow to converge with unit cell size, it is appropriate to apply a finite size correction to compensate for this error.

The anisotropic screening correction developed by Kumagai and Oba [161] builds on the point charge correction developed by Freysoldt, Neugebauer and Van de Walle (FNV) [162] by using atomic site potentials rather than planar averaged electrostatic potentials. Using the atomic site electronic potentials of supercells with ($V_{def,q}$) and without (V_{perf}) defects, E_{corr} for a defect with charge q is calculated:

$$E_{corr} = E_{PC} - q\Delta V_{PC,q/b}|_{far} \tag{3.51}$$

$$\Delta V_{PC,q/b} = V_{q/b} - V_{PC,q} \tag{3.52}$$

$$V_{q/b} = V_{def,q} - V_{perf} \tag{3.53}$$

$\Delta V_{PC,q/b}$ is the potential difference between the defect induced potential ($V_{q/b}$) and the point charge (PC) potential, $V_{PC,q}$. $\Delta V_{PC,q/b}|_{far}$ is $\Delta V_{PC,q/b}$ at a position far from the defect site but still within the supercell. E_{PC} is the PC correction, calculated for each charged defect using equation 3.54:

$$E_{PC} = \frac{1}{2} q^2 v_M^{scr} \tag{3.54}$$

where v_M^{scr} is the Madelung potential for a point charge in a general 3-dimensional box screened by a general dielectric. Taking into account the anisotropic dielectric properties of Li_8PbO_6, a value of v_M^{scr} using the system's dielectric tensor, $\bar{\epsilon}$, calculated using the method described by Murphy and Hine [163]:

$$\begin{aligned} v_M^{scr} = & \sum_{\mathbf{R}_i}^{i \neq 0} \frac{1}{\sqrt{\det \bar{\epsilon}}} \frac{\operatorname{erfc}(\gamma \sqrt{\mathbf{R}_i \cdot \bar{\epsilon}^{-1} \cdot \mathbf{R}_i})}{\sqrt{\mathbf{R}_i \cdot \bar{\epsilon}^{-1} \cdot \mathbf{R}_i}} \\ & + \sum_{\mathbf{G}_i}^{i \neq 0} \frac{4\pi}{V_c} \times \frac{\exp(-\mathbf{G}_i \cdot \bar{\epsilon} \cdot \mathbf{G}_i / 4\gamma^2)}{\mathbf{G}_i \cdot \bar{\epsilon} \cdot \mathbf{G}_i} - \frac{2\gamma}{\sqrt{\pi \det \bar{\epsilon}}} - \frac{\pi}{V_c \gamma^2} \end{aligned} \tag{3.55}$$

where, the sum extends over all basis vectors of the direct ($\mathbf{R}_i$) and reciprocal ($\mathbf{G}_i$) lattices, γ is a suitably chosen convergence parameter, and V_c is the volume of the supercell.

Chapters 4 and 5 utilise only the Madelung point charge correction E_{PC} as the charges of the defects considered in these chapters are low enough that the Coulombic correction alone is sufficient, whereas the remaining chapters utilise the full Kumagai and Oba anisotropic screening correction.

3.5 Nudged Elastic Band

To examine possible reaction pathways for defects within DFT, the Nudged Elastic Band (NEB) method [164] may be used. The primary objective of NEB is to find the optimal reaction pathway between two energy minima along the potential energy surface.

In the standard NEB approach, a series of intermediate images are placed along the path between the initial and final states. The total number of images used to describe a reaction pathway should be suitably large to reach sufficient convergence towards the optimal reaction pathway. The initial reaction pathway is determined using an interpolation method (most commonly a linear interpolation) to acquire the initial set of intermediate images. Optimising the pathway is done by introducing an iterative algorithm beginning with the initial interpolated pathway.

Keeping the initial and final reaction coordinates fixed, a gradient-based optimisation method is used in conjunction with an effective NEB force acting on the atoms. The effective NEB force contains two components, a spring force tangential to the reaction pathway $\mathbf{F}^{\parallel}$, and a restoring force perpendicular to the path $\mathbf{F}^{\perp}$, and is given by:

$$\boldsymbol{F}_i = \boldsymbol{F}_i^{\parallel} + \boldsymbol{F}_i^{\perp} \tag{3.56}$$

where the perpendicular restoring force is found via the following equation:

$$\boldsymbol{F}_i^{\perp} = \nabla E(\boldsymbol{R}_i) - \nabla E(\boldsymbol{R}_i) \cdot \hat{\boldsymbol{\tau}}_i \tag{3.57}$$

where $\hat{\boldsymbol{\tau}}_i$ is the local unit tangent for image i, where the unit tangent is taken as the normalised tangent along the pathway of the current and neighbouring higher energy image [165], and $\boldsymbol{R}_i$ is the 3M-dimensional coordinates of the ion along the reaction pathway for image i. At the extrema, the unit tangent is taken as the normalised energy weighted average of the two connected line segments connected either side.

The spring force controls the distribution of images along the reaction pathway, and is given by the following:

$$\boldsymbol{F}_i^{\parallel} = (k_i^{\parallel}|\boldsymbol{R}_{i+1} - \boldsymbol{R}_i| - k_{i-1}^{\parallel}|\boldsymbol{R}_i - \boldsymbol{R}_{i-1}|)\hat{\boldsymbol{\tau}}_i \tag{3.58}$$

where $k_i^{\parallel}$ is the spring constant. An illustration of the migration of an image from the initial migration pathway to the minimum energy path is shown in Figure 3.2. All NEB simulations performed in this thesis utilise a value of 5 eV/Å^2, as it provides sufficient force to keep the distribution of images equidistant from one another without compromising on time to convergence.

The energy maximum along the final reaction pathway gives an approximation for the energy barrier required for the reaction to occur. For standard NEB calculations as described using equations 3.57 and 3.58, the tangential force applied to the highest energy image in many instances may prevent full convergence to the saddle point (as an equal spring constant for each line segment will result in the images being placed equidistantly) so only serves as a rough approximation to the actual energy barrier. A more accurate approach is to treat the tangential forces applied to the highest energy image in such a way that the image is forced upwards on the energy surface towards the saddle point. This method is known as the climbing Nudged Elastic band (cNEB) method [167].

Following a few iterations of standard NEB optimisation, a climbing image (highest energy image which will be pushed towards the saddle point) is chosen. Should in subsequent steps an alternate image to the currently designated climbing image exceed that of the climbing image, the alternate image will be converted into the climbing image instead, and ensures the climbing image will reach the saddle point for the reaction pathway. The effective force on the climbing image in equation

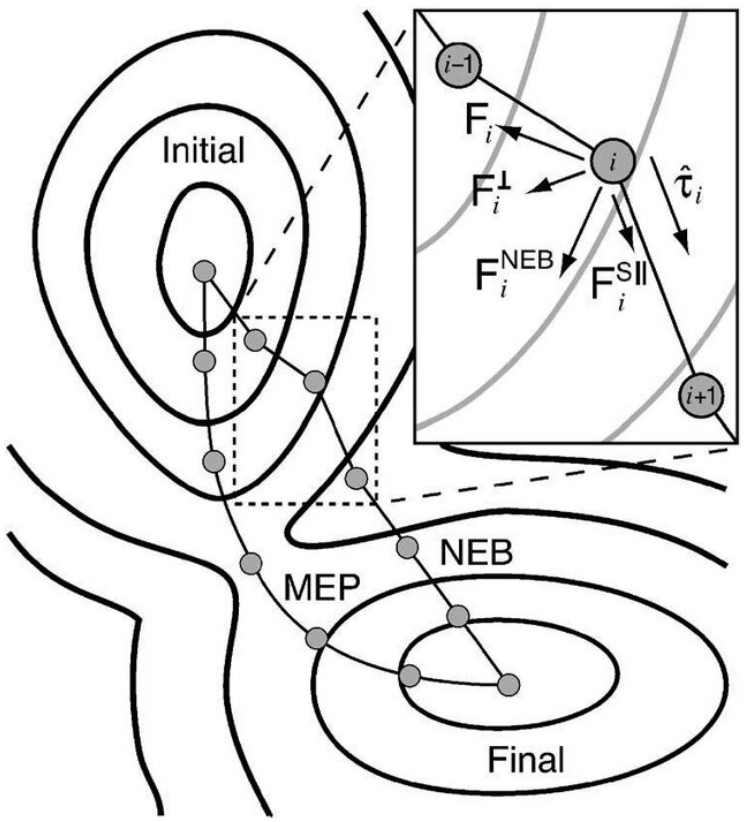

Figure 3.2: Illustrative example of the reaction pathway migration towards the minimum energy path (MEP) using the NEB method. Taken from Sheppard *et al.* [166].

3.56 is modified to become:

$$\boldsymbol{F}_i^{CI} = -\nabla E(\boldsymbol{R}_i^{CI}) + 2\nabla E(\boldsymbol{R}_i^{CI}) \cdot \hat{\boldsymbol{\tau}}_i^{CI} \hat{\boldsymbol{\tau}}_i^{CI} \tag{3.59}$$

where CI represents the climbing image. This modification removes the dependence of the force experienced by the climbing image on the tangential spring force, effectively pushing the image towards the saddle point. At convergence, the climbing image will rest at the saddle point and represents the energy barrier for the reaction process. As the climbing image is pushed towards the saddle point, the reaction coordinate of the images on one side of the climbing image will become compressed, and the other side will try to spread out. It is also possible to specify more than one climbing image in the event that multiple distinct energy barriers are expected.

Chapter 4

Fundamental properties of Li_8PbO_6

The contents of this chapter has been published in:
A. W. Davies, S. T. Murphy, Fundamental properties of octalithium plumbate ceramic breeder material, J. Nucl. Mater. 552 (2021) 152982. [168]

4.1 Introduction

Of the ceramic breeder materials recent attention has focused on two leading candidates, lithium orthosilicate (Li_4SiO_4) and lithium metatitanate (Li_2TiO_3), with some more recent studies looking at developing hybrid ceramic breeder pebbles [169] or creating core shell Li_2TiO_3/Li_4SiO_4 pebbles [108, 109]. Irrespective, it is necessary to enrich with ^{6}Li and to employ a neutron multiplier to achieve the desired TBR. The principle neutron multiplier material is beryllium (typically in $Be_{12}Ti$) [170], however, there is now a desire to reduce the reliance on this element as it is relatively rare and is found to contain traces of uranium [17]. As a consequence, Hernandez and Pereslavtsev re-examined a wide range of solid breeder materials [18]. Of the oxides considered, octalithium plumbate (Li_8PbO_6) was predicted to offer the highest Tritium Breeding Rate (TBR), at least partially due to the Pb which also offers an (*n,2n*) neutron multiplying reaction. Previous experiments have also indicated favourable tritium release characteristics [19]. Palermo *et al.* have proposed a design for a solid breeder blanket based on Li_8PbO_6 via a neutronics assessment which also suggested potential for high tritium release [171]. There are, however, concerns regarding the high temperature stability of the material. Importantly, Hernandes *et al.* suggest the melting temperature of Li_8PbO_6 to have a minimum of 800 °C, although little else is known on the thermodynamics of Li_8PbO_6.

Despite its potential for use as a breeder material in a future fusion reactor, the fundamental properties of Li_8PbO_6 have not been widely studied and there is a requirement to understand more about this material, including basic thermodynamic and elastic data (such as formation energies, heat capacities and elasic moduli) as well as how tritium may be accommodated in the lattice. In recent years there has been a significant growth in the use of atomistic simulation to examine the properties of ceramic breeder materials [172, 173] as well as tritium solubility [122, 174] and diffusivity [123]. Therefore, the present Chapter will use DFT, to calculate key electronic, elastic and thermodynamics properties of Li_8PbO_6 as well as offering a first examination of how tritium may be accommodated in the lattice.

4.2 DFT Parameterisation

Simulations presented were performed using a combination of both VASP (version 5.4.4) [175] and CASTEP (version 18.1) [176, 177] planewave pseudopotential codes. Within DFT an infinite crystal is described using supercells and periodic boundary conditions with special point integration over the Brillouin zone. The majority of simulations for both codes employed the generalised gradient approximation (GGA) of Perdew, Burke and Ernzerhof (PBE) [146], however, due to the failure of such semi-local functionals to accurately reproduce band gaps of materials some hybrid simulations employed the hybrid functional of Heyd, Scuseria and Ernzerhof (HSE06) [160]. Integration over the Brillouin zone was performed using a Monkhorst-Pack grid [178] with 6×6×2 k-points in the unitcell, corresponding to a separation between points of $0.0316\times2\pi$ Å^{-1} in the z-axis and $0.0344\times2\pi$ Å^{-1} along the x and y axes. Note that the k-point grid was reduced to a single k-point at Γ for the hybrid simulations in CASTEP due to computational constraints. Atoms in CASTEP simulations were represented using norm-conserving pseudopotentials based on the default settings in CASTEP 18.1, whereas VASP simulations employed projector augmented wave (PAW) [179] pseudopotentials. Consequentially, the difference in pseudopotentials used requires different planewave cutoff energies are used to ensure similar convergence. Due to the hardness of the oxygen pseudopotential used in CASTEP a high cutoff energy of 1150 eV was required to ensure a structural convergence of 0.01 eV per atom. PAW pseudopotentials in VASP allowed the use of a lower cutoff energy of 520 eV to maintain the same level of convergence, although this value was increased by 30% to 650 eV to ensure correct evaluation of the elastic tensor and remained consistent across all calculations. The energy criteria for electronic convergence was set to 10^{-8} eV for both VASP and CASTEP simulations. The inclusion of spin-orbit coupling in simulations was not found to have a significant contribution on results. Both codes were able to reproduce the lattice parameters for Li_8PbO_6 and many of its subsystems as illustrated in Table 4.1.

Phonon calculations for VASP were performed using the Phonopy [155] post-processing software, and utilised a much larger supercell and finer k-point grid. For example, Li_8PbO_6 utilised a 3×3×1 supercell of the 45-atom unitcell, with a 2×2×2 k-point grid. A Monkhorst-pack 15×15×15 q-point grid centred on the Γ-point is also used. Parameterisation used for all Phonon calculations performed using the Phonopy software are included in Table A.1 in Appendix A.

Simulations of defects were performed under similar parameterisation. Beginning with the relaxed 45-atom unitcell, a 2×2×1 supercell is utilised to minimise defect interactions with neighbouring periodic cells, and the volume of the supercell is kept fixed.

Table 4.1: Table showing the lattice parameters for Li_8PbO_6 and its subsystems compared to experimental values.

System	Property	CASTEP	VASP	Literature Value	% Difference CASTEP	% Difference VASP	Reference
Li_8PbO_6	a /Å	5.59	5.58	5.55	0.72	0.54	[125]
	c /Å	15.83	15.81	15.64	1.21	1.09	
Li_2O	a /Å	4.62	4.62	4.54	1.76	1.76	[180]
PbO_2	a /Å	5.07	5.10	4.971	1.99	2.60	[181]
	b /Å	6.05	6.07	5.95	1.68	2.01	
	c /Å	5.55	5.58	5.43	2.21	2.76	
Li	a /Å	3.43	3.46	3.51	2.28	1.42	[182]
Pb	a /Å	5.02	5.06	4.95	1.41	2.22	[183]
O_2	r (O-O) /Å	1.24	1.23	1.21	2.48	1.65	[184]

4.3 Results and Discussion

4.3.1 Electronic Properties

The density of states for both models was calculated using both PBE and HSE functionals, due to the tendency for semi-local functionals to underestimate band gaps. A comparison between density of states calculated in VASP and CASTEP are shown in Figure 4.1.

There is a strong agreement in the structure of the electronic density of states between both simulation packages, with both showing roughly the same increase in bandgap energy between semi-local and hybrid functionals. PBE bandgap energies of 2.05 eV and 1.94 eV and HSE bandgap energies of 3.25 eV and 3.36 eV were predicted for CASTEP and VASP softwares respectively.

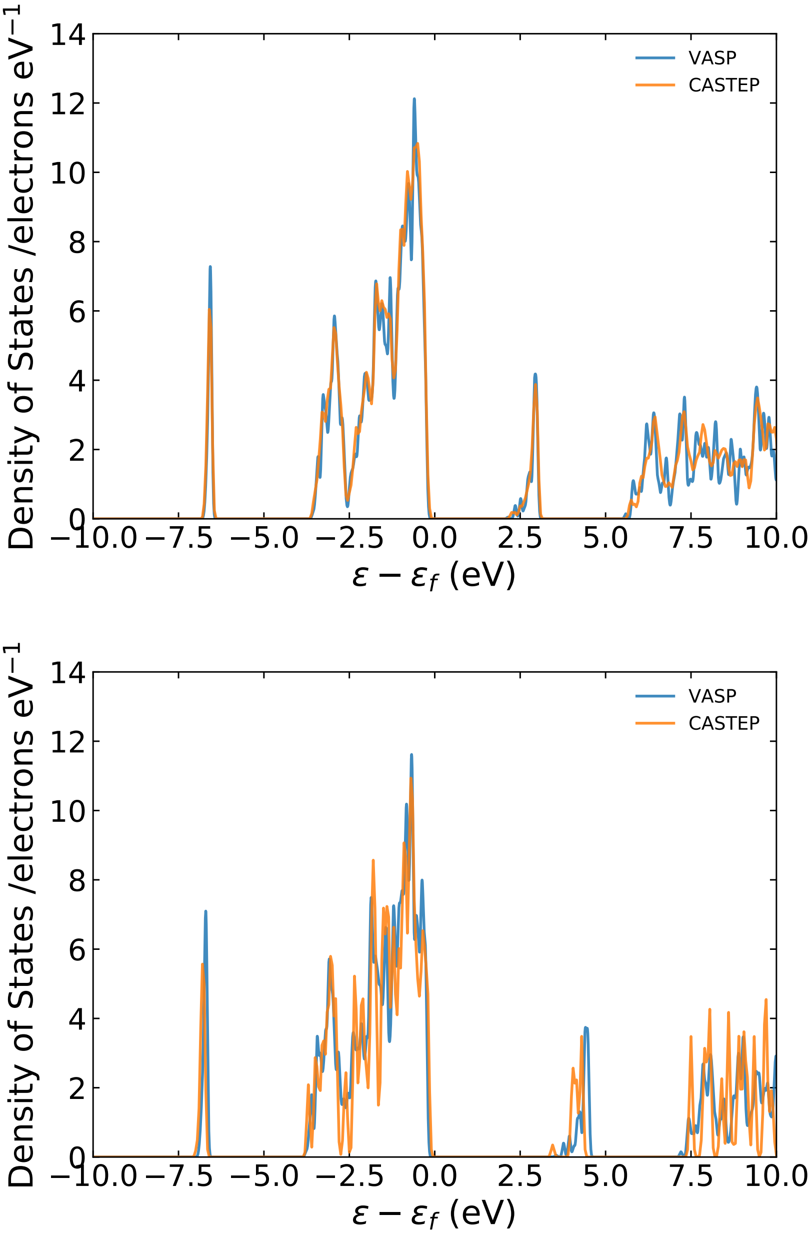

Figure 4.1: Electronic density of states for Li_8PbO_6 using the PBE and HSE exchange-correlation functionals. Top = PBE, bottom = HSE

The dielectric tensor is calculated using Density Functional Perturbation Theory (DFPT) for both VASP [185] and CASTEP [186] simulation codes. The symmetry of the crystal structure illustrated by the unit cell in Figure 2.14 suggests the dielectric constant in the z axis will differ from the values predicted in the x and y axes, which are expected to be the same. Static and high frequency dielectric tensors were calculated using both CASTEP (equations 4.1 & 4.2) and VASP (equations 4.3 & 4.4) simulation packages and are shown below. Both codes are in close agreement with one another, which are in consensus with the expected anisotropic behaviour of the crystal structure.

$$\bar{\epsilon}_0^{\mathrm{CASTEP}} = \begin{bmatrix} 12.89 & 0 & 0 \\ 0 & 12.89 & 0 \\ 0 & 0 & 13.84 \end{bmatrix} \tag{4.1}$$

$$\bar{\epsilon}_\infty^{\mathrm{CASTEP}} = \begin{bmatrix} 3.67 & 0 & 0 \\ 0 & 3.67 & 0 \\ 0 & 0 & 3.93 \end{bmatrix} \tag{4.2}$$

$$\bar{\epsilon}_0^{\mathrm{VASP}} = \begin{bmatrix} 13.09 & 0 & 0 \\ 0 & 13.09 & 0 \\ 0 & 0 & 14.29 \end{bmatrix} \tag{4.3}$$

$$\bar{\epsilon}_\infty^{\mathrm{VASP}} = \begin{bmatrix} 3.96 & 0 & 0 \\ 0 & 3.96 & 0 \\ 0 & 0 & 4.25 \end{bmatrix} \tag{4.4}$$

The dielectric tensor for $\mathrm{Li_8PbO_6}$ is comparatively low in comparison to other proposed ceramic breeder materials such as $\mathrm{Li_2TiO_3}$ [163], which may have a significant impact on ionic conductivity and the mobility of tritium ions in the crystal, due to the low mass of tritium and the similar charge magnitude tritium has with an electron.

4.3.2 Elastic Properties

The elastic tensor is derived from the stress-strain relationship predicted by performing finite distortions on the crystal in both codes. The elastic response of $\mathrm{Li_8PbO_6}$ is summarised in the elastic constant tensor shown in Table 4.2. According to Neumann's rules there are seven unique elastic constants for the $R\bar{3}H$ space group, these are c_{11}, c_{12}, c_{13}, c_{14}, c_{15}, c_{33} and c_{44}. Seven more elastic constants can be derived from equivalences with these values, these are: $c_{22} = c_{11}$, $c_{23} = c_{13}$, $c_{24} = -c_{56} = c_{14}$, $c_{25} = c_{64} = -c_{15}$ and $c_{55} = c_{44}$. The final elastic constant is related to these unique elastic constants according to $c_{66} = (c_{11} - c_{12})/2$. It is clear from the data presented that this relation holds for Li_8PbO_6.

Table 4.2: Table showing the elastic constants for Li_8PbO_6.

Parameter	CASTEP (GPa)	VASP (GPa)
c_{11}	191.54	163.54
c_{12}	54.27	55.32
c_{13}	53.80	50.11
c_{14}	20.74	21.87
c_{15}	-1.10	-1.98
c_{33}	150.90	161.56
c_{44}	64.50	54.46
c_{66}	68.64	52.63
Bulk modulus	94.74	88.46
Shear modulus	61.61	51.11
Young's Modulus		
x	155.14	121.85
y	155.14	120.03
z	127.34	138.74

Elastic constants were calculated using a 6×6×2 k-point grid on the relaxed hexagonal unit cell. Despite general agreement between codes, there is a slight discrepancy between the c_{11} elastic constants.

The inconsistency in c_{11} manifests in the Young's modulus. Due to the large contribution the c_{11} elastic constant plays, particularly in the x and y directions, large differences in c_{11} values between codes can produce radically different values for the Young's moduli. The CASTEP code predicts the x and y components of the Young's modulus is over 25% greater in comparison with the VASP code. This consequentially equates to CASTEP suggesting Li_8PbO_6 is stiffer in the x and y directions compared with z, in contrast to VASP which suggests the opposite.

4.3.3 Thermodynamics Properties

Due to the scarcity of literature on the physical characteristics of Li_8PbO_6, thermodynamic properties of Li_8PbO_6 were examined in VASP using the finite differences method in the Phonopy post-processing package [155] and using default phonon DFPT calculations provided by CASTEP [187]. As mentioned previously, parameterisation of phonon calculations has been included in Table A.1 in Appendix A. As ceramic breeder materials are expected to transfer heat to the reactor coolant and maintain performance in high temperature regimes ($>800°C$), an understanding of the thermal properties such as the heat capacity is critical for determining the efficacy of Li_8PbO_6 as a breeder material. Phonon density of states for both simulation packages are included in Figure 4.2.

As there is no published value in the literature for the enthalpy of formation of Li_8PbO_6 from Li_2O and PbO_2, Born-Haber cycles were created to illustrate enthalpies of fomation of the Li_8PbO_6 compound from its constitiuent elements. There is general agreement in enthalpies of formation between simulation packages. Given that the formation energies of Li_2O and PbO_2 are in reasonable agreement with the literature, the enthalpy of formation of Li_8PbO_6 estimated is likely a reasonable approximation to the true value.

The relationship between the Helmholtz free energies, internal energy and entropy have been calculated from the phonon density of states. There is very strong agreement between simulation packages as might be expected from the close agreement with the phonon density of states. The internal energy shown in Figure

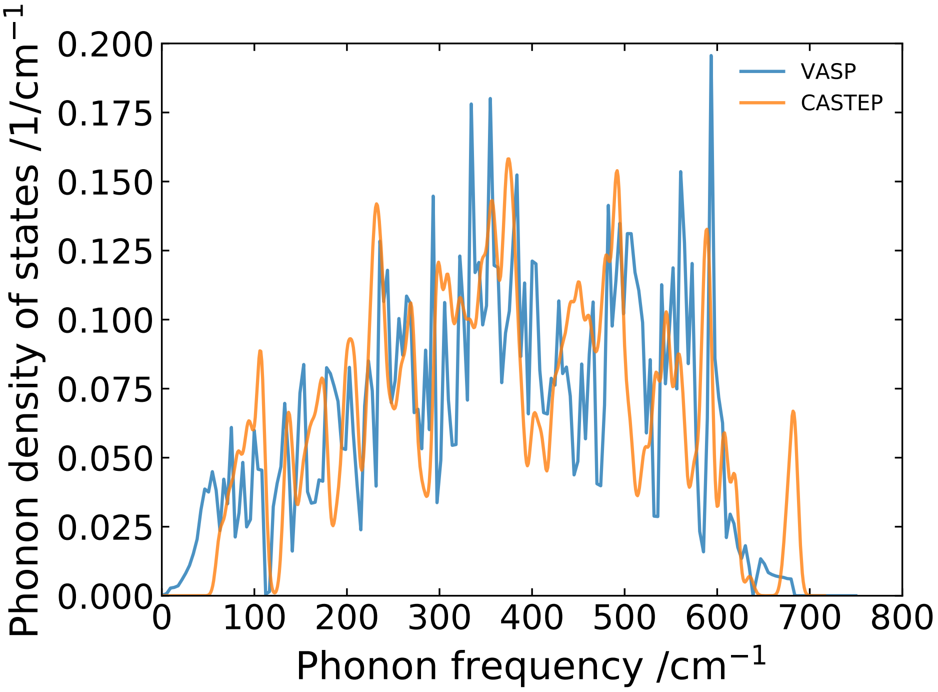

Figure 4.2: Phonon density of states for Li_8PbO_6.

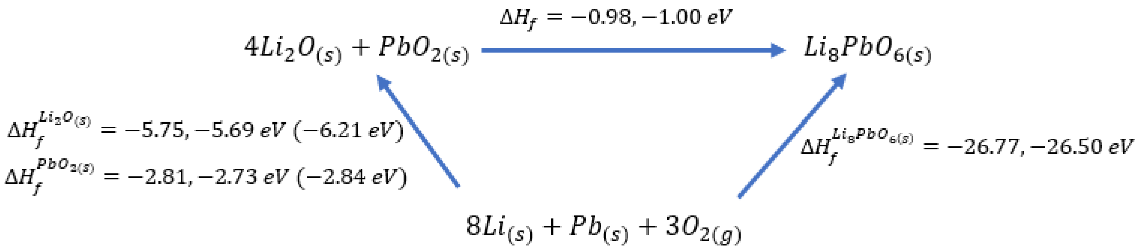

Figure 4.3: Born-Haber cycle for Li_8PbO_6 and its constituents. First value = VASP, second = CASTEP and bracketed values are obtained from literature [158].

4.4 becomes roughly linear above approximately 500 K. The contribution given by the entropy of the crystal plays a major role in the final result for Helmholtz free energy at high temperatures.

The specific heat for a constant volume C_V has also been calculated and is illustrated in Figure 4.5. An understanding of the specific heat for Li_8PbO_6 is

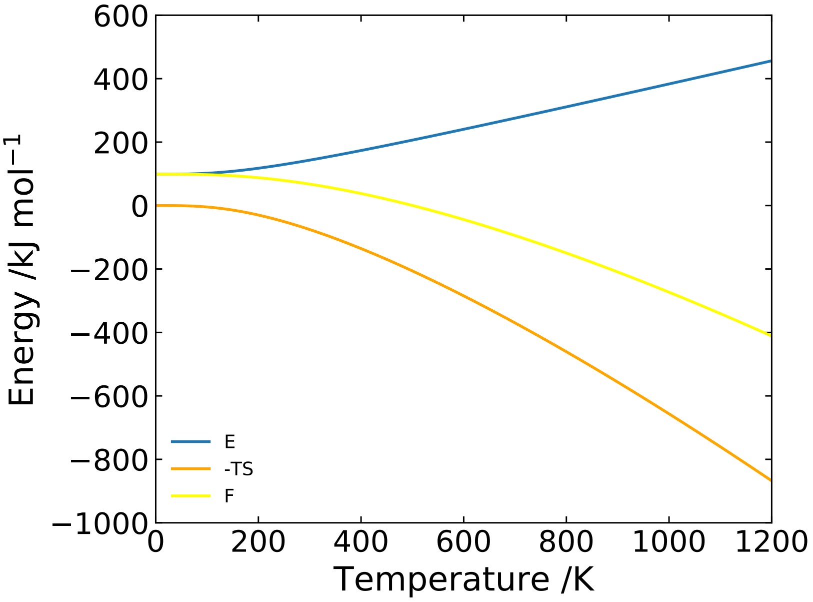

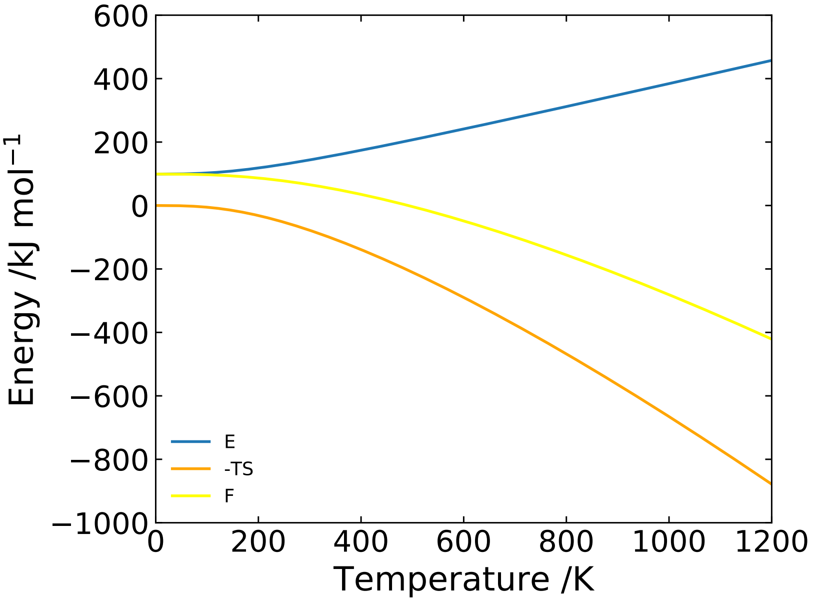

Figure 4.4: Helmholtz free energy (F), phonon contributions to internal energy (E) and entropy (S) as a function of temperature per mole of Li_8PbO_6. Top = CASTEP, bottom = VASP

important as ceramic breeder materials are often used dually as a means to transfer heat to the reactor coolant to generate power, due to their close proximity to the fusion plasma. The predicted specific heat of Li_8PbO_6 is generally lower than

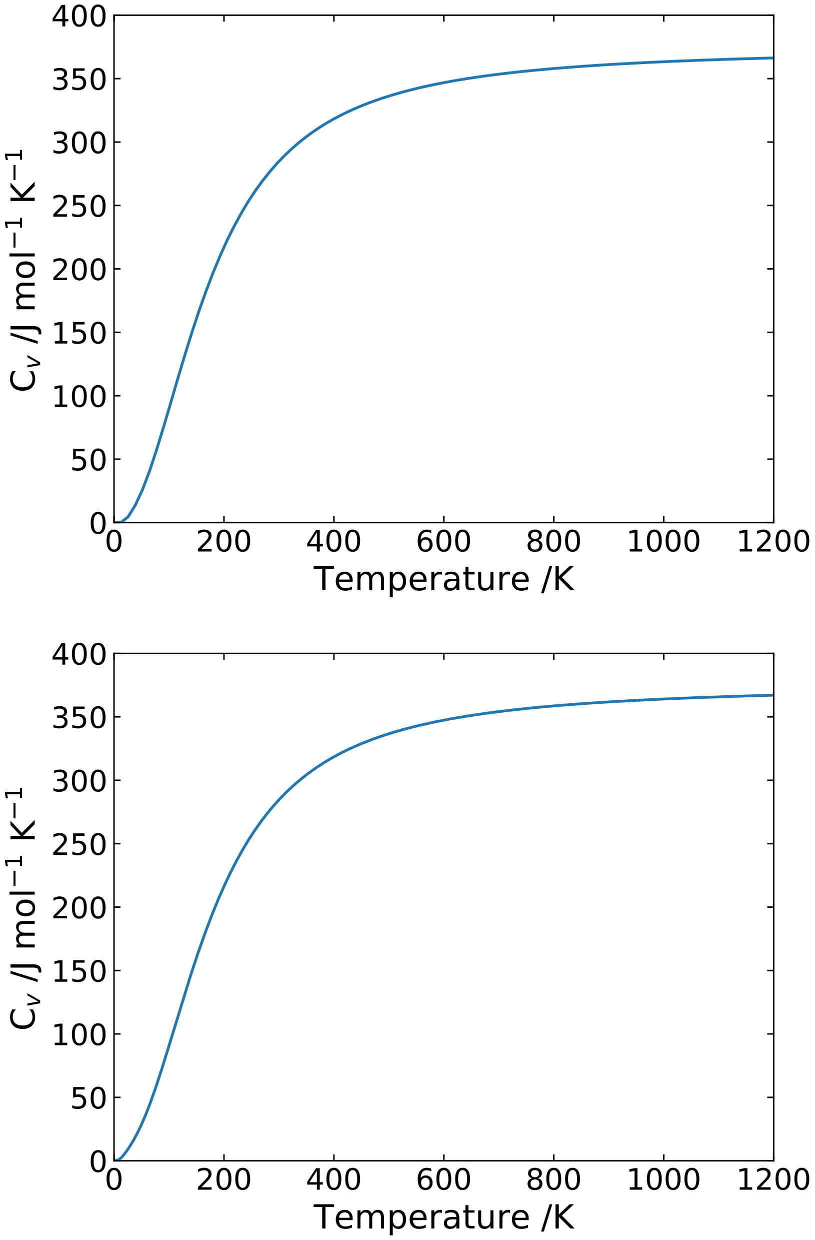

Figure 4.5: Specific heat for constant volume of Li_8PbO_6 as a function of temperature. Top = CASTEP, bottom = VASP

estimates for other lithium-ceramics, such as the DFT-calculated estimate made by Wan *et al.* for β-Li_2TiO_3 [188] and that of Yan *et al.* for Li_4TiO_4 [189], indicating Li_8PbO_6 may be more susceptible to experiencing higher temperatures during reactor operation compared to other proposed breeder blanket materials.

Comparisons with other materials such as Li_2SiO_3 [190] predicted by Ma *et al.* indicate a much higher heat capacity for Li_8PbO_6, with a heat capacity more than twice as large at 300 K, with 267.19 J K^{-1} mol $^{-1}$ for Li_8PbO_6 compared with 101.79 J K^{-1} mol $^{-1}$ for Li_2SiO_3.

4.3.4 High Temperature Stability

The stability of Li_8PbO_6 at high temperatures has been examined by implementing the quasi-harmonic approximation given by the Phonopy package to introduce a volume dependence onto the thermal properties of Li_8PbO_6, as well as its constituents. The molar heat for constant pressure C_P, volume-dependent enthalpies and Gibbs free energies were calculated for Li_8PbO_6, Li_2O, PbO_2 and Li_4PbO_4 (sharing the same energy cut-off and k-point density), as traces of Li_4PbO_4 were found to be present during the sintering process for temperatures of 600-800°C, although no traces were found at 1000°C over a period of 24 hours [121]. Therefore, the key processes to consider are:

$$\mathrm{Li_4PbO_4} + 2\mathrm{Li_2O} \rightarrow \mathrm{Li_8PbO_6} \tag{4.5}$$

$$\mathrm{PbO_2} + 4\mathrm{Li_2O} \rightarrow \mathrm{Li_8PbO_6} \tag{4.6}$$

$$\mathrm{PbO_2} + 2\mathrm{Li_2O} \rightarrow \mathrm{Li_4PbO_4} \tag{4.7}$$

Due to the similarity in results for thermodynamic properties between simulation packages, results for this section were produced using only the VASP software. Volumes in the range of ±15% of the relaxed crystal were used in steps of 3% for all materials examined. The resulting heat capacities are presented in Figure 4.6.

Using these specific heats, it is possible to determine the enthalpy changes associated with reactions 4.5 - 4.7, these are illustrated in Figure 4.7. Figure 4.7 shows that the enthalpy changes are negative across the temperature range, implying the Li_8PbO_6 is the more favourable state and only grows more favourable with

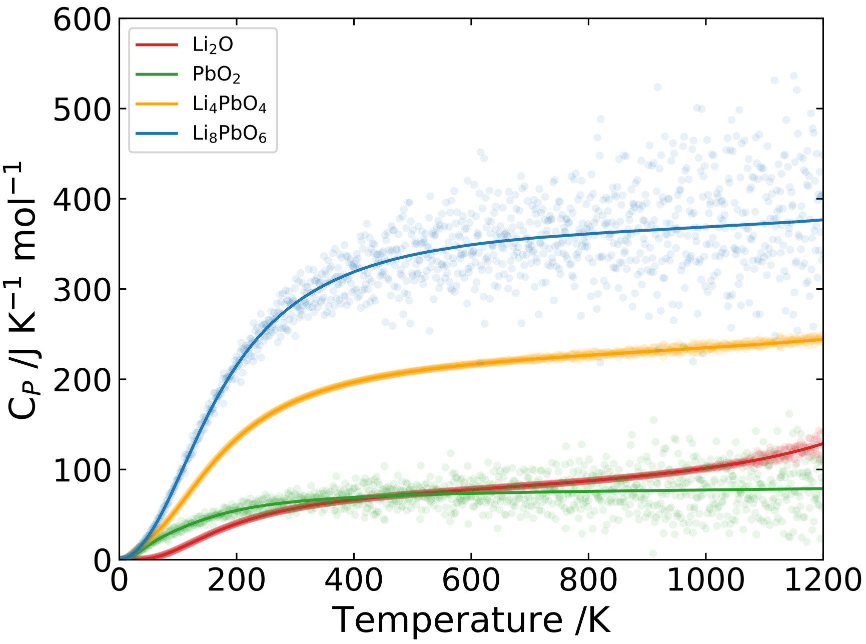

Figure 4.6: Specific heat for constant pressure of Li_8PbO_6 and its constituents (per mole) as a function of temperature.

increasing temperature. The enthalpy of formation of the reaction $PbO_2 + 2Li_2O \rightarrow Li_4PbO_4$ was also found to be negative, although with a marginal preference towards the formation of Li_8PbO_6 over Li_4PbO_4 and this preference increasing with temperature.

Examination of the Gibbs formation energy is critical in discussion of the phase stability of Li_8PbO_6. The Gibbs formation energy of Li_8PbO_6 and Li_4PbO_4 from PbO_2 and Li_2O are strongly negative. Due to the smaller entropy in the formation of Li_8PbO_6 compared to Li_4PbO_4, the Gibbs formation energy rises above that of the formation of Li_4PbO_4 at roughly 1000 K. Implying that the Li_8PbO_6 phase is unstable at higher temperatures. This result suggests that Li_8PbO_6 may be inappropriate for application in fusion reactors, therefore, this will be explored in more detail in Chapter 5.

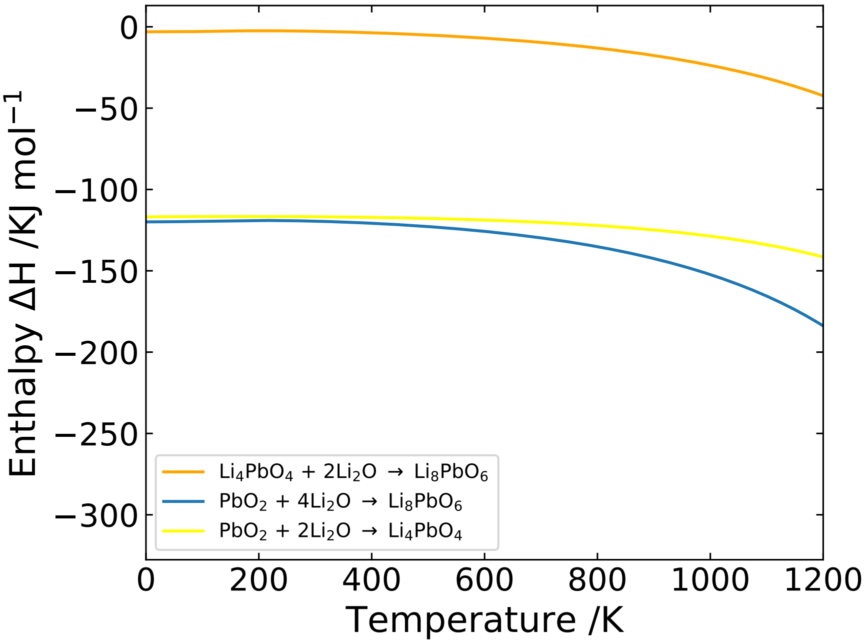

Figure 4.7: Enthalpy of formation of Li_8PbO_6 and its constituents as a function of temperature.

4.3.5 Lithium Vacancy Defects

During operation, the ceramic breeder material ages and the lithium will be burnt-up to produce tritium, resulting in a reduction in its availability in the matrix. This paucity of lithium will be accommodated by point defects such as interstitials and vacancies. As discussed for other ceramic breeder materials it is anticipated that the lithium vacancy defects will play a significant role in the accommodation of this substochiometry [122]. Therefore, the formation energy for the formally charged, V_{Li}^{-1}, is examined here and other defects and charge states will be the focus of future work.

As discussed in the Literature Review, there are two symmetrically distinct lithium sites in Li_8PbO_6, therefore the defect formation energy for the two different sites has been calculated and the energies presented in Table 4.3.

The data presented in Table 4.3 shows that the formation energy for the vacancy on the tetrahedrally co-ordinated 18f site is lower than on the octahedrally co-

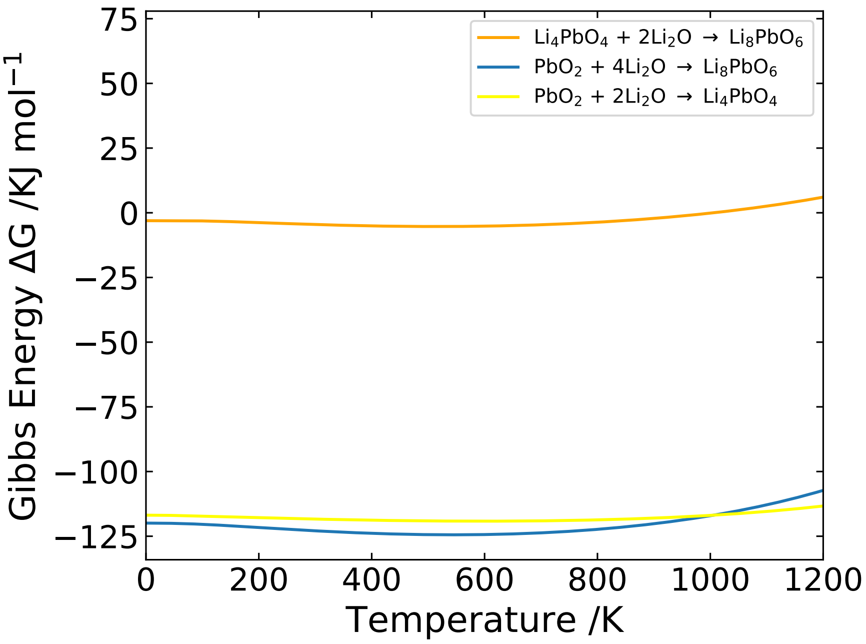

Figure 4.8: Gibbs formation energy of Li_8PbO_6 and its constituents as a function of temperature.

Table 4.3: Defect formation energies for the lithium vacancy defects in Li_8PbO_6.

		CASTEP	VASP
Lithium site	Wychoff notation	E_f /eV	E_f /eV
Li1	18f	3.728	3.641
Li2	6c	4.071	4.007

ordinated 6c site. This implies that the majority of such defects will occur on the 18c Li1 site. Defect formation energies between codes show remarkable agreement with a deviation of less than 0.1 eV between each other for both lithium sites, with VASP measurements being slightly lower. The difference between the two vacancy defects is similar between DFT simulation packages, with values of 0.34 eV and 0.37 eV for CASTEP and VASP respectively. This is larger than the difference between possible Li sites in Li_2TiO_3 [172] although significantly smaller than predicted for

Li_4SiO_4 [191]. In Li_8PbO_6, the origin of this discrepancy is the increased electrostatic attraction between the Li^{1+} ion and the six surrounding O^{2-} ions making it more difficult to remove the lithium from the 6c site.

4.3.6 Tritium Solubility at Lithium Sites

Given the likely high concentration of lithium vacancy defects as the material ages it is anticipated that this defect will play an important role in the accommodation and diffusion [89] of tritium in the crystal. Therefore, the substitution of tritium onto the lithium sublattice will be examined (i.e. $\mathrm{T}^0_{\mathrm{Li}}$). Previous DFT studies of tritium accommodation in Li_2TiO_3 show that the tritium will move from the Li site and bond with a nearest neighbour oxygen atom to form a hydroxide that could be considered to be a $\{V^{-1}_{\mathrm{Li}} : T^1_i\}^0$ cluster [122]. Li *et al.* have shown that the energy of the resulting hydroxide bond depends on exactly which of the nearest neighbour oxygens the tritium ion bonds to [123]. Therefore, the energy for all possible hydroxide orientations around both Li vacancies in Li_8PbO_6 is investigated, and the results are presented in Table 4.4.

The data presented in Table 4.4 shows that there are four symmetrically distinct $\{V^{-1}_{\mathrm{Li}} : T^1_i\}^0$ clusters involving the tetrahedral Li1 site. By contrast, despite there being six oxygen nearest neighbours surrounding the Li2 site, there appear to be just two symmetrically distinct hydroxides formed in both VASP and CASTEP models due to the symmetry of the crystal. Once again, like the lithium vacancy defects there is excellent agreement in formation energies produced by both codes, with a discrepancy of less than 20 meV. Visualisations of the $\{V^{-1}_{\mathrm{Li}} : T^1_i\}^0$ defect clusters are given in Figures 4.9 and 4.10.

The formation energies for the $\{V^{-1}_{\mathrm{Li}} : T^1_i\}^0$ defect indicate that tritium will preferentially form a hydroxide that is bound to an Li1 site.

Table 4.4: Defect formation energies for the tritium accommodation at lithium vacancy defects in Li_8PbO_6. Also included are the resulting O-H bond distances

		CASTEP		VASP	
Lithium site	O atom	E_f /eV	$r\,(\mathrm{O-H})$ /Å	E_f /eV	$r\,(\mathrm{O-H})$ /Å
Li1	1	1.591	0.988	1.593	0.989
(18f)	2	1.437	0.980	1.438	0.980
	3	1.491	0.986	1.490	0.990
	4	1.747	0.990	1.747	0.991
Li2	1	1.769	0.982	1.783	0.984
(6c)	2	1.769	0.982	1.785	0.983
	3	1.769	0.982	1.784	0.986
	4	1.880	0.985	1.892	0.988
	5	1.880	0.985	1.891	0.986
	6	1.880	0.985	1.889	0.987

4.4 Conclusion

Thermal, elastic and electronic properties of Li_8PbO_6 have been examined using first principles simulations using DFT. Application of Li_8PbO_6 as a breeding material may be inadequate due to the potential for Li_8PbO_6 to undergo a change of phase into Li_4PbO_4 at high temperatures, as is suggested by the Gibbs formation energy of Li_8PbO_6 from Li_4PbO_4 at temperatures above 1000 K. Formation energies for lithium vacancy defects and $\{V_{\mathrm{Li}}^{-1} : T_i^{1}\}^0$ defect clusters have been determined. Despite the different basis sets used, there is a remarkable level of agreement between codes for many of the fundamental properties properties of Li_8PbO_6. This is especially true for defect formation energy calculations, which are accurate to within 0.1 eV of each other. It is shown there is a preference in Li_8PbO_6 for lithium vacancies to form at 18f Wyckoff sites and consequently it is expected more native

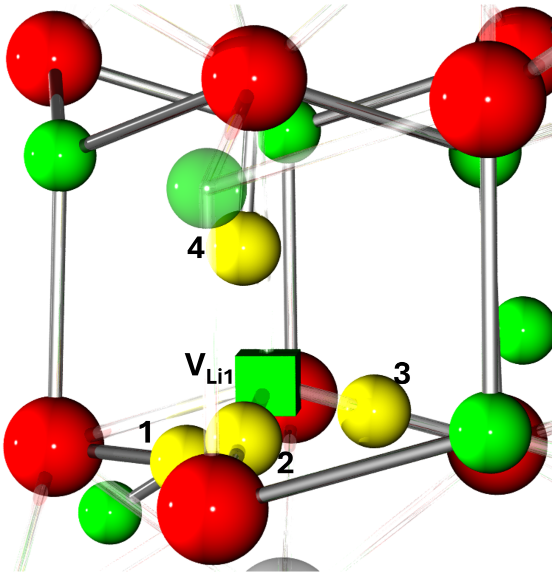

Figure 4.9: Possible tritium sites for $\{V_{\mathrm{Li}}^{-1} : T_i^1\}^0$ defect clusters at the Li1 site. Grey, green and red spheres represent the lead, lithium and oxygen ions respectively. Yellow spheres represent the possible tritium sites and the green cube represents a lithium vacancy site.

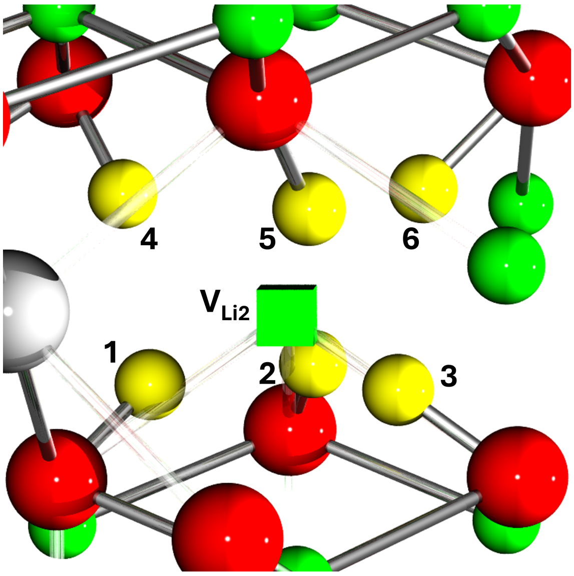

Figure 4.10: Possible tritium sites for $\{V_{\mathrm{Li}}^{-1} : T_i^1\}^0$ defect clusters at the Li2 site.

vacancies will form here rather than at 6c sites. It is also shown there is a preference for tritium to bond to nearest neighbour oxygen sites at lithium 18f sites over 6c sites, suggesting higher accommodation of tritium at the 18f sites in general.

Chapter 5

Thermodynamics of octalithium ceramics

The contents of this chapter has been published in:
A. W. Davies, S. T. Murphy, Thermodynamics and phase stability of Li_8XO_6 octalithium ceramic breeder materials (x = Pb, Ce, Ge, Zr, Sn), J. Phys.: Condens. Matter 34 (2022) 355701. [192]

5.1 Introduction

Octalithium ceramics such as Li_8SnO_6 [193] and Li_8ZrO_6 [194] have typically only been considered in the literature for use as cathode materials for Li-ion batteries, owing predominantly to their favourably high lithium content. In a recent review of candidate breeder materials, Hernandez and Pereslavtsev [18] suggested that octalithium compounds may be attractive candidates for use as breeder blanket materials due to their high stoichiometric concentration of lithium and, in some materials, intrinsic neutron multiplier (i.e. Pb). Such properties lead to high TBRs relative to Li_2TiO_3 and Li_4SiO_4, though there are concerns surrounding the stability of these materials at high temperatures and many possess relatively low melting temperatures compared to other candidates. As a consequence of these assumptions, the octalithium ceramics as a whole have received very little attention, with the exception of Li_8ZrO_6, which has been the most studied in recent years [195, 196].

In the previous chapter we identified a potential concern regarding the phase stability of Li_8PbO_6 at high temperature. Therefore, in this Chapter we reexamine the issue of the thermodynamic stability of Li_8PbO_6 at high temperature and broaden our study to examine other octalithium compounds that may be interesting as potential breeder material, specifically $Li_8\{Pb,Ce,Ge,Zr,Sn\}O_6$. Due to the dual application of breeder blankets to act as a heat exchanger, the specific heat capacities of this class of material are also investigated and included in Appendix A.

5.1.1 Crystallography

As shown in Table 5.1, all octalithium compounds examined contain an atomic lithium density greater than both Li_4SiO_4 and Li_2TiO_3 (0.0482 and 0.0376 a/$\mathring{A}^3$ respectively), due to their intrinsically higher stoichiometric concentration of lithium, which has been shown by Okuno and Kudo to directly impact tritium mobility [197]. They also offer estimated TBRs in the range of 1.19-1.21, equating to an improvement of 3.5-5.2% versus Li_4SiO_4 and 6.3-8.0% for Li_2TiO_3.

The octalithium ceramics exhibit one of two space groups. $Li_8\{Pb,Zr,Sn,Ce\}O_6$ exhibit the trigonal $R\bar{3}H$ (number 148) space group and Li_8GeO_6 crystallises in the hexagonal $P6_3cm$ (number 185) space groups.

The $R\bar{3}H$ structure has been previously shown in Chapter 2 in Figure 2.13, whereas the $P6_3cm$ structure is shown in Figure 5.1. In $Li_8\{Pb,Zr,Sn,Ce\}O_6$ candidates, their constituents also share the same Wyckoff positions. Oxygen ions and the unique component metals (Pb,Zr,Sn,Ce) are equivalent and occupy the 18f and 3a sites respectively. The lithium ions occupy two symmetrically distinct positions, which are the 18f and 6c sites. For the $P6_3cm$ space group, the oxygen ions occupy three distinct sites which are the 6c, 4b and 2c positions. Germanium exclusively occupies the 2c position whereas the lithium, much like the $R\bar{3}H$ space group, also possesses two symmetrically distinct sites which are the 4b and 6c

Table 5.1: Tritium breeding ratios (TBRs) of chosen candidate octalithium ceramics with 60% Li^6 enrichment [18]. †Li_8PbO_6 remains a solid when sintered at 1000 °C [121] and is thus treated as a minimum.

Compound	Li atomic density (a/$\mathring{A}^3$)	Melting point (°C)	TBR
Li_8PbO_6	0.0575	>1000†	1.21
Li_8GeO_6	0.0567	Unknown	1.19
Li_8CeO_6	0.0537	Unknown	1.19
Li_8ZrO_6	0.0591	1336	1.20
Li_8SnO_6	0.0608	1050	1.19

positions. All unique metals for the $R\bar{3}H$ space group are octahedrally coordinated in the +4 charge state, surrounded by 6 oxygen ions. On the other hand, in the $P6_3cm$ space group germanium is tetrahedrally coordinated with 4 neighbouring oxygen ions, leading to a relatively low ionic radius in comparison.

5.2 DFT Parameterisation

Given the similarity between the CASTEP and VASP results presented in Chapter 4, we choose to proceed using VASP alone as the reduced planewave cutoff energies for the pseudopotentials ensures a reduced computational cost. DFT simulations were performed using the Vienna Ab Initio Simulation Package (VASP - version 5.4.4) planewave pseudopotential code [175], employing projector augmented wave (PAW) pseudopotentials [179]. All simulations (unless otherwise stated) utilised the generalised gradient approximation (GGA) of Perdew, Burke and Ernzerhof (PBE) [146]. Integration over the Brillouin zone for all materials investigated was performed using a Monkhorst-Pack grid [178] with an approximate separation between k-points of 0.03 - $0.04\times2\pi$ Å^{-1} along each axis. The exact k-point grids for each material

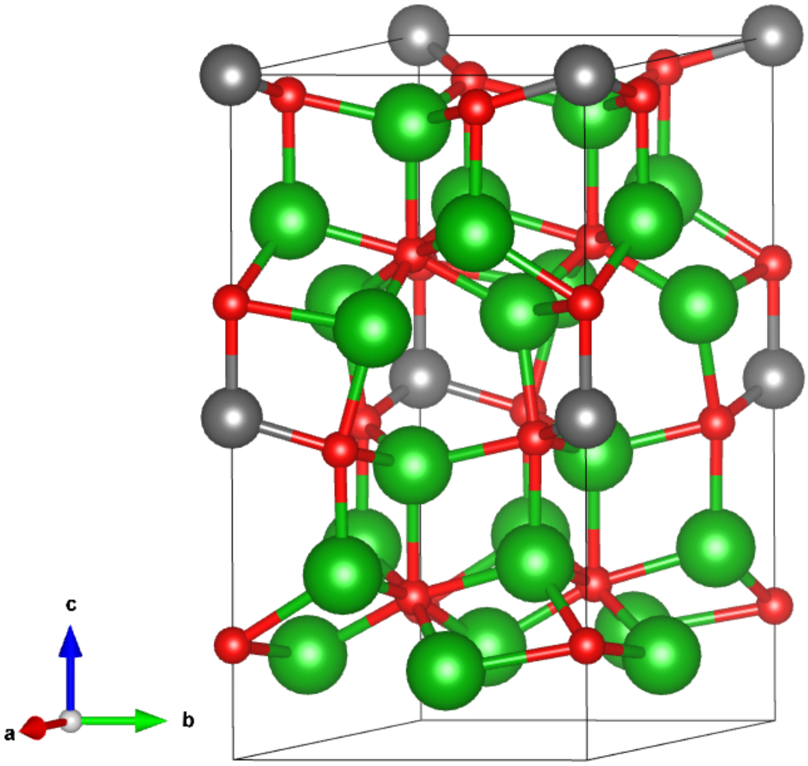

Figure 5.1: Structure of 30-atom unitcell in the *P*6_3*cm* space group used by the Li_8GeO_6 ceramic. Green, red and grey spheres correspond to Li, O and Ge respectively.

are included in Table A.1 in Appendix A. The planewave cutoff energy was set to 650 eV for all materials to ensure a minimum convergence of 0.01 eV per atom. In order to demonstrate the efficacy of the DFT model the energy minimised lattice parameters for the octalithium compounds as well as a number of related systems is presented in Table 5.2 alongside their existing experimental values. As evident from Table 5.2, the predicted lattice parameters are in excellent agreement with experimental values.

Due to the inability of semi-local functionals, to accurately replicate experimentally measured bandgaps, the hybrid functional of HSE06 [160] was employed. Due to computational restraints imposed by the use of hybrid functionals, a single k-point was used at the Γ-point for simulations using the HSE06 functional to calculate the

Table 5.2: DFT-predicted lattice parameters compared with literature.

Compound	a/Å	b/Å	c/Å	α/°	β/°	γ/°	Space group	Reference
$\mathbf{Li_8PbO_6}$	5.58	5.58	15.81	90	90	120	$R\bar{3}H$ (148)	[168]
	5.55	5.55	15.64	90	90	120		[125]
Li_4PbO_4	7.36	8.46	6.63	90	90	90	$Cmcm$ (63)	
	7.30	8.31	6.52	90	90	90		[198]
PbO_2	5.10	6.07	5.58	90	90	90	$Pbcn$ (60)	[168]
	4.97	5.95	5.43	90	90	90		[181]
$\mathbf{Li_8GeO_6}$	5.53	5.53	10.78	90	90	120	$P6_3cm$ (185)	
	5.51	5.51	10.72	90	90	120		[113]
Li_4GeO_4	7.38	7.84	6.11	90	90	90	$Cmcm$ (63)	
	7.36	7.76	6.05	90	90	90		[199]
GeO_2	5.07	5.07	5.76	90	90	120	$P3_121$ (152)	
	4.99	4.99	5.65	90	90	120		[200]
$\mathbf{Li_8CeO_6}$	5.63	5.63	16.20	90	90	120	$R\bar{3}H$ (148)	
	5.64	5.64	16.03	90	90	120		[114]
Li_2CeO_3	4.50	9.59	3.56	90	90	90	$Cmmm$ (65)	
	4.49	9.67	3.55	90	90	90		[201]
CeO_2	5.46	5.46	5.46	90	90	90	$Fm\bar{3}m$ (225)	
	5.41	5.41	5.41	90	90	90		[202]
$\mathbf{Li_8ZrO_6}$	5.50	5.50	15.55	90	90	120	$R\bar{3}H$ (148)	
	5.48	5.48	15.45	90	90	120		[203]
$Li_6Zr_2O_7$	10.48	6.01	10.26	90	100.26	90	$C2/c$ (15)	
	10.45	5.99	10.20	90	100.26	90		[204]
ZrO_2	5.19	5.24	5.38	90	99.67	90	$P2_1/c$ (14)	
	5.15	5.20	5.32	90	99.20	90		[205]
$\mathbf{Li_8SnO_6}$	5.49	5.49	15.43	90	90	120	$R\bar{3}H$ (148)	
	5.46	5.46	15.27	90	90	120		[116]
Li_2SnO_3	5.35	9.29	10.11	90	100.38	90	$C2/c$ (15)	
	5.29	9.19	10.03	90	100.35	90		[206]
SnO_2	4.83	4.83	6.48	90	90	90	$P4_2/mnm$ (136)	
	4.74	4.74	6.38	90	90	90		[207]
$\mathbf{Li_2O}$	4.62	4.62	4.62	90	90	90	$Fm\bar{3}m$ (225)	[168]
	4.54	4.54	4.54	90	90	90		[180]

electronic density of states, although it is not expected to have a significant impact on calculated band gap.

To account for finite size effects arising due to the relatively small simulation cells used when studying defects, an electrostatic correction, dE, is added to the defect formation energy, previously defined in equation 3.51. As only single lithium vacancy point defects are considered, the potential alignment correction is assumed to be negligible [208]. The chemical potential for lithium used in this paper is taken directly from the lithium metal.

5.3 Results and Discussion

5.3.1 Cation Radius

In the first instance we explore the dependence of some key material properties as a function of the ionic radii of the tetravalent cation. Specifically, the lattice parameters and band gaps derived from the electronic density of states as a function of cation radii. Cation radii for the tetravalent metals in the octalithium compounds studied are included in Table 5.3.

Table 5.3: Cation radii for the unique metals occupying the octalithium compounds studied. Radii were taken from the revised effective ionic radii measured by R. D. Shannon [209].

Metal	Charge	Coordination	Ionic radius ($\AA$)
Pb	4	VI	0.775
Ge	4	IV	0.39
Ce	4	VI	0.87
Zr	4	VI	0.72
Sn	4	VI	0.69

Shown in Figure 5.2 is the relationship between lattice parameter length and cation radius in $R\bar{3}H$ ceramics. From the figure, it is obvious the lattice parameter scales proportionally to the radius of the cation.

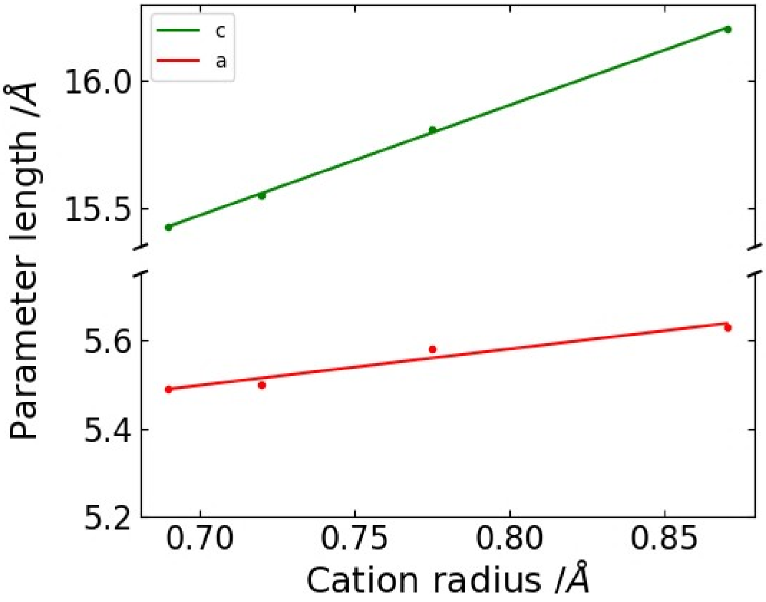

Figure 5.2: Comparison of lattice parameters for materials in the $R\bar{3}H$ space group with cation radii.

Table 5.4: PBE and HSE-predicted electronic band gaps.

Compound	PBE (eV)	HSE (eV)
Li_8PbO_6	1.94	3.36
Li_8GeO_6	3.24	4.86
Li_8CeO_6	2.02	4.06
Li_8ZrO_6	4.55	6.17
Li_8SnO_6	3.59	5.15

No discernible correlation was found between both the PBE and HSE band gaps and the cation radii, shown in Table 5.4. For both the PBE and HSE functionals the band gaps for Li_8PbO_6 is predicted to be the lowest at 1.94 and 3.36 eV respectively. By contrast, Li_8ZrO_6 is predicted to have the largest band gap, despite the similar cation radii of the constituent metals.

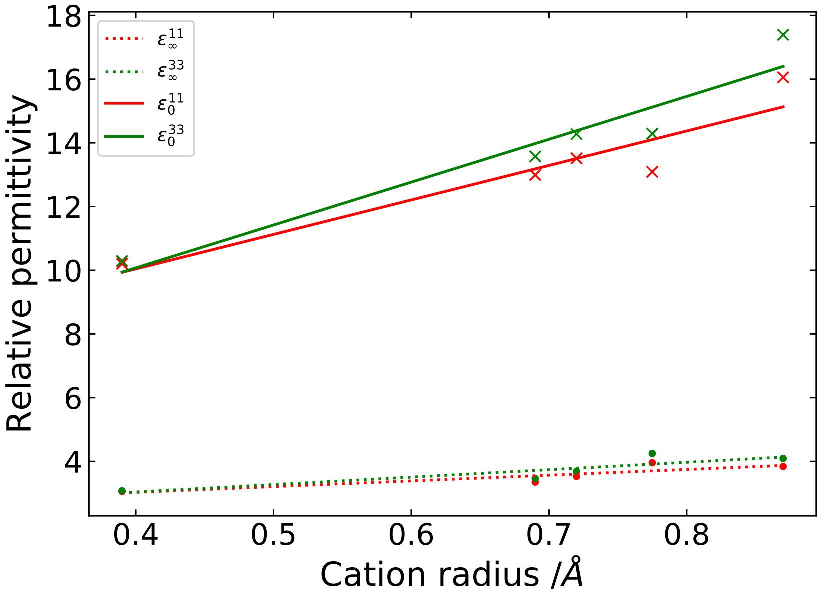

Figure 5.3: Permittivity as a function of cation radius for octalithium compounds.

Static and high-frequency dielectric tensors for the octalithium compounds were also measured using DFPT implemented in the VASP simulation software for application in the finite size correction used in defect formation energy calculations. Due to the symmetry of both $R\bar{3}H$ and $P6_3cm$ crystal structures, the dielectric tensor ϵ_{ij} can be reduced to only the ϵ_{11}, ϵ_{22} and ϵ_{33} components, where $\epsilon_{11} = \epsilon_{22}$. Figure 5.3 shows the permittivity as a function of cation radius for all octalithium compounds considered. The permittivity along the z-axis regardless of cation radius was measured to be slightly greater than along x and y. Both static and high frequency permittivities are generally predicted to increase with cation radius.

Charged lithium vacancy formation energies were calculated for ceramics belonging to the $R\bar{3}H$ space group and are shown as a function of cation radius in Figure 6.2. Excluding Li_8GeO_6, the formation energies of the lithium vacancy defects at the Valence Band Maximum in the $R\bar{3}H$ compounds decrease with increasing

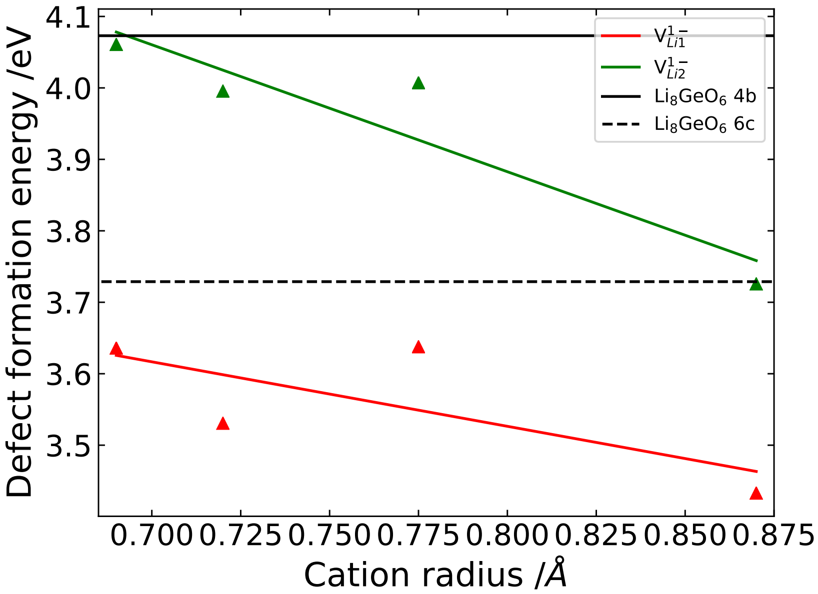

Figure 5.4: Comparison of lithium vacancy formation energies at the Valence Band Maximum in the $R\bar{3}H$ space group with cation radii. V_{Li1} defects occupy the tetrahedrally coordinated 18f sites and V_{Li2} occupy the octahedrally coordinated 6c sites. Horizontal lines represent V_{Li} defects in Li_8GeO_6.

cation radius of the constituent metal. Consequently, Li_8CeO_6 is predicted to have the lowest lithium vacancy formation energies for both unique sites. Conversely, Li_8SnO_6 is predicted to have the highest lithium vacancy formation energy for each site.

5.3.2 Specific Heat Capacity

Due to the proximity of the breeder blanket to the fusion plasma, an understanding of the temperature distribution through the breeder blanket as well as the quality of heat transfer from the blanket material to the reactor coolant is essential for determining the feasibility of candidate ceramics as breeder materials. The temperature-dependent specific heat capacities for constant volume C_V were predicted using the finite displacement method in the Phonopy package [155, 154], and the QHA was used to predict the specific heat capacities for constant pressure C_p. The size of the supercell used was set to a minimum lattice parameter of 10Å. Note that the specific heats for all compounds considered here are presented in Appendix A. Due to the large number of materials explored, the exact size of the supercells as well as the corresponding k-point and q-point grids used for each material are detailed in Table A.1 in Appendix A.

Experimental and theoretical predictions for heat capacities for a significant majority of the materials examined are not available in the literature. In the cases where this data could be found it is plotted in Figure 5.5. The results show that for PbO_2 and ZrO_2, specific heat capacities are closely aligned with the NIST database [210] and results for Li_2SnO_3 replicated experimental measurements conducted by Asou *et al.* [211]. Overall, in the cases where experimental data are available there is excellent agreement between the calculated specific heats and values in the literature.

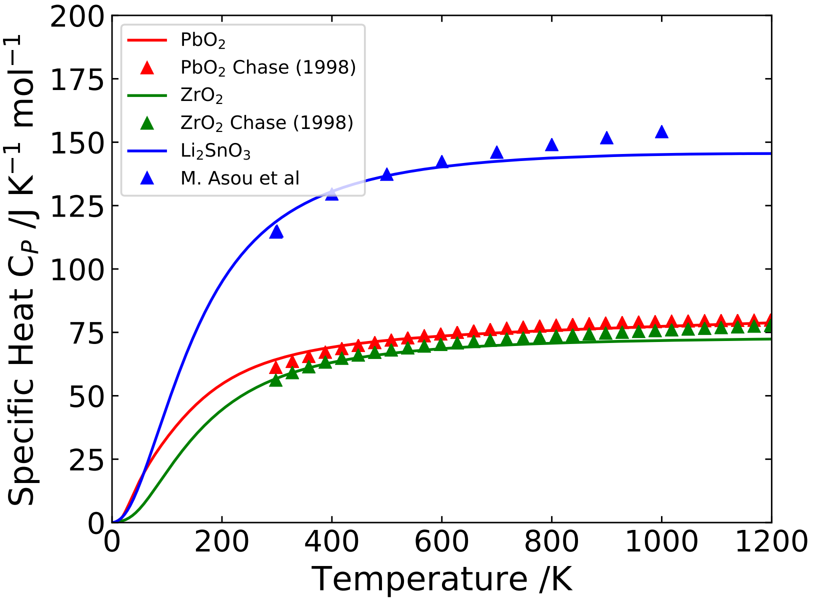

Figure 5.5: Comparison of QHA-derived specific heat capacities for PbO_2, ZrO_2 and Li_2SnO_3 with literature [210, 211].

Of particular interest for the present work is the specific heat capacity for Li_2O, which is plotted in Figure 5.6. For low temperatures, the heat capacity predicted by the QHA is in excellent agreement with the experimental measurements. However, at 600 K, an obvious deviation begins to appear showing an upward trend in gradient. It is known that the fundamental assumptions at the heart of the QHA start to break down at higher temperatures, however, this is not seen in any of the 18 other materials examined here, with the minor exception of CeO_2 that exhibits a slight increase in gradient at high temperatures (see Figure A.3), but not as severe. For some crystal structures, such as FCC, phonon-phonon interactions neglected by the quasi-harmonic model can become a significant contribution to the specific heat capacity [212]. As Li_2O exhibits the antifluorite structure, where the oxygen sublattice adopts an FCC structure ($Fm\bar{3}m$ [225]), anharmonicity in the crystal may be contributing significantly leading to the observed deviation. To account for this, specific heat capacities for Li_2O taken from Chase [210] and Johnston and Bauer [213] were combined and used as an alternative in subsequent sections. CeO_2 shares the same structure as Li_2O, but due to the significant mass difference between Ce and Li, this effect is notably smaller and thus a specific heat capacity from literature is not used for the CeO_2 case.

5.3.3 Formation Enthalpy

The formation enthalpy of a compound is simply the difference in enthalpy between the final compound and the reactants: $\Delta H = H_{product} - \sum_\alpha n_\alpha H_\alpha$ where n_α is the quantity of reactant α.

The processes considered for the formation of $Li_8\{Pb,Ce,Ge,Zr,Sn\}O_6$ and other minor ternary compounds are:

$$Li_4PbO_4 + 2Li_2O \rightarrow Li_8PbO_6 \tag{5.1}$$

$$PbO_2 + 4Li_2O \rightarrow Li_8PbO_6 \tag{5.2}$$

$$PbO_2 + 2Li_2O \rightarrow Li_4PbO_4 \tag{5.3}$$

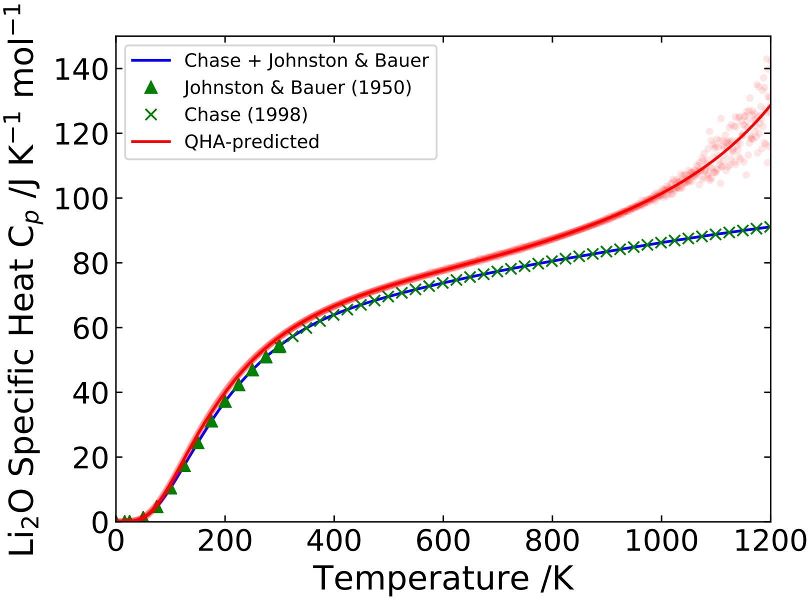

Figure 5.6: Deviation of QHA-predicted C_p for Li_2O from the literature [210, 213].

$$Li_4GeO_4 + 2Li_2O \rightarrow Li_8GeO_6 \tag{5.4}$$

$$GeO_2 + 4Li_2O \rightarrow Li_8GeO_6 \tag{5.5}$$

$$GeO_2 + 2Li_2O \rightarrow Li_4GeO_4 \tag{5.6}$$

$$Li_2CeO_3 + 3Li_2O \rightarrow Li_8CeO_6 \tag{5.7}$$

$$CeO_2 + 4Li_2O \rightarrow Li_8CeO_6 \tag{5.8}$$

$$CeO_2 + Li_2O \rightarrow Li_2CeO_3 \tag{5.9}$$

$$0.5Li_6Zr_2O_7 + 2.5Li_2O \rightarrow Li_8ZrO_6 \tag{5.10}$$

$$ZrO_2 + 4Li_2O \rightarrow Li_8ZrO_6 \tag{5.11}$$

$$2ZrO_2 + 3Li_2O \rightarrow Li_6Zr_2O_7 \tag{5.12}$$

$$Li_2SnO_3 + 3Li_2O \rightarrow Li_8SnO_6 \tag{5.13}$$

$$SnO_2 + 4Li_2O \rightarrow Li_8SnO_6 \tag{5.14}$$

$$SnO_2 + Li_2O \rightarrow Li_2SnO_3 \tag{5.15}$$

The experimentally measured constant pressure heat capacity for Li_2O was used to calculate the enthalpy using the following equation:

$$H(T) = E_0 + E_{ZPE} + \int_{T=0}^{T} C_p \, dT \tag{5.16}$$

where E_0 is the energy of the relaxed primitive cell of Li_2O and E_{ZPE} is the zero-point energy contribution given by Phonopy.

Formation enthalpies were plotted for reactions 5.1 - 5.15 in Figures 5.7a - 5.7e. A comparison is made between formation enthalpies using the QHA-derived enthalpy for Li_2O and the enthalpy derived from the experimental pressure-dependent specific heat capacity.

The formation enthalpy for Li_8GeO_6 lies close to 0 J/mol, with -790 J/mol at 0 K and increases above 0 at temperatures of >358.5 K and >170.5 K for QHA and experimental Li_2O respectively. Using the enthalpy derived from experimental C_p for Li_2O, Li_2GeO_3 is the preferred state above 170.5 K, whereas using the QHA-predicted Li_2O enthalpy, Li_8GeO_6 becomes the preferred state once again at 1125.1K. For Li_8CeO_6, degradation into Li_2CeO_3 is preferred at low temperatures (<392.3 K and <686.7 K for QHA and experimental Li_2O respectively) but for higher temperatures, Li_8CeO_6 is the preferred state. Similarly with Li_8ZrO_6, $Li_6Zr_2O_7$ is slightly preferred for temperatures above 231.5 K using the QHA-derived Li_2O enthalpy and 326.9 K using the experimentally derived enthalpy. There is a clear enthalpic driving force for the formation of both Li_8PbO_6 and Li_8SnO_6 across the entire temperature range explored, particularly for higher temperatures. The Li-Sn-O system is the most promising of the candidates tested, showing a marked preference for Li_8SnO_6 over Li_2SnO_3, even at 0 K. The enthalpy of formation for octalithium compounds generally appears to increase in negativity with temperature, with the exception of the Li_8GeO_6.

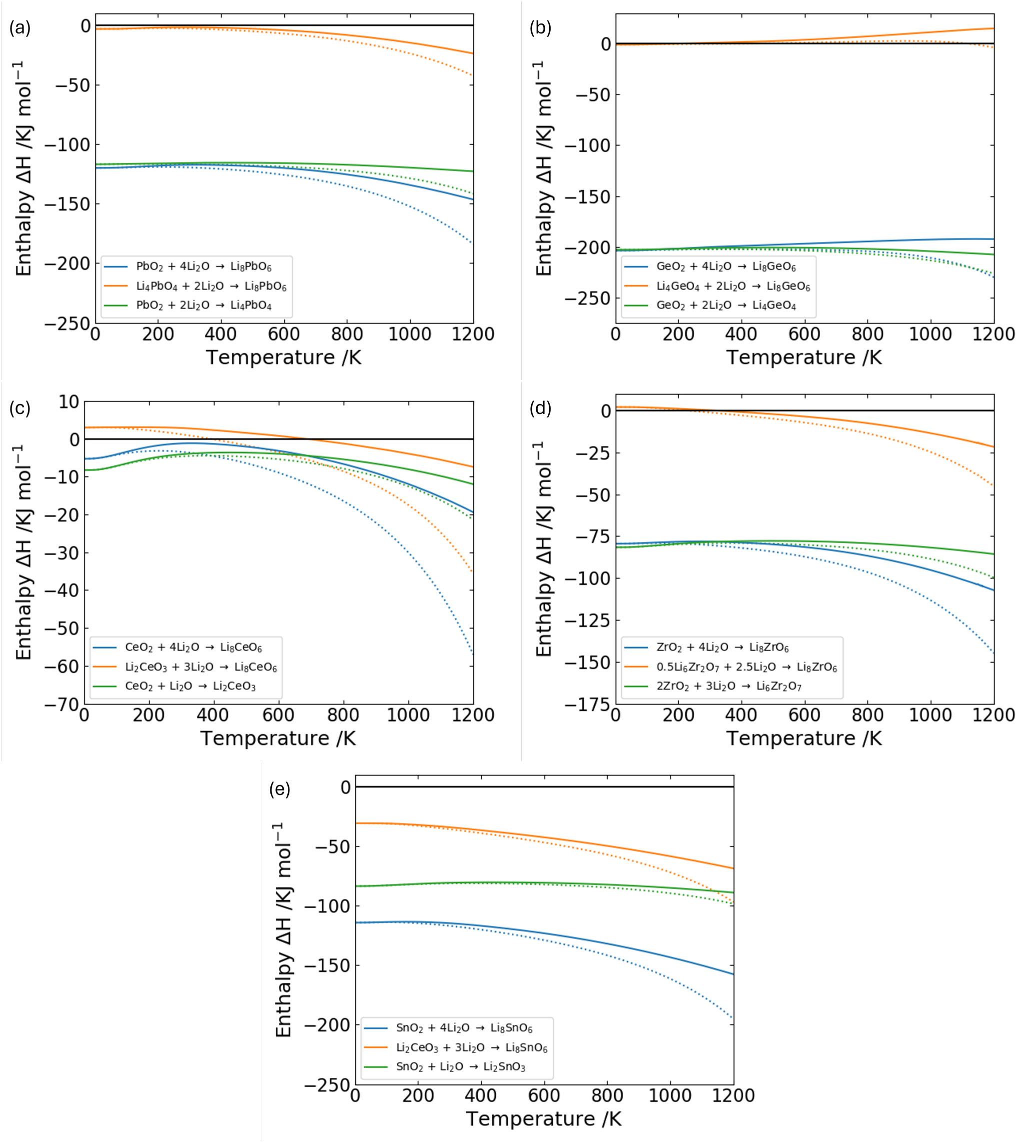

Figure 5.7: Formation enthalpies in the Li-X-O phase group. X = Pb, Ge, Ce, Zr, Sn for subfigures a-e respectively. Bold lines represent the use of literature-obtained C_p to derive the enthalpy of Li_2O. Dotted lines represent the use of QHA-derived Li_2O C_p containing the uncorrected anharmonicity.

5.3.4 Gibbs Formation Energy

Enthalpy of formation alone is not enough to determine the phase stability of a compound, the Gibbs formation energy ultimately determines this. The Gibbs formation energy can be used to predict the stability of a substance, and is calculated in the same manner as the formation enthalpy: $\Delta G = G_{product} - \sum_{\alpha} n_{\alpha} G_{\alpha}$. A negative Gibbs formation energy implies there is a driving force for the forward reaction , whereas a positive energy implies the direction of the reaction is reversed.

The Gibbs formation energy for Li_2O can, much like the enthalpy, be derived from the pressure-dependant specific heat capacity using the equation $G = H - TS$. Writing the entropy in terms of the specific heat capacity, the following expression can be used to calculate the Gibbs energy of Li_2O:

$$G(T) = H(T) - T \int_{T=0}^{T} \frac{C_p}{T} \, dT \tag{5.17}$$

where $H(T)$ is the enthalpy derived from equation 5.16.

Figures 5.8a - 5.8e show the Gibbs formation energies for the octalithium compounds. The figures show that only the group-IV-containing octalithium compounds are stable. The similar electron configuration of the group-IV metals is likely the dominant factor in deciding the phase stability of the crystal rather than the cation radius, as the outermost electrons of Ge, Sn, and Pb occupy the 4p^2, 5p^2 and 6p^2 orbitals respectively versus the less stable Zr and Ce, which occupy the 5s^2 and 6s^2 orbitals. Of the Ge, Sn and Pb-containing compounds, Li_8SnO_6 is the only material shown to break down using both the QHA-predicted and literature-referenced Gibbs energy for Li_2O, at temperatures of 991.8 K and 1168.3 K respectively. Li_8PbO_6 is only predicted to break down when using the QHA-predicted Li_2O Gibbs energy at a temperature of 1005.9 K. By contrast to both Li_8SnO_6 and Li_8PbO_6, Li_8GeO_6 from a Gibbs energy perspective, is predicted to be entirely stable up to 1200 K. Despite this, Li_8PbO_6 appears to be the most viable candidate of all the materials assessed, due to the lack of phase change below 1200 K when using the literature-referenced Gibbs energy for Li_2O.

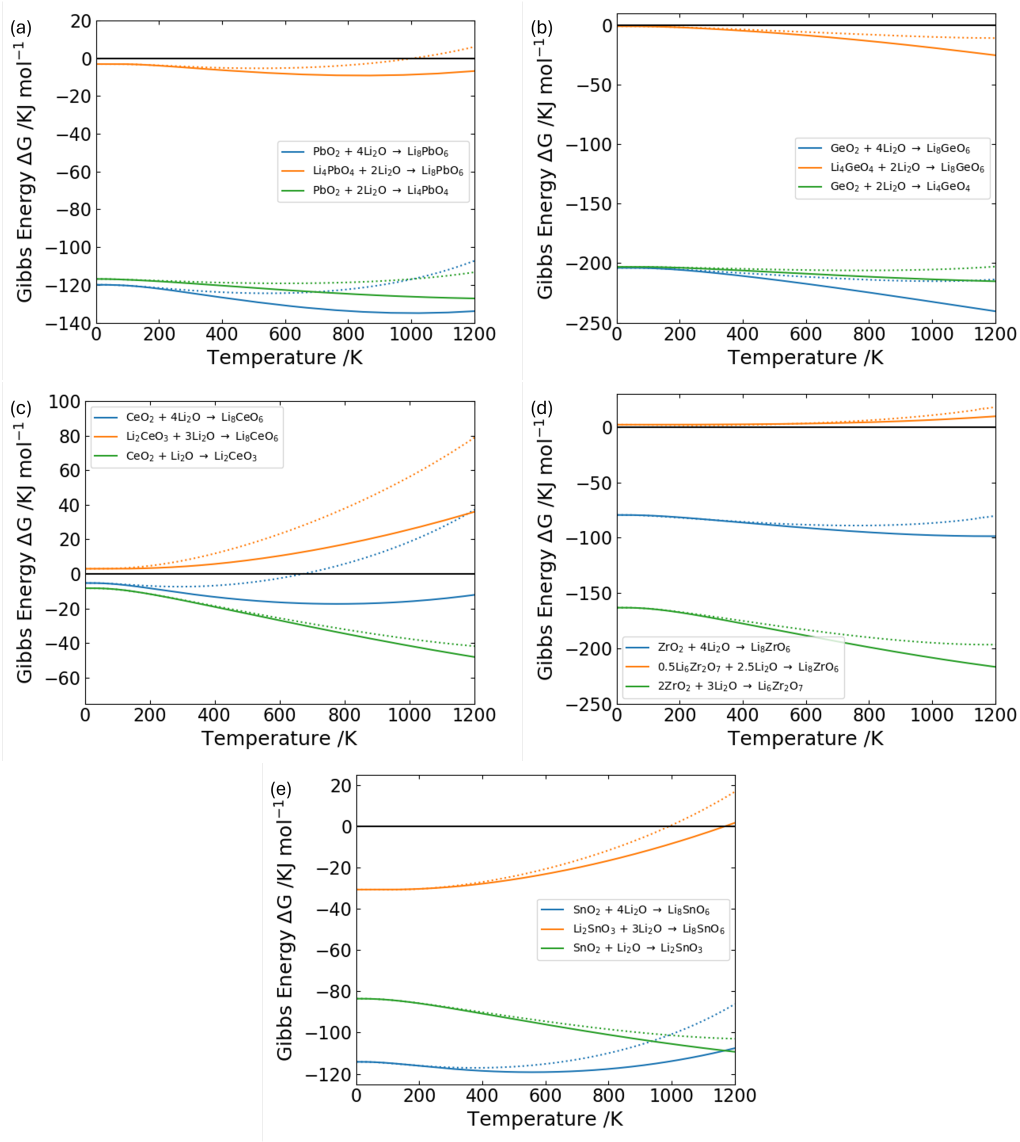

Figure 5.8: Gibbs formation energies in the Li-X-O phase group. X = Pb, Ge, Ce, Zr, Sn for subfigures a-e respectively. Bold lines represent the use of literature-obtained C_p to derive the Gibbs formation energy of Li_2O. Dotted lines represent the use of QHA-derived Li_2O C_p containing the uncorrected anharmonicity.

5.4 Conclusion

The fundamental thermodynamic properties of $Li_8\{Pb,Ce,Ge,Zr,Sn\}O_6$ octalithium ceramics have been investigated using the QHA. Despite the potentially high tritium breeding rates of all the ceramics investigated, many are prone to degradation, even at relatively low temperatures, with the exception of compounds containing group-IV elements. Although materials such as Li_8SnO_6 and Li_8GeO_6 show promising thermal properties, the potential for Li_8PbO_6 exceeds the others, with the octalithium phase predicted to be most stable up to temperatures of 1200 K. With a sufficiently high TBR of 1.21 in combination with the lack of signs of degradation compared to the other materials tested, Li_8PbO_6 may be the most viable candidate to pursue as a breeder blanket material, followed closely by Li_8SnO_6. Therefore, as the plumbate appears to be the most promising breeder material, we will investigate the defect chemistry and tritium accommodation and diffusion in this material in Chapters 6 and 7.

Chapter 6

Intrinsic defect chemistry

The contents of this chapter have been published in:
A. W. Davies, W. D. Neilson, R. T. Bedford, S. T. Murphy, The High Temperature Intrinsic Defect Chemistry of Li_8PbO_6 Ceramic Breeding Material, J. Phys. Chem. C. 127 (2023) 22265. [214]

6.1 Introduction

Previous Chapters examined the thermodynamic stability of a range of different octalithium ceramics within the quasiharmonic approximation and predicted that of the candidates tested, octalithium plumbate (Li_8PbO_6, with a predicted TBR of 1.21) appears thermodynamically stable enough to justify further investigation. The work of Hayashi *et al.* showed that Li_8PbO_6 exhibits excellent tritium release characteristics [19], however, what is less clear is how this will change during operation. Lithium burn-up and radiation damage will introduce defects into the material, that could have a significant impact on tritium release. Therefore, due to the importance of point defects for controlling tritium mobility through the bulk crystal, this work focuses on understanding the intrinsic defect chemistry of Li_8PbO_6 using a point defect model similar to the works of Murphy and Hine [122, 215]. High temperatures expected during reactor operation will be a significant contributor towards the defect composition. Thus, we also explore in this Chapter a modified method to include temperature incorporation into the defect chemistry, by calculating the constituent chemical potentials used in the defect formation energy calculations from the T-dependent Gibbs free energies of the reactants, as is described in section 3.3.2.

6.2 Crystallography

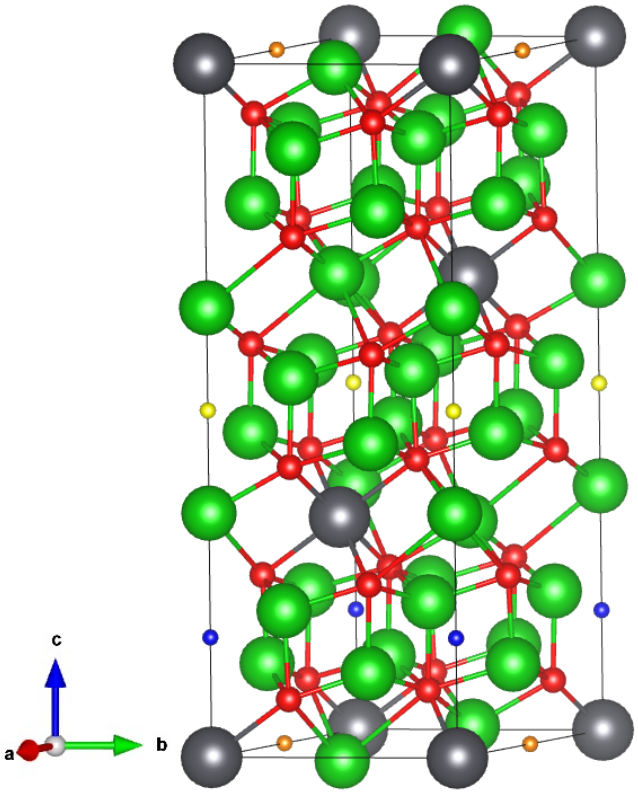

Figure 6.1: Structure of 45-atom unitcell of Li_8PbO_6. Green spheres represent Li ions, red spheres represent O ions and the grey spheres represent Pb ions. Interstitial sites 1 - 3 are illustrated as orange, blue, and yellow and ions respectively. Not all possible interstitial sites are shown in the figure.

The crystal structure of Li_8PbO_6 is introduced in Chapter 2, however, a summary is provided to aid understanding the results in this Chapter. Li_8PbO_6 adopts the trigonal $R\bar{3}H$ [148] space group [125]. Within the unitcell, Li occupies two symmetrically distinct Wyckoff positions, which are the tetragonally-coordinated $18f$ sites and the octahedrally-coordinated $6c$ sites. The O and Pb ions occupy the $18f$ and $3a$ Wyckoff positions respectively. Li_8PbO_6 adopts a complex layered structure alternating between a pure Li layer and a mixed Li-Pb layer in the following sequence: $PbLi_2$-O_3-Li_3-Li_3-O_3. In the pure Li layers, Li occupies the tetrahedrally-coordinated site exclusively, whereas in the mixed Li-Pb layer Li occupies the octahedrally-coordinated site. For the remainder of this chapter, the tetragonally-coordinated Li will be referred to as Li_1 and the octahedrally-coordinated Li will be referred to as Li_2. Three symmetrically distinct interstitial sites were identified in Li_8PbO_6. The coordinates of the interstitial sites are presented in Table 6.1 and the sites are indicated in Figure 6.1.

Table 6.1: Interstitial sites in Li_8PbO_6 in fractional coordinates.

Interstitial site	x	y	z
1	0.25	0	0
2	0	0	0.17275
3	0	0	0.5

6.3 Parameterisation

Parameterisation of the DFT simulations is similar to that introduced in Chapter 4, which establishes the efficacy of the computational model. A summary of the parameterisation is nonetheless provided in this section. DFT simulations were performed using the VASP planewave pseudopotential code [175], employing PAW pseudopotentials [179]. All defect simulations utilised GGA PBE functionals [146]. Integration over the Brillouin zone was performed using a $6 \times 6 \times 2$ Monkhorst-Pack grid [178] corresponding to a separation between k-points of $0.0316 \times 2\pi$ Å^{-1} along the x and y axes and $0.0344 \times 2\pi$ Å^{-1} along the z-axis. The planewave cutoff energy was set to 650 eV, the energy threshold for electronic convergence is set as 10^{-8} eV, and structural convergence was deemed complete when the forces on all atoms did not exceed 0.01 eV Å^{-1}. Defects are inserted into a supercell constructed from $2 \times 2 \times 1$ repetitions of the 45-atom, $5.58 \times 5.58 \times 15.81$ Å^{-1} unit cell, resulting in a supercell containing 180 atoms. Defect charges are modelled by adding or removing electrons from the supercell.

6.3.1 Finite Size Effects

6.3.1.1 Finite size effects

The introduction of charged defects into relatively small supercells in DFT results in the presence of finite size artefacts. The main source of these artefacts is the Coulombic interaction between the defect and its periodic image and the neutralizing background charge. Finite size effects are accounted for in the defect formation energy via implementation of a charge correction term, labelled E_{corr} in equation 3.35.

In this chapter, the anisotropic screening correction developed by Kumagai and Oba [161] is utilised, which builds on the point charge correction developed by Freysoldt, Neugebauer and Van de Walle (FNV) [162]. Kumagai and Oba build on the method by utilising atomic site potentials instead of planar averaged electrostatic potentials utilised by FNV. A summary is outlined in section 3.3.4.

6.3.1.2 Phonon calculations

The Gibbs free energies of Li_2O, PbO_2 and Li_8PbO_6 can be obtained using the finite displacement method. Gibbs free energies for Li_8PbO_6 and the reactant PbO_2 are taken from Chapter 5, examining thermodynamic properties of octalithium ceramics [192] using QHA. QHA calculations were performed for additional binary and ternary compounds in the Li-Pb-O phase group (Li_2PbO_3, PbO-M (orthorhombic), PbO-L (tetragonal), Pb_3O_4), with a k-point separation of 0.2-0.3×2π Å^{-1}, and using 11 different volumes in equal steps of 3% within a range of ±15% of the respective relaxed unit cell. Specific parameterisation details of the supercell size, k-point and q-point grids for these materials are included in Table B.2 in Appendix B. Lattice parameters and heat capacities for the additional compounds included in this Chapter are also included in Appendix B. The energy for Li_2O is taken from specific heat capacities obtained using a combination of Chase [210] and Johnston and Bauer [213], due to the presence of phonon-phonon interactions in Li_2O which cause an overestimate of heat capacities in FCC lattice structures [212]. Due to computational limitations with performing finite displacement simulations of point defects (particularly due to the asymmetry introduced), finite displacement simulations for the point defects were not performed in this work, although it is noted that this could impact the high temperature defect chemistry [216].

6.3.1.3 Defect analysis

Vacancy, interstitial, and antisite-type defects in Li_8PbO_6 have been investigated. All possible charge states are studied for each of these defects and a full list of the defects considered in this study are presented in Table 6.2, using Kröger–Vink notation, modified to display relative charge as an integer value [130].

Final calculation of the defect concentrations at a given temperature and oxygen partial pressure can be obtained by determining the Fermi energy that achieves charge neutrality according to equation 3.33. The Fermi level is determined using a linear bisection approach in the Defect Analysis Package (DefAP)[217].

6.4 Results and Discussion

Table 6.2: Defect formation energies at the valence band maximum at 1000 K under $\mathrm{Li_2O}$-rich conditions with an oxygen partial pressure of 0.2 atm. The E_f values are those where the energy minimised values for the reference states are employed and $\mathrm{E}_f^{inc}(T)$ have temperature effects incorporated into the reference states for the solids. Note that for the oxygen defects the values are identical as they have no dependence on the reference states.

	Defect	E_f (eV)	$\mathrm{E}_f^{inc}(T)$ (eV)		Defect	E_f (eV)	$\mathrm{E}_f^{inc}(T)$ (eV)
1	V_{Li1}^{-1}	2.261	1.909	29	Li_{i3}^{0}	2.509	2.861
2	V_{Li1}^{0}	1.179	0.827	30	Li_{i3}^{1}	-0.826	-0.474
3	V_{Li2}^{-1}	2.663	2.312	31	Li_{i4}^{0}	2.849	3.201
4	V_{Li2}^{0}	1.526	1.175	32	Li_{i4}^{1}	-0.433	-0.081
5	V_{Pb}^{-4}	10.238	8.698	33	Pb_{i1}^{0}	8.773	10.314
6	V_{Pb}^{-3}	8.110	6.569	34	Pb_{i1}^{1}	5.988	7.529
7	V_{Pb}^{-2}	6.514	4.974	35	Pb_{i1}^{2}	3.142	4.682
8	V_{Pb}^{-1}	5.376	3.835	36	Pb_{i1}^{3}	1.822	3.363
9	V_{Pb}^{0}	4.968	3.427	37	Pb_{i1}^{4}	0.259	1.800
10	V_{O}^{0}	2.870	2.870	38	Pb_{i2}^{0}	6.799	8.340
11	V_{O}^{1}	0.484	0.484	39	Pb_{i2}^{1}	3.950	5.491
12	V_{O}^{2}	-1.813	-1.813	40	Pb_{i2}^{2}	1.108	2.649
13	$\mathrm{Pb}_{\mathrm{Li1}}^{0}$	4.939	6.128	41	Pb_{i2}^{3}	-0.316	1.225
14	$\mathrm{Pb}_{\mathrm{Li1}}^{1}$	1.638	2.827	42	Pb_{i2}^{4}	-1.766	-0.225
15	$\mathrm{Pb}_{\mathrm{Li1}}^{2}$	-0.102	1.087	43	Pb_{i3}^{0}	8.021	9.562
16	$\mathrm{Pb}_{\mathrm{Li1}}^{3}$	-1.789	-0.600	44	Pb_{i3}^{1}	4.696	6.236
17	$\mathrm{Pb}_{\mathrm{Li2}}^{0}$	3.964	5.154	45	Pb_{i3}^{2}	1.544	3.084
18	$\mathrm{Pb}_{\mathrm{Li2}}^{1}$	0.689	1.879	46	Pb_{i3}^{3}	-0.025	1.515
19	$\mathrm{Pb}_{\mathrm{Li2}}^{2}$	-1.162	0.027	47	Pb_{i3}^{4}	-1.640	-0.099
20	$\mathrm{Pb}_{\mathrm{Li2}}^{3}$	-2.980	-1.791	48	O_{i1}^{-2}	8.181	8.181
21	$\mathrm{Li}_{\mathrm{Pb}}^{-3}$	7.435	6.246	49	O_{i1}^{-1}	4.751	4.751
22	$\mathrm{Li}_{\mathrm{Pb}}^{-2}$	5.651	4.461	50	O_{i1}^{0}	1.739	1.739
23	$\mathrm{Li}_{\mathrm{Pb}}^{-1}$	4.363	3.175	51	O_{i2}^{-2}	7.601	7.601
24	$\mathrm{Li}_{\mathrm{Pb}}^{0}$	3.640	2.451	52	O_{i2}^{-1}	5.057	5.057
25	Li_{i1}^{0}	3.006	3,358	53	O_{i2}^{0}	3.578	3.578
26	Li_{i1}^{1}	-0.305	0.046	54	O_{i3}^{-2}	7.789	7.789
27	Li_{i2}^{0}	2.666	3.018	55	O_{i3}^{-1}	4.985	4.985
28	Li_{i2}^{1}	-0.605	-0.253	56	O_{i3}^{0}	3.553	3.553

6.4.1 Defect Formation Energies

In the following subsection, defect formation energies under Li_2O-rich conditions with an oxygen partial pressure of 0.2 atmospheres (atm) at 1000 K are examined. Defect formation energies for all possible intrinsic point defects and their respective charge states at the valence band maximum have been included in Table 6.2.

Lithium vacancy defects for both unique lattice sites occupy the -1 charge state across the entire band gap, with the Li1 site having a lower formation energy, as seen in Figure 6.2. This suggests the majority of lithium vacancy defects will occur at the tetrahedrally coordinated $18f$ Wyckoff position, rather than the octahedral $6c$ site. This is simply due to the requirement to break fewer bonds to remove the tetrahedrally coordinated atom, as discussed in Chapter 4.

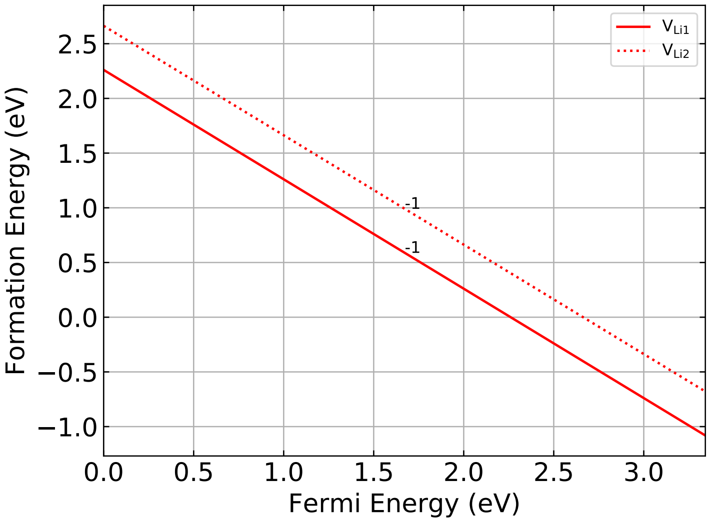

Figure 6.2: Formation energy of the lithium vacancy defects as a function of the Fermi energy (relative to the valence band maximum).

The formation energies for the oxygen and lead vacancy defects as a function of the Fermi level are presented in Figures 6.3 and 6.4. At the valence band maximum the oxygen vacancy is predicted to be in the +2 charge state. The same charge state is predicted to dominate for the majority of the band gap. At roughly 2.3 eV there is a transition to the +1 charge state, although the region where this state

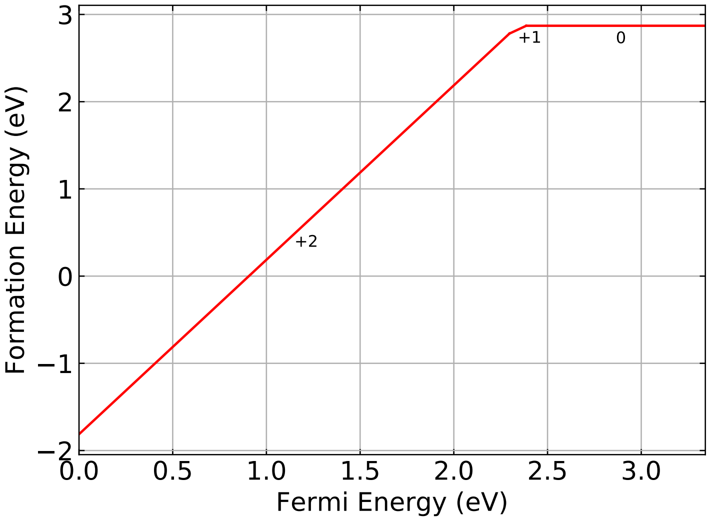

Figure 6.3: Formation energy of the oxygen vacancy defect as a function of the Fermi energy.

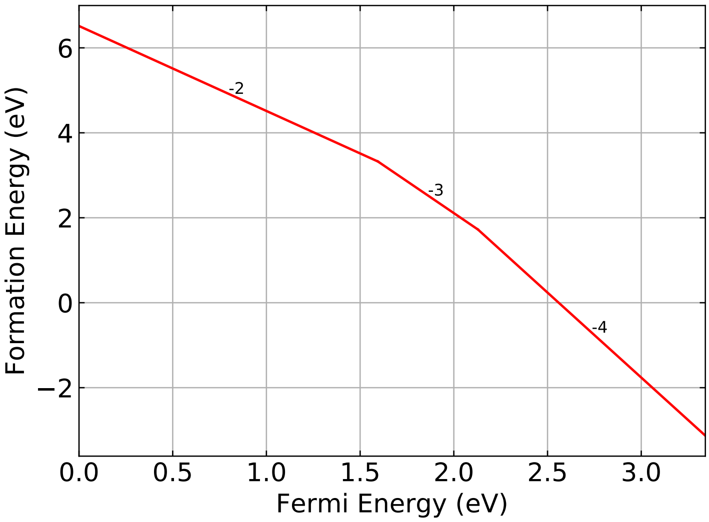

Figure 6.4: Formation energy of the lead vacancy defect as a function of the Fermi energy.

dominates is relatively small. As the Fermi level approaches the conduction band the charge neutral oxygen vacancy dominates. For the lead vacancy defect (Figure 6.4) only the highly charged states -2, -3 and -4 are predicted to be stable across the width of the band gap.

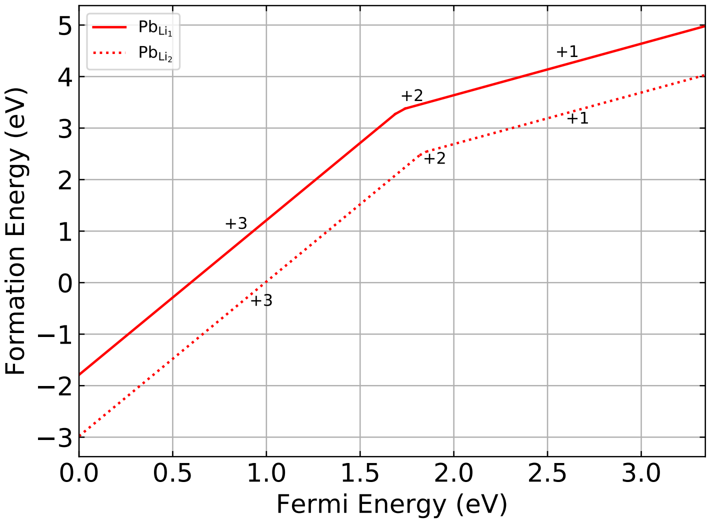

Figure 6.5: Formation energies for lead substitution on the lithium sites as a function of the Fermi energy.

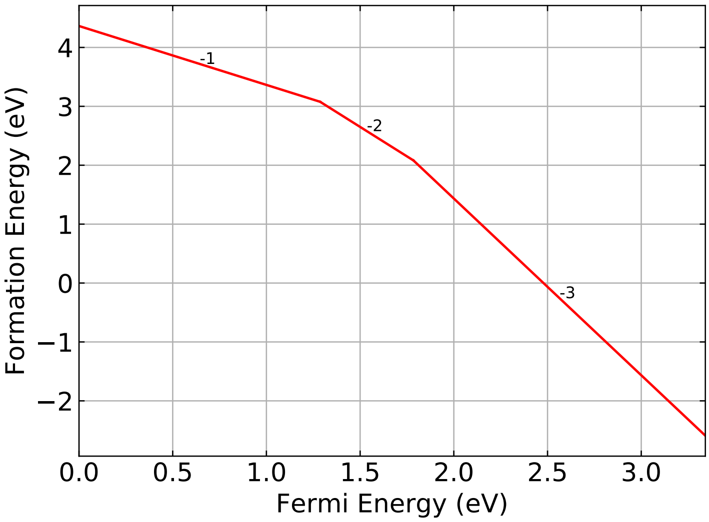

Figure 6.6: Formation energy for lithium substitution on the lead site as a function of the Fermi energy.

Figures 6.5 and 6.6 shows the formation energies for the antisite defects in Li_8PbO_6 (Pb_{Li} and Li_{Pb} respectively). Lead may substitute for lithium on either of the two symmetrically distinct sites. Both sites show broadly the same distribution of charge states as a function of the Fermi Energy. Figure 6.5 suggests that it is thermodynamically preferable for lead to occupy the octahedrally coordinated 6*c* position in the mixed Li-Pb layer, rather than the pure lithium layer, due to the greater number of nearest neighbour oxygen ions. $\mathrm{Pb_{Li}}$ does not appear to occupy the charge-neutral state, and instead broadly favours the +3 and +1 states at the valence band maximum and conduction band minimum respectively, with some minor transitional occupation of the +2 state. The dominance of the +3 and +1 defect charge states correspond to lead in the +4 and +2 oxidation states occupying a $\mathrm{V_{Li}^{-1}}$ vacancy. For lithium substitution onto the lead site, the -1 charge state is predicted to dominate at the valance band maximum, while the -3 charge state dominates at the conduction band minimum. The transitions between charge states occur in very similar positions in the bandgap to the lead vacancy defect.

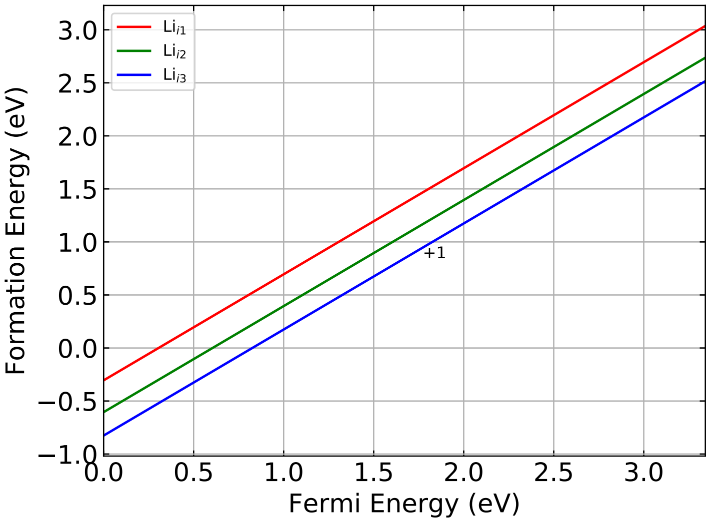

Figure 6.7: Formation energies for lithium interstitial defects as a function of the Fermi energy.

Figures 6.7 - 6.9 show the formation energies for the interstitial defects as a function of the Fermi energy. Lithium interstitial defects (Figure 6.7) are predicted to exist in the +1 charge state across the entire width of the band gap. Li interstitial defects are predicted to be most favourable on sites 2 and 3, which are located between the two pure Li planes. By contrast interstitial site 1, which lies in the

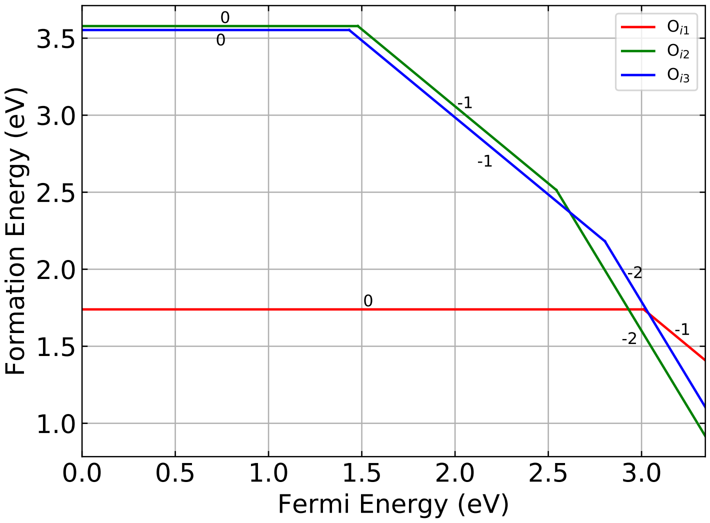

Figure 6.8: Formation energies for oxygen interstitial defects as a function of the Fermi energy.

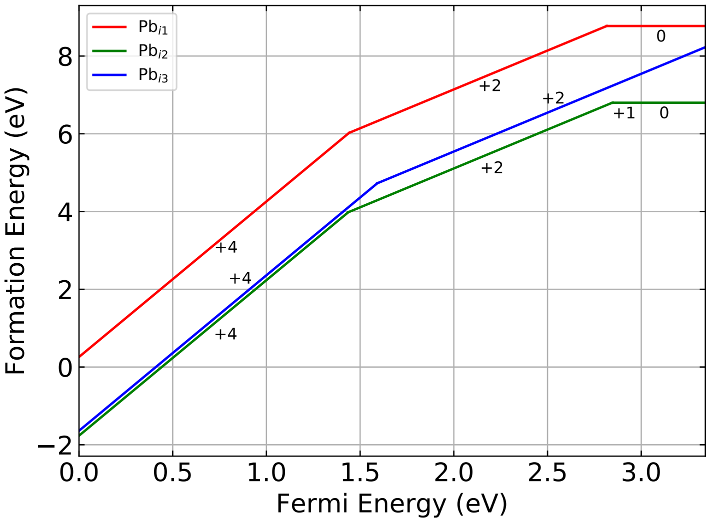

Figure 6.9: Formation energies for the lead interstitial defects as a function of the Fermi energy.

mixed Li-Pb plane, is shown to have a high formation energy, which is likely due to the proximity to a positively charged lead ion. It should be noted that a split interstitial site was found in the Li interstitial case within the mixed Li-Pb layer, distinct from site 1. The site is visualised in Figure 6.10.

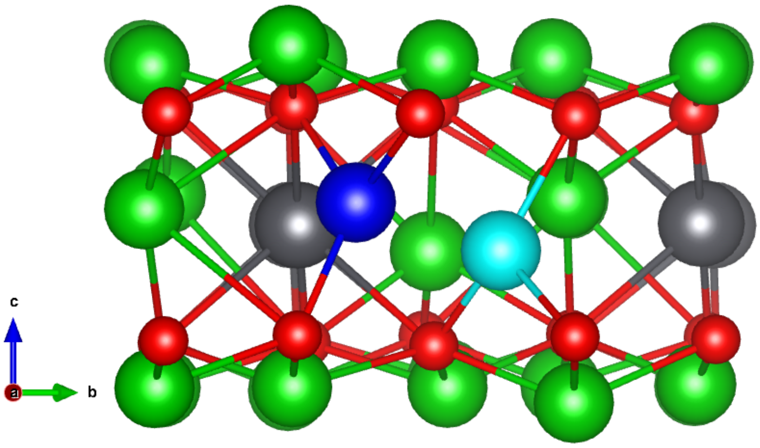

Figure 6.10: Li split interstitial defect in the mixed Li-Pb plane. The blue sphere represents the lithium ion placed into the unit cell, which forms a split interstitial with the displaced lithium ion represented using the teal sphere.

As shown in Figure 6.8, the oxygen interstitial defects exhibit significantly different behaviour depending on the site they occupy. The most favourable interstitial site for oxygen to occupy was found to be site 1 in the mixed Li-Pb plane, where the charge-neutral defect dominates across nearly the entire width of the band gap, with some occupation of the -1 state towards the edge of the conduction band. Sites 2 and 3 exhibit a similar trend in formation energies as a function of the Fermi Energy, with the -1 and charge-neutral states dominating across the majority of the band gap and the -2 states only becoming important close to the conduction band.

For the lead interstitial defect, it is predicted that site 2 is the most thermodynamically stable. For all 3 sites, the majority of the band gap is occupied by the +4 and +2 charge states, indicating depopulation of the outermost p orbitals in both cases, and both p and s orbitals in the +4 state. For site 3 the +2 charge state extends up to the conduction band minimum, whereas for sites 1 and 2, there are transitions to lower charge states evident.

Almost all defects shown in Figures 6.7 - 6.9 occupy primarily their formal charge states, with the exception of the oxygen interstitial defect that appears to have a slight preference for the -1 state. As most defects occupy their formal charge states, there will be few states in bandgap and, consequently, the widely known self interaction error will not significantly impact the defect chemistry predicted here [218].

6.4.2 Temperature of Stable Phases

Due to the lack of literature available on the stability of Li_8PbO_6, phase diagrams were constructed to explore stable regions in the Li-Pb-O system. Compounds examined other than Li_8PbO_6 include Li_2O and PbO_2 (both reactants used in the sintering process for Li_8PbO_6), Li_2PbO_3 and Li_4PbO_4 (a trace compound found during sintering). Alternative binary oxide phases in the Li-O [219] (Li_2O_2, LiO_2) and Pb-O [220] (PbO-M, PbO-L, Pb_3O_4) groups have been considered, although the alternative binary oxide phases are not shown to have a significant impact on the phase stability region of Li_8PbO_6, particularly alternative Li-O phases, as under the conditions considered for this work, Li_2O is predicted to be the most thermodynamically preferred phase [221].

In this chapter, a comparison is made between use of the internal and Gibbs free energies for the binary and ternary compounds in the Li-Pb-O system in determination of phase stability. The alternative Pb-O phases have been included in the phase stability diagrams presented in Figures 6.11 and 6.12.

For low temperatures, there is a clear distinction between the plots given in Figure 6.11 as to whether there exists a region where Li_8PbO_6 is stable. If the Gibbs free energy is not accounted for in the constituent compounds Li_2O and PbO_2, Li_8PbO_6 is deemed unstable, with significant quantities of Li_4PbO_4 and Li_2PbO_3 appearing within the system. By contrast, using the Gibbs free energies there is a small stable region for Li_8PbO_6 where no formation of secondary phases is expected, suggesting if accounted for, Li_8PbO_6 may form at 300 K. The stable region is bordered by boundaries of Li_4PbO_4 and Li_2O regions so the presence of trace quantities of Li_2O and Li_4PbO_4 is likely. Aside from a single paper exploring

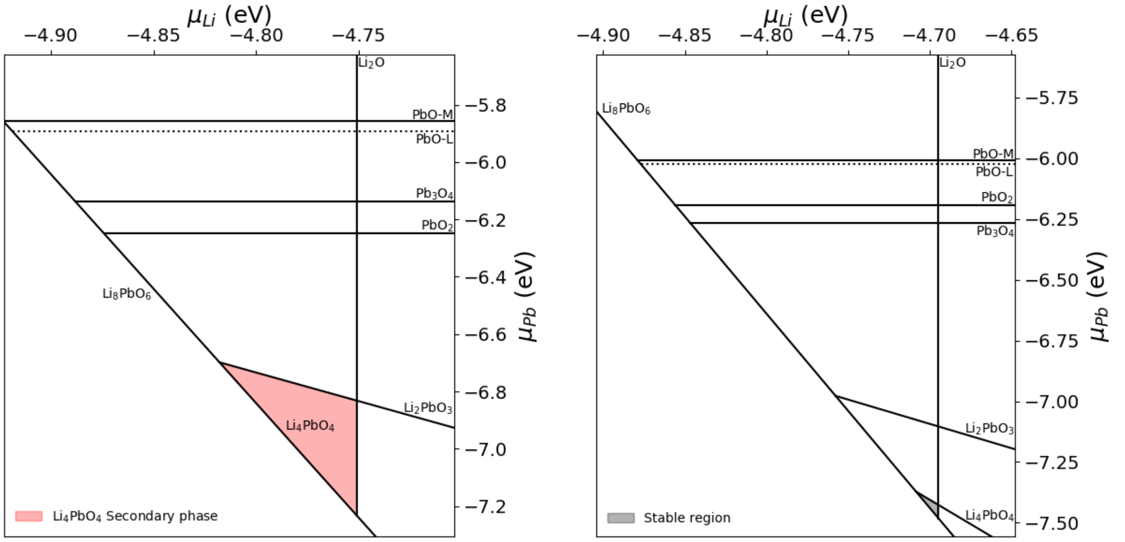

Figure 6.11: Phases of Li-Pb-O system as a function of Li and Pb chemical potentials using internal (left) and Gibbs free energies (right) respectively. Each line represents the minimum boundary of $\sum_i \mu_i$ where the respective compound is stable. The grey shaded region illustrates the phase space where formation is exclusively Li_8PbO_6 over any other phase (i.e. E(Li_8PbO_6) $<\sum_i \mu_i$, $\forall$ E(compound $\neq$ Li_8PbO_6)), and the red region shows the region where Li_4PbO_4 is a secondary phase to Li_8PbO_6. The dotted line represents PbO-L to better distinguish between PbO phases. T = 300 K, Oxygen partial pressure (OPP) = 0.2 atm, $\mu_{\frac{1}{2}O_2}$ = -4.78 eV.

the sintering process for Li_8PbO_6 from Li_2O and PbO_2 by Colominas *et al.* [121], there is a lack of literature on fabrication of Li_8PbO_6, with which to compare our results.

For high temperatures (figure 6.12), there is a stark difference between the internal and Gibbs free energy phase diagrams. At 1000 K, both the massicot and litharge phases of PbO and Pb_3O_4 are predicted to have more favourable internal energies compared to PbO_2, as expected. Although Pb_3O_4 is predicted to have a slightly lower Gibbs formation energy compared to PbO. The stability region for Li_8PbO_6 is not impacted by any of the alternative phases excluding Li_4PbO_4, which accords with formation of a trace amount of Li_4PbO_4 as seen in Colominas *et al.*

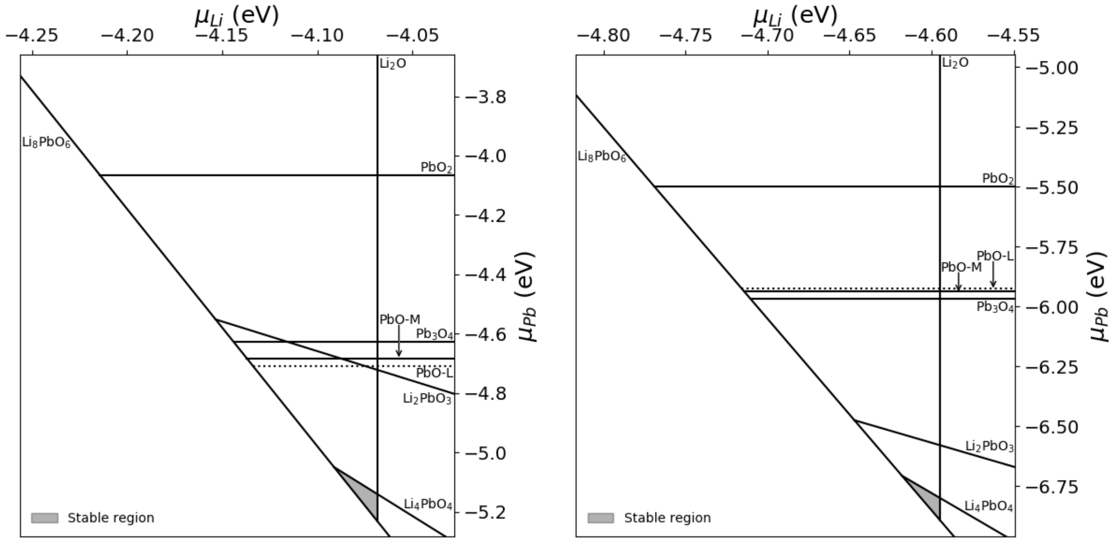

Figure 6.12: Stable phases of Li-Pb-O system as function of Li and Pb chemical potentials using internal (left) and Gibbs free energies (right) respectively. T = 1000 K, OPP = 0.2 atm, $\mu_{\frac{1}{2}O_2}$ = -5.60 eV.

[121]. Unfortunately, the exclusive region for Li_8PbO_6 formation in the chemical potential phase space is relatively quite small, regardless of the choice of method, and it is expected the formation of Li_8PbO_6 will thus only occur close to the Li_2O-rich limit.

6.4.3 Intrinsic Defect Chemistry

Having defined the region of chemical potential space where Li_8PbO_6 is thermodynamically stable, we now explore the defect chemistry of the material in this region. Figures 6.11 and 6.12, show that the Li_8PbO_6 phase is not stable at the PbO_2 saturation limit, due to the formation of Li_4PbO_4 and Li_2PbO_3 phases. By contrast, there is a region where the octalithium compound is stable at the Li_2O saturation limit. Therefore, this region is explored first. A comparison is made between the predicted defect chemistry where the temperature effects are included in the energies for the references states and where they are not. This is important due to the high operational temperatures anticipated in breeder blanket materials, which have a maximum operational temperature of 920°C for the ceramic in HCPB designs [222]. As the expected OPP is not known, typical atmospheric conditions are assumed, and also serves as a natural maximum for the oxygen concentration the blanket may need to endure.

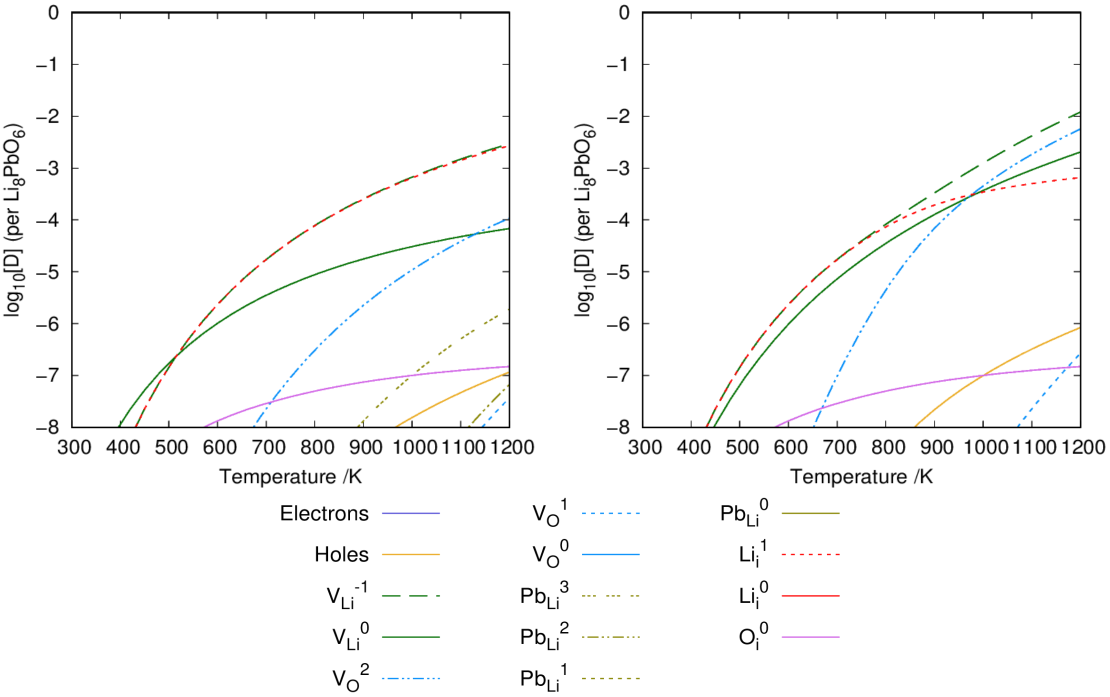

Figure 6.13: Defect chemistry of Li_8PbO_6 under Li_2O-rich conditions ignoring and incorporating temperature contributions to the energies of the reference states respectively. OPP = 0.2 atm.

Under Li_2O-rich conditions (Figure 6.13), charged lithium vacancy defects are the dominant type of defect across the entire temperature range, which is significant as the lithium vacancy may act as a trapping site for tritium [89]. The method of charge compensation, however, is shown to be different when including temperatures effects for the reference states. If temperature effects are neglected, charge compensation is provided by oppositely-charged lithium interstitials for the entire temperature range. The Li_i^1 is also predicted to provide charge balance at low temperatures (<980 K) when the reference states are modified to include temperature. By contrast, for high temperatures (>980 K), incorporating temperature into the energies for reference states changes the charge compensation mechanism to the V_O^2 defect. Further, the introduction of temperature effects also reduces the overall concentration of lead-containing defects at high temperature. Overall, the modification of the defect chemistry due to incorporating temperature into the reference states demonstrates the importance of including these for study of materials operating at high temperatures.

6.4.4 Oxygen Partial Pressure

Next, the dependence of the defect chemistry on the oxygen partial pressure at the Li_2O saturation limit in Li_8PbO_6 at high temperatures using both procedures is examined in Figure 6.14.

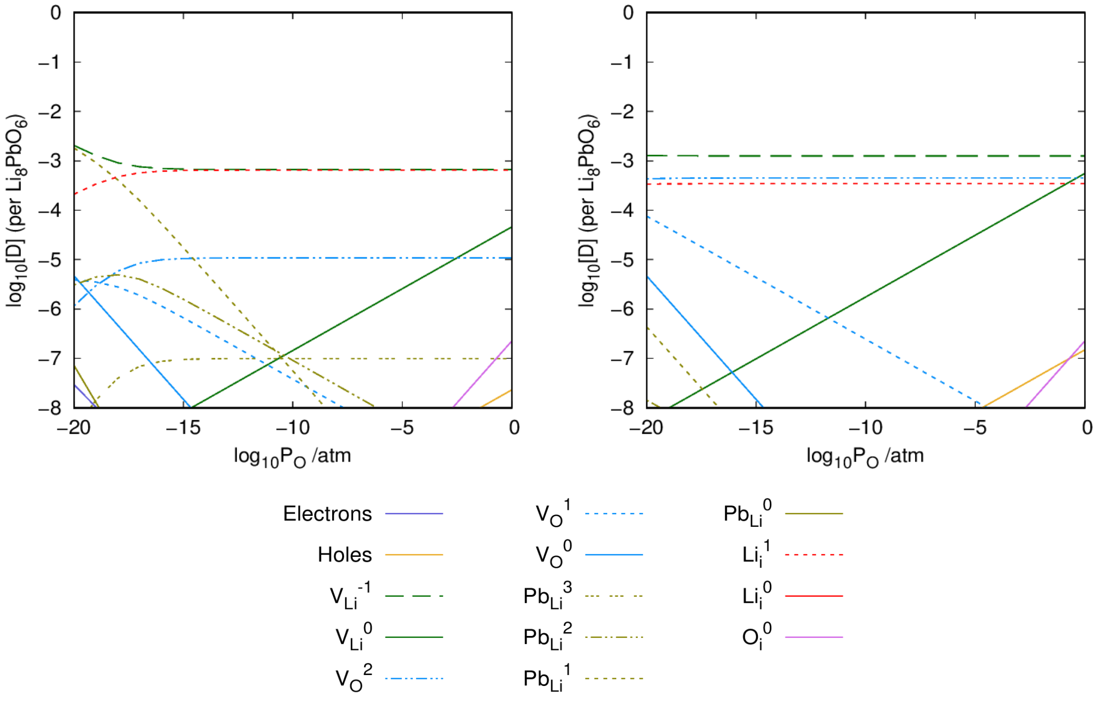

Figure 6.14: Oxygen partial pressure dependence of intrinsic defects in Li_8PbO_6 under Li-rich conditions ignoring and incorporating temperature contributions to the energies of the reference states respectively. The temperature is fixed to 1000 K.

Figure 6.14 further highlights the differences that arise due to incorporating temperature effects in a more complete manner. When temperature contributions to the reference states are ignored the lithium vacancy defect is expected to be dominant across the partial pressure range. At low oxygen partial pressures charge compensation is provided by the $\mathrm{Pb}_{\mathrm{Li}}^{1}$ defect. At higher partial pressures there is a transition to a point where the Li_{i}^{1} defect provides charge compensation. This is a marked contrast to what is predicted if the temperature contributions are added. This model predicts that the $\mathrm{V}_{\mathrm{Li}}^{-1}$ defect is dominant with charge compensation coming from a combination of the $\mathrm{V}_{\mathrm{O}}^{2}$ and Li_{i}^{1} defects.

6.4.5 Dominant defects in stable regions

In this section, the defect chemistry of $\mathrm{Li_8PbO_6}$ away from the saturation limit for $\mathrm{Li_2O}$ is explored, by plotting the dominant defects or compounds as a function of the rich/poor fraction, f (see equation 3.40) and the temperature in Figure 6.15.

Throughout this subsection, only the defect chemistry with temperature effects introduced into the reference states is presented.

As would be expected from Figures 6.11 and 6.12, the only region where $\mathrm{Li_8PbO_6}$ is predicted to dominate over competing phases is close to the $\mathrm{Li_2O}$ saturation limit. At the $\mathrm{PbO_2}$ limit, the $\mathrm{Li_2PbO_3}$ phase is the most stable, particularly for higher temperatures. The narrow width of the $\mathrm{Li_8PbO_6}$ region may place a limit on the operational lifetime of the material when employed as a ceramic breeding material, as the quantity of Li that can undergo transmutation before the material undergoes a phase change is quite low.

Inspecting the dominant defects in the $\mathrm{Li_8PbO_6}$ phase, it is clear that the charged lithium vacancy defect dominates almost the entire defect profile, with a small region where oxygen interstitial defects become the most common defect at room temperature. The primary charge-compensation mechanism is the Li_{i}^{1} lithium interstitial, followed by the $\mathrm{V}_{\mathrm{O}}^{2}$ vacancy at high temperatures. Due to the $\mathrm{Li_8PbO_6}$ phase only being stable close to the $\mathrm{Li_2O}$ saturation limit, the defect chemistry of

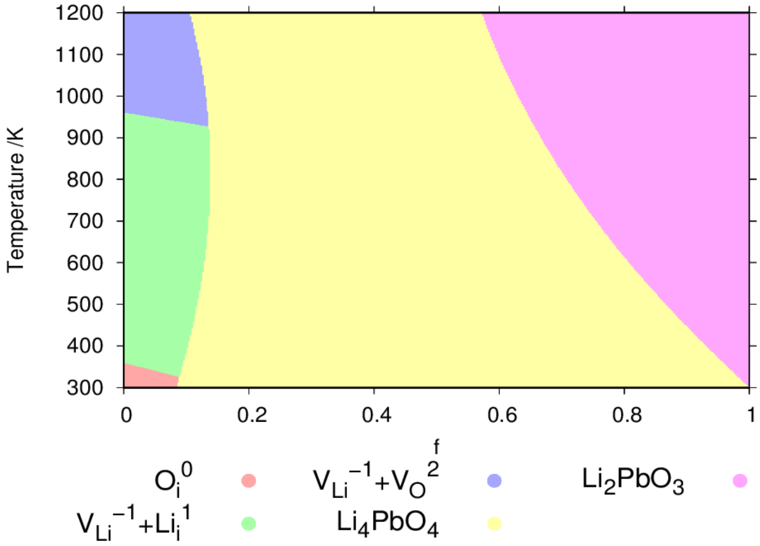

Figure 6.15: Phase diagram illustrating stable regions for the Li-Pb-O ternary system as a function of stoichiometry and temperature. 0 represents the Li_2O-rich limit and 1 represents that for PbO_2. The yellow and pink regions represent areas where a competing Li-Pb-O ternary compound becomes the dominating phase. Regions occupied by Li_8PbO_6 are shown as the dominant defect predicted in the respective region. OPP = 0.2 atm.

Li_8PbO_6 is essentially very similar to that of the Li_2O-rich material (Figures 6.13 and 6.14).

As illustrated in Figure 6.16, regardless of choice of oxygen partial pressure in the atmosphere and temperature, the V_{Li}^{-1} defect is predicted to be the dominant defect for nearly the entire phase space, with the primary charge-compensation mechanism being the Li_i^1 interstitial at low-moderate temperatures and V_O^2 at high temperatures above roughly 960 K, where the change in charge-compensation mechanism for the V_{Li}^{-1} defect to V_O^2 acts almost completely independently of oxygen partial pressure.

At low oxygen partial pressures and high temperatures the concentration of V_O defects increases. Initially charge-compensating for the lithium vacancies in the form of the V_O^2 defect in oxygen-rich conditions, a transition where the V_O^1 defect becomes the most common defect as temperature increases at low oxygen partial

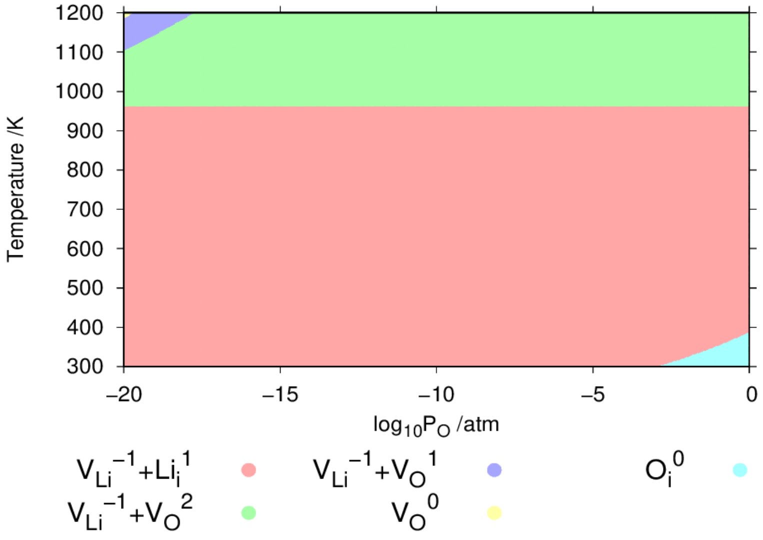

Figure 6.16: Phase diagram illustrating regions for predictions of the dominant defect in the temperature-oxygen partial pressure space under Li_2O-rich conditions.

pressure before finally in the extreme case, a small region appears at concentrations of 10^{-20} atm and at 1200 K where V_O^0 begins to dominate.

6.4.6 Li burn-up

The defect chemistry is expected to change throughout the operating lifetime of the ceramic as lithium is progressively used up due to transmutation. Figures 6.17, 6.18 and 6.19 show the defect chemistry of Li_8PbO_6 as a function of the Li:Pb ratio in the system at 800 K, 1000 K and 1200 K respectively. In each case, the x-axis extends to point at which the chemical potential reaches the PbO_2 saturation point. This measure is analogous to presented the changing defect chemistry throughout the temporal lifetime of Li_8PbO_6.

At 800 K (Figure 6.17), the limit at which PbO_2 saturation limit is reached is predicted to be at a ratio of Li/Pb of 7.991(5), meaning there is very little room for lithium burn-up before a transition to an alternative ternary phase at this temperature. Examining the defect chemistry, as expected, the lithium vacancy is the dominant defect and becomes more pronounced as lithium is depleted from

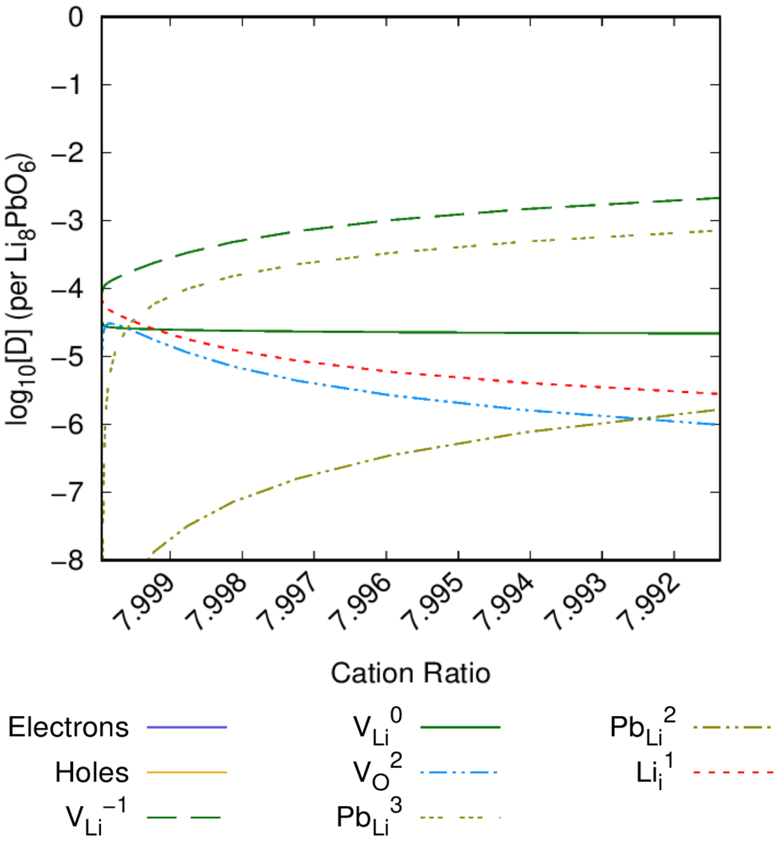

Figure 6.17: Intrinsic defect concentration in Li_8PbO_6 as a function of lithium burn-up. T = 800 K, OPP = 0.2 atm.

the system, with Li_i^1 interstitials depleting proportionally with the increase in V_{Li}^{-1}. Lead begins to occupy the newly vacant V_{Li}^{-1} sites as the charged Pb_{Li}^{3} substitutional. All charge states of Pb_{Li} as expected increase as the proportion of overall lead in the system increases. Interestingly, the number of oxygen vacancy V_{O}^{2} defects begins to drop as Li/Pb decreases, due to the overall increase in stoichiometric concentration of oxygen as lithium drops.

At 1000 K (Figure 6.18), the minimum possible ratio of Li to Pb is predicted to be 7.937, the limit at which a precipitate begins to form. The overall defect chemistry is broadly very similar to the 800 K case, although the primary charge-compensation mechanism is instead the V_{O}^{2} vacancy defect at high Li/Pb ratio, rather than Pb_{Li}^{3}.

At 1200 K (Figure 6.19), PbO_2 will begin to form a precipitate at a much

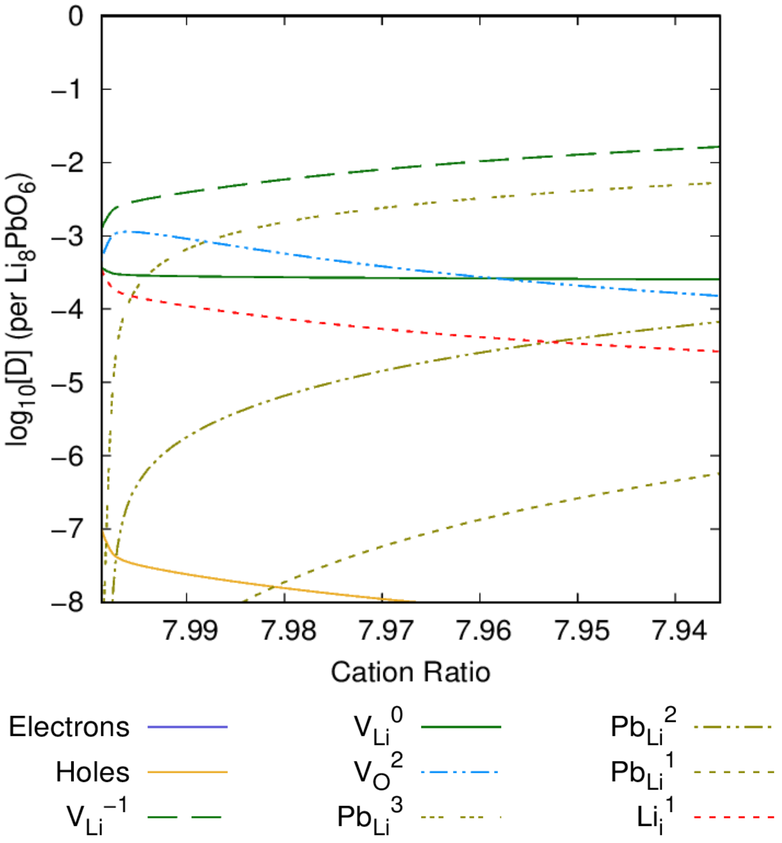

Figure 6.18: Intrinsic defect concentration in Li_8PbO_6 as a function of lithium burn-up. T = 1000 K, OPP = 0.2 atm.

lower proportion of Li/Pb, at a ratio of 7.75. The concentration of lithium vacancy V^{1}_{Li} is much greater at higher temperatures. The charge-compensation mechanism for V^{1}_{Li} is similar to that at 1000 K, although the ratio of Li/Pb at which the compensation mechanism changes from V^{2}_{O} to Pb^{3}_{Li} is markedly lower (7.88 Li/Pb). At 1200 K, the overall concentration of the non-charge-compensating defects is much higher compared to lower temperatures, as is to be expected. Interestingly, the interdependence of Li^{1}_{i} interstitials and V^{0}_{Li} charge-neutral vacancies on one another are relatively insensitive to temperature.

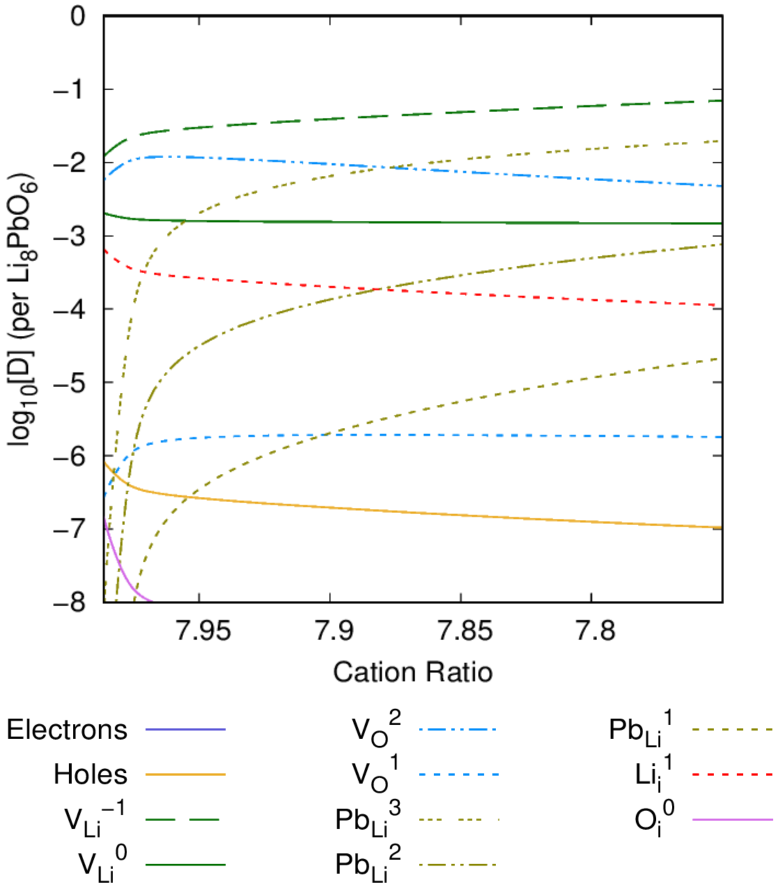

Figure 6.19: Intrinsic defect concentration in Li_8PbO_6 as a function of lithium burn-up. T = 1200 K, OPP = 0.2 atm.

6.5 Conclusion

The phase stability and intrinsic defect chemistry of Li_8PbO_6 was explored in this Chapter. Importantly, the appropriateness of accounting for vibrational contributions in the phase stability and the defect chemistry by incorporating temperature contributions into the chemical potential reference states is discussed. For high temperatures, it is shown that including these temperature effects does have a significant influence on the defect chemistry. This indicates that when considering the defect chemistry of materials at high temperatures, it is inappropriate to neglect the temperature induced changes to the reservoirs as is widely done in the literature.

Charged lithium vacancy defects appear to dominate the intrinsic defect chemistry for Li_8PbO_6 under almost every condition measured. Incorporating temperature effects appears to predominantly impact the high temperature charge compensation mechanism for V_{Li}^{-1}. This may have a significant impact on the tritium migration mechanism through the crystal lattice, predominantly due to the higher predicted concentrations of oxygen vacancy defects at reactor operating temperatures. Most importantly, Li_8PbO_6 has been predicted to only have a stable phase close to the Li_2O saturation limit. The low threshold of lithium loss for a phase change to Li_4PbO_4 to occur indicates Li_8PbO_6 may have a short operational lifetime within a reactor, due to the inherent burnup of lithium.

Chapter 7

Mechanisms for tritium migration

The contents of this chapter have been submitted as an article for peer review as: A. W. Davies, S. T. Murphy, Tritium accommodation and diffusion in Li_8PbO_6 from first-principle simulations, J. Phys. Chem. C. (in peer review)

7.1 Introduction

Although a prediction for the TBR of Li_8PbO_6 has been made, the mechanisms for tritium release are entirely unknown for this material. After tritium has successfully formed and been accommodated into the crystal, the tritium must diffuse through the bulk material until it reaches a grain boundary where it can then be transported to the surface and extracted by a helium purge gas. The rate limiting step for tritium recovery in the entire process of diffusion to the surface of the pebble is the migration of the tritium through the bulk until reaching a grain boundary.

Atomistic simulation studies of migration pathways of tritium in other ceramic breeding materials such as Li_2TiO_3 have utilised a point defect model in order to predict defect migration barriers [89]. As observed by other studies, the amount of doping of lithium into the ceramic likely determines the mode of tritium transport. If there is a lithium excess, tritium is expected to migrate almost exclusively as an interstitial and bond with a neighbouring oxygen ion to form a hydroxyl. If there is a depletion of lithium (which is expected to occur as the material ages), tritium is more likely to form a $\{T_i^1 : V_{Li}^{-1}\}$ defect complex, becoming bound to a lithium vacancy defect. In this Chapter, DFT is used to examine the accommodation of tritium according to typical reactor conditions, followed by characterisation of the possible and likely migration pathways for tritium in the bulk crystal with and without the presence of lithium vacancy defects.

7.2 Methodology

For this chapter, the computational procedure and parameterisation follows that of Chapter 6. The behaviour of tritium in DFT simulations is analogous to hydrogen, thus hydrogen ions in the DFT simulations performed throughout this chapter are treated as tritium ions. The chemical potential of tritium is taken as half the DFT lattice energy of the H_2 dimer. Simulating the H_2 dimer utilised an energy cut-off of 650 eV. The electronic convergence criteria was taken as 10^{-8} eV, and 0.01 eV $Å^{-1}$ as the maximum force per atom to achieve structural convergence. A single H_2 dimer is placed in the centre of a 20 Å × 20 Å × 20 Å unit cell, with a single k-point at Γ.

Activation energy barriers for defect migration were predicted using the climbing Nudged Elastic Band method (cNEB) [167, 165]. NEB is a method for finding minimum energy paths by following saddle points between reactants. A series of images of the defect along the migration pathway is generated and optimised, and a tangential spring force applied to each image to find the optimal pathway between images. A small spring force is applied between images ensure they are as equally spaced as possible. cNEB differentiates by instead pushing the image with the highest energy upwards towards the saddle point by inverting the tangential force at this image such that it tries to maximise its energy along the pathway. As the maximised image does not feel the same spring force between neighbouring images, the images are no longer evenly spaced like in regular NEB.

For each migration pathway considered in this work, 6 images were generated between the initial and final sites. The spring constant used was kept as the default -5 eV/$\AA^2$. As the images are placed at sub-optimal positions for ionic convergence to be reached, the requirement for structural convergence is modified so that instead of requiring the total forces on all atoms to fall below 0.01 eV Å^{-1}, this is raised to 0.08 eV Å^{-1} to ensure sufficient convergence can be achieved.

7.3 Results and Discussion

7.3.1 Tritium Defect Formation Energies

Four symmetrically distinct interstitial sites for tritium were found in the vicinity of the Li1 site (labelled *a* - *d* in Figure 7.1) by performing a geometry optimisation of a charged tritium ion at the midpoint of the connecting Li-O bonds and allowing the tritium to form a hydroxyl with a neighbouring oxygen ion. In Chapter 4, the 6 Li-O bonds surrounding the Li2 site were examined, and showed that irrespective of starting point, all initial arrangements relaxed to give the *a* configuration. Site *a* occupies the mixed Li-Pb layer, wherein there are two parallel planes within the same Li-Pb layer stacked on top of one another. The stacking behaviour is shown in Figure 7.1. The planes occupied by *d* also stack on top of one another, but unlike occupation in the mixed Li-Pb layer, this is due to the stacking of the pure Li layers in Li_8PbO_6. The *b* and *c* sites are found within the pure O layer. The arrangement of the interstitial sites across each layer are shown in Figures 7.2 - 7.4.

For NEB calculations, the inclusion of a finite size correction for calculation of diffusion activation energies is not required, thus is not included in the NEB calculations.

Introduction of T into a V_{Li} defect by repeating the same method of allowing T to relax from the midpoint between the lithium vacancy and the neighbouring oxygen ions to form a $\{T_i^{+1}{:}V_{Li}^{-1}\}^{\times}$ defect cluster, as observed in Li_2TiO_3 [122], causes the hydroxyl to point almost directly towards the lithium vacancy. Surrounding the

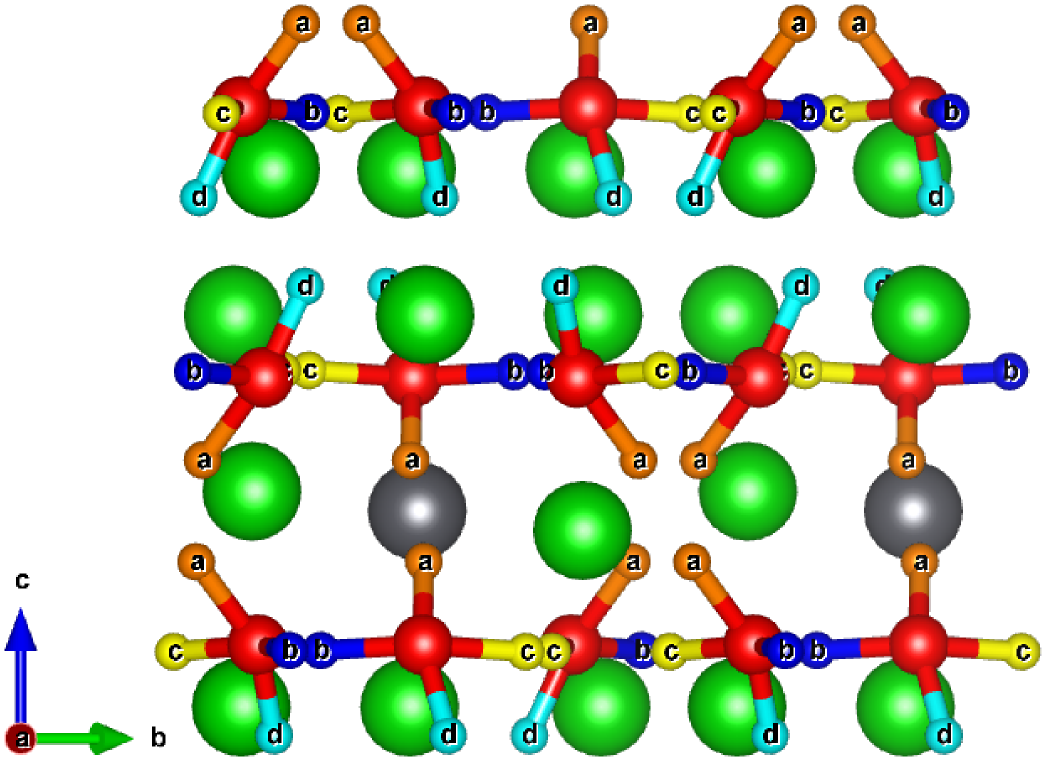

Figure 7.1: Location of tritium interstitial sites in Li_8PbO_6. Orange, blue, yellow, and teal ions represent tritium interstitial sites a - d respectively.

V_{Li2} defect, there are now 2 symmetrically distinct sites for the tritium to occupy. In V_{Li1}, there are four unique sites. For clarity, the four symmetrically distinct sites found in V_{Li1} corresponding to interstitial sites a-d shall be labelled a'-d'. The two new sites found surrounding V_{Li2} shall be labelled with e' and f'. Illustrations of the $\{T_i^{+1}$:$V_{Li}^{-1}\}$ defect cluster at the Li1 and Li2 sites are shown in Figures 7.5-7.6.

Formation energies for all tritium-accommodating defects are presented in Table 7.1. A comparison is drawn (as was performed for the defect chemistry in Chapter 6) on the incorporation of temperature effects into the chemical potentials for the constituent compounds Li_2O, PbO_2 as well as Li_8PbO_6 used in calculating the defect formation energies.

In the interstitial case, regardless of charge state tritium prefers to occupy the

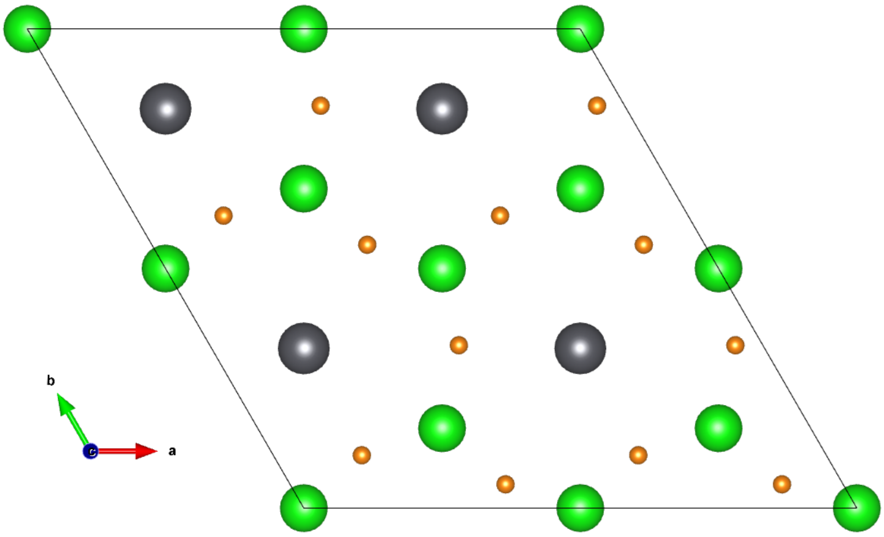

Figure 7.2: Mixed Li-Pb plane and occupation of T at interstitial site a, represented by orange-coloured ions.

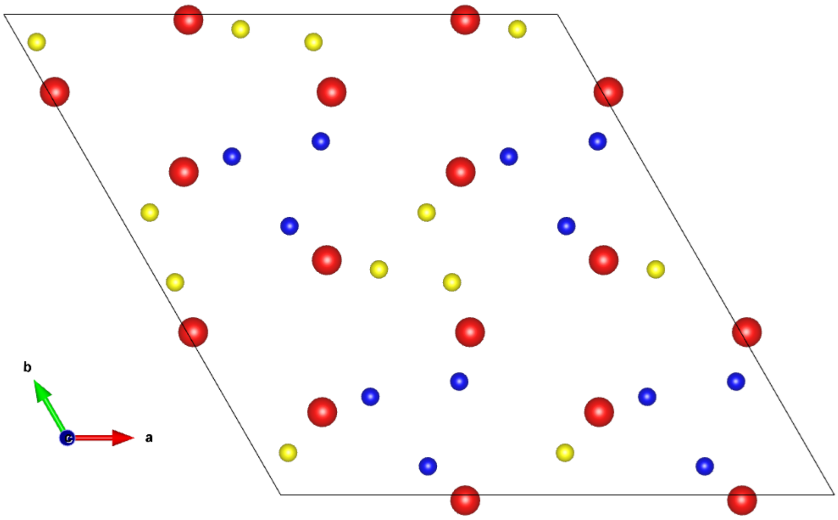

Figure 7.3: Pure O plane and occupation of T at interstitial sites b and c, represented by blue and yellow-coloured ions respectively.

mixed Li-Pb plane at site a, and least prefers site d in between the pure Li planes with a relative formation energy 0.49 eV greater than site a. The energy for the two sites in the oxygen plane (b and c) are predicted to have very similar energies. An

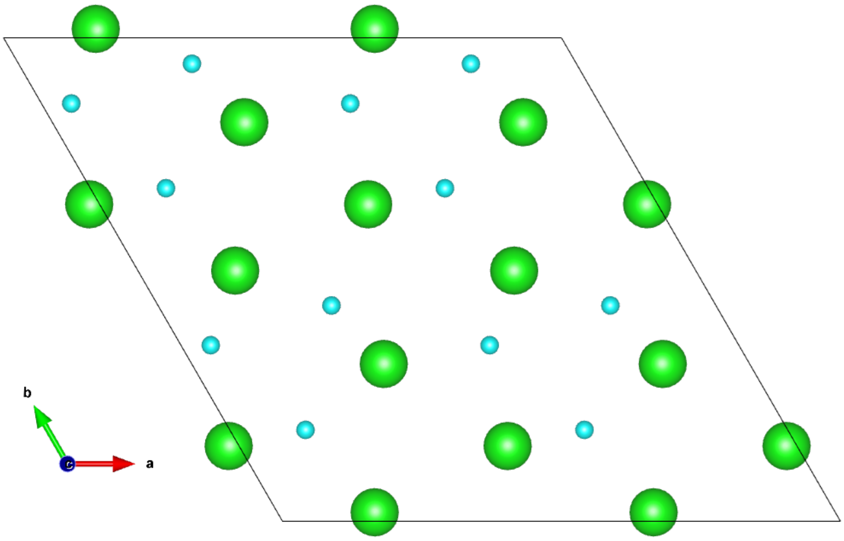

Figure 7.4: Pure Li plane and occupation of T at interstitial site *d*, represented by teal-coloured ions.

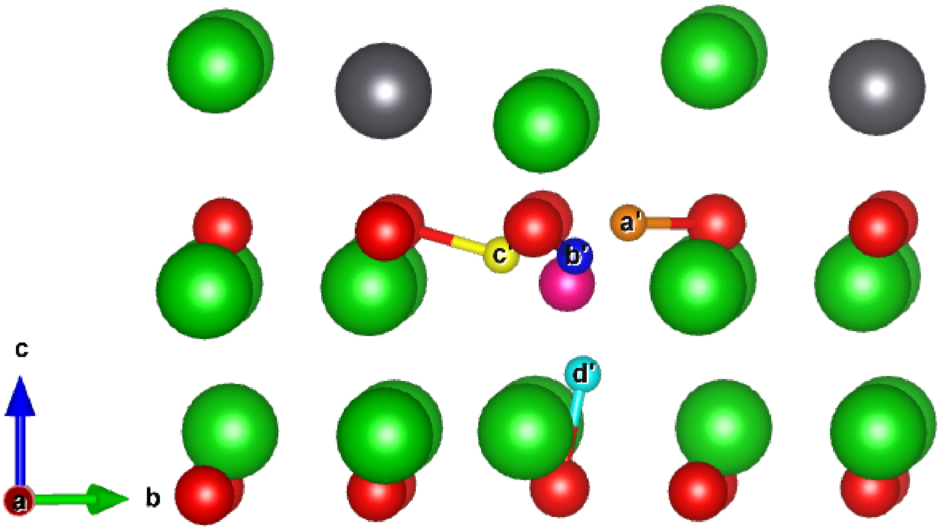

Figure 7.5: Possible tritium hydroxyl sites within the V_{Li1} defect. Orange, blue, yellow and teal ions represent the a' - d' sites respectively. The pink ion represents the position of the lithium vacancy defect.

illustration of the formation energies for the charge states of the tritium interstitial defects relative to the Fermi level within the band gap is given in Figure 7.8, and

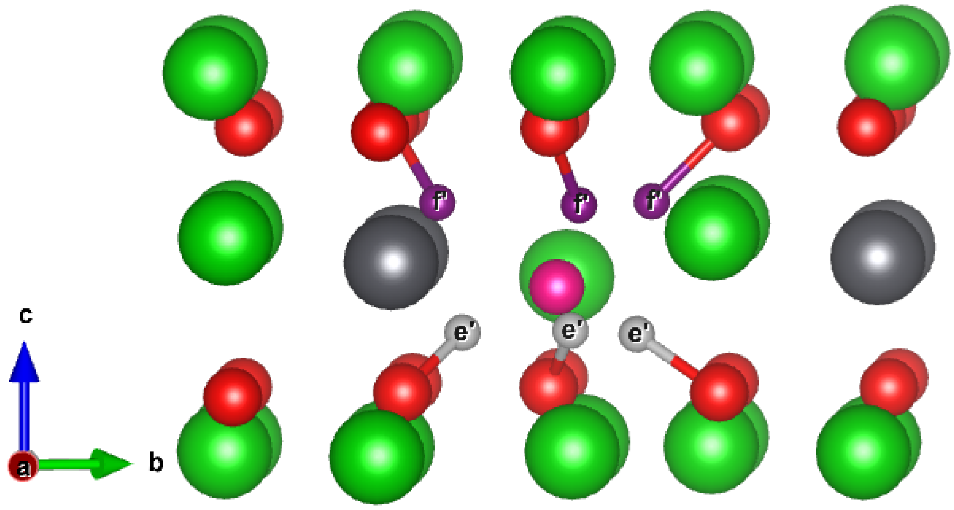

Figure 7.6: Possible tritium hydroxyl sites within the V_{Li2} defect. Dark red and purple ions represent the e' - f' sites respectively.

demonstrates the preference for tritium to occupy the +1 charge state, rather than the charge-neutral state.

For the $\{T{:}V_{Li}\}$ defect clusters, the overall charge state of the cluster ultimately determines the preferred occupation of the defect in the material. In the charge-neutral case, the c' site is the preferred occupation state for the cluster situated on the Li1 site and for the Li2 site, e' is preferred over f'. When a +1 charge is introduced the preference for the cluster around Li1 site changes to the a' configuration, which is the lowest energy configuration overall. Although, as the majority of tritium formed is expected to form as a T^{+1} defect in the charge-neutral $\{T_i^{+1}{:}V_{Li}^{-1}\}^0$ cluster due to the transmutation of lithium ions in the crystal, the overall population of the $\{T_i{:}V_{Li}\}^{+1}$ defect is predicted to be low [19], as is evident from Figure 7.8.

The discrepancy in formation energies predicted between E_f and $E_f^{inc}(T)$ is effectively negligible, with a roughly 0.02 eV difference in the substitutional cases, and in the interstitial case, there is a 0.19 eV discrepancy, much smaller than what was previously seen in the intrinsic case [214]. However, this is to be expected due

Table 7.1: Formation energies of tritium accommodating defects in Li_8PbO_6 under Li_2O-rich conditions at the VBM. T = 1000 K, OPP = 0.2 atm, [T] = 10^{-5} pfu ([T] represents the concentration of tritium).

	Defect	Site	E_f (eV)	E_f^{inc}(T) (eV)
1	T_i^0	a	2.85	3.04
2	T_i^0	b	3.11	3.30
3	T_i^0	c	3.05	3.24
4	T_i^0	d	3.34	3.53
5	T_i^{+1}	a	-0.30	-0.11
6	T_i^{+1}	b	0.06	0.25
7	T_i^{+1}	c	-0.07	0.12
8	T_i^{+1}	d	0.10	0.29
9	T_{Li1}^0	a'	1.27	1.25
10	T_{Li1}^0	b'	1.17	1.15
11	T_{Li1}^0	c'	1.12	1.09
12	T_{Li1}^0	d'	1.43	1.40
13	T_{Li2}^0	e'	1.46	1.44
14	T_{Li2}^0	f'	1.57	1.55
15	T_{Li1}^{+1}	a'	0.15	0.13
16	T_{Li1}^{+1}	b'	0.22	0.19
17	T_{Li1}^{+1}	c'	0.31	0.28
18	T_{Li1}^{+1}	d'	0.43	0.41
19	T_{Li2}^{+1}	e'	0.49	0.47
20	T_{Li2}^{+1}	f'	0.60	0.58

to the chemical potentials of Li and Pb derived from Gibbs energies of Li_2O and PbO_2 having no impact on the chemical potential of hydrogen used in DefAP, as

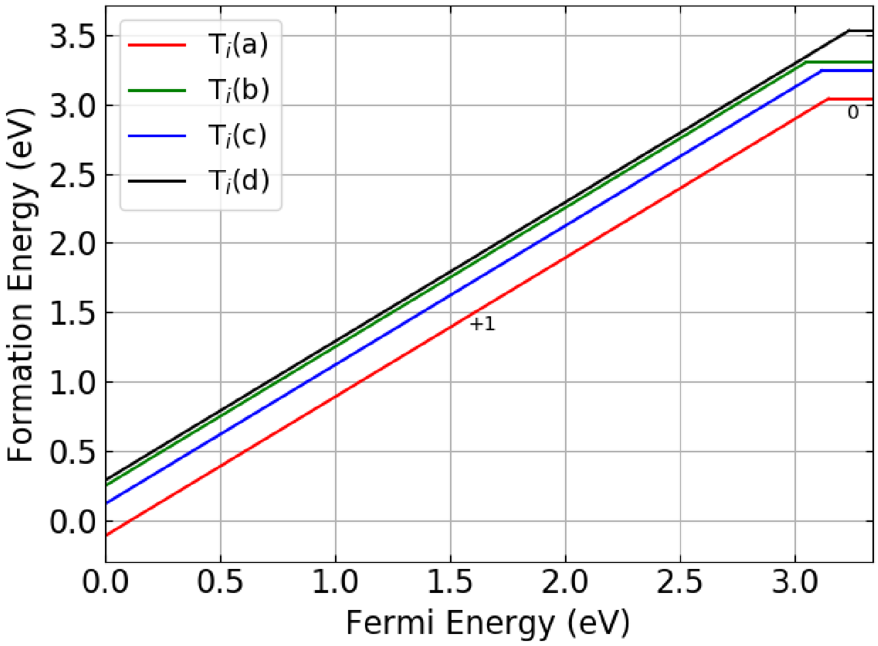

Figure 7.7: Defect formation energies for the tritium interstitial in Li_8PbO_6 as a function of the Fermi energy.

well as the fixing of the hydrogen chemical potential to half the DFT lattice energy of a H_2 dimer as opposed to using the Gibbs energy.

7.3.2 Tritium accommodation

Similar to the approach adopted in Chapter 6, the DefAP [217] code is used to predict defect concentrations under different environmental conditions. Once more, a comparison is drawn between inclusion of temperature effects into the chemical potentials used in the calculation of defect formation energies in Figure 7.9. In construction of these plots the tritium concentration is set to 10^{-5} per formula unit.

Li_8PbO_6 is expected to be stable under Li_2O-rich conditions according to the Li_2O-PbO_2 phase diagram described in Chapter 6 [214], and thus only tritium accommodation under these conditions are considered here. In Li_8PbO_6, tritium is accommodated primarily as a substitutional defect on the V_{Li} vacancy site as

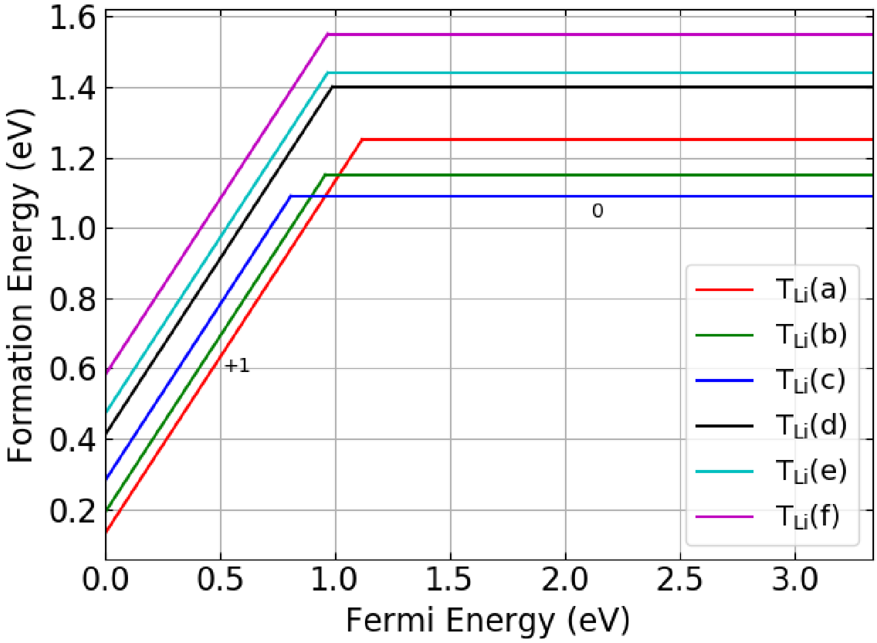

Figure 7.8: Defect formation energies for the $\{T{:}V_{Li}\}$ defect cluster in Li_8PbO_6 as a function of the Fermi energy.

a charge-neutral $\{T_i^{+1}{:}V_{Li}^{-1}\}$ cluster (Figure 7.9). For moderate temperatures in the range of 600-900 K, the charged interstitial becomes the dominant tritium-accommodating defect in the crystal, although when chemical potentials for Li and Pb are derived from lattice energies of the constituent compounds rather than incorporating temperature effects into the reference states, the interstitial remains the dominant form of accommodation for tritium for temperatures above 600 K.

Similar to the previous chapter examining the intrinsic chemistry of Li_8PbO_6 [214], the defect chemistry during Li burn-up has been predicted with the inclusion of tritium in Figure 7.10 under various temperatures. As seen for all temperatures in Figure 7.10, tritium will be trapped almost exclusively in the lithium vacancy throughout the entire lifetime of the blanket, particularly for high temperatures.

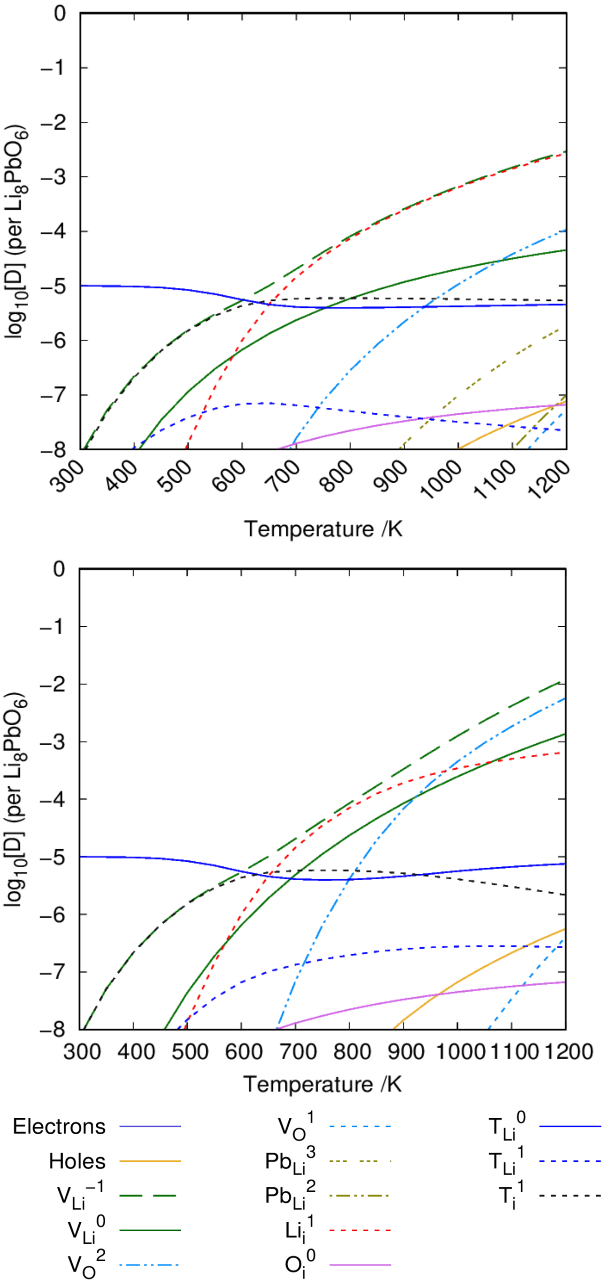

Figure 7.9: Defect chemistry of tritium-accommodated Li_8PbO_6 under Li_2O-rich conditions. The top figure uses the lattice energies of constituent compounds to derive the chemical potentials of Li and Pb, whereas the bottom figure incorporates temperature contributions to the energies of the reference states. OPP = 0.2 atm. $[T] = 10^{-5}$ per formula unit. DefAP fits the chemical potential for T.

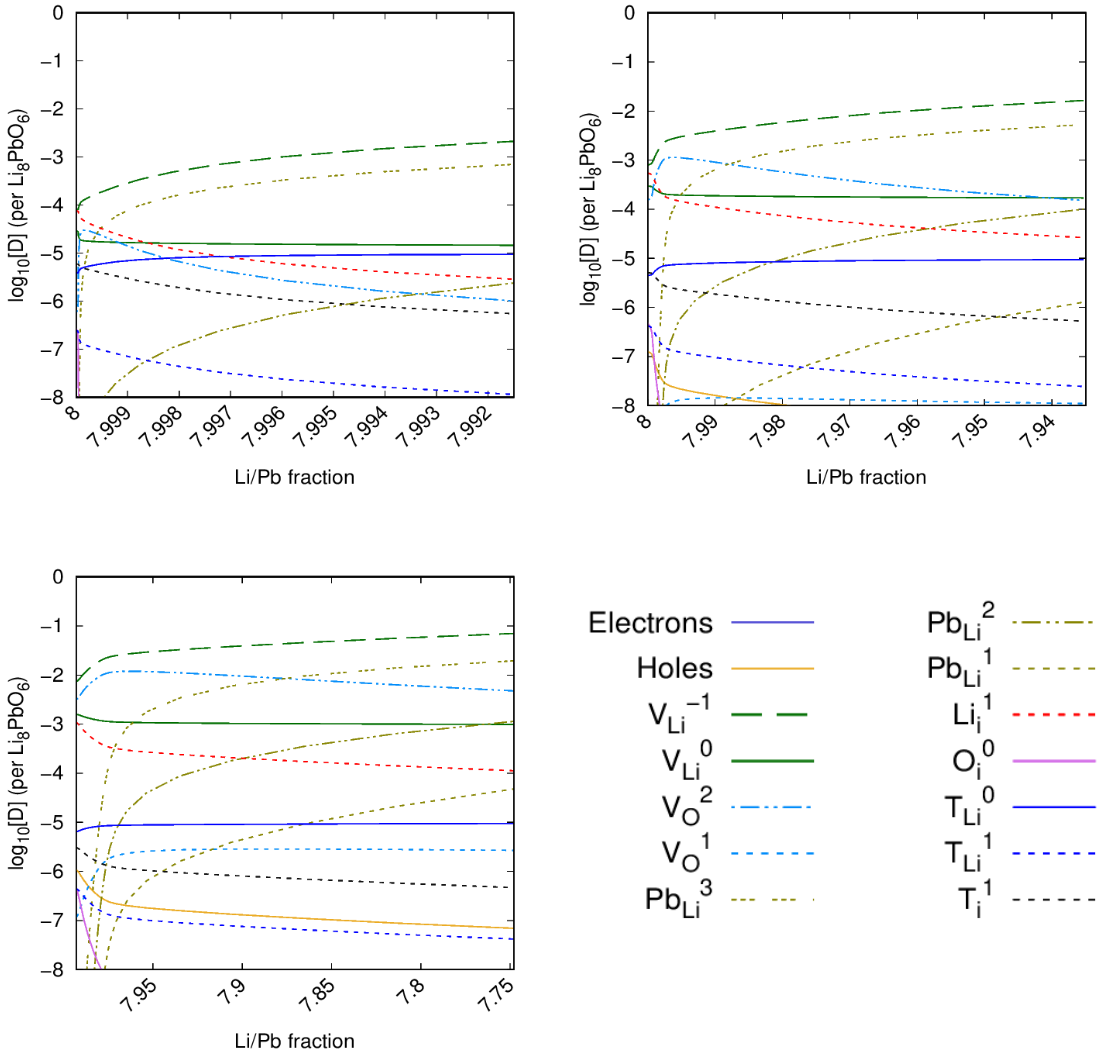

Figure 7.10: Tritium solubility in Li_8PbO_6 as a function of lithium burn-up (Li:Pb ratio). OPP = 0.2 atm. Top left: T = 800 K. Top right: T = 1000 K. Bottom left: T = 1200 K. [T] = 10^{-5} per formula unit.

7.3.3 V_{Li} migration

The lithium vacancy is predicted to be the dominant intrinsic defect in Li_8PbO_6, therefore, it is important to understand how it behaves in the crystal as well as its interaction with tritium.

The neighbouring cation environments for Li1 and Li2 are illustrated in Figure 7.11. Surrounding the Li1 site are 12 neighbouring cations, 11 of which are other

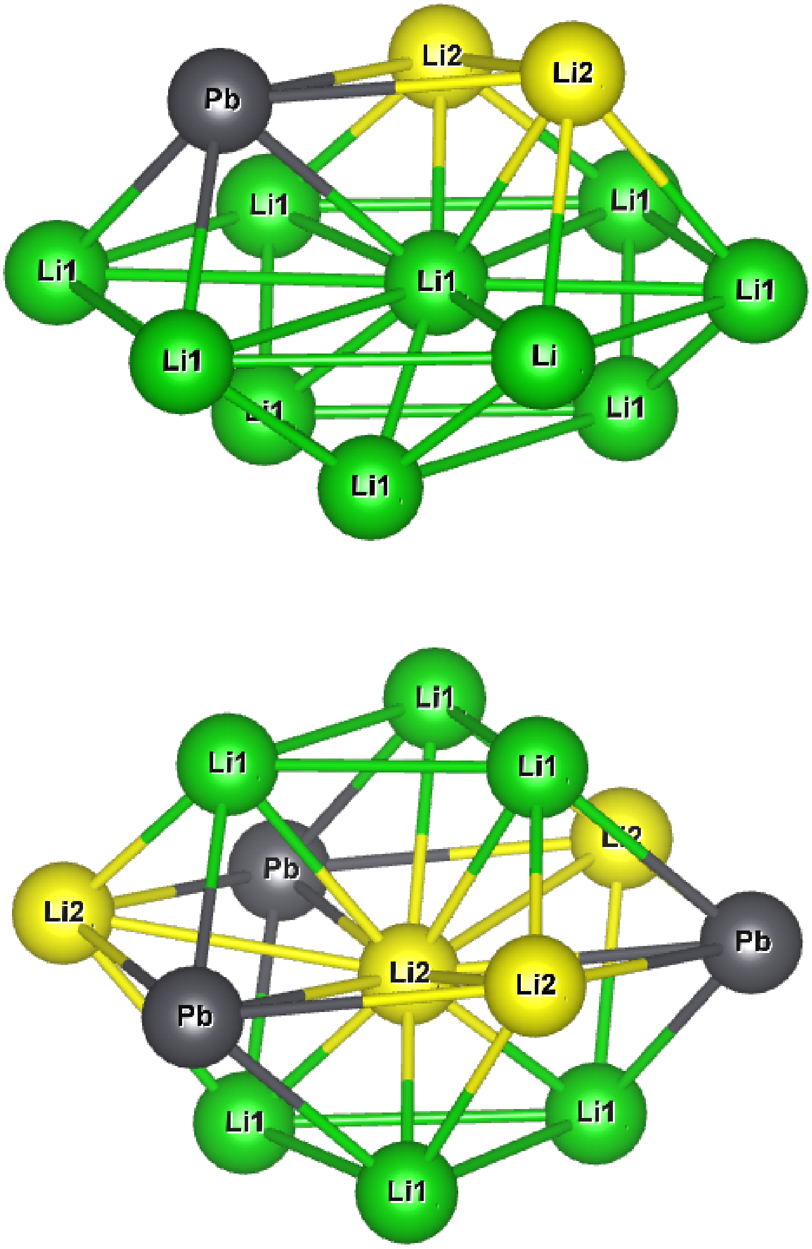

Figure 7.11: Neighbouring cation environment for the Li1 and Li2 lithium sites.

lithium ions: 6 in the same pure lithium plane, 3 in the neighbouring lithium plane and 2 in the mixed Li-Pb plane. Although due to symmetry, there are only 6 distinct nearest neighbour pathways for the lithium vacancy to migrate: 3 within the same pure-Li plane; 1 into the neighbouring pure-Li plane; and 2 into the mixed Li-Pb plane. Li2 also has 12 neighbouring cations, although 3 of these are lead ions in the same mixed Li-Pb plane, resulting in 9 neighbouring lithium ions. Of which, there are only 3 symmetrically distinct pathways: 1 within the same mixed Li-Pb plane, and 1 in each of the neighbouring pure-Li planes above and below. Activation energies for these processes are presented in Table 7.2.

Table 7.2: Activation energies for the migration of V_{Li}^{-1} lithium vacancy defects.

Plane	Pathway	d (Å)	Forward (eV)	Reverse (eV)
Above Li-Pb	$V_{Li1} \rightarrow V_{Li2}$	2.784	0.49	0.14
	$V_{Li1} \rightarrow V_{Li2}$	2.486	0.44	0.10
Same Li	$V_{Li1} \rightarrow V_{Li1}$	2.932	0.52	0.52
	$V_{Li1} \rightarrow V_{Li1}$	3.499	1.61	1.61
	$V_{Li1} \rightarrow V_{Li1}$	3.267	0.84	0.84
Below Li	$V_{Li1} \rightarrow V_{Li1}$	2.374	0.33	0.33
Above Li	$V_{Li2} \rightarrow V_{Li1}$	2.784	0.14	0.49
Same Li-Pb	$V_{Li2} \rightarrow V_{Li2}$	3.278	0.72	0.72
Below Li	$V_{Li2} \rightarrow V_{Li1}$	2.486	0.10	0.44

It was found regardless of which charge state was chosen for the V_{Li} defect, there is virtually no difference in activation energy, with the greatest difference in activation energies occurring in the transition between the V_{Li2} and V_{Li1} states with the charge-neutral state possessing an activation energy 11 meV greater than for the charged defect migration. Due to this, we assume the barriers for diffusion of both charge states for the V_{Li} defect to be the same.

The lowest migration barriers found are those for V_{Li2} migrating to the V_{Li1} site, with barriers of 0.10 and 0.14 eV, showing a strong desire for the vacancies to migrate towards the pure lithium plane, rather than occupy the mixed Li-Pb layer.

This can be explained by the lower formation energy possessed by V_{Li1} compared to the V_{Li2} defect [168] caused by the lower number of Li-O bonds the Li^{+1} ion has to break to remove from the Li1 site.

Once the lithium vacancy is in a pure-Li plane, the optimal pathway for it to migrate is to the neighbouring pure-Li plane with an activation barrier of 0.33 eV. The optimal migration pathway for the lithium vacancy defect is to hop between and migrate through the pure-Li layers in the xy-plane until a grain boundary is reached, rather than migrate to a mixed Li-Pb plane, which has migration barriers of 0.44 and 0.49 eV. An illustration of the lithium migration is shown in Figure 7.12. An illustration of the reaction pathway is also shown in Figure 7.13.

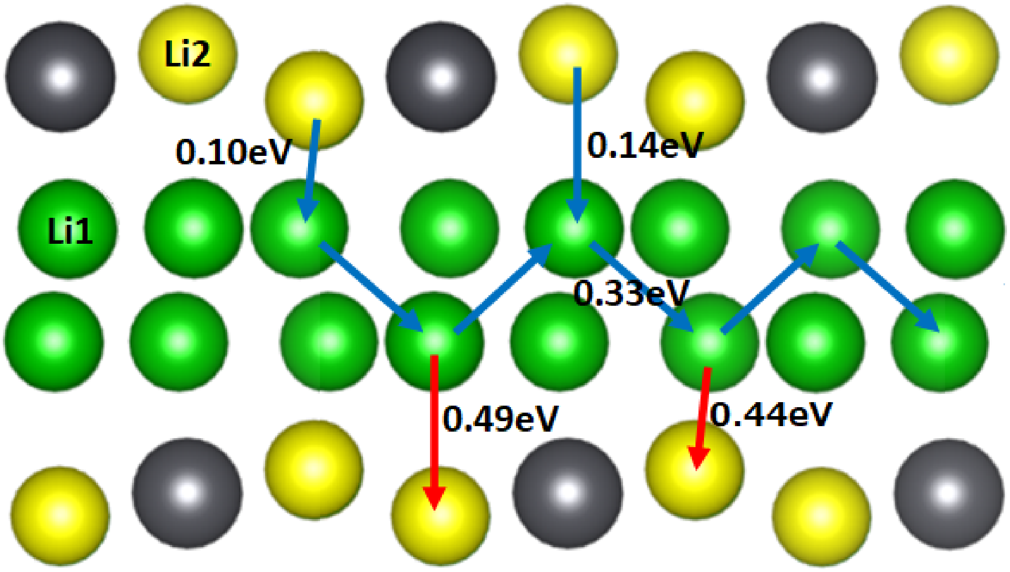

Figure 7.12: Optimal migration pathway for escape of the V_{Li}^{-1} defect. Green and yellow ions are the Li1 and Li2 sites respectively. Oxygen ions are not shown to enable easier visualisation.

Therefore, the overall barrier for migration in the xy-plane is 0.33 eV through the pure-Li plane, and diffusion in the z-direction is 0.44 eV.

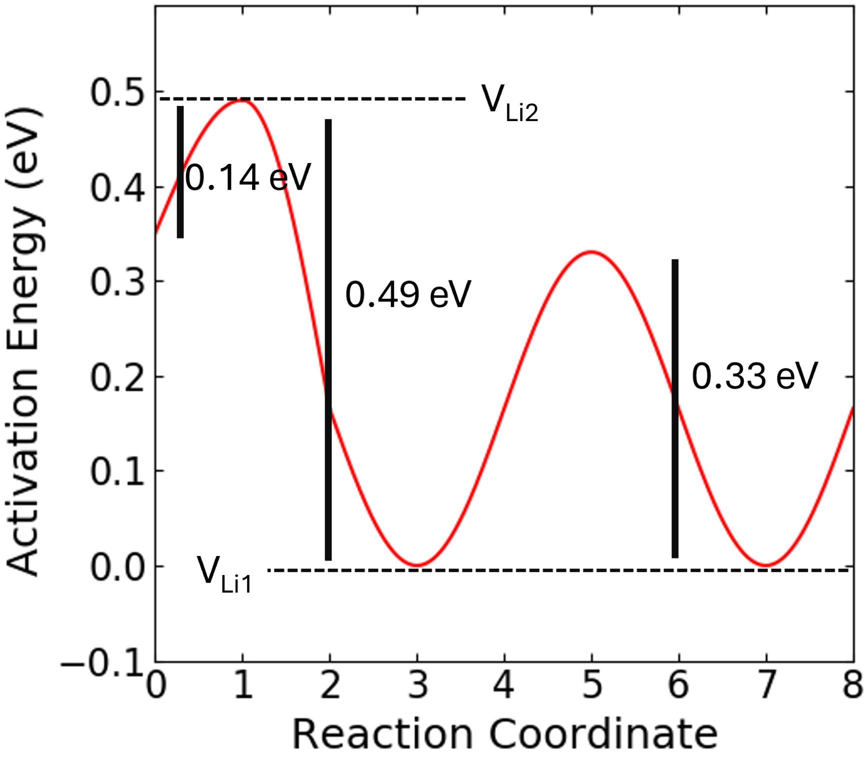

Figure 7.13: Reaction pathway for escape of the V_{Li}^{-1} defect.

7.3.4 T interstitial migration

As illustrated in Figures 7.1 - 7.4 in section 7.3.2, there are 4 unique interstitial sites the tritium can occupy: site a in the mixed Li-Pb plane; two sites b and c within the oxygen plane which lies between the pure Li and mixed Li-Pb Planes; and finally site d, which exists in the pure Li plane. In total, 23 unique pathways for tritium interstitial migration were found and considered. The pathways and their respective activation energies are presented in Table 7.3.

Given the high quantity of options available to the tritium interstitial, it is more suitable to discuss only the most favourable pathways along each axis. Considering first the migration of the tritium interstitial within the mixed Li-Pb, oxygen and pure-Li planes separately, migration exclusively through the oxygen plane is found to have a relatively high potential barrier, with a pathway of $b \rightarrow b \rightarrow c \rightarrow c \rightarrow$

Table 7.3: Activation energies for the migration of T^{+1} tritium interstitial defects. Accented sites represent interstitials which lie on a neighbouring interstitial plane.

Initial Plane	Final Plane	Pathway	d (Å)	Forward (eV)	Reverse (eV)
Li-Pb	Li-Pb	$a \rightarrow a$	2.729	0.56	0.56
		$a \rightarrow a$	2.943	0.77	0.77
		$a \rightarrow \bar{a}$	1.199	0.29	0.29
		$a \rightarrow \bar{a}$	2.630	0.88	0.88
	Oxygen	$a \rightarrow b$	2.042	0.74	0.47
		$a \rightarrow b$	1.397	0.26	0
		$a \rightarrow c$	1.902	0.56	0.34
		$a \rightarrow c$	1.355	0.22	0
Oxygen	Oxygen	$b \rightarrow b$	1.808	0.48	0.48
		$c \rightarrow b$	2.555	0.73	0.67
		$c \rightarrow b$	1.992	1.89	1.84
		$c \rightarrow c$	1.486	0.35	0.35
Pure-Li	Li-Pb	$d \rightarrow a$	2.683	0.46	0.90
	Oxygen	$d \rightarrow b$	2.043	0.29	0.45
		$d \rightarrow b$	2.226	0.47	0.63
		$\bar{d} \rightarrow b$	1.580	0.32	0.48
		$d \rightarrow c$	2.378	0.46	0.68
		$d \rightarrow c$	2.293	0.47	0.69
		$\bar{d} \rightarrow c$	1.304	0	0.20
	Pure-Li	$d \rightarrow d$	2.528	0.50	0.50
		$d \rightarrow d$	3.247	0.13	0.13
		$d \rightarrow \bar{d}$	2.065	0.45	0.45
		$d \rightarrow \bar{d}$	2.364	0.27	0.27

b, and a total barrier of 0.73 eV for the entire migratory process. If instead of migrating directly between sites b and c (which share the same T-O hydroxyl bond), an intermediary step is placed by allowing the hydroxyl to rotate into the mixed Li-Pb plane to site a such that $b \rightarrow a \rightarrow c$ (and vice-versa), the activation energy of the migration along the oxygen plane is relatively unchanged, with an energy of 0.74 eV and a full pathway of $b \rightarrow b \rightarrow a \rightarrow c \rightarrow c \rightarrow a \rightarrow b$. As it is difficult to visualise such a pathway, an illustrative example of this pathway is presented in Figure 7.14.

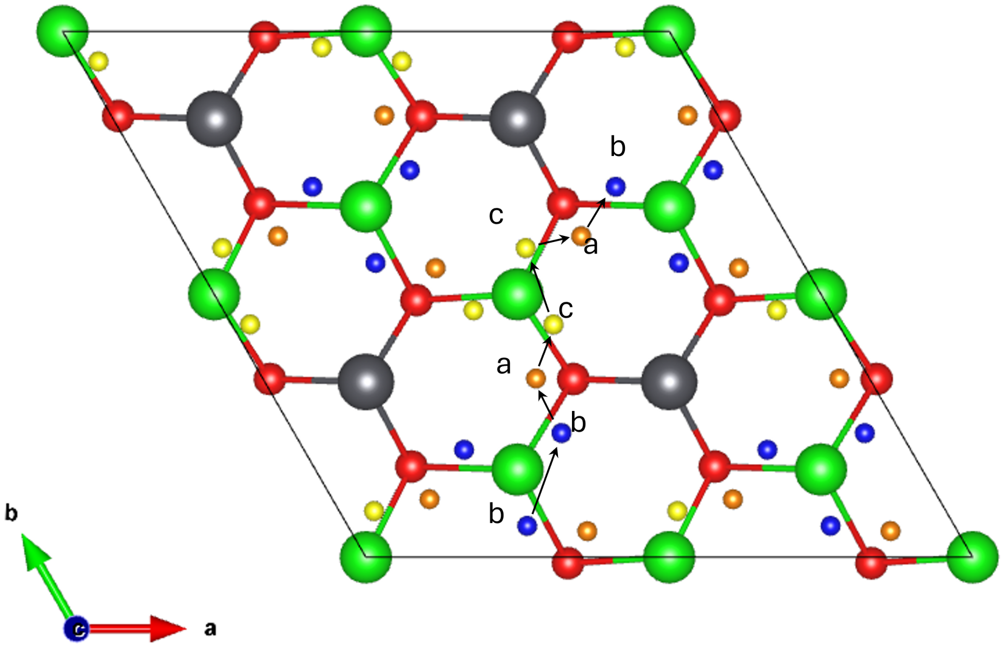

Figure 7.14: Illustration of a migration pathway of tritium through the combined mixed Li-Pb and pure oxygen planes ($b \rightarrow b \rightarrow a \rightarrow c \rightarrow c \rightarrow a \rightarrow b$).

Migrating through the mixed Li-Pb plane results in a very similar migration barrier to that for the case of migration through the oxygen plane, although using a completely different mechanism. As seen in Figure 7.1, within the mixed Li-Pb plane, there exists two stacked planes the tritium interstitial can occupy (site a). The most efficient pathway is for the tritium to hop between the two sub-planes once for every occurrence the tritium migrates within the same sub-plane, i.e. $a \rightarrow a \rightarrow \bar{a} \rightarrow \bar{a} \rightarrow a$, and the bar indicates the interstitial sits on the neighbouring sub-plane. With such a pathway, a total activation energy for the entire migration is 0.56 eV.

Migration exclusively within the pure-Li plane of the tritium interstitial defect appears much more favourable. Much like the case of migration through the mixed Li-Pb plane, there are two sub-planes the tritium interstitial occupies within the pure-Li plane stacked on top of one another, and the tritium utilises both planes in order to migrate. Relative to the previous pathways considered, migration anywhere through the pure-Li plane yields a lower activation barrier, with a maximum barrier of 0.50 eV. The pathway yielding the lowest activation barrier is that of the migration $d \rightarrow \bar{d} \rightarrow \bar{d} \rightarrow d$, with a total barrier of 0.27 eV for the entire process. An illustration of the migration pathway is given by Figure 7.15. Such a low barrier is due to the presence of a semi-stable site for the tritium interstitial along the sub-path $d \rightarrow d$ yielding a barrier of 0.13 eV. It is expected that the majority of tritium interstitial migration will occur along the pure-Li plane, as the tritium is predicted to vacate the mixed Li-Pb and oxygen planes via $c \rightarrow a$. The barrier for this pathway is very low and is effectively 0 eV. However, there must be a barrier as the final position is a stable site. This is similar to the observations made by Shi *et al.* for Li_2TiO_3, and deduce the tritium sites associated with such low barriers are not true energy minimums, but cusps along a flat energy surface.

In the vertical direction perpendicular to the mixed Li-Pb and pure-Li planes, the optimal pathway is predicted to have an activation energy of 0.69 eV. Beginning in the mixed Li-Pb plane from site a, the optimal pathway for the tritium interstitial to take is predicted to be $\bar{a} \rightarrow a \rightarrow c \rightarrow \bar{d} \rightarrow d \rightarrow \bar{c} \rightarrow \bar{a}$, with a step between the d and c sites possessing the highest activation energy for the entire migratory process with a barrier of 0.42 eV.

Overall, the pathway containing the semi-stable state through the pure-Li plane along the xy-axes via the process $d \rightarrow \bar{d} \rightarrow \bar{d} \rightarrow d$ is the most preferred, with an energy barrier of 0.27 eV. The activation energy for migration is anisotropic, as is expected from the intrinsicially anisotropic crystal structure of Li_8PbO_6, with a barrier along the z-axis of 0.69 eV.

7.3.5 $\{T_i^{+1}{:}V_{Li}^{-1}\}^{0}$ internal migration

Figures 7.5 and 7.6 illustrate the possible hydroxyl positions for the tritium to form within the V_{Li1} and V_{Li2} environments, where due to Coulombic attraction, the

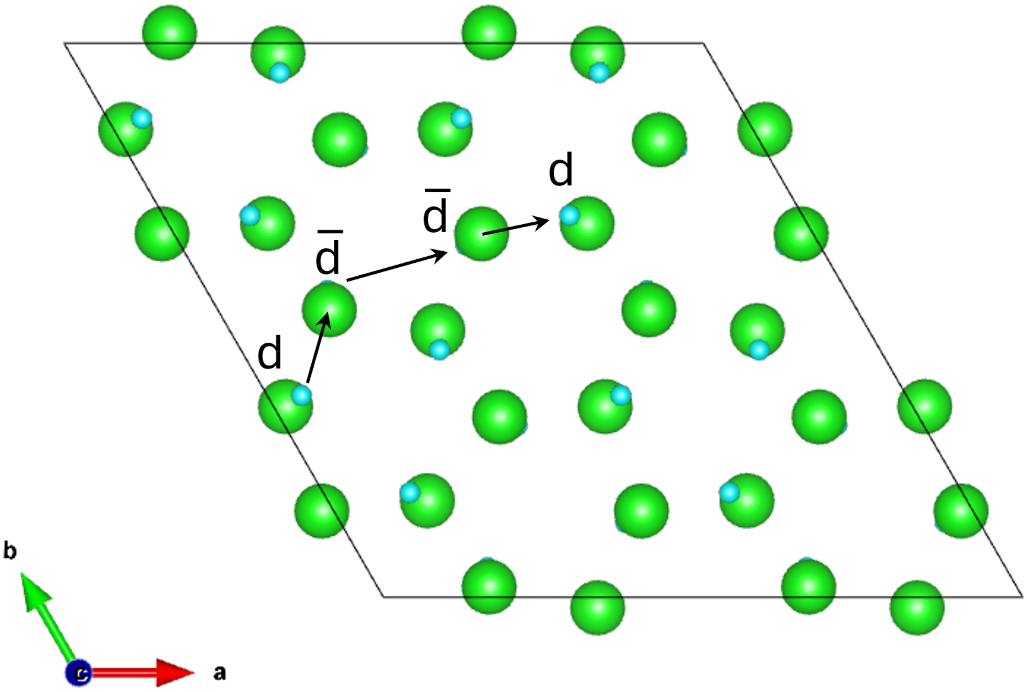

Figure 7.15: Illustration of the optimal migration pathway of tritium through the pure lithium plane ($d \rightarrow \bar{d} \rightarrow \bar{d} \rightarrow d$).

hydroxyls have re-orientated such that the tritium is directed towards the vacancy. It is expected the tritium trapped within these $\{\mathrm{T}_i^{+1}{:}\mathrm{V}_{\mathrm{Li}}^{-1}\}$ defect clusters will re-orient themselves prior to escaping the trapping site. Therefore, in Table 7.4, activation energies for the internal migration of tritium within these defect clusters is presented.

From Table 7.4, it is clear introducing a +1 charge state does not have a significant impact on the activation energies, with differences ranging from 0.05 - 0.07 eV. We can see from the table that there are 6 possible re-orientations around the $\mathrm{V}_{\mathrm{Li1}}$ site and only 4 surrounding $\mathrm{V}_{\mathrm{Li2}}$ due to symmetry.

First observing $\mathrm{V}_{\mathrm{Li1}}$, a' is found to be the most favourable position for the other hydroxyl groups to re-orient towards, and d' the least favourable, with the highest barrier for re-orientation towards a' of 0.47 eV and the lowest barrier for re-orientation towards d' of 0.67 eV in the $\{\mathrm{T}_i^{+1}{:}\mathrm{V}_{\mathrm{Li}}^{-1}\}^0$ charge-neutral defect cluster case, which is in agreement with the formation energies of the T^{+1} defects seen in

Table 7.4: Activation energies for the internal migration of tritium within the V_{Li1} and V_{Li2} vacancy defects.

			Barrier$\{\mathrm{T}_i^{+1}\mathrm{:V}_{\mathrm{Li}}^{-1}\}^0$		Barrier $\{\mathrm{T}\{T_i^{+1}\mathrm{:V}_{\mathrm{Li}}^{-1}\}^{+1}\mathrm{:V}_{\mathrm{Li}}^{0}\}^{+1}$	
Vacancy site	Pathway	d (Å)	Forward (eV)	Reverse (eV)	Forward (eV)	Reverse (eV)
V_{Li1}	$a' \rightarrow b'$	1.319	0.49	0.43	0.56	0.50
	$a' \rightarrow c'$	1.311	0.54	0.38	0.60	0.46
	$a' \rightarrow d'$	1.599	0.78	0.47	0.84	0.56
	$b' \rightarrow c'$	1.566	0.76	0.66	0.81	0.72
	$b' \rightarrow d'$	1.395	0.67	0.42	0.74	0.52
	$c' \rightarrow d'$	1.542	0.77	0.62	0.83	0.69
V_{Li2}	$e' \rightarrow e'$	1.757	0.71	0.71	0.78	0.78
	$e' \rightarrow f'$	2.067	0.58	0.47	0.65	0.54
	$e' \rightarrow f'$	2.375	1.06	0.95	1.12	1.01
	$f' \rightarrow f'$	2.153	1.01	1.01	1.08	1.08

Table 7.1.

For re-orientation around the V_{Li2} defect, the hydroxyl groups are predicted to migrate towards the e' position, rather than f', with the lowest barrier for migration being 0.47 eV from f' to e', as expected from the formation energies presented in Table 7.1. Interestingly, the second lowest energy barrier is the reverse process for the same pathway, with 0.58 eV, so it is expected that the hydroxyl will primarily only swap positions along this pathway, rather than migrate to a symmetric hydroxyl site, or take the alternative e' to f' pathway.

7.3.6 Tritium escape

For tritium to escape from the lithium vacancy cluster it is expected to re-orient itself around the oxygen it is bound to, until it is directed away from the lithium vacancy site, where the tritium is far enough away from the lithium vacancy defect to be treated as an interstitial. In this section, the activation energy barriers for rotation of

Table 7.5: Barriers for tritium escape from the $\{T^{+1}{:}V_{Li}^{-1}\}$ defect cluster. An * indicates an implausible reaction pathway due to a failure to converge.

Vacancy site	Escape pathway	d (Å)	Forward (eV)	Reverse (eV)
V_{Li1}	$a' \rightarrow d$	1.676	>5*	>5*
	$b' \rightarrow a$	1.825	0.43	0.13
	$b' \rightarrow c$	2.210	0.82	0.37
	$c' \rightarrow a$	1.804	0.39	0.10
	$c' \rightarrow b$	2.132	0.47	0
	$d' \rightarrow a$	2.136	5.02*	5.01*
V_{Li2}	$e' \rightarrow d$	1.762	0.91	0.20
	$f' \rightarrow c$	1.709	0.42	0
	$f' \rightarrow d$	2.022	4.36*	3.69*

the hydroxyl groups away from the $\{T_i^{+1}{:}V_{Li}^{-1}\}^0$ defect cluster are predicted, wherein tritium can then be treated as an interstitial.

The final positions for re-orientation are assumed to be the previously considered interstitial sites *a*-*d*, and beginning from each initial position a'-f', each initial site has 3 potential final sites. For example, a' may re-orient itself into the *b*, *c*, or *d* positions. The final positions were first allowed to structurally relax, and following relaxation, of the 18 potential final sites for the tritium (3 for each initial site), only 9 were found to be stable at the interstitial positions. The rest either migrated to a more stable position, or re-oriented back into the defect cluster. The activation energies for tritium escape via re-orientation of the hydroxyl around a bound oxygen are shown in Table 7.5, and illustrations of the possible re-orientation pathways away from the V_{Li1} and V_{Li2} trapping sites are shown in Figures 7.16 and 7.17 respectively.

Escape from the V_{Li1} trapping site showed reasonably low activation energies for re-orientation between 0.43 and 0.82 eV. As expected, the reverse process for each

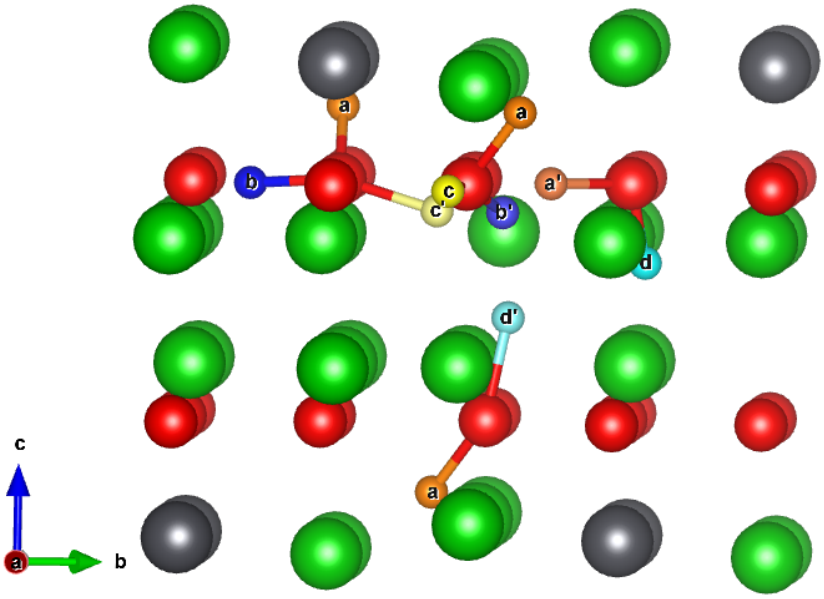

Figure 7.16: Re-orientation pathways for escape from the $\{T_i^{+1}{:}V_{\mathrm{Li1}}^{-1}\}$ defect.

migration is significantly lower, due to the attraction of the T^{+1} interstitial to the oppositely charged V_{Li}^{-1} defect. The migration pathways from $a' \rightarrow d$ and $d' \rightarrow a$ were found to have very high activation energies, suggesting these mechanisms are unlikely to contribute to tritium diffusion. It is much more likely the pathways for escape from a' and d' to first include a re-positioning to b' or c' before attempting to escape the defect cluster. For a', the optimal pathway for escape is to re-orient to b' with a barrier of 0.47 eV, followed by escape to a outside the defect cluster with a barrier of 0.43 eV. The optimal pathway for escape from the d' site also requires a re-orientation to b' within the cluster first, with an activation energy for the process of re-orientation being 0.42 eV. For the lowest escape barrier considered of $c' \rightarrow a$, it is expected once the tritium is at the a site it will migrate towards the pure-Li plane to utilise the $d \rightarrow \bar{d} \rightarrow \bar{d} \rightarrow d$ pathway, which possesses a barrier of 0.27 eV, and will reach this pathway via: $c' \rightarrow a \rightarrow \bar{a} \rightarrow \bar{c} \rightarrow d$, and has a total activation energy of 0.71 eV.

Only three unique pathways were found for escape from the V_{Li2} site. Once again, much like we observed in the case of escape from the V_{Li1} trapping site,

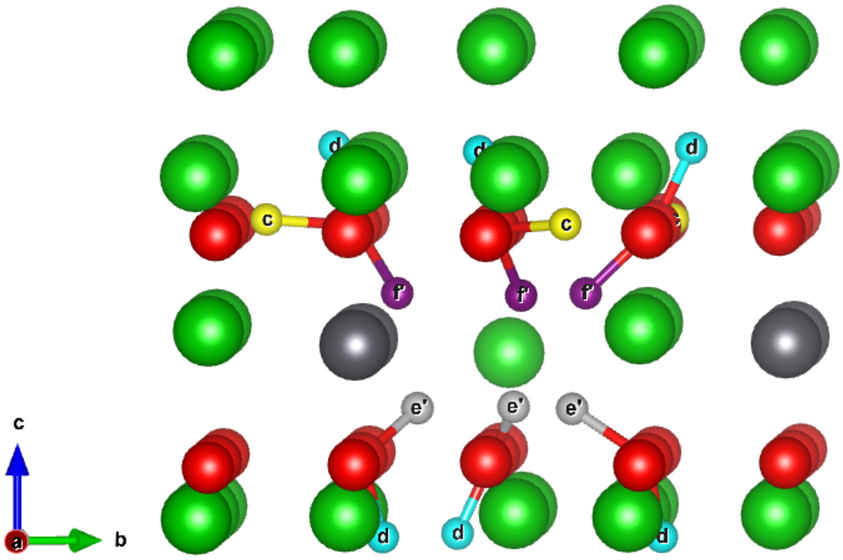

Figure 7.17: Re-orientation pathways for escape from the $\{T_i^{+1}:V_{Li2}^{-1}\}$ defect.

the $f' \rightarrow d$ pathway possesses a very high activation energy. As f' already has an alternative escape pathway to c instead of d, and as the activation energy for migration from $c \rightarrow d$ has been previously estimated to be 0 from Table 7.3, the pathway for diffusion along $f' \rightarrow d$ can be assumed to have a barrier of 0.42 eV, the same as that for $f' \rightarrow c$. As the final interstitial site is expected to either be d, or have an immeasurably small barrier to migrate to d from c, the migration pathway following escape from the cluster is expected to be $f' \rightarrow c \rightarrow d \rightarrow \bar{d} \rightarrow \bar{d} \rightarrow d$, with a total barrier for escape from the crystal entirely from the cluster of 0.69 eV, virtually identical to the size of the barrier for escape in the Li1 case.

Overall, in comparison with other materials such as Li_2TiO_3, the barriers for escape from the $\{T_i^{+1}:V_{Li}^{-1}\}$ trapping site overall are notably lower, with pathways all below 0.91 eV, and the lowest pathways for escape from the V_{Li1} and V_{Li2} trapping sites being 0.39 and 0.42 eV respectively, compared to that for Li_2TiO_3, which sees the lowest barriers possessing activation energies of 0.55 and 0.66 eV for Li_2TiO_3 [89]. Comparing escape barriers from the crystal as a whole, Li_8PbO_6 exhibits significantly lower activation barriers in comparison with Li_2TiO_3, with barriers of

0.69 - 0.71 eV in the Li_8PbO_6 case, compared to that of Li_2TiO_3 which is predicted to have a minimum barrier of 1.05 eV, which may culminate in a higher tritium release rate for Li_8PbO_6 overall as tritium is less bound to the trapping sites.

7.3.7 $\{T_i^{+1}:V_{Li}^{-1}\}$ cluster migration

Table 7.6: Migration barriers for the $\{T_i^{+1}:V_{Li}^{-1}\}$ defect cluster.

V_{Li}^{-1} pathway	T^{+1} pathway	d_T (Å)	$d_{V_{Li}}$ (Å)	Forward (eV)	Reverse (eV)
$V_{Li1}^{-1} \rightarrow V_{Li1}^{-1}$	$a' \rightarrow b'$	1.660	2.932	1.08	1.03
	$b' \rightarrow c'$	2.202	3.499	2.30	2.19
	$c' \rightarrow a'$	1.778	3.267	3.73	3.88
	$a' \rightarrow d'$	1.712	2.374	2.20	1.89
	$b' \rightarrow d'$	1.475	2.374	1.20	0.94
	$c' \rightarrow d'$	1.264	2.374	0.85	0.70
$V_{Li2}^{-1} \rightarrow V_{Li2}^{-1}$	$e' \rightarrow f'$	1.361	3.278	2.61	2.50
$V_{Li2}^{-1} \rightarrow V_{Li1}^{-1}$	$e' \rightarrow a'$	0.838	2.486	0.78	1.12
	$e' \rightarrow c'$	1.010	2.486	0.50	0.69
	$f' \rightarrow a'$	0.961	2.784	0.73	1.18
	$f' \rightarrow b'$	1.499	2.784	0.26	0.66

In this section, instead of considering the migration of the tritium alone, we instead consider the migration of the whole defect cluster, examining if simultaneous migration with the lithium vacancy defect helps to aid in migration of tritium. The process for cluster migration is broken down into two stages: The first is a collaborative diffusion where a tritium hydroxyl simultaneously re-orients around the bound oxygen as the lithium vacancy it is trapped in also migrates. The second is the breaking of the hydroxyl bond such that the tritium internally diffuses within the newly positioned lithium vacancy, as described in section 7.3.5. An illustrative example of the complete migration process for a defect cluster is shown in Figure 7.18.

A total of 11 possible migration pathways for the collaborative diffusion mechanism were found. 6 beginning and ending at Li1 lithium sites exclusively ($\mathrm{V}_{\mathrm{Li1}}^{-1} \rightarrow \mathrm{V}_{\mathrm{Li1}}^{-1}$), 4 which change lithium vacancy sites between Li1 and Li2, and only one site where the lithium vacancy site begins and ends at Li2. Energy barriers for the collaborative diffusion pathways are presented in Table 7.6.

The lowest migration barriers for the collaborative diffusion mechanism were found to be those along the $\mathrm{V}_{\mathrm{Li2}}^{-1} \rightarrow \mathrm{V}_{\mathrm{Li1}}^{-1}$ pathway, with barriers ranging from 0.26 - 0.78 eV. Due to such low barriers, it is evident there is indeed collaborative diffusion occurring between the migration of the lithium vacancy and tritium interstitial sites in $\mathrm{Li_8PbO_6}$. Between Li1 sites, the lowest barrier was found to be 0.70 eV, and the highest 3.88 eV, although half of all barriers are relatively small, with sizes at or smaller than 1.25 eV. Considering the most energetically favourable collaborative diffusion process ($\mathrm{V}_{\mathrm{Li2}}^{-1} \rightarrow \mathrm{V}_{\mathrm{Li1}}^{-1}$) followed by an internal migration within the new lithium vacancy site, as described in section 7.3.5, the total barrier for diffusion ranges between 0.27 - 0.78 eV. Alternatively, if the $\mathrm{V}_{\mathrm{Li2}}^{-1} \rightarrow \mathrm{V}_{\mathrm{Li1}}^{-1}$ pathway is considered first, the total barrier for diffusion is between 0.77 - 1.18 eV.

Comparing with the escape pathways of tritium from the trapping sites and from the bulk crystal, tritium has a slight preference for utilising the defect cluster as a primary mechanism for diffusion throughout the bulk crystal, due to the low activation energies possessed by the $e' \rightarrow c'$ and $f' \rightarrow b'$ defect cluster pathways compared to the 0.69 - 0.71 eV required for the tritium to escape from the cluster and entirely from the crystal. Therefore, it is expected that tritium will likely initially migrate collaboratively as part of a defect cluster before eventually escaping from the cluster and diffusing through the pure-Li plane before escaping the crystal entirely.

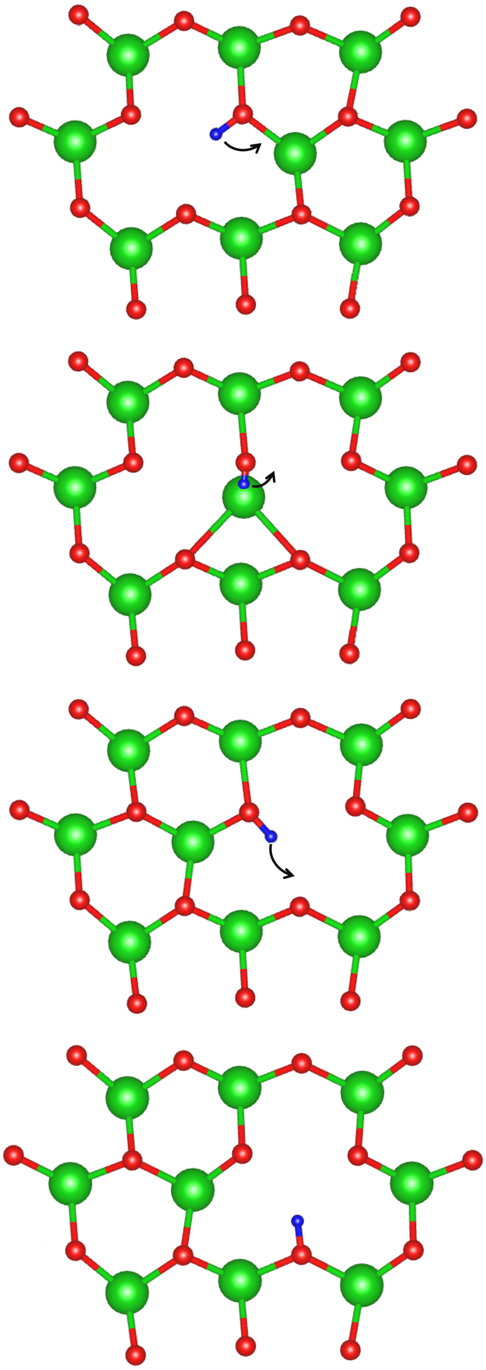

Figure 7.18: Illustration of migration of a $\{\mathrm{T}_i^{+1}{:}\mathrm{V}_{\mathrm{Li}}^{-1}\}$ defect cluster. In this example, the cluster migrates along the $\mathrm{V}_{\mathrm{Li1}}^{-1}$, $\mathrm{T}(a') \rightarrow \mathrm{V}_{\mathrm{Li1}}^{-1}$, $\mathrm{T}(b')$ pathway, before the T-O bond is broken and migrates via the $\mathrm{T}(b') \rightarrow \mathrm{T}(a')$ pathway internally within the new lithium vacancy defect.

7.4 Conclusion

In this chapter, it is explored how tritium is accommodated and the mechanisms for tritium diffusion through bulk Li_8PbO_6. Tritium is expected to primarily occupy the lithium vacancy sites as a hydroxyl, forming a defect cluster, rather than as an isolated interstitial. The barriers for diffusion of tritium interstitials is anisotropic in nature, with a barrier of 0.27 eV in the xy-plane through the pure-Li planes and 0.69 eV vertically along the z direction. Similar anisotropy is also true for the lithium vacancy defect, which prefers to occupy and migrate through the pure-Li plane. The barrier for tritium to escape from a $\{\mathrm{T}_i^{+1}\text{:}\mathrm{V}_{\mathrm{Li}}^{-1}\}$ defect cluster possessed energies ranging between 0.39 - 0.91 eV, and to escape from the cluster and from the crystal entirely, a minimum barrier of 0.69 - 0.71 eV was found for escape from the Li1 and Li2 sites. For migration of the clusters as a whole, the smallest activation energies were that between the $\mathrm{V}_{\mathrm{Li1}}$ and $\mathrm{V}_{\mathrm{Li2}}$ sites ranging between 0.27 - 0.78 eV, implying a collaborative diffusion mechanism between the tritium interstitials and lithium vacancy defects. Due to such low barriers, the aging of the blanket caused by lithium burn-up will have a smaller impact on tritium release compared to other materials.

Chapter 8

Summary and future work

The overall objective of this thesis was to assess the feasibility of using octalithium plumbate as a breeder material for fusion using DFT. To this end, the fundamental properties of the crystalline Li_8PbO_6 were initially explored, as there is a paucity of this information in the literature. In this initial study, a comparison is drawn using the two different DFT codes, CASTEP and VASP.

Chapter 4 presents the fundamental physical, electronic and thermodynamic properties of Li_8PbO_6, and draws a comparison between DFT codes CASTEP and VASP, as aside from the lattice parameters, there is no experimental data on most of the fundamental physical properties of octalithium plumbate. Overall, both codes were found to be comparable with the exception of the C_{11} lattice parameter, which was found to be lower in the VASP code compared to CASTEP, which has ramifications for the Young's modulus, which despite both codes correctly predicting the material to be anisotropic in the z axis, the CASTEP code predicts the x and y components of the Young's modulus to be around 22% greater than the z component, whereas VASP predicts the x and y axes to be approximately 16% smaller, i.e. the anisotropy of the tensile stiffness is inverted depending on the code used.

As shown in Chapter 4, semi-local functionals, such as the GGA, predict bandgaps that are roughly 20% below the values determined from experiment. There are a number of approaches to ameliorating this error, with the most common being the adoption of hybrid functionals and the use of Hubbard U parameter. When the hybrid HSE06 functional was employed the bandgap in Li_8PbO_6 is 3.36 eV as opposed to 1.94 eV predicted using the PBE functional. This underestimation of the bandgap has implications for the calculation of the formation energies presented in Chapters 6 and 7.

The defect chemistry may be significantly impacted by the choice of functionals used, and it may be preferable to employ a hybrid functional rather than the PBE functional used for much of this thesis. In the instance of octalithium plumbate, the presence of the Pb-d orbital complicates things further, as exchange-correlation in higher order orbitals (d, f, etc.) are not well described using the PBE functionals, although the computational cost of using a hybrid functional is a significant limiting factor, as they typically demand orders of magnitude more computational power in comparison with cheaper functionals such as LDA or PBE. It is possible to account for this somewhat by introducing a correction term to the exchange-correlation functional using DFT+U and fitting the correction to some desired parameter using a cheaper PBE functional. Although, in the instance of octalithium plumbate, fitting to the hybrid HSE electronic band gap resulted in a U parameter on both the Pb-d orbitals and on the O-p orbitals of 8 eV each. If the correction is only applied to the Pb-d orbitals, the correction term exceeds 10 eV due to the Pb_d orbitals being unoccupied (as Pb in Li_8PbO_6 exists as Pb^{+4}). A hybrid HSE06 functional was also employed on the charged lithium vacancy defect using a slightly lower energy-cutoff of 520 eV, a Γ-centred k-point grid of the same density as the PBE functional, and an electronic convergence criteria for the SC loop of 10^{-5} eV. The hybrid functional predicted a formation energy difference for the V_{Li1}^{-1} defect of $\Delta E_f = 0.1$ eV compared to the PBE functional, suggesting the benefits of using a hybrid functional are not significant enough to outweigh the computational cost, and the PBE functional without any U correction is likely accurate enough to appropriately describe the defect chemistry.

In future studies, it may be worthwhile to introduce a hybrid functional into the studies performed in chapters 6 and 7. Although, this will invariably be very computationally expensive, in particular for NEB simulations. Throughout this thesis, a 180 atom supercell was employed for all defect simulations, future studies performing hybrid simulations to study the defect properties of Li_8PbO_6 and other similarly structured materials will likely require a much smaller supercell as a compromise to reduce computational demand.

In the initial discussion of the fundamental properties of Li_8PbO_6, a potential issue surrounding its thermal stability at high temperatures was identified. In response, the thermal stability of the plumbate at high temperatures was explored, in conjunction with other potential octalithium compounds. Chapter 5 presents predictions using finite displacement simulations of the fundamental thermodynamic properties of a range of octalithium ceramics, and their relative thermal stabilities are compared to propose what the optimal candidates for use in an operational setting might be. From this study, octalithium plumbate was determined to be the most suitable candidate, which did not show any suggestion of a thermally-driven phase transformation into an alternative phase for the temperature ranges considered.

A drawback of the finite displacement method is the thermodynamic properties are extrapolated from the phonon density of states at 0 K, limiting the reliability of the thermodynamics severely to low temperatures. This is due to the the assumption that the energy well surrounding the minimum is harmonic in nature, which is false for high temperatures.For the harmonic approximation, the reliable temperature range is much wider than that for QHA. The assumption that the potential energy surface can be approximated as harmonic starts to break down as the temperature increases, therefore, while our study indicates that Li_8PbO_6 is suitable for high temperature operation, this should be confirmed experimentally.

In performing this wider study of thermal stability of octalithium compounds, it was observed that there was an issue in the prediction of the specific heat for the Li_2O compound, arising from the FCC structure adopted by the oxygen ions.

Therefore, the DFT predicted specific heat was substituted with the experimental values and then not only is Li_8PbO_6 expected to be stable at high temperatures, it may also be the best octalithium ceramic in this regard.

Future works should look to employ molecular dynamics simulations to develop a better understanding of the thermodynamics of the system instead of using DFT. Unfortunately, no set of pair potentials exists for the Li_8PbO_6 system. At present, a primitive set of Buckingham pair potentials using the Potential Pro-Fit simulation package [223] has been derived by fitting to the lattice and elastic parameters. Unfortunately they do not accurately represent some of the key elastic constants of the material (particularly C_{11} which is underestimated by approximately 20%) due to a combination of over-fitting restricting the parameter space, and restricting the partial charges. The final pair potential fits also failed when introduced into molecular dynamics simulations by overestimating the attempt frequency for the diffusivity of the intrinsic species, in particular Pb, as well as the lattice expansion which showed contraction along the z-axis. One may find greater success by employing slightly higher partial charges ($q_{Li} > 0.549$), as this may increase the elastic tensor and may make finding a suitable parameter space for the pair potentials much easier. Another alternative to both approaches might be to use *ab initio* molecular dynamics which utilises DFT as an alternative to describe the forces between ions, circumventing the need to rely on a pre-established set of interatomic potentials.

Having established that the underlying perfect crystal Li_8PbO_6 is still a viable breeder material, the defect chemistry is explored in Chapter 6. Chapter 6 predicts the intrinsic defect chemistry of Li_8PbO_6 under various operational environments, including low and high oxygen partial pressures, and operational temperature.

The intrinsic defect chemistry of Li_8PbO_6 is dominated primarily by the lithium vacancy defects. At low temperatures, the charged lithium vacancy defect is charge-compensated for by the lithium interstitial, whereas at high temperatures the oxygen vacancy defect plays a central role in maintaining charge-neutrality in the bulk crystal, particularly in the region close to the Li_2O saturation limit. The high concentration of lithium vacancies regardless of the atmospheric and thermal conditions suggests suggests this defect will be integral to understanding the mechanisms for tritium release, as the lithium vacancy is infamous for acting as a trapping site due to the similar mass and charge states lithium and tritium share. Li_8PbO_6 is also predicted to be able to burn off significantly more lithium at higher temperatures, suggesting the material may be able to accommodate higher tritium production with increasing temperature before undergoing a change in phase to an alternative compound.

Having established how the defect chemistry of Li_8PbO_6 changes in response to lithium burn-up, the implications for tritium release have been explored. Chapter 7 presents the tritium-accommodating defect chemistry of Li_8PbO_6, and the mechanisms for tritium escape, in particular exploring the potential for the lithium vacancy defect to act as either a trapping site or to collaboratively assist tritium migration.

The T_i^{+1} tritium interstitial defect is predicted to have the lowest formation energy of the tritium-accommodating defects in Li_8PbO_6. Due to the high concentration of lithium vacancy defects, tritium is predicted to be highly soluble in the ceramic matrix, becoming bound to the lithium vacancy defect via the formation of a hydroxide with a neighbouring oxygen ion as a $\mathrm{T}_{\mathrm{Li}}^{0}$ defect. Although at temperatures between 600 - 900 K, tritium is predicted to favour the T_i^{+1} interstitial configuration in the ceramic.

Regardless of the accommodation mechanism in the bulk, accommodation of tritium on the lithium vacancy site as a $\{\mathrm{T}_i^{+1} : V_{\mathrm{Li}}^{-1}\}$ defect complex does not seem to impact the overall tritium release rate from the bulk ceramic, as is seen in other ceramics such as Li_2TiO_3. The tritium release rate was found to be comparatively similar between interstitial and defect complex migration of tritium, although there is anisotropy where the interstitials favour migration planarly through the x and y axes, whereas the collaborative migration of tritium and the Li vacancy as the

$\{T_i^{+1} : V_{\mathrm{Li}}^{-1}\}$ defect complex favours migration through the z axis.

Activation energies for diffusion of both the interstitial and the defect complex are comparable to those measured from experiment, with activation energies for net tritium escape of 0.78 eV, although in experiment the accommodation and mechanisms for migration are not distinguished so a true comparison is difficult, particularly as the attempt frequencies for migration are not predicted in this thesis. To predict the attempt frequencies, it may be necessary to employ transition state theory to extract the phonon density of states at the peak barrier position of the migration pathways. From the phonon density of states, it is then possible to extract the attempt frequency and calculate the temperature-dependent rate of diffusion. Regardless, the comparable activation energies for escape of tritium between DFT and experiment is reassuring, although it is important to stress the need for further experimental validation of the bulk of this section, as only the activation energies for tritium escape are the only aspect of this section which have such a comparison at present.

8.1 Future of octalithium plumbate

The tritium release characteristics for octalithium plumbate are predicted to be highly favourable relative to other ceramic breeding materials such as lithium metatitanate (Li_2TiO_3) and lithium orthosilicate (Li_4SiO_4). In combination with the comparatively high TBRs predicted for Li_8PbO_6, octalithium plumbate has excellent performance potential as a tritium breeding material for spherical tokamak fusion reactors.

A major concern for the applicability of octalithium plumbate as a tritium breeding material is the thermal stability. At present, the melting temperature is not known in the literature, and from the manufacturing process trace secondary phases of Li_4PbO_4 are generally present. In Chapter 6, the intrinsic defect chemistry was explored under various different processing conditions, and the results suggest that the octalithium plumbate should only be stable under highly lithium-rich conditions, and cannot accommodate significant lithium burn-up unless high temperatures are used. Octalithium plumbate is expected to transition to an alternate phase when the chemical potential fraction reaches 0.15 from the Li_2O-rich limit into Li_4PbO_4. At low temperatures it is thus predicted to transition at extremely low Li burn-up, and may have significant ramifications for the total operational lifetime of octalithium plumbate. Degradation into Li_4PbO_4 (or any alternative phase for that matter) introduces mixed materials with differing densities which may gradually cause swelling/fracturing of the pellets. Pellet swelling/fracturing will reduce the flow rate of the purge gas, reducing the total amount of that can be extracted and reducing the cooling of the ceramic pebbles, potentially leading to melting of the ceramic inside the blanket. Reducing the amount of oxygen available in the environment will reduce the amount available to be converted into an alternative phase and extend the lifetime of octalithium plumbate before it degrades, as the alternative Li_4PbO_4 and Li_2PbO_3 require much lower stoichiometric concentrations of oxygen relative to the cation species compared with Li_8PbO_6. Depending on the coolant used, it may be necessary to include a coating on the Li_8PbO_6 pellets similar to other core-shell pebble designs, such coating would form a protective layer for the octalithium plumbate from oxidation and may improve the overall mechanical stability of the pellet.

A potential route for future research could be to mix the Pb cation with alternatives such as Zr or Sn, similarly to what is currently being explored in the wider literature with Li_4SiO_4. Mixing the cation species should help to increase the mechanical stability of the compound whilst maintaining a sufficiently high TBR, and also increasing the Li/Pb cation ratio, potentially extending the lifetime of the ceramic in reactor without having to resort to a core-shell pebble design. Given the structural similarity between octalithium compounds (most occupying the $R\bar{3}H$ space group) the mechanisms for diffusion of defects, in particular tritium, should be very similar. Future works could explore a hybridisation between octalithium compounds, e.g. a mixed zirconium-lead compound such as $Li_8Pb_{0.5}Zr_{0.5}O_6$. If the thermal and mechanical stability of such compounds does turn out to be sufficiently favourable, it may not be necessary to discard the use of helium as the primary coolant/purge gas, and the HCPB may be used.

In summary, octalithium plumbate has great potential to perform as a tritium breeding material under ideal operating conditions and is predicted to have excellent tritium release characteristics, although there are concerns surrounding the thermal and phase stability of the compound. Such concerns can be mitigated by ensuring a sufficiently anoxic operational environment. The phase stability may also be improved by mixing the octalithium plumbate with alternative octalithium compounds, increasing the total lithium burn-up before phase change.

Appendix A

Thermodynamics of octalithium ceramics

A.1 Phonopy parameterisation

Table A.1: k-point and q-point parameterisation of binary and ternary compounds studied in Chapters 4 and 5. A Γ-centred Monkhorst-Pack grid is used for k-points and q-points. A finer k-point grid is used for supercells compared to the initial geometry optimisation.

Compound	k-point grid (Unit cell relaxation)	Supercell size	Number of atoms	k-point grid	q-point grid
Li_8PbO_6	6×6×2	3×3×1	405	2×2×2	15×15×15
Li_4PbO_4	6×6×6	2×2×3	432	2×2×2	15×15×15
PbO_2	6×6×6	3×3×3	324	3×3×3	17×17×17
Li_2O	6×6×6	3×3×3	324	3×3×3	17×17×17
Li_8GeO_6	6×6×4	4×4×2	960	2×2×2	13×13×13
Li_4GeO_4	6×6×6	2×2×3	432	2×2×2	15×15×15
GeO_2	6×6×6	3×3×3	243	3×3×3	17×17×17
Li_8CeO_6	6×6×2	3×3×1	405	2×2×2	15×15×15
Li_2CeO_3	6×4×6	4×2×5	480	2×2×2	13×13×13
CeO_2	6×6×6	3×3×3	324	3×3×3	17×17×17
Li_8ZrO_6	6×6×2	3×3×1	405	2×2×2	15×15×15
$Li_6Zr_2O_7$	4×6×4	2×3×2	720	2×2×2	13×13×13
ZrO_2	6×6×6	3×3×3	324	3×3×3	17×17×17
Li_8SnO_6	6×6×2	3×3×1	405	2×2×2	15×15×15
Li_2SnO_3	6×4×4	4×2×2	768	2×2×2	13×13×13
SnO_2	6×6×6	3×3×3	324	3×3×3	17×17×17

A.2 Specific Heat Capacities

Figures are divided into groups of identical ternary components (e.g. figure A.1 contains specific heat data for Li_8PbO_6, Li_4PbO_4 and PbO_2, all of which occupy the Li-Pb-O phase group).

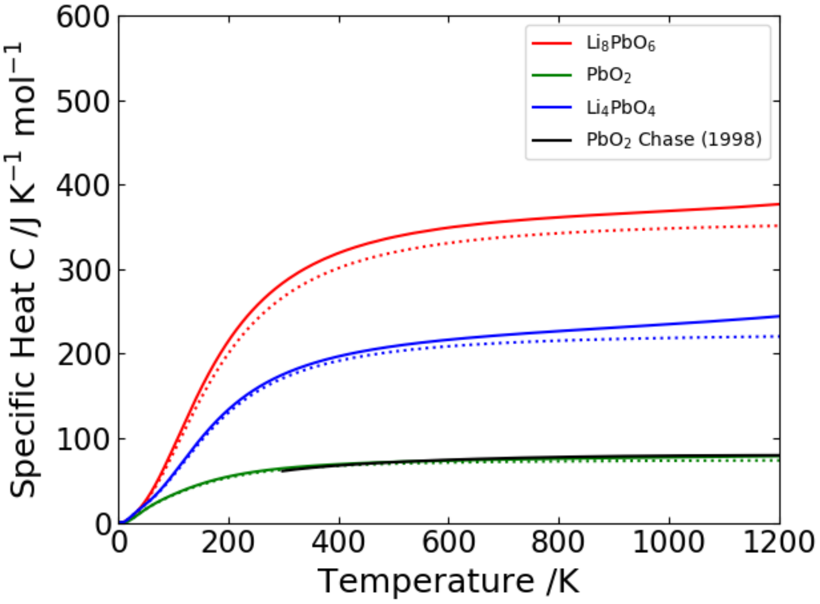

Figure A.1: Specific heat capacities of compounds in the Li-Pb-O phase group. Dotted lines represent C_V and bold lines represent C_p for Figures A.1 - A.5[168]

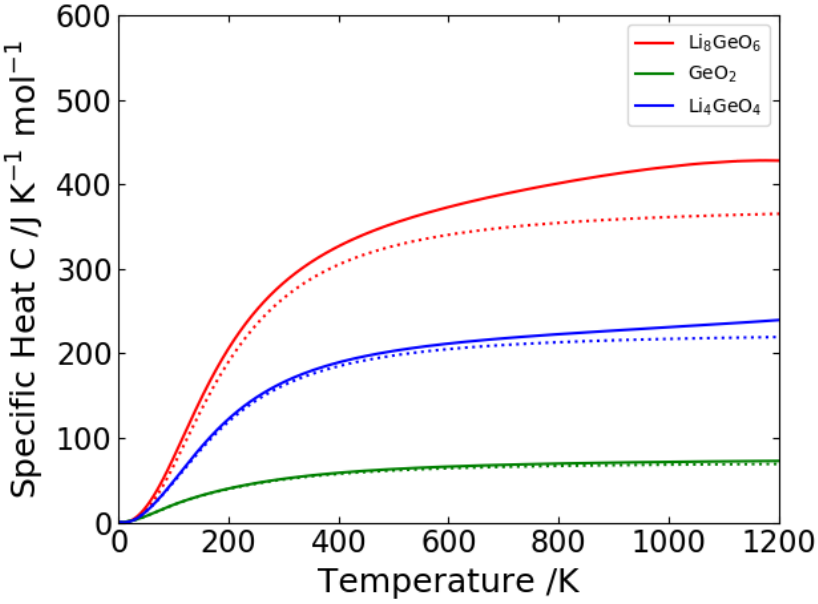

Figure A.2: Specific heat capacities in the Li-Ge-O phase group.

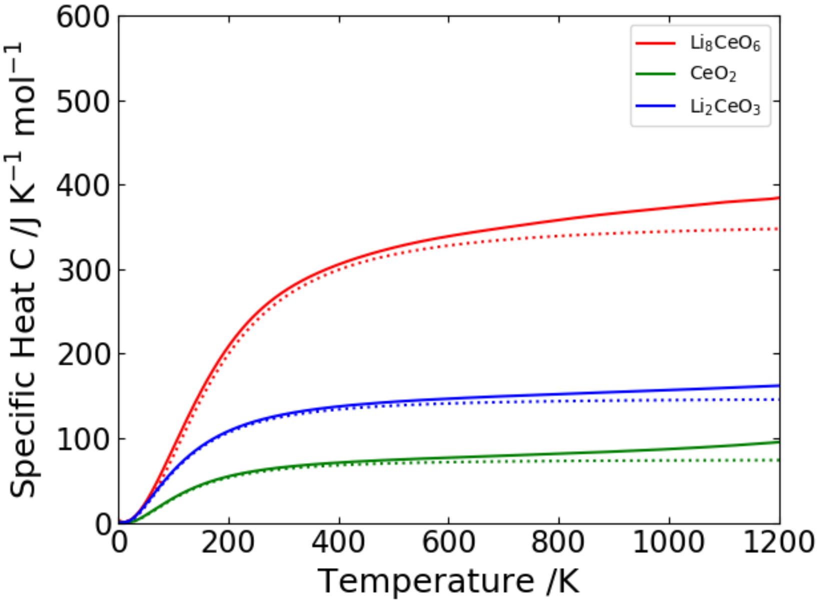

Figure A.3: Specific heat capacities in the Li-Ce-O phase group.

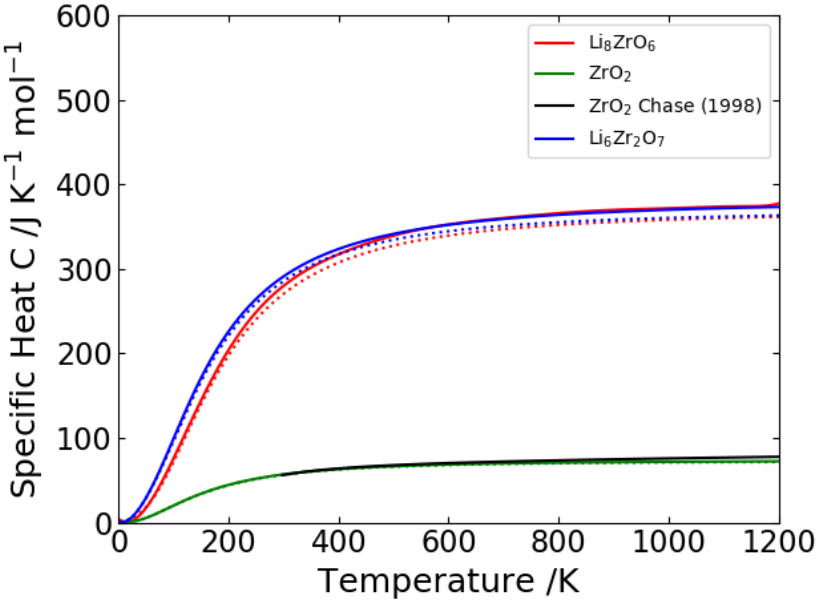

Figure A.4: Specific heat capacities in the Li-Zr-O phase group.

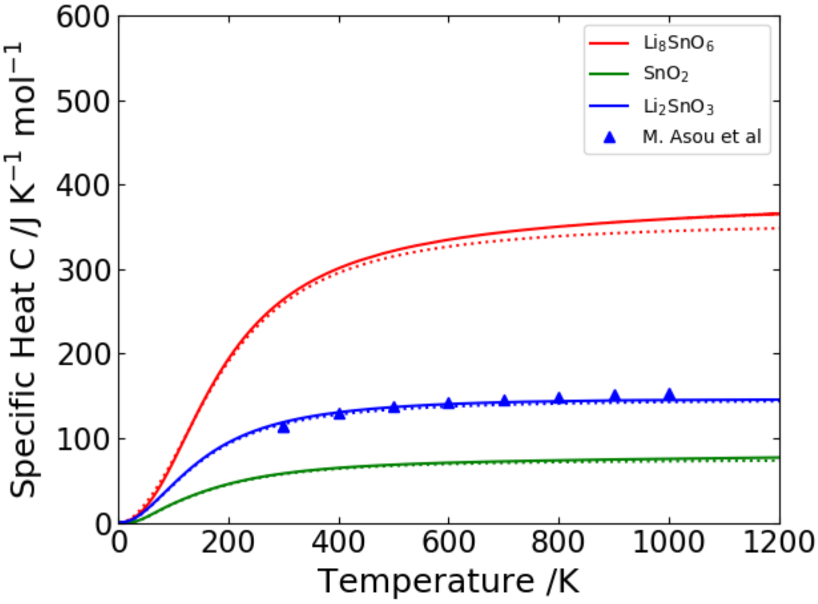

Figure A.5: Specific heat capacities in the Li-Sn-O phase group.

A.3 NASA Polynomial Coefficients

Table A.2: NASA polynomial coefficients A-G fitted to QHA-derived thermodynamics data. (300-1200K)

Compound	A (10^{-5})	B (10^{-7})	C (10^{-10})	D (10^{-13})	E (10^{-17})	F (10^{0})	G (10^{-4})
Li_2O	-3.809×10^{-2}	3.654	-5.694	4.394	-12.74	-1.729	-0.3834
PbO_2	4.328	1.996	-3.135	2.311	-6.395	-1.883	-1.944
CeO_2	4.453	1.947	-2.851	2.004	-4.600	-3.142	-2.141
GeO_2	1.156	2.734	-3.972	2.750	-7.346	-2.291	-0.6568
ZrO_2	2.084	2.709	-4.270	3.099	-8.521	-3.443	-1.169
SnO_2	2.090	2.776	-4.318	3.132	-8.557	-2.225	-1.152
Li_4PbO_4	5.491	8.806	-13.70	9.926	-26.58	-5.432	-3.149
Li_2CeO_3	8.707	3.899	-6.104	4.531	-12.41	-4.856	-4.085
Li_4GeO_4	2.522	9.691	-14.92	10.73	-28.79	-5.948	-2.003
$Li_6Zr_2O_7$	10.44	13.95	-21.91	15.91	-43.83	-12.20	-5.898
Li_2SnO_3	5.398	5.124	-8.129	5.896	-16.21	-4.032	-2.808
Li_8PbO_6	7.646	15.00	-23.48	16.79	-44.76	-8.840	-4.756
Li_8CeO_6	9.041	13.38	-20.92	15.81	-45.20	-9.942	-5.279
Li_8GeO_6	2.636	17.40	-27.17	21.08	-63.25	-9.352	-2.793
Li_8ZrO_6	4.739	16.07	-24.67	17.45	-46.88	-10.35	-3.702
Li_8SnO_6	4.164	15.43	-24.01	17.46	-48.12	-9.176	-3.320

$$C_P = R(A + BT + CT^2 + DT^3 + ET^4) \tag{A.1}$$

$$H = RT\left(A + \frac{BT}{2} + \frac{CT^2}{3} + \frac{DT^3}{4} + \frac{ET^4}{5} + \frac{F}{T}\right) \tag{A.2}$$

$$S = R\left(AlnT + BT + \frac{BT^2}{2} + \frac{DT^3}{3} + \frac{ET^4}{4} + G\right) \tag{A.3}$$

Appendix B

Intrinsic defect chemistry

B.1 Lattice Parameters

Table B.1: DFT-calculated lattice parameters of additional compounds in the Li-Pb-O phase group introduced in Chapter 6.

Compound	a/Å	b/Å	c/Å	$\alpha/^\circ$	$\beta/^\circ$	$\gamma/^\circ$	Space group	Reference
Li_2PbO_3	5.48	9.39	5.55	90	110.84	90	C2/c [15]	
	5.37	9.28	5.46	90	110.34	90		[224]
Pb_3O_4	9.02	9.02	6.77	90	90	90	$P4_2$/mbc [135]	
	8.86	8.86	6.66	90	90	90		[225]
PbO-L	4.05	4.05	5.49	90	90	90	P4/nmm [129]	
	3.96	3.96	5.01	90	90	90		[226]
PbO-M	4.82	5.73	6.15	90	90	90	Pbcm [57]	
	4.75	5.49	5.89	90	90	90		[227]
Li_2O_2	3.16	3.16	7.67	90	90	120	$P6_3$/mmc [194]	
	3.14	3.14	7.65	90	90	120		[228]

B.2 Parameterisation

Table B.2: k-point and q-point parameterisation of binary and ternary compounds studied in Chapter 6. A Γ-centred Monkhorst-Pack grid is used for k-points and q-points. A finer k-point grid is used for supercells compared to the initial geometry optimisation.

Compound	k-point grid (Unit cell relaxation)	Supercell size	Number of atoms	k-point grid	q-point grid
Li_2PbO_3	6×4×6	4×2×4	768	2×2×2	13×13×13
Pb_3O_4	4×4×6	2×2×3	336	2×2×2	17×17×17
PbO-L	8×8×6	4×4×3	192	3×3×3	19×19×19
PbO-M	6×6×6	3×3×3	216	3×3×3	19×19×19
Li_2O_2	8×8×6	5×5×2	400	3×3×3	15×15×15

B.3 Specific Heat Capacities

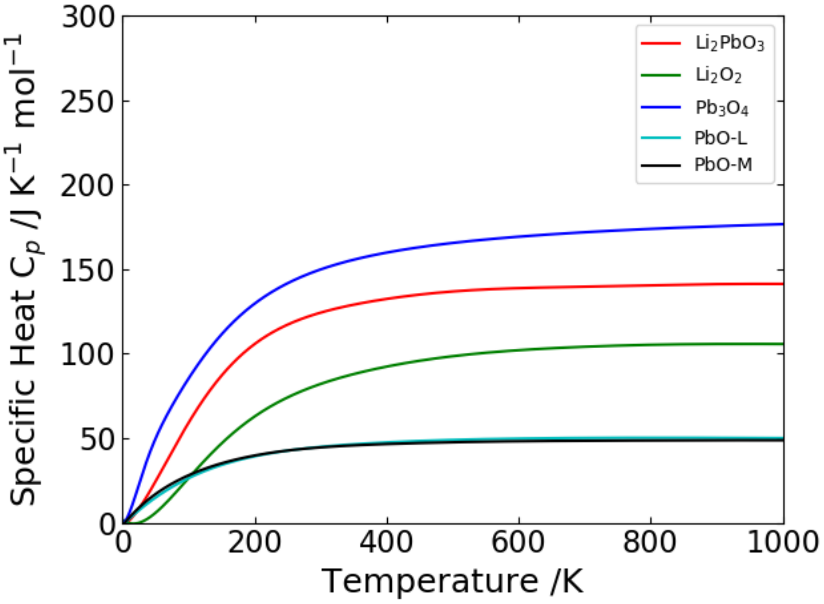

Figure B.1: Specific heat capacity C_p of additional compounds in the Li-Pb-O phase group introduced in Chapter 6.

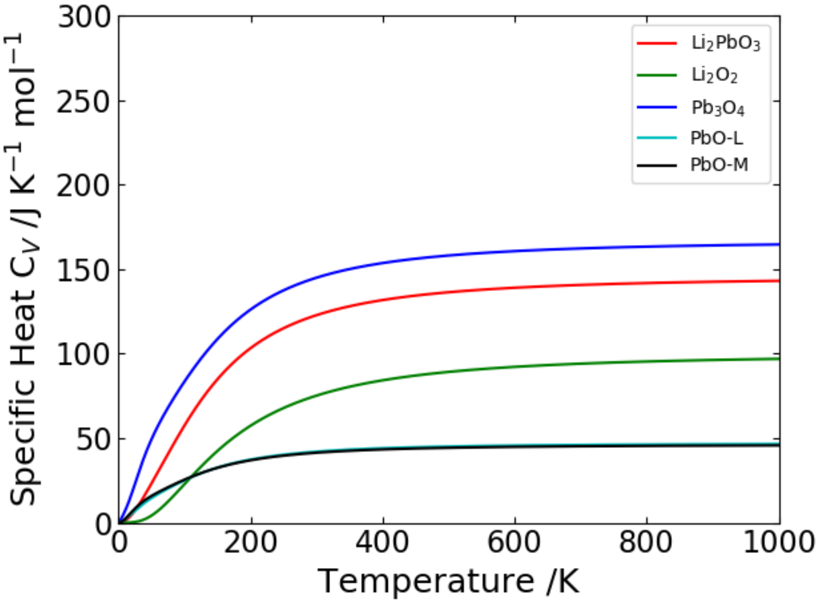

Figure B.2: Specific heat capacity C_V of additional compounds in the Li-Pb-O phase group introduced in Chapter 6.

References

[1] S. E. Vollset et al. “Fertility, mortality, migration, and population scenarios for 195 countries and territories from 2017 to 2100: a forecasting analysis for the Global Burden of Disease Study”. In: *Lancet* 396.10258 (2020), pp. 1285–1306.

[2] B. Never et al. *Carbon consumption patterns of emerging middle classes.* 13/2020. Discussion Paper, 2020.

[3] R. K. *et al.* Pachauri. *Climate change 2014: synthesis report. Contribution of Working Groups I, II and III to the fifth assessment report of the Intergovernmental Panel on Climate Change.* Tech. rep. 2014.

[4] *GISTEMP Team, 2024: GISS Surface Temperature Analysis (GISTEMP), version 4.* `https://data.giss.nasa.gov/gistemp/`. Dataset accessed: 2010-01-15.

[5] N. Lenssen et al. “Improvements in the GISTEMP uncertainty model”. In: *J. Geophys. Res. Atmos.* 124.12 (2019), pp. 6307–6326.

[6] H. *et al.* Lee. *Climate Change 2023: Synthesis Report. Contribution of Working Groups I, II and III to the Sixth Assessment Report of the Intergovernmental Panel on Climate Change.* Tech. rep. 2023.

[7] S. Jack. *Hinkley C: UK nuclear plant price tag could rocket by a third.* `https://www.bbc.co.uk/news/business-68073279`. 23/01 2024.

[8] M. V. Ramana. “Nuclear power and the public”. In: *Bull. At. Sci.* 67.4 (2011), pp. 43–51.

[9] M.S. Kazimi. “Safety aspects of fusion”. In: *Nucl. Fusion* 24.11 (1984), p. 1461.

[10] R. Hagemann, G. Nief, and E. Roth. “Absolute isotopic scale for deuterium analysis of natural waters. Absolute D/H ratio for SMOW”. In: *Tellus A: Dyn. Meteorol. Oceanogr.* 22 (1970).

[11] Harmon Craig and Devendra Lal. “The Production Rate of Natural Tritium”. In: *Tellus A: Dyn. Meteorol. Oceanogr.* (1961).

[12] M. Windridge. “Tokamak Energy”. In: *Commercialising Fusion Energy.* 2053-2563. IOP Publishing, 2020, 5-1 to 5–15.

[13] L.M. Giancarli et al. “Overview of the ITER TBM Program”. In: *Fus. Eng. Des.* 87 (2012), pp. 395–402.

[14] F. Hernández et al. “A new HCPB breeding blanket design for DEMO: Evolution, rationale and preliminary performances”. In: *Fus. Eng. Des.* 124 (2017), pp. 882–886.

[15] K. Kreiss, G. A. Day, and C. R. Schuler. “Beryllium: A Modern Industrial Hazard”. In: *Rev. Public Health* 28.1 (2007), pp. 259–277.

[16] B. N. Kolbasov, V. I. Khripunov, and A. Yu. Biryukov. “On use of beryllium in fusion reactors: Resources, impurities and necessity of detritiation after irradiation”. In: *Fus. Eng. Des.* 109-111 (2016), pp. 480–484.

[17] M. R. Gilbert et al. “Waste implications from minor impurities in European DEMO materials”. In: *Nucl. Fus.* 59.7 (2019), p. 076015.

[18] F. A. Hernandez and P. Pereslavtsev. “First principles review of options for tritium breeder and neutron multiplier materials for breeding blankets in fusion reactors”. In: *Fus. Eng. Des.* 137 (2018), pp. 243–256.

[19] T. Hayashi, S. Konishi, and K. Okuno. “Tritium release behavior from neutron-irradiated Li_8PbO_6”. In: *J. Nucl. Mater.* 170 (1990), pp. 60–65.

[20] F. A. Hernández et al. “Overview of the HCPB research activities in EUROfusion”. In: *IEEE Trans. Plasma Sci.* 46.6 (2018), pp. 2247–2261.

[21] J. Yablon. “Predicting the Binding Energies of the 1s Nuclides with High Precision, Based on Baryons which Are Yang-Mills Magnetic Monopoles”. In: *J. Mod. Phys.* 4.4A (2013), pp. 70–93.

[22] T. Tanabe. *Tritium: Fuel of Fusion Reactors.* Springer, 2016.

[23] J. D. Lawson. “Some Criteria for a Power Producing Thermonuclear Reactor”. In: *Proceedings of the Physical Society. Section B* 70.1 (Jan. 1957), p. 6.

[24] H. S. Bosch and G. M. Hale. “Improved formulas for fusion cross-sections and thermal reactivities”. In: *Nucl. Fusion* 32.4 (1992), p. 611.

[25] S. E. Wurzel and S. C. Hsu. “Progress toward fusion energy breakeven and gain as measured against the Lawson criterion”. In: *Phys. Plasmas* 29.6 (2022), p. 062103.

[26] G. G. Dolgov-Saveliev et al. “Investigations of the Stability and Heating of Plasmas in Toroidal Chambers”. In: *United Nations (UN)* (1958), pp. 82–91.

[27] *EUROfusion website.* URL: `%5Curl%7Bhttps://www.euro-fusion.org/.%7D`.

[28] J. L. Bromberg. *Fusion: science, politics, and the invention of a new energy source.* MIT Press, 1982. URL: `https://www.osti.gov/biblio/6686640`.

[29] T. *et al.* Klinger. “Overview of first Wendelstein 7-X high-performance operation”. In: *Nucl. Fusion* 59 (2019).

[30] *Max-Planck-Institut für Plasmaphysik, IPP, diagram of the W7-X stellarator.* URL: `%5Curl%7Bhttps://www.ipp.mpg.de/wendelstein7x%7D`.

[31] K. Okuno, A. Shikov, and N. Koizumi. “Superconducting magnet system in a fusion reactor”. In: *J. Nucl. Mater.* 329-333 (2004), pp. 141–147.

[32] R. Flükiger et al. "Microstructure, composition and critical current density of superconducting Nb3Sn wires". In: *Cryogenics* 48.7-8 (2008), pp. 293–307.

[33] M Suenaga and K. M. Ralls. "Some superconducting properties of Ti–Nb–Ta ternary alloys". In: *J. Appl. Phys.* 40.11 (1969), pp. 4457–4463.

[34] *Tokamak Energy, 2023, Photograph of the ST-40 compact spherical tokamak.* `https://tokamakenergy.com/`.

[35] R. Armar, P. Barabaschi, and Y. Shimomura. "The ITER design". In: *Plasma Phys. Control. Fusion* 44 (2002), pp. 519–565.

[36] M. Keilhacker. "The JET programme to 1996 and beyond". In: *JET-P-94-13* P00022732 (1994).

[37] J. G. Bednorz and K. A. Müller. "Possible high T_c superconductivity in the Ba-La-Cu-O system". In: *Z. Physik B - Condensed Matter* 64 (1986), pp. 189–193.

[38] M. K. Wu et al. "Superconductivity at 93 K in a new mixed-phase Y-Ba-Cu-O compound system at ambient pressure". In: *Phys. Rev. Lett* 58 (1987), p. 908.

[39] L. L. Lucas and M. P. Unterweger. "Comprehensive review and critical evaluation of the half-life of tritium". In: *J. Res. Natl. Inst. Stand. Technol.* 105 (2000), p. 541.

[40] S. Zheng et al. "Fusion reactor start-up without an external tritium source". In: *Fus. Eng. Des.* 103 (2016), pp. 13–20.

[41] R. M. Brown and W. E. Grummitt. "The determination of tritium in natural waters". In: *Can. J. Chem.* 105.4 (1956), pp. 220–226.

[42] A. V. Grosse et al. "Tritium in Nature". In: *Science* 113 (1951), pp. 1–2.

[43] M. Ni et al. "Tritium supply assessment for ITER and DEMOnstration power plant". In: *Fusion Eng. Des.* 88 (2013), pp. 2422–2426.

[44] K. A. Burns, E. F. Love, and C. K. Thornhill. *Description of the tritium-producing burnable absorber rod for the commercial light water reactor TTQP-1-015 Rev 19.* Tech. rep. Pacific Northwest National Lab.(PNNL), Richland, WA (United States), 2012.

[45] M. Kaufmann and R. Neu. "Tungsten as first wall material in fusion devices". In: *Fus. Eng. Des.* 82.5-14 (2007), pp. 521–527.

[46] T. Yamashina and T. Hino. "Overall evaluation study for isotropic graphite as fusion first wall material in Japan". In: *J. Nucl. Mater.* 162 (1989), pp. 841–850.

[47] M. Utili et al. "Status of Pb-16Li technologies for European DEMO fusion reactor". In: *Fus. Eng. Des.* 146 (2019), pp. 2676–2681.

[48] I. R. *et al.* Kirillov. "Lithium cooled blanket of RF DEMO reactor". In: *Fus. Eng. Des.* 49 (2000), pp. 457–465.

[49] M. Eboli et al. "Simulation study of pressure trends in the case of loss of coolant accident in Water Cooled Lithium Lead blanket module". In: *Fus. Eng. Des.* 98 (2015), pp. 1763–1766.

[50] T. Yoneoka, S. Tanaka, and T. Terai. "Compatibility of SiC/SiC composite materials with molten lithium metal and Li16-Pb84 eutectic alloy". In: *Mater. Trans.* 42.6 (2001), pp. 1019–1023.

[51] W. Farabolini et al. "Tritium control modelling for a helium cooled lithium–lead blanket of a fusion power reactor". In: *Fusion Engineering and Design* 81.1-7 (2006), pp. 753–762.

[52] D. K. Sze et al. "Conceptual design of a self-cooled FLiBe blanket". In: *Fusion Technol.* 10.3P2A (1986), pp. 624–632.

[53] T. Ihli et al. "Review of blanket designs for advanced fusion reactors". In: *Fus. Eng. Des.* 83.7-9 (2008), pp. 912–919.

[54] L. C. Cadwallader and G. R. Longhurst. *FLiBe Use in Fusion Reactors-An Initial Safety Assessment.* Tech. rep. Idaho National Lab.(INL), Idaho Falls, ID (United States), 1999.

[55] J. Aubert et al. "Status on DEMO Helium Cooled Lithium Lead breeding blanket thermo-mechanical analyses". In: *Fus. Eng. Des.* 109 (2016), pp. 991–995.

[56] L. Giancarli et al. "Test blanket modules in ITER: An overview on proposed designs and required DEMO-relevant materials". In: *J. Nucl. Mater.* 367 (2007), pp. 1271–1280.

[57] G. Aiello et al. "Development of the helium cooled lithium lead blanket for DEMO". In: *Fus. Eng. Des.* 89.7-8 (2014), pp. 1444–1450.

[58] L. V. Boccaccini et al. "Objectives and status of EUROfusion DEMO blanket studies". In: *Fus. Eng. Des.* 109 (2016), pp. 1199–1206.

[59] A. Del Nevo et al. "Recent progress in developing a feasible and integrated conceptual design of the WCLL BB in EUROfusion project". In: *Fus. Eng. Des.* 146 (2019), pp. 1805–1809.

[60] W. E. Lee et al. "Opportunities for Advanced Ceramics and Composites in the Nuclear Sector". In: *J. Amer. Ceram. Soc.* 96[7] (2013), pp. 2005–2030.

[61] J. Reimann and S. Hermsmeyer. "Thermal conductivity of compressed ceramic breeder pebble beds". In: *Fus. Eng. Des.* 61-62 (2002), pp. 345–351.

[62] M. Abdou et al. "Blanket/first wall challenges and required R&D on the pathway to DEMO". In: *Fus. Eng. Des.* (2015), pp. 2–43.

[63] S. J. Piet et al. "Liquid metal chemical reaction safety in fusion facilities". In: *Fus. Eng. Des.* 5 (1983), pp. 273–298.

[64] T. Ihli et al. "Review of blanket designs for advanced fusion reactors". In: *Fus. Eng. Des.* 83 (2008), pp. 912–919.

[65] G. Zhou et al. “Design study on the new EU DEMO HCPB breeding blanket: Thermal analysis”. In: *Prog. Nucl. Energy* 98 (2017), pp. 167–176.

[66] F. A. Hernández et al. “Consolidated design of the HCPB Breeding Blanket for the pre-Conceptual Design Phase of the EU DEMO and harmonization with the ITER HCPB TBM program”. In: *Fus. Eng. Des.* 157 (2020), p. 111614.

[67] G. Federici et al. “An overview of the EU breeding blanket design strategy as an integral part of the DEMO design effort”. In: *Fus. Eng. Des.* 141 (2019), pp. 30–42.

[68] M. Enoeda et al. “Development of the water cooled ceramic breeder test blanket module in Japan”. In: *Fus. Eng. Des.* 87.7-8 (2012), pp. 1363–1369.

[69] R. Bhattacharyay and Indian TBM Team *et al.* “Status of Indian LLCB TBM program and R&D activities”. In: *Fus. Eng. Des.* 89.7-8 (2014), pp. 1107–1112.

[70] H. L. Swami et al. “Neutronic performance of Indian LLCB TBM set conceptual design in ITER”. In: *Fus. Eng. Des.* 113 (2016), pp. 71–81.

[71] B. K. Yadav et al. “Design updates for helium cooling system of Indian LLCB blanket”. In: *Fus. Eng. Des.* 167 (2021), p. 112342.

[72] M. Zmitko et al. “Development and qualification of functional materials for the EU Test Blanket Modules: Strategy and RD activities”. In: *J. Nucl. Mater.* 417 (2011), pp. 678–683.

[73] C. E. Johnson and G. W. Hollenberg. “Recent advances in the development of solid breeder blanket materials”. In: *J. Nucl. Mater.* 123 (1984), pp. 871–881.

[74] K. Tobita et al. “Water-Cooled Solid Breeding Blanket for DEMO”. In: *Proceedings of ITC18 P1-43* (2008), pp. 285–288.

[75] W. Jiang et al. “Deuterium diffusion in -$LiAlO_2$ pellets irradiated with He+ and D2+ ions”. In: *J. Nucl. Mater.* 538 (2020), p. 152357.

[76] R. Knitter et al. “Fabrication of modified lithium orthosilicate pebbles by addition of titania”. In: *J. Nucl. Mater.* 442 (2013), S433–S436.

[77] C. Alvani et al. “Li_2TiO_3 pebbles reprocessing, recovery of ^6Li as Li_2CO_3”. In: *J. Nucl. Mater.* 307-311 (2002), pp. 837–841.

[78] K. Kataoka et al. “Crystal Growth and Structure Refinement of Monoclinic Li_2TiO_3”. In: *Mater. Res. Bull.* 44 (2009), pp. 168–172.

[79] D Tranqui et al. “Crystal structure of ordered Li4SiO4”. In: *Acta Crystallogr. B* 35.11 (1979), pp. 2479–2487.

[80] H. Kleykamp. “Phase equilibria in the Li–Ti–O system and physical properties of Li_2TiO_3”. In: *Fus. Eng. Des.* 61 (2002), p. 361.

[81] T. Hoshino. “Optimization of sintering conditions of advanced tritium breeder pebbles fabricated by the emulsion method”. In: *Fus. Eng. Des.* 98 (2015), pp. 1788–1791.

[82] B. Konar, M. Van Ende, and I. Jung. “Critical evaluation and thermodynamic optimization of the Li-O, and Li_2O-SiO_2 systems”. In: *J. Eur. Ceram. Soc.* 37.5 (2017), pp. 2189–2207.

[83] R. Knitter et al. “Recent Developments of solid breeder fabrication”. In: *J. Nucl. Mater.* 442 (2013), S420–S424.

[84] K. M. Feng et al. “New progress on design and R&D for solid breeder test blanket module in China”. In: *Fus. Eng. Des.* 89.7-8 (2014), pp. 1119–1125.

[85] J. D. Lulewicz and N. Roux. “Fabrication of Li_2TiO_3 pebbles by the extrusion–spheronisation–sintering process”. In: *J. Nucl. Mater.* 307-311 (2002), pp. 803–806.

[86] R. Knitter and B. Löbbecke. “Reprocessing of lithium orthosilicate breeder material by remelting”. In: *J. Nucl. Mater.* 361 (2007), pp. 104–111.

[87] B. S. Sahu et al. “Synthesis and Sintering of Nanosize Li_2TiO_3 Ceramic Breeder Powder prepared by Autocombustion Technique”. In: *Proc. of Twentieth Annual Conference of Indian Nuclear Society (INSAC-2009)* (Jan. 2010), p. 10.

[88] T. Hoshino and F. Oikawa. “Trial fabrication tests of advanced tritium breeder pebbles using sol–gel method”. In: *Fus. Eng. Des.* 86 (2011), pp. 2172–2175.

[89] K. N. Goswami and S. T. Murphy. “Influence of Lithium Vacancy Defects on Tritium Diffusion in β-Li_2TiO_3”. In: *J. Phys. Chem. C* 124.23 (2020), pp. 12286–12294.

[90] A. Tsuchiya et al. “Influence of surface condition on deuterium release from Li_2TiO_3 pebble”. In: *Fus. Eng. Des.* 89.7-8 (2014), pp. 1280–1283.

[91] T. Kulsartov et al. “Study of Tritium and Helium Release from Irradiated Lithium Ceramics Li_2TiO_3”. In: *Fus. Sci. Technol.* 60 (2011), pp. 1139–1142.

[92] Q. Qi et al. “Investigation on effects of tritium release behavior in Li4SiO4 pebbles”. In: *Nucl. Mater. Energy.* 28 (2021), p. 101036.

[93] L. Zhao et al. “Tritium release in Li_4SiO_4 and $Li_{4.2}Si_{0.8}Al_{0.2}O_4$ ceramics”. In: *J. Nucl. Mat.* 482 (Dec. 2016), pp. 42–46.

[94] C. Xiao et al. “Tritium release kinetics in lithium orthosilicate ceramic pebbles irradiated with low thermal-neutron fluence”. In: *J. Nucl. Mat.* 438 (July 2013), pp. 46–50.

[95] T. Kinjyo et al. “Tritium Diffusivity in Crystal Grain of Li_2TiO_3 and Tritium Release Behavior Under Several Purge Gas Conditions”. In: *Fus. Eng. Des.* 83 (2008), pp. 580–587.

[96] T. Tanifuji et al. “Tritium Release Behavior from Neutron-irradiated Li_2TiO_3 Single Crystal”. In: *J. Nucl. Mater* 258-263 (1998), pp. 543–548.

[97] D. Zhu et al. “Release Behavior of Hydrogen Isotopes Thermally Sorbed in Li_2TiO_3 Single Crystal”. In: *J. Nucl. Mater.* 442 (2013), S437–S441.

[98] W. Kohn and L. J. Sham. “Self-consistent equations including exchange and correlation effects”. In: *Phys. Rev.* 140 (1965), A1133.

[99] P. Hohenberg and W. Kohn. “Inhomogeneous Electron Gas*”. In: *Phys. Rev.* 136 (1964), B864.

[100] Y. Shi et al. “Anisotropic Diffusion of a Charged Tritium Interstitial in Li_2TiO_3 from First-Principles Calculations”. In: *Phys. Rev. Appl.* 10 (2 2018), p. 024021.

[101] J. Wang et al. “Influence of ion irradiations on the microstructure in the tritium breeder material Li_2TiO_3”. In: *Nuclear Instruments and Methods in Physics Research Section B: Beam Interactions with Materials and Atoms* 450 (2019), pp. 189–194.

[102] A. Kumar et al. “Validation of induced radioactivity calculations for candidate fusion materials through measurements in a graphite-centered assembly”. In: *Fus. Eng. Des.* 42.1-4 (1998), pp. 319–327.

[103] P. J. Gierszewski and J. D. Sullivan. “Ceramic sphere-pac breeder design for fusion blankets”. In: *Fus. Eng. Des.* 17 (1991), pp. 95–104.

[104] A. R. Raffray et al. In: *J. Nucl. Mater.* 307 (2002), p. 21.

[105] T. Hoshino et al. “New synthesis method of advanced lithium titanate with Li_4TiO_4 additives for ITER-TBM”. In: *Fus. Eng. Des.* 84.2-6 (2009), pp. 956–959.

[106] J. Han et al. “Fabrication of a Li_4SiO_4–Pb tritium breeding material”. In: *Fus. Eng. Des.* 89.12 (2014), pp. 3046–3053.

[107] G. Schumacher et al. “Improvement of the mechanical stability of lithium-orthosilicate pebbles”. In: *Fus. Eng. Des.* 17 (1991), pp. 31–36.

[108] M. Xiang et al. “Preparation of Li_2TiO_3-Li_4SiO_4 core-shell ceramic pebbles with enhanced crush load”. In: *J. Nucl. Mater.* 466 (2015), pp. 477–483.

[109] R. Chen et al. “Development of an advanced core-shell ceramic pebble with Li_4TiO_4 pure phase core and Li_2TiO_3 nanostructured shell by a physical coating method”. In: *J. Nucl. Mater.* 520 (2019), pp. 252–257.

[110] V. Barabash et al. “Chemical composition and some properties of materials for the ITER in-vessel components for type B radioactive waste assessment”. In: *Internal ITER Document, ITER Document Management (IDM) № ITER_D_2DKPK7 v1* 3.24.05 (2010).

[111] Y. Someya et al. “Fusion DEMO reactor design based on nuclear analysis”. In: *Fus. Eng. Des.* 136 (2018), pp. 1306–1312.

[112] J. H. Kim, S. Nakano, and M. Nakamichi. “A novel method to stably secure beryllium resources for fusion blankets”. In: *J. Nucl. Mater.* 542 (2020), p. 152522.

[113] R. Hofmann and R. Hoppe. “Ein neues oxogermanat: $Li_8GeO_6 = Li_8O_2[GeO_4]$. (Mit einer bemerkung über Li_8SiO_6 und Li_4GeO_4)”. In: *Z. Anorg. Allg. Chem.* 555 (1987), pp. 118–128.

[114] P. Kroeschell, R. Wolf, and R. Hoppe. “Neue Vertreter der Li_8SnO_6-Familie: Li_8IrO_6, Li_8CeO_6 und Li_8CeO_6 [1,2]”. In: *Z. Anorg. Allg. Chem.* 536 (1986), pp. 81–91.

[115] G. P. Wyers and E. H. P. Cordfunke. “Phase relations in the system Li_2O-ZrO_2”. In: *J. Nucl. Mater.* 168.1 (1989), pp. 24–30.

[116] R. Hoppe and R. M Braun. “Die Kristallstruktur von Li_8SnO_6”. In: *Z. Anorg. Allg. Chem.* 433 (1977), pp. 181–188.

[117] M. Jansen and R. Hoppe. “Zur Kenntnis von Li_8CoO_6”. In: *Z Anorg Allg Chem* 898 (1973), pp. 54–62.

[118] S. Saito et al. “Density dependence on thermal properties of Li_2TiO_3 pellets”. In: *J. Nucl. Mater.* 253.1 (1998), pp. 213–218.

[119] S. Claus, H. Kleykamp, and W. Smykatz-Kloss. “Phase equilibria in the Li_4SiO_4-Li_2SiO_3 region of the pseudobinary Li_2O-SiO_2 system”. In: *J. Nucl. Mater.* 230.1 (1996), pp. 8–11.

[120] S. Konishi et al. “Investigation of Lithium Diffusion in Octalithium Plumbate by Conductivity and NMR Measurements”. In: *Journal of the American Ceramic Society* 73.6 (1990), pp. 1710–1713.

[121] S. Colominas et al. “Octalithium plumbate as a breeding blanket ceramic: Neutronic performances, synthesis and partial characterization”. In: *Fus. Eng. Des.* 87 (2012), pp. 482–485.

[122] S. T. Murphy. “Tritium solubility in Li_2TiO_3 from first principles simulations”. In: *J. Phys. Chem. C* 118 (2014), pp. 29525–29532.

[123] K. Li, W.-H. Wang, and Y. T. Li. “First Principles Study of Tritium Diffusion in Li_2TiO_3 Crystal with Lithium Vacancy”. In: *Mater. (Basel)* 11 (2018), p. 2383.

[124] K. Momma and F. Izumi. “*VESTA3* for three-dimensional visualization of crystal, volumetric and morphology data”. In: *J. Appl. Crystallogr.* 44.6 (2011), pp. 1272–1276.

[125] B. Barzel and R. Hoppe. “Zur Kristallstruktur von Li_8PbO_6”. In: *Z. Anorg. Allg. Chem* 515 (1984), pp. 81–86.

[126] M. Trömel, J. Maetz, and M. Müllner. “Die Kristallstruktur von Li_8PbO_6”. In: *Zeitschrift für anorganische und allgemeine Chemie* 449.1 (1979), pp. 102–104.

[127] M Haüy. *Essai D'une theorie sur la structure des crystaux, appliquee a plusieurs genres de substances crystallisees.* Chez Gogue & Nee de la Rochelle Librares, 1784.

[128] P. Flowers et al. *Chemistry 2e.* OpenStax, 2019.

[129] N. N. Greenwood. *Ionic Crystals, Lattice Defects and Nonstoicheometry.* Vol. 1. Butterworths, 1968.

[130] F.A. Kröger. *The chemistry of imperfect crystals.* 2nd. Vol. 2. North-Holland Publishing Company, Ltd., 1974, p. 82.

[131] M. Oyaidzu et al. "Correlation between annihilation of radiation defects and tritium release in Li_2TiO_3". In: *J. Nucl. Mater.* 329 (2004), pp. 1313–1317.

[132] L Boltzmann. "Über die Natur der Gasmoleküle". In: *Philos. Mag.* 3.18 (1877), p. 320.

[133] T. Graham. "A short account of experimental researches on the diffusion of gases through each other, and their separation by mechanical means". In: *Quarterly J., N. S.* (1829).

[134] A Fick. "Ueber Diffusion". In: *Phil. Mag. and Jour. Sci.* 10 (1855), p. 31.

[135] S. Arrhenius. "Über die Dissociationswärme und den Einfluss der Temperatur auf den Dissociationsgrad der Elektrolyte". In: *Z. Phys. Chem.* 4U.1 (1889), pp. 96–116.

[136] D. G. Truhlar, B. C. Garrett, and S. J. Klippenstein. "Current status of transition-state theory". In: *J. of Phys. Chem.* 100 (1996), p. 12771.

[137] T. Wyttenbach et al. "Ion mobility analysis of molecular dynamics". In: *Rev. Phys. Chem.* 65 (2014), pp. 175–196.

[138] J. M. Delaye et al. "Molecular dynamics simulation of radiation damage in glasses". In: *J. Non Cryst. Solids.* 357.14 (2011), pp. 2763–2768.

[139] J. J. Li et al. "The incorporation of xenon at point defects and bubbles in uranium mononitride". In: *J. Nucl. Mater.* 586 (2023), p. 154656.

[140] M. Born and R. Oppenheimer. In: *Ann. Physik* 84 (1927), p. 457.

[141] W. Pauli. “Über den Zusammenhang des Abschlusses der Elektronengruppen im Atom mit der Komplexstruktur der Spektren”. In: *Z. Physik* 31 (1925), pp. 765–783.

[142] J. C. Slater. “The theory of complex spectra”. In: *Phys. Rev.* 34 (1929), p. 1293.

[143] D. Hartree. “The Wave Mechanics of an Atom with a Non-Coulomb Central Field. Part I. Theory and Methods”. In: *Math. Proc. Camb. Philos. Soc.* 24 (1928), pp. 89–110.

[144] J. P. Perdew and A. Zunger. “Self interaction correction to density functional approximations for many electron systems”. In: *Phys. Rev. B* 23 (1981), p. 5048.

[145] D. M. Ceperley and B. J. Alder. “Ground State of the Electron Gas by a Stochastic Method”. In: *Phys. Rev. Lett.* 45.7 (1980).

[146] J. P. Perdew, K. Burke, and M. Ernzerhof. “Generalized Gradient Approximation Made Simple”. In: *Phys. Rev. Lett.* 77(18) (1996), p. 3868.

[147] F. Bloch. “Über die Quantenmechanik der Elektronen in Kristallgittern”. In: *Z. Physik* 52 (1929), pp. 555–600.

[148] J. C. Phillips and L. Kleinman. “New Method for Calculating Wave Functions in Crystals and Molecules”. In: *Phys. Rev.* 116 (1959), p. 287.

[149] M. C. Payne et al. “Iterative Minimization Techniques for Ab Initio Total-Energy Calculations: Molecular Dynamics and Conjugate Gradients”. In: *Rev. Mod. Phys.* 64 (1992), pp. 1045–1097.

[150] D. R. Hamman, M. Schlüter, and C. Chiang. “Norm-conserving pseudopotentials”. In: *Phys. Rev. Lett.* 43 (1979), p. 1494.

[151] D. Vanderbilt. “Soft self-consistent pseudopotentials in a generalized eigenvalue formalism”. In: *Phys. Rev. B* 41 (1990), pp. 7892–7895.

[152] Peter E Blöchl. “Projector augmented-wave method”. In: *Phys. Rev. B* 50.24 (1994), p. 17953.

[153] X. Gonze and C. Lee. “Dynamical matrices, Born effective charges, dielectric permittivity tensors, and interatomic force constants from density-functional perturbation theory”. In: *Phys. Rev. B* 55 (1997), p. 10335.

[154] L. Chaput et al. “Phonon-phonon interactions in transition metals”. In: *Phys. Rev. B.* 84 (2011), p. 094302.

[155] A Togo and I Tanaka. “First principles phonon calculations in materials science”. In: *Scr. Mater.* 108 (Nov. 2015), pp. 1–5.

[156] A. Togo et al. “First principles phonon calculations of thermal expansion in Ti_3SiC_2, Ti_3AlC_2 and Ti_3GeC_2”. In: *Phys. Rev. B* 81 (2010), p. 174301.

[157] M. W. Finnis, A. Y. Lozovoi, and A. Alavi. “The Oxidation of NiAl: What Can We Learn from Ab Initio Calculations?” In: *Annu. Rev. Mater. Res.* 35 (2005), pp. 167–207.

[158] M. W. Chase Jr. et al. *NIST JANAF thermochemical tables 1985.* NIST, 1986.

[159] *Linstrom, P. J. and Mallard, W. J.* NIST Chemistry WebBook, NIST Standard Reference Database Number 69.

[160] J. Heyd, G. E. Scuseria, and M. Ernzerhof. “Hybrid functionals based on a screened Coulomb potential”. In: *J. Chem. Phys.* 118 (2003), p. 8207.

[161] Y. Kumagai and F. Oba. “Electrostatics-Based Finite-Size Corrections for First-Principles Point Defect Calculations”. In: *Phys. Rev. B* 89 (2014), p. 195205.

[162] C. Freysoldt, J. Neugebauer, and C. G. Van de Walle. “Fully *ab initio* finite-size corrections for charged-defect supercell calculations”. In: *Phys. Rev. Lett.* 102 (2009), p. 016402.

[163] S. T. Murphy and N. D. M. Hine. “Anisotropic Charge Screening and Supercell Size Convergence of Defect Formation Energies”. In: *Phys. Rev. B* 87 (2013), p. 094111.

[164] H. Jónsson, G. Mills, and K. W. Jacobsen. “Classical and Quantum Dynamics in Condensed Phase Simulations”. In: *Classical and Quantum Dynamics in Condensed Phase Simulations* (1998), pp. 385–404.

[165] G. Henkelman and H. Jónsson. “Improved tangent estimate in the nudged elastic band method for finding minimum energy paths and saddle points”. In: *J. Chem. Phys.* 113 (2000), p. 9978.

[166] D. Sheppard, R. Terrell, and G. Henkelman. “Optimization methods for finding minimum energy paths”. In: *J. Chem. Phys.* 128.13 (2008), p. 134106.

[167] G. Henkelman, B. P. Uberuaga, and A. Jónsson. “A climbing image nudged elastic band method for finding saddle points and minimum energy paths”. In: *J. Chem. Phys.* 113 (2000), p. 9901.

[168] A. W. Davies and S. T. Murphy. “Fundamental properties of octalithium plumbate ceramic breeder material”. In: *J. Nucl. Mater.* 552 (2021), p. 152982.

[169] M. H. H. Kolb et al. “Li_4SiO_4 based breeder ceramics with Li_2TiO_3, $LiAlO_2$ and $Li_XLa_YTiO_3$ additions, part I: Fabrication”. In: *Fus. Eng. Des.* 115 (2017), pp. 39–48.

[170] M. L. Jackson, P. A. Burr, and R. W. Grimes. “Defect processes in Be12X (X=Ti,Mo,V,W)”. In: *Nucl. Fus.* 57 (2017), p. 086049.

[171] I. Palermo et al. “Preliminary neutronic assessment of a helium-cooled Li8PbO6 breeding blanket design for DEMO”. In: *Fus. Eng. Des.* 87 (2012), pp. 195–199.

[172] S. T. Murphy et al. “Atomistic Simulation of the Structural, Thermodynamic and Elastic Properties of Li_2TiO_3”. In: *J. Phys. Chem. C* 115 (2011), pp. 21874–21881.

[173] T. Tang and D-L Luo. “Density functional theory study of electronic structures 3 in lithium silicates: Li_2SiO_3 and Li_4SiO_4”. In: *J. At. Mol. Sci.* 1.3 (2010), pp. 185–200.

[174] Y. Shi et al. “Density functional study of lithium vacancy in Li_4SiO_4: Trapping of tritium and helium”. In: *J. Nucl. Mater.* 467 (2015), pp. 519–526.

[175] G. Kresse and J. Furthmüller. “Efficient iterative schemes for ab initio total-energy calculations using a plane-wave basis set”. In: *Phys. Rev. B* 54 (1996), p. 11169.

[176] M. D. Segall et al. “First-principles simulation: ideas, illustrations and the CASTEP code”. In: *J. Phys.: Condens. Matter* 14 (2002), pp. 2717–2744.

[177] S. Clark et al. “First Principles Methods Using CASTEP”. In: *Z. Kristallogr.* 220 (2005), pp. 567–570.

[178] H. J. Monkhorst and J. D. Pack. “Special points for Brillouin-zone integrations”. In: *Phys. Rev. B* 13 (1976), p. 5188.

[179] G. Kresse and D. Joubert. “From ultrasoft pseudopotentials to the projector augmented-wave method”. In: *Phys. Rev. B* 59 (1999), p. 1758.

[180] S. Hull et al. “The elastic properties of lithium oxide and their variation with temperature”. In: *J. Nucl. Mater.* 160 (1988), pp. 125–134.

[181] J. E. Taggart et al. “Scrutinyite, natural occurrences of alpha PbO_2 from Bingham, New Mexico, U.S.A., and Mapimi, Mexico Scrutinyite, natural occurrences of alpha PbO_2 from Bingham, New Mexico, U.S.A., and Mapimi, Mexico”. In: *Can. Miner.* 26 (1988), pp. 905–910.

[182] E. J. Convington and D. J. Montgomery. “Lattice constants of separated lithium isotopes”. In: *J. Chem. Phys.* 27 (1957), pp. 1030–1032.

[183] H. P. Klug. “A redetermination of the lattice constant of lead”. In: *J. Am. Chem. Soc.* 68 (1946), pp. 1493–1494.

[184] K. P. Huber and G. Herzberg. *Molecular Spectra and Molecular Structure.* Springer, 1979.

[185] M. Gajdoš et al. "Linear optical properties in the projector-augmented wave methodology". In: *Phys. Rev. B* 73 (2006), p. 045112.

[186] S. Baroni et al. "Phonons and related crystal properties from density-functional perturbation theory". In: *Rev. Mod. Phys.* 73 (2001), p. 515.

[187] K. Refson, S. J. Clark, and P. R. Tulip. "Variational density functional perturbation theory for dielectrics and lattice dynamics". In: *Phys. Rev. B* 73 (2006), p. 155114.

[188] Z. Wan et al. "First-principles study of electronic, dynamical and thermodynamic properties of Li_2TiO_3". In: *Eur. Phys. J. B* 85 (2012), p. 181.

[189] J. Yan et al. "First-principles calculation of the structural, electronic, dynamical, and thermodynamic properties of Li4TiO4". In: *Fus. Eng. Des.* 129 (2018), pp. 241–246.

[190] S. Ma et al. "A new interatomic pair potential for the modeling of crystalline Li_2SiO_3". In: *Mater. Des* 118 (2017), pp. 218–225.

[191] X. Xiang et al. "Density functional theory calculations of point defects and hydrogen isotopes in Li_4SiO_4". In: *AIP Adv.* 5 (2015), p. 107136.

[192] A. W. Davies and S. T. Murphy. "Thermodynamics and phase stability of Li_8XO_6 octalithium ceramic breeder materials (X = Pb, Ce, Ge, Zr, Sn)". In: *J. Phys.: Condens. Matter* 34 (2022), p. 355701.

[193] N. Kuganathan et al. "Defects, diffusion and dopants in Li_8SnO_6". In: *Heliyon* 7 (2021), e07460.

[194] S. Huang et al. "Y-doped Li_8ZrO_6: A Li-ion battery cathode material with high capacity". In: *J. Am. Chem. Soc.* 137 (2015), pp. 10992–11003.

[195] M. Übeyli. “Investigation on tritium breeding capability of solid-liquid breeders in a (DT) fusion driven hybrid reactor”. In: *Czech. J. Phys.* 56 (2006), B170–B175.

[196] K. Shin-mura et al. “Li vaporization property of Li_8ZrO_6 and Li_5AlO_4 as tritium breeders”. In: *Fus. Eng. Des.* 136 (2018), pp. 869–873.

[197] K. Okuno and H. Kudo. “Tritium diffusivity in lithium-based ceramic breeders irradiated with neutrons”. In: *Fus. Eng. Des.* 8 (1989), pp. 355–358.

[198] H. Stoll and R. Hoppe. “Eine notiz über $Li_4[PbO_4]$ [1, 2]”. In: *Z. Naturforsch. B* 39 (1984), pp. 566–576.

[199] H. Völlenkle and A. Wittman. “Die Kristallstruktur von Li_4GeO_4”. In: *Z. Kristallogr. Krist.* 128 (1969), pp. 66–71.

[200] V. V. Atuchin et al. “Low-temperature chemical synthesis and microstructure analysis of GeO_2 crystals with α-quartz structure”. In: *Cryst. Growth Des.* 9 (2009), pp. 1829–1832.

[201] A. Jain et al. “The Materials Project: A materials genome approach to accelerating materials innovation”. In: *APL Mater.* 1 (2013), p. 011002.

[202] *Joint Committee on Powder Diffraction Standards, JSPDS 34-0394.*

[203] *Joint Committee on Powder Diffraction Standards, JSPDS 26-0867.*

[204] W. Czekalla R.and Jeitschko. “Preparation and crystal structure of $Li_6Zr_2O_7$ and $Li_6Hf_2O_7$”. In: *Z. Anorg. Allg. Chem.* 619 (1993), pp. 2038–2042.

[205] F. J. Torres, J. M. Amigó, and J. Alarcón. “X-ray powder diffraction study of monoclinic V^{4+}-ZrO_2 solid solutions obtained from gels”. In: *J. Solid State Chem.* 173 (2003), pp. 40–44.

[206] J. L. Hodeau et al. “Neutron profile refinement of the structures of Li_2SnO_3 and Li_2ZrO_3”. In: *J. Solid State Chem.* 45 (1982), pp. 170–179.

[207] *Joint Committee on Powder Diffraction Standards, JSPDS 41-1445.*

[208] T. R. Durrant et al. “Relation between image charge and potential alignment corrections for charged defects in periodic boundary conditions”. In: *J. Chem. Phys.* 149 (2018), p. 024103.

[209] R. D. Shannon. “Revised effective ionic radii and systematic studies of interatomic distances in halides and chalcogenides”. In: *Acta Cryst. A* 32 (1976), pp. 751–767.

[210] M. W. Jr. Chase. *NIST-JANAF Thermochemical Tables, Fourth Edition.* NIST, 1998.

[211] M. Asou, T. Terai, and Y. Takahashi. “Enthalpy and heat capacity of $LiAlO_2$ and Li_2SnO_3 from 300 to 1000 K”. In: *J. Nucl. Mater.* 175 (1990), pp. 42–46.

[212] A. Glensk et al. “Understanding Anharmonicity in fcc Materials: From its Origin to *ab initio* Strategies beyond the Quasiharmonic Approximation”. In: *Phys. Rev. Lett.* 114 (19 2015), p. 195901.

[213] H. L. JohnSton and T. W. Bauer. “Low temperature heat capacities of inorganic solids, VII. Heat capacity and thermodynamic functions of Li_2O. Thermodynamics of the Li_2O-H_2O system”. In: *J. Am . Chem. Soc.* 73 (1951), pp. 1119–1122.

[214] A. W. Davies et al. “The High Temperature Intrinsic Defect Chemistry of Li_8PbO_6 Ceramic Breeding Material”. In: *J. Phys. Chem. C.* 127 (2023), pp. 22265–22276.

[215] S. T. Murphy and N. D. M. Hine. “Point Defects and Non-stoichiometry in Li_2TiO_3”. In: *Chem. Mater.* 26 (2014), pp. 1629–1638.

[216] M. W. D. Cooper, S. T. Murphy, and D. A. Andersson. “The defect chemistry of UO2±x from atomistic simulations”. In: *J. Nucl. Materials* 504 (2018), pp. 251–260.

[217] W. D. Neilson and S. T. Murphy. “DefAP: A Python code for the analysis of point defects in crystalline solids”. In: *Comput. Mater. Sci.* 210 (2022), p. 111434.

[218] Patrick Rinke et al. "Defect Formation Energies without the Band-Gap Problem: Combining Density-Functional Theory and the *GW* Approach for the Silicon Self-Interstitial". In: *Phys. Rev. Lett.* 102 (2 Jan. 2009), p. 026402.

[219] H. Okamoto. "Li-O (Lithium-Oxygen)". In: *J. Phase Equilibria Diffus.* 34.2 (2013), p. 169.

[220] D. Risold, J. I. Nagata, and R. O. Suzuki. "Thermodynamic description of the Pb-O system". In: *J. Phase Equil.* 19 (1998), pp. 213–233.

[221] K. C. Lau, L. A. Curtiss, and J. Greeley. "Density Functional Investigation of the Thermodynamic Stability of Lithium Oxide Bulk Crystalline Structures as a Function of Oxygen Pressure". In: *J. Phys. Chem. C* 115.47 (2011), pp. 23625–23633.

[222] F. Hernandez, F. Cismondi, and B. Kiss. "Thermo-mechanical analyses and assessment with respect to the design codes and standards of the HCPB-TBM Breeder Unit". In: *Fus. Eng. Des.* 87 (2012), pp. 1111–1117.

[223] M. J. Rushton. *mjdrushton/potential-pro-fit (available at:.* `https://github.com/mjdrushton/potential-pro-fit`).

[224] B. Brazel and R. Hoppe. "Ueber oxoplumbate(iv). die kristallstruktur von HT-Li_2PbO_3." In: *Z. Naturforsch. B.* (33,1978-41,1986) (1982), 37:1369–1374.

[225] S. T. Gross. "The crystal structure of Pb_3O_4". In: *J. Am. Chem. Soc.* 65.6 (1943), pp. 1107–1110.

[226] J. Leciejewicz. "On the crystal structure of tetragonal (red) PbO". In: *Acta Crystallogr.* 14.12 (1961), pp. 1304–1304.

[227] R. J. Hill. "Refinement of the structure of orthorhombic PbO (massicot) by Rietveld analysis of neutron powder diffraction data". In: *Acta Crystallogr. C* 41.9 (1985), pp. 1281–1284.

[228] H. Föppl. "Die Kristallstrukturen der Alkaliperoxyde". In: *Z. anorg. allg. Chem.* 291.1-4 (1957), pp. 12–50.